Rafael Silva Nunes

Internal standard for amorphous pharmaceuticals products quantification and an application of parametric Rietveld refinement using time, temperature and relative humidity as 'non-crystallographic' parameters

Padrão interno para quantificação de fármacos amorfos e uma aplicação do refinamento de Rietveld paramétrico usando tempo, temperatura e umidade relativa como parâmetros "não cristalográficos"

Thesis submitted to Institute of Chemistry, of Paulista State University, as part of the requirements for obtaining the PhD degree in Chemistry

Supervisor: Carlos de Oliveira Paiva Santos

Araraquara

2014

FICHA CATALOGRÁFICA

Nunes, Rafael Silva
N972i Internal standard for amorphous pharmaceuticals products quantification and an application of Parametric Rietveld refinement using time, temperature and relative humidity as 'non-crystallographic' parameters = Padrão interno para quantificação de fármacos amorfos e uma aplicação do refinamento de Rietveld paramétrico usando tempo, temperatura e umidade relativa como parâmetros 'não cristalográficos'/ Rafael Silva Nunes. – Araraquara : [s.n], 2014
116 p. : il.

Tese (doutorado) – Universidade Estadual Paulista, Instituto de Química
Orientador: Carlos de Oliveira Paiva Santos

1. Físico-química. 2. Norfloxacino. 3. Refinamento de Rietveld paramétrico. 4. Fármacos. 5. Amorfos. I. Título.

Elaboração: Diretoria Técnico de Biblioteca e Documentação do Instituto de Química de Araraquara
Seção Técnica de Aquisição e Tratamento da Informação

Curriculum data

Name: Rafael Silva Nunes

email address: rafael.silvanunes@gmail.com

2010-2014	PhD degree in Chemistry. Universidade Estadual Paulista Júlio de Mesquita Filho, UNESP, Sao Paulo, Brazil with **Sandwich Doctorate** in Durham University (Supervisor: John S. O. Evans) Supervisor: Carlos de Oliveira Paiva Santos Scholarship from: Fundação de Amparo à Pesquisa do Estado de São Paulo

Complementary Education

2013 - 2013	Short Term Course in: Local structure of crystalline materials using PDF. The University of Warwick, Warwick, England Scholarship from: Fundação de Amparo à Pesquisa do Estado de São Paulo
2013 - 2013	Short Term Course: International Workshop on Powder & Electron Crystallography (Protein). University of Patras, Rio, Greece Scholarship from: Fundação de Amparo à Pesquisa do Estado de São Paulo
2012 - 2012	Short Term Course: Powder Diffraction & Rietveld Refinement School. Durham University, Durham, England Scholarship from: Fundação de Amparo à Pesquisa do Estado de São Paulo

2011 - 2011	Short Term Course: 7th TOPAS Course, Bruker Corporation, Bruker, Germany Sydney, Australia Scholarship from: Fundação de Amparo à Pesquisa do Estado de São Paulo
2011 - 2011	Short Term Course in: Aplicações da teoria de grafos à cristalografia. Universidade de São Paulo, Sao Paulo, Brazil
2010 - 2010	Short Term Course: Workshop on Representation Theory of Space Groups. Universidade de la Republica do Uruguai, Montevideo, Uruguay Scholarship from: Fundação de Amparo à Pesquisa do Estado de São Paulo
2010 - 2010	Short Term Course: International School on Fundamental Crystallograph. Universidad de la Republica Uruguay, Montevideo, Uruguay Scholarship from: Fundação de Amparo à Pesquisa do Estado de São Paulo

Professional Experience

Universidade Estadual Paulista Júlio de Mesquita Filho

2011 - 2011	Contract: Bolsista Didático , Position: Bolsista , Working hours (weekly): 4, Schemes of job: Part-time
2011 - 2011	Contract: Bolsista Didático , Position: Bolsista , Working hours (weekly): 4, Schemes of job: Part-time

Projects

2012	Preparation of a standard material for quantification of amorphous in crystalline drug without knowledge of the crystal structure. Description: Research propose to Brazilian Synchrotron (LNLS), Centro Nacional de Pesquisa em Energia e Materiais (CNPEM). Members: Rafael Silva Nunes, Fabiano Yokaichiya, Margareth Kazuyo Kobayashi Dias Franco, Fabio Furlan Ferreira, Carlos O. Paiva Santos (responsible).

2013	Characterization of compounds with transition metals triethanolamine. Description: Research propose to Brazilian Synchrotron (LNLS), Centro Nacional de Pesquisa em Energia e Materiais (CNPEM). Members: Rafael Silva Nunes, Selma Gutierrez Antonio, Carlos O. Paiva Santos, Stanlei Ivair Klein (responsible).

Other activities

2010 a 2011	Alternate student representative of Board of Departamento de Físico-química, Universidade Estadual Paulista, Araraquara, Brazil.

Scientific production

Papers published in journals

1. Nunes, R. S., Fontoura, A. F. M., Canova, H. F., Yokaichiya, F., Franco, M. K. K. D., Paiva-Santos, Carlos O., Evans, John S. O. TUCANO: *in situ* experiments using x-ray powder diffraction at LNLS with temperature and relative humidity control, Journal of Synchrotron Radiation

2. Nunes, R. S., Evans, J. S. O., Paiva-Santos, C. O. Internal standard for pharmaceuticals products I: amorphous quantification at room temperature, Journal of Applied Crystallography

3. Nunes, R. S., Eliziario, S. A., Paiva-Santos, C. O., Evans, J. S. O. Internal standard for pharmaceuticals products II: *in situ* amorphous quantification, Journal of Applied Crystallography

4. Nunes, R. S., Paiva-Santos, C. O., Evans, J. S. O. Internal standard for pharmaceuticals products III: relative humidity application, Journal of Applied Crystallography

Published works in events

1. Nunes, R. S., Fontoura, A. F. M., Evans, J. S. O., Canova, H. F., Scherer, J. A., Paiva-Santos, C. O., Yokaichiya, F., Franco, M. K. K. D. TUCANO: *in situ* temperature- humidity-controlled experiments using powder X-ray diffraction at LNLS. In: 24th Annual Users Meeting of LNLS/CNPEM, 2014, Campinas, Brazil.

2. Nunes, R. S., Evans, J. S. O., Paiva-Santos, C. O. Internal standard for amorphous quantification of pharmaceuticals. In: 28th European Crystallography Meeting, 2013, Warwick, United Kingdom.

3. Nunes, R. S., Sabino, J. R., Lima, E. C. O., Franco Junior, A. Application of Rietveld analysis to determine cations distribution in cobalt ferrite by X-ray dispersion effects. In: 21st Annual Users Meeting of LNLS/CNPEM, 2011, Campinas, Brazil.

4. Nunes, R. S., Paiva-Santos, C. O. Aplicar ou não aplicar a correção de Brindley? In: I Encontro dos Usuários de Técnicas de Difração da CEM, Santo Andre, Brazil.

5. Nunes, R. S., Sabino, J. R., Lima, E. C. O., Franco Junior, A. Cations distribution in ferrites by Rietveld analysis. In: Australian X-ray Analytical Association Workshops, Conference and Exhibition, 2011, Sydney, Australia.

6. Nunes, R. S., Antonio, S. G., Maia, N., Paiva-Santos, C. O. Lithium carbonate as internal standard. In: Australian X-ray Analytical Association Workshops, Conference and Exhibition, 2011, Sydney, Australia.

7. Nunes, R. S., Antonio, S. G., Maia, N., Paiva-Santos, C. O. Standard material for quantification of amorphous in pharmaceuticals. In: 20th Reunião da Associação Brasileira de Cristalografia, 2011, Campinas, Brazil.

8. Nunes, R. S., Bezzon, V. D. N., Ruiz, M. Inserção do software Mercury no ensino de cristalografia como recurso didático motivador. In: IX Evento de Educação em Química, 2011, Araraquara, Brazil.

9. Nunes, R. S., Sabino, J. R., Lima, E. C. O., Franco Junior, A. Application of Rietveld analysis to determine cations distribution in cobalt ferrite and magnesium ferrite. In: International School on Fundamental Crystallography, 2010, Montevideo, Uruguay.

Presentation of lectures

1. Nunes, R. S., Evans, J. S. O., Paiva-Santos, C. O. Internal standard for amorphous quantification of pharmaceuticals; European Young Crystallographers Satellite Meeting, 2013. University of Warwick, Warwick, United Kingdom.

2. Nunes, R. S. Além das aplicações clássicas da difração de raios x por pó, Seminário Geral, 2012. Universidade Estadual Paulista, UNESP, Araraquara, Brazil.

Participation in events

24th Annual Users Meeting of LNLS/CNPEM, March 11th-12th 2014, Campinas, Brazil.

28th European Crystallography Meeting, August 25th-29th 2013, Warwick, United Kingdom.

1st European Young Crystallographers Satellite Meeting, August 25th 2013, Warwick, United Kingdom.

22nd Annual Users Meeting of LNLS/CNPEM, February 28th-29th 2012, Campinas, Brazil.

I Encontro dos Usuários de Técnicas de Difração da CEM, December 7th-8th 2011, Santo Andre, Brazil.

20th Reunião da Associação Brasileira de Cristalografia, February 24th-25th 2011, Campinas, Brazil.

21st Annual Users Meeting of LNLS/CNPEM, February 22nd-23rd 2011, Campinas, Brazil.

Australian X-ray Analytical Association Workshops, Conference and Exhibition, February 6th-11th 2011, Sydney, Australia.

RAFAEL SILVA NUNES

Tese apresentada ao Instituto de Química, Universidade Estadual Paulista, como parte dos requisitos para obtenção do título de Doutor em Química.

Araraquara, 25 de setembro de 2014.

BANCA EXAMINADORA

Prof. Dr. Carlos de Oliveira Paiva Santos (Orientador)
Instituto de Química – UNESP, Araraquara

Prof. Dr. Fernando Luis Fertonani
Instituto de Biociências, Letras e Ciências Exatas – UNESP, São José do Rio Preto

Prof. Dr. Paulo César Pires Rosa
Faculdade de Ciências Médicas - UNICAMP, Campinas

Drª Cristiane Barbieri Rodella
Centro Nacional de Pesquisa em Energia e Materiais - CNPEM, Campinas

Prof. Dr. Adailton João Bortoluzzi
Universidade Federal de Santa Catarina - UFSC, Florianópolis

To my wife, my mother and my father.

Acknowledgments

I am grateful to all energy produced by these 4 years of PhD. Positive or negative, all evolution during this time was due to its influence;

To Professor Carlos Paiva, for the opportunity to work with him (the greatest Brazilian reference in XRPD), for the unforgettable gastronomic experiences and for support my ideas;

To Professor John Evans, for the greatest science discussions (classes) we've had and for the opportunity of learn the Parametric Rietveld method, created by him;

To my beloved wife Sayonara, the greatest witness of all the difficulties and achievements during these four years and, of course, for all patience;

To my family, grandparents (Marlene, Adélia and Waldivino), mother (Cristina), father (Reinaldo), brothers and sister (Rômulo, Ana and Felipe), cousin/brother (Gabriel), cousins (Brenda, Tom Jr., Fernanda, Lorena, Thais, Diego, Flávia, Flora and Luana), uncles/aunts (Ricardo, Paula, Marystela, Thomas, Marisilva, Peter, Marilene and Tom), nephews and niece (Samuel, João Vitor, Letícia and João Lucas), mother-in-law/father-in-law (Socorro and Pedro) and sisters-in-law/brother-in-law (Mariana, Aline, Érika, Quéginho and Giogio). The simple fact of their presence in my life is responsible for giving me the strength to continue my climb;

To special friends present in these 4 years: Zé, Luna, Mike, Juninho, Gisele, Tarek, Mailer (in memory), Tiago, Brennda, Ludmilla, Bel and Luiz;

To great friend physicists: Udson, Anderson and Tião, and all members of the "Fisicachaça forever";

To my friends in United Kingdom: Raminder, Luiza, Alec, Ivana Evans, Andrew, Mikaëlle, Matt, Chuang Hai and Victoria.

To Chemistry Institute, IQ-UNESP, for the great support to the development of science in Brazil;

To groups Liec, IRE/JSOE and Labcacc (Diego, Neide, Simone and Selma) for all support during these 4 years;

To Vinicius, for been an unexpected friend in a hard time and for all help when necessary;

To LNLS due a key contribution in this project, especially Dr. Fabiano Yokaichiya, Dra. Cristiane Rodella and technician Adalberto Fontoura;

And last but not least, to FAPESP for the financial support to my PhD degree in Brazil and during the time in UK.

"Man is the measure of all things: of things which are, that they are,

and of things which are not, that they are not."

Protagoras (490 BC – 420 BC)

Abstract

Recent studies on solid polycrystalline drugs by x-ray powder diffraction (XRPD) in Brazil, has demonstrated how important this technique can be, especially joined to Rietveld method, for structural understanding of these materials. Amorphous material has a higher internal energy than crystalline materials, what alters their therapeutic effects and it makes of amorphous quantification an important study. As an internal standard with international recognition for this purpose, such as NIST SRM-676a (Al_2O_3), can be economically unviable, a systematic characterization, mainly by XRPD, of a cheap material with liner coefficient absorption of same order of this organic products, to use as internal standard for quantitative phase analysis was made. Good results obtained with LiF, as internal standard, for amorphous pharmaceutical quantification at room temperature, shows its potential for a large-scale application (when compared to results obtained using NIST standard SRM-676a, considering microabsorption effect). Other important focus of this work was i*n situ* XRPD applied to pharmaceutical products and had as highlights: a chamber called TUCANO, to use relative humidity in experiments of *in situ* XRPD, developed with cooperation of Brazilian Synchrotron Light Source (LNLS); the Parametric Rietveld refinement, pioneered applied in Brazil; the first use of relative humidity as 'non-crystallographic' parameter in this refinement; and the application of internal standards (SRM-676a and LiF) during experiments in function of time (at constant temperature), temperature and relative humidity (RH). Norfloxacin (NF, $C_{16}H_{18}FN_3O_3$), has a high structural susceptibility to RH and after crystallization of Norfloxacin sesquihydrate form (the only with known crystal structure) starts, at high RH, the behaviour of its cell parameters were parameterized to obtain a smoothly behaviour between all powder patterns collected during RH variation (0% < RH < 96%), consequently, it was possible to correct the value of the relative humidity really felt by the drug during the experiment and the behaviour of this RH correction seems to fit well to a natural logarithm function. To Mebendazole (MBZ, $C_{16}H_{13}N_3O_3$), also used during amorphous quantification at room temperature, a kinetic study, using Arrhenius plot, from powder patterns collected in function of time at different temperatures between 130°C and 160°C, compare the activate energy calculated, for

transformation of Form C to Form A, using sequential Rietveld refinement and Parametric Rietveld refinement, with and without amorphous quantification (LiF as internal standard). This comparison demonstrates the better efficiency of Parametric refinement and shows how can be the influence of consider amorphous quantification during a kinetic study of a phase transition, which for MBZ a small difference was calculated. A recrystallization of Mebendazole Form B in Ethyl acetate, described in literature, allowed a better exploration of its structural behaviour as a function of temperature and a new crystal structure, crystallized from Form B transformation, was observed. Because of this new crystal structure and due amorphous generation during Form C transformation, new possibilities of MBZ polymorphic map were proposed.

Resumo

Os estudos recentes sobre fármacos sólidos por difração de raios X por pó (DRXP) no Brasil vem demonstrando o quão importante pode ser esta técnica, principalmente aliada ao método de Rietveld, para a compreensão estrutural destes materiais. Materiais amorfos tem uma energia interna maior que a energia interna de materiais cristalinos. Isto pode influenciar diretamente o efeito terapêutico de um medicamento, e isto faz da quantificação de amorfo um estudo importante. Como a utilização de um padrão com reconhecimento internacional, como o padrão NIST SRM-676a (Al_2O_3), pode ser economicamente inviável, foi feito uma caracterização sistemática, principalmente por DRXP, de um material barato e com coeficiente de absorção linear dos raios X da ordem destes produtos orgânicos, a ser usado como padrão interno em análises quantitativas de fases. Os bons resultados obtidos com LiF, como padrão interno, na quantificação de amorfo à temperatura ambiente, mostrou seu potencial para uma aplicação em larga escala (quando comparados aos obtidos pelo padrão NIST SRM-676a, considerando o efeito de microabsorção). Outro importante foco deste trabalho foi a DRXP *in situ* aplicada aos produtos farmacêuticos e teve como destaques: uma câmara chamada TUCANO, para aplicar umidade relativa em experimentos de difração de raios x por pó *in situ*, desenvolvida em colaboração com o Laboratório Nacional de Luz Síncrotron (LNLS); a aplicação, pioneira no Brasil, do refinamento de Rietveld Paramétrico e o primeiro uso da umidade relativa como parâmetro "não cristalográfico" neste refinamento; e aplicação dos padrões internos (SRM-676a e LiF) em experimentos em função do tempo (com temperatura constante), temperatura e umidade relativa (UR). Norfloxacino (NF, $C_{16}H_{18}FN_3O_3$), possui uma alta suscetibilidade estrutural à umidade relativa e depois da cristalização da forma sesquihidratada do Norfloxacino (única estrutura cristalina conhecida) começa, em alta UR, o comportamento dos seus parâmetros de rede foram parametrizados para obter um comportamento suave entre todos os difratogramas coletados durante a variação da UR ($0\% < UR < 96\%$), consequentemente, foi possível corrigir o valor da umidade relativa realmente sentida pelo fármaco durante o experimento e o comportamento desta correção da UR parece se ajustar bem à uma função de logaritmo natural. Para o Mebendazol (MBZ, $C_{16}H_{13}N_3O_3$), também utilizado na quantificação

de amorfo à temperatura ambiente, um estudo cinético, usando a equação de Arrhenius, a partir dos difratogramas coletados em função do tempo em diferentes temperaturas entre 130°C e 160°C, compara a energia de ativação calculada para transformação da Forma C em Forma A, usando o refinamento de Rietveld sequencial e o refinamento de Rietveld Paramétrico, com e sem quantificação de amorfo (LiF como padrão interno). Esta comparação demostra a melhor eficiência do refinamento Paramétrico e mostra como pode ser a influência de considerar a quantificação de amorfo durante um estudo cinético de transição de fase, que para o MBZ uma pequena diferença foi calculada. Uma recristalização do Mebendazol Forma B em acetato de etila, descrito na literatura, permitiu uma melhor exploração do seu comportamento estrutural em função da temperatura e uma nova estrutura cristalina foi observada. Por causa desta nova estrutura cristalina e devido a formação de amorfo durante a transformação da Forma C, novas possibilidades de mapa polimórfico do MBZ são propostos.

List of figures

List of tables

List of abbreviations

DOC – Degree of Crystallinity

DSC – Differential Scanning Calorimetry

FT-Raman – Fourier-Transform Raman spectroscopy

FWHM – Full Width at Half Maximum

ICSD – Inorganic Crystal Structure Database

IR – Infrared spectroscopy

LabCACC – Crystallographic and Crystalline Computational Analysis Laboratory

LCM – Linear Calibration Model

LNLS – Brazilian Synchrotron Light Source

MBZ – Mebendazole

MBZA – Mebendazole Form A

MBZB – Mebendazole Form B

MBZC – Mebendazole Form C

NF – Norfloxacin

PONCKS – Partial or No Known Crystal Structure

Pw – Water vapour pressure

Pws – Saturation water vapour pressure

QPA – Quantitative Phase Analysis

RH – Relative Humidity

ss-NMR – Solid state Nuclear Magnetic Resonance

T_A – Applied temperature

T_G – Gas temperature

TG – Thermogravimetry

T_S – Sample temperature

UNESP – Paulista State University

XRPD – X-Ray Powder Diffraction

WHO – World Health Organization

Contents

Chapter 1
Motivation, Introduction and Goals

Crystallographic and Crystalline Computational Analysis Laboratory (LabCACC), funded by Carlos Paiva in 1993, has focus on pharmaceutical products since 2007. Since then, one Thesis and three Dissertations were published at UNESP library with titles:

"Application of XRPD and Rietveld refinement in crystalline pharmaceutical polymorphs" (Antonio, 2010);

"Polymorphism in generic and similar drugs" (Salvi, 2012);

"Limits for identification and quantification of finasteride polymorphs by XRPD" (Bezzon, 2013);

"Polymorphic characterizations of tablets from public distribution by XRPD" (Tita, 2014).

This thesis, supported by FAPESP (process numbers: 2010/08789-4; 2012/09935-0), explored points of interest for pharmaceutical industries, as previous group's works. The thesis presentation is the union of four main chapters, where each chapter represents a paper to be published in journals of International Union of Crystallography[1-4].

Chapter 2[2] presents a comparison between two potential materials, LiF and Li_2CO_3, for amorphous pharmaceutical quantification at room temperature with linear absorption coefficient (μ) of same order of organic compounds. Beyond the importance of have a material for amorphous quantification in large-scale, once their higher internal energy than for

---

[1]NUNES, R. S.; FONTOURA, A. F. M.; CANOVA, H. F.; YOKAICHIYA, F.; FRANCO, M. K. K. D.; PAIVA-SANTOS, C. O.; EVANS, J. S. O. TUCANO: in situ experiments using x-ray powder diffraction at LNLS with temperature and relative humidity control. **Journal of Applied Crystallography**.

[2]NUNES, R. S.; EVANS, J. S. O.; PAIVA-SANTOS, C. O. Internal standard for pharmaceuticals products I: amorphous quantification at room temperature. **Journal of Applied Crystallography**.

[3]NUNES, R. S.; ELIZIARIO, S. A.; PAIVA-SANTOS, C. O.; EVANS, J. S. O. Internal standard for pharmaceuticals products II: in situ amorphous quantification. **Journal of Applied Crystallography**.

[4]NUNES, R. S.; ANTONIO, S. G.; PAIVA-SANTOS, C. O.; EVANS, J. S. O. Internal standard for pharmaceuticals products III: relative humidity application. **Journal of Applied Crystallography**.

crystalline material, this chapter shows an important microabsorption study between LiF and Al_2O_3, where the Brindley analysis (Brindley, 1945), a mathematical method for microabsorption correction implemented in TOPAS-Academic, does not work (see appendix A). Chapter 2 also shows the applicability of LiF tested during Mebendazole (MBZ, $C_{16}H_{13}N_3O_3$) amorphous quantification (see appendix B).

Polymorphism is a very important crystallographic property of pharmaceuticals products. The high number of phase transition possibilities, depending on external parameters (temperature, relative humidity, pressure, etc.), represents an abundant area to explore, but a concerned more for pharmaceutical industry.

The stability of a medicine, according World Health Organization (WHO), needs to be tested on different environments conditions (temperature + relative humidity) and subdivided the planet into four zones, as showed in Table 1.1 (Brazil is zone IVB):

Table 1.1: World subdivided by WHO into four zones according temperature and relative humidity.

Climatic zone	Definition	Conditions
I	Temperate climate	21°C/ 45% RH
II	Subtropical and Mediterranean climate	25°C/ 60% RH
III	Hot and dry climate	30°C/ 35% RH
IVA	Hot and humid climate	30°C/ 65% RH
IVB	Hot and very humid climate	30°C/ 75% RH

Source: Created by the author.

In fact, pharmaceutical products with hydrate forms can be very susceptible to relative humidity. However, as the dehydration/rehydration is a reversible process *ex situ* XRPD measurements can be not effective. There was already a small list of chambers with temperature- humidity-controlled to proceed this *in situ* x-ray powder diffraction, but not in Brazil. Therefore, a project in collaboration with Brazilian Synchrotron (LNLS) developed a furnace called TUCANO.

Chapter 3[1] contains a technical presentation and the limits determination for temperature and relative humidity application of TUCANO. It allows applying temperature variation, at N_2 atmosphere, from room temperature up to 250°C and with relative humidity control around 90% from room temperature up to 50°C. In this chapter the temperature applied is corrected by

Parametric Rietveld refinement showing a good control of temperature up to 180°C (see annex C).

Chapter 4[4] shows an application of relative humidity to a drug. Norfloxacin (NF, $C_{16}H_{18}FN_3O_3$), initially present in Form B, transforms into a hydrate form, after exposed to a high RH, and the structural behaviour of this Norfloxacin sesquihydrate analysed in function of RH variation. A peak at 6.5° was observed and its presence depends if the RH is high (appears) or low (disappears). This 'reversible peak' demonstrates the importance of *in situ* experiments.

From four different experiments (RH variation), chapter 4 explores internal standard application, RH variation influence and the behaviour of an API in a medicine form (with excipients), however, the highlight of this chapter is the first parameterization, in function of RH applied, of NF sesquihydrate cell parameters (see annex D). The correction applied to the external parameter fits well to a natural logarithm function, resulted by difficult control of gas flux.

Several pharmaceutical products have one or more phase transitions up to 250°C and amorphous quantification during a phase transition process, induced by temperature, is other interesting point.

Chapter 5[3] quantified the Mebendazole amorphous for each temperature (between 130°C and 160°C), using LiF as internal standard, after an interaction test from thermal analysis (TG and DSC). A simple kinetic study from *in situ* x-ray powder diffraction, using Arrhenius plot, compares the influence of amorphous quantification on activation energy in transformation process of MBZ Form C to MBZ Form A. The quantitative phase analysis, made from sequential Rietveld refinement and Parametric Rietveld refinement, demonstrate the better efficiency of Parametric refinement, mainly when the presence of MBZ Form C is very low (see comparison between cell behaviour with and without correction in annex E).

The recrystallization of Mebendazole Form B in Ethyl acetate, in chapter 5, brings a polemic scientific discussion about its true powder pattern. For this material, assumed in this work as Form B, three possibilities of indexation were tested (see annex F) and its structural behaviour explored as a function of temperature. A new crystal structure, crystallized from Form B transformation, was observed. Because of this new crystal structure and due amorphous generation during Form C transformation, new possibilities of MBZ polymorphic map were proposed.

Chapter 2

Internal standard for amorphous pharmaceuticals products quantification at room temperature

An amorphous, as opposed to a crystalline material, does not have long-range order along three dimensions, but just a short-range order with higher internal energy. This can imply in significant impact on physicochemical properties, such as solubility (Hancock & Zografi, 1997).

Although the pharmaceutical industry apply all effort to obtain a high purity material, during the synthesis of a drug, polymorphic and pseudo-polymorphic forms as well as

amorphous material are frequently formed (Hancock & Zografi, 1997; Bernstein, 2002). Hancock & Zografi described two main situations when amorphous material occurs: (*i*) all the sample is amorphous or (*ii*) partially amorphous sample. In fact, all materials can be considered to have a degree of amorphous-like character, as the surface layer will lose symmetry, perturbing the structure (Cline *et al.*, 2011).

Many analytical techniques can quantify the amorphous present in pharmaceutical products. Those commonly used include X-ray powder diffraction (XRPD), differential scanning calorimetry (DSC), infrared spectroscopy (IR), Fourier-transform Raman spectroscopy (FT-Raman), solid state nuclear magnetic resonance (ss-NMR) and others (Shah *et al.*, 2006). XRPD is the most widely accessible technique for this purpose.

There are several methods that can be applied for amorphous quantification using XRPD, with two different approaches: (*i*) direct approach and (*ii*) indirect approach (Madsen *et al.*, 2011). For direct approaches such as Single Peak, Partial or No Known Crystal Structure (PONKCS), Linear Calibration Model (LCM), Degree of Crystallinity (DOC) and Full Structure, it is necessary to have previous information about the amorphous component such as its intensity contribution to the pattern. For this reason, the methods are applicable when

amorphous presence in the powder pattern is evident. Indirect approaches such as internal and external standard method have the advantage that they do not need previous knowledge about the amorphous component or an evident contribution to the intensity (Madsen *et al.*, 2011).

The most common method to determine amorphous material by XRPD is the internal standard method (Klug & Alexander, 1974). It consists of adding a material with known crystallinity and can be applied through Rietveld quantitative analysis (Rietveld, 1969; Hill & Howard, 1987), equation 2.1,

$$C_\alpha = \frac{S_\alpha (ZMV)_\alpha}{\sum_i S_i (ZMV)_i}, \quad (2.1)$$

where C_α is concentration of phase α and S, Z, M and V are scale factor, number of formula units per unit cell, mass of the formula unit and the unit cell volume. The amorphous amount (C_{amor}) is calculated by difference, using equation 2.2 (Madsen *et al.*, 2011),

$$C_{amor} = 1 - \sum Corr(C_\alpha), \quad (2.2)$$

and the real concentration of phase α, $Corr(C_\alpha)$, is given by equation 2.3,

$$Corr(C_\alpha) = C_\alpha \frac{C_{s,weighed}}{C_{s,calculated}}, \quad (2.3)$$

where $C_{s,weighed}$ is the concentration of standard added to the mixture and $C_{s,calculated}$ is the concentration calculated from Rietveld analysis.

Al_2O_3 is commonly used for amorphous quantification. The NIST standard SRM 676a has been developed for this purpose and characterized as having a crystallinity of 99.02% (NIST, 2008; Cline *et al.*, 2011). SRM 676a has two potential disadvantages to use in the routine quantification of pharmaceutical materials. First, the high price of this process when applied batch to batch. Second, the high contrast in the linear absorption factor (μ). For corundum it is about ten times of the pharmaceutical products ($\mu_{Al_2O_3}$ = 124.9 cm^{-1}). This contrast implies in microabsorption effect and the accuracy of phase quantification will be impaired (Taylor & Matulis, 1991). There are two potential ways to avoid this problem, either an internal standard with lower absorption or to change the X-ray energy used to minimize this effect.

Important points to choose an internal standard are, according Langford & Loüer (1996), a material that does not present preferred orientation and with high symmetry (cubic and hexagonal), mainly to avoid peak overlap. However, for pharmaceutical products, it is also very important make sure that no interaction occurs between the internal standard and the drug, because polymorphism is a recurring structural property in pharmaceuticals, and the transformation between polymorphic forms is also well known (Bernstein, 2002).

To choose an appropriate internal standard from the big range of materials with low linear absorption is not trivial. The large use of excipients in medicines could suggests the use of a stable organic compound as lactose or any other, but an excipient can initiates a physical interaction and a more careful interaction study needs to be done (Bharate *et al.*, 2010).

This chapter explores the former option and investigates two potential candidates to be internal standard: LiF and Li_2CO_3, μ_{LiF} =30.8 cm^{-1} and $\mu_{Li_2CO_3}$ = 17.4 cm^{-1} (Cu_α – radiation), with same order of magnitude of absorption as pharmaceuticals. For example, the anthelmintic Mebendazole (MBZ), $C_{16}H_{13}N_3O_3$, the cholesterol absorption inhibitor Ezetimibe, $C_{24}H_{21}F_2NO_3$, and the antibacterial Norfloxacin, $C_{16}H_{18}FN_3O_3$, have μ at λ = 1.5406 Å equal to 8.2 cm^{-1}, 8.6 cm^{-1} and 9.4 cm^{-1} respectively. LiF and Li_2CO_3 have, besides the low linear coefficient absorption, a low price, which is also useful for a large-scale applicability.

To correct the microabsorption effect in the relative intensities, Brindley (1945) made an approach that requires an isotropic particle with homogeneous size. Taylor and Matulis (1991) proposed an implementation of Brindley correction for quantitative phase analysis (QPA) through Rietveld method, using the equation 2.4,

$$C_\alpha = \frac{S_\alpha (ZMV)_\alpha / \tau_\alpha}{\sum_i S_i (ZMV)_i / \tau_i}, \quad (2.4)$$

where the particle absorption factor, τ, is calculate by numerical methods from equation 2.5,

$$\tau_i = \frac{1}{V_i} \int_0^{V_i} exp[-(\mu_i - \bar{\mu})x] dv_i, \quad (2.5)$$

where V_i is the volume of a particle, μ_i is the linear absorption coefficient of phase i, $\bar{\mu}$ is the mean linear absorption coefficient of the mixture and x is the radiation path inside the particle.

After crystallinity determination of these two materials, with SRM-676a as internal standard, they were applied to amorphous quantification of Mebendazole (MBZ), an arbitrary pharmaceutical chose for study in this chapter; it has three polymorphic forms described in the literature, forms A, B and C, where polymorph C (MBZC) transforms to polymorph A (MBZA) (Himmelreich *et al.*, 1977). The amorphous content of MBZ, quantified by LiF and Li_2CO_3 were compared with quantity calculated from SRM-676a. To correct microabsorption effect in the relative intensities of both patterns (MBZ and internal standard), the Brindley approach (1945) was applied as implemented in TOPAS-Academic. Finally, an independent amorphous quantification is made adding different quantities of a pure amorphous material, polystyrene $(C_8H_8)_n$, to the samples of LiF/MBZ

2.1. Experimental section

2.1.1. Sample preparation

All materials analysed are industrially produced. LiF (Êxodo Científica, 99.5%), Li_2CO_3 (LabSynth/Hexis, 99.0% purity) and Al_2O_3 (market, purity); MBZ containing MBZA and MBZC was sourced by Formil Quimica Ltda.. Both NIST standard SRM-676a (Al_2O_3) and commercial Al_2O_3, were used for quantitative phase analyses. For convenience they are label the NIST standard Al_2O_3 as 'SRM-676a' and the commercial Al_2O_3 as 'α-Al_2O_3'.

LiF and Li_2CO_3 were sieved in 200 mesh sieve. Seven different mixtures (15/85; 30/70; 40/60; 50/50; 60/40; 70/30; 85/15 by weight) for α-Al_2O_3/LiF, SRM-676a/LiF, and SRM-676a/Li_2CO_3 were prepared. In SRM-676a/LiF case, two more ratios (5/95; 95/5) were added to these seven different mixtures.

MBZ was carefully mixed in a 50/50 weight ratio, with each internal standard (LiF, Li_2CO_3 and SRM-676a) and more nine mixtures of LiF/MBZ/$(C_8H_8)_n$, 50/(45/5; 40/10; 35/15; 30/20; 25/25; 20/30; 15/35; 10/40; 5/45; 0/50), were prepared (see Table 4).

2.1.2. Data collection

Scanning electron microscopy (SEM) images were taken from samples (LiF, Li_2CO_3 and α-Al_2O_3) that had been dispersed in isopropyl alcohol with help of an ultrasonic tip by a Field Emission Gun JEOL JSM-7500F® model. XRPD studies used conventional and synchrotron radiation in three different diffractometers: a Rigaku RINT2000 and a Bruker D8 diffractometers equipped with Cu K_α radiation were used. For synchrotron radiation, the XPD-D12B line at the National Laboratory of Synchrotron Light (LNLS) in Brazil (Ferreira *et al.,* 2006) with energy of 8 KeV (λ = 1.5498 Å) was used.

All samples (LiF/SRM-676a, LiF/α-Al_2O_3 and Li_2CO_3/SRM-676a) had data collected three times each, in the D8 diffractometer over 10-140° 2θ with a 0.02° step using variable divergence slit 6 mm and 1 second per step. For three of these ratios (30/70; 50/50; 70/30), of LiF/SRM-676a and Li_2CO_3/SRM-676a data were collected on the RINT2000 and at LNLS.

The samples LiF/MBZ and Li_2CO_3/MBZ, had data collected during 10 hours, over 3-10° 2θ with a 0.02° step and 20 seconds per step, in RINT2000. All samples with MBZ (LiF/MBZ, Li_2CO_3/MBZ, SRM-676a/MBZ and LiF/MBZ/$(C_8H_8)_n$) were collected three times over 3-85° 2θ on the D8 and the samples LiF/MBZ, Li_2CO_3/MBZ and SRM-676a/MBZ were also collected in RINT2000 and at LNLS

2.1.3. Analysis Methods

The size distributions and mean size of LiF, Li_2CO_3 and Al_2O_3 were determined from SEM images analysed with the software Image J (Rasband, 2014) considering 200 particles.

All quantitative phase analyses (QPA) were performed in TOPAS-Academic software (Coelho, 2012). For Rietveld refinements the crystal structures of inorganic materials, were obtained from the ICSD (ICSD, 2009) with numbers 31548 (Al_2O_3), 53839 (LiF) and 9009641 (Li_2CO_3); for MBZ polymorphs, the crystal structures were obtained from literature MBZA (Ferreira *et al.*, 2010) and MBZC (Martins *et al.*, 2009).

In all refinements were applied linear absorption correction for adjusting the peak shape due to sample transparency, 14 terms in Chebychev background polynomial, and refined scale factor for each phase, lattice parameters, peak shapes and one general atomic displacement parameter; for MBZA and MBZC, the preferred orientation were corrected by March Dollase model. For data from D8, the refinement applied corrections for: axial divergence (simple axial model), specimen displacement, tube tails correction, variable divergence intensity and a modelled small portion of K_β radiation; with data from RINT2000, only simple axial model and specimen displacement has been applied; and in data collected at LNLS, simple axial model and zero error.

2.2. Results

2.2.1. Crystallinity determination

The LiF used has cubic morphology and a number-weighted average size of D = 0.92 μm (Figure 2.1). Li_2CO_3 has an irregular morphology and a number-weighted particle size of D = 8.14 μm and Figure 2.2 shows the size distribution. Figure 2.3 shows the particle size distribution for α-Al_2O_3 with average size D = 57.89 μm.

Figure 2.1: Cubic morphology of LiF with particle size distribution.

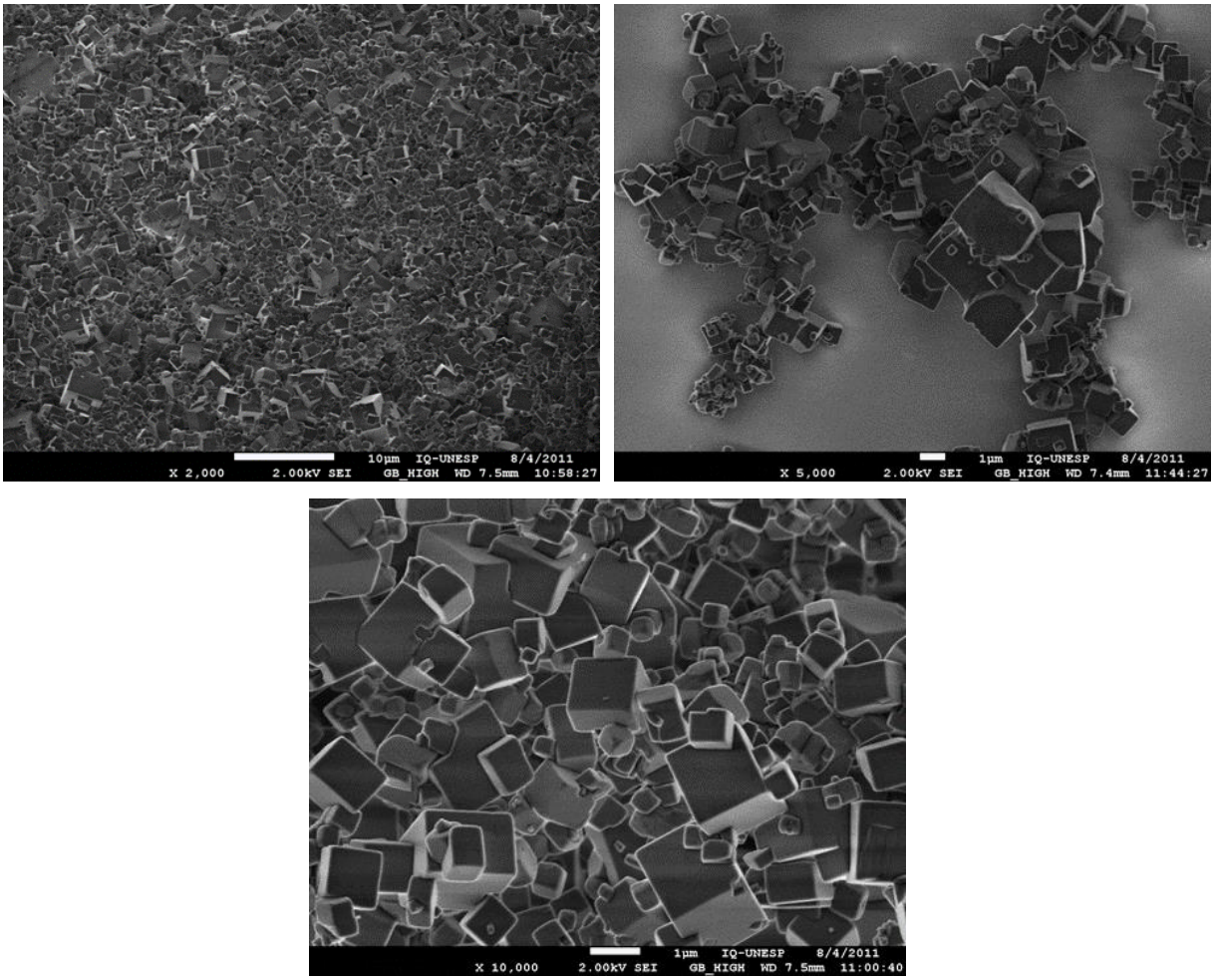

Source: Created by the author.

Figure 2.2: Li_2CO_3 morphology with many defects in its surface layer and size distribution.

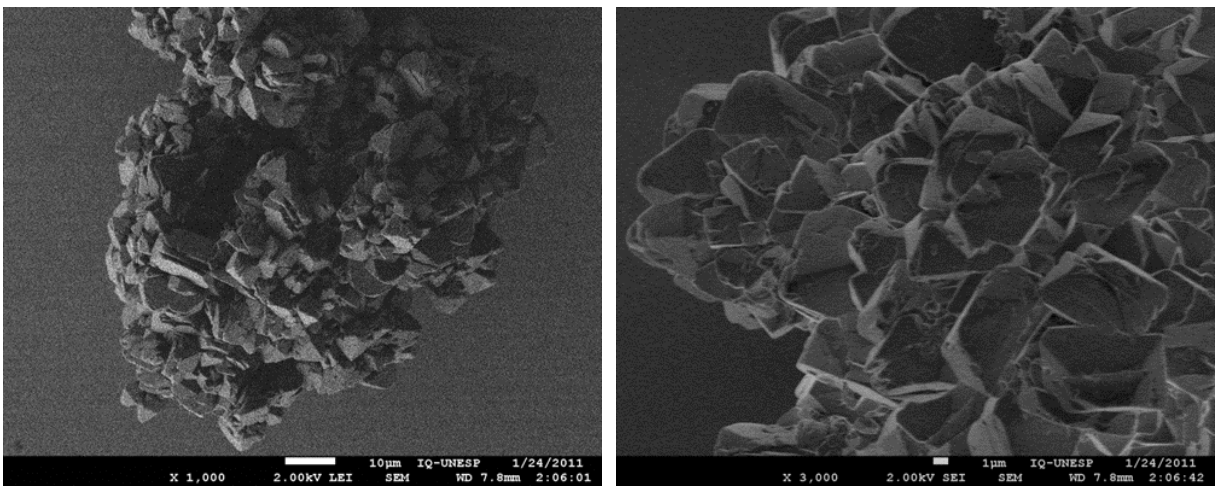

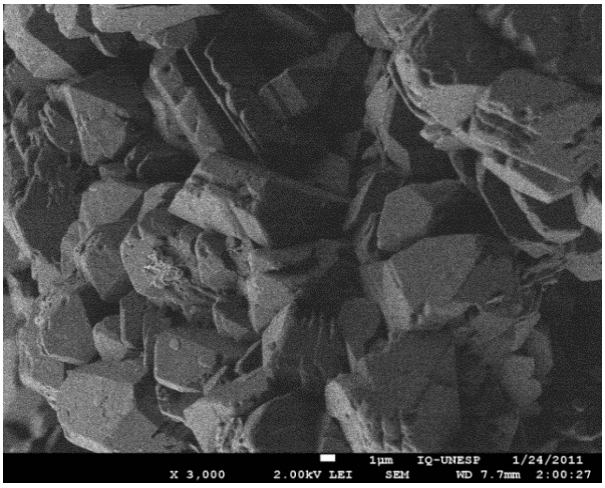

Source: Created by the author.

Figure 2.3: α-Al_2O_3 with particle size distribution.

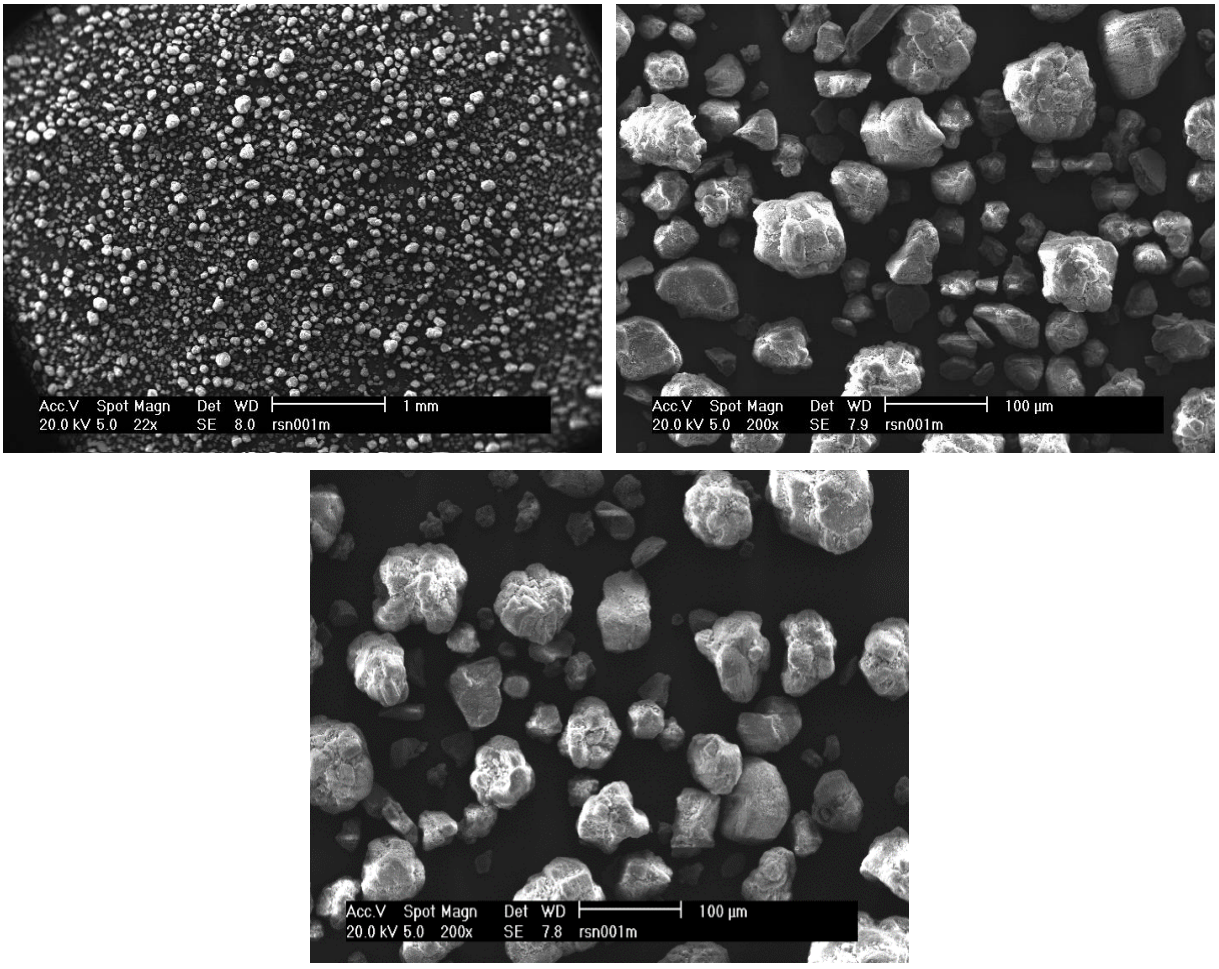

Source: Created by the author.

To quantify the amorphous content for the LiF and Li_2CO_3, SRM-676a was used as an internal standard and was considered as 100% crystalline (Madsen *et al.*, 2011). Table 2.1 contains results of quantitative Rietveld refinement for each material using different ratios of sample to standard on the three instrumental set ups. For LiF, the extracted weight percentage was higher than expected (Table 2.1) for all ratios quantified. This quantification results in a negative amorphous quantity that cannot be correct. The same situation is observed on each instrument (Table 2.1).

Table 2.1: LiF calculated from mixtures with SRM-676a and average R_{wp} (%) and *g.o.f.* values from Rietveld analysis for different ratios (30/70; 50/50; 70/30) collected in three different set-ups: D8, RINT2000 and LNLS.

Set-up	30% LiF			50% LiF			70% LiF		
	LiF %	**R_{wp}**	***g.o.f.***	**LiF %**	**R_{wp}**	***g.o.f.***	**LiF %**	**R_{wp}**	***g.o.f.***
D8	30.87(6)	4.42	1.659	51.35(9)	3.94	1.661	71.79(8)	3.90	1.662
RINT2000	30.5(4)	12.70	1.289	51.1(3)	10.92	1.221	72.0(2)	10.39	1.230
LNLS	31.8(7)	6.38	1.072	52.3(8)	6.79	1.172	73.25(11)	6.86	1.241
D8 (α-Al2O3)	40(3)	4.53	2.350	62(3)	4.19	2.341	76.6(9)	3.75	2.155

Source: Created by the author.

The origin of this effect is almost certainly microabsorption due to the different materials present. The severity of this effect was estimated by preparing a second series of samples using α-Al_2O_3 with a mean particle size of D = 58 μm (Figure 2.3). Table 2.1 contains extracted weight percentages for these samples. Figure 2.4 compares the Rietveld-extracted wt% of LiF with that weighed for the two sets of samples in both cases the weight percentage of LiF is higher than expected and the effect is more severe with the large α-Al_2O_3 particles. This is consistent with the effects of microabsorption.

One approach to correct these effects is to apply a Brindley correction. Figures 2.4a and 2.4b include weight fractions after such a correction. Using particle sizes in this work, the 2 μm size reported by Cline (2011) for SRM-676a and a packing fraction of 0.6 (Coelho, 2013).

Whilst the correction applied improves the agreement between extracted and true wt% of LiF, the LiF quantity is still higher than expected. To fully correct the 50/50 mixture would

require D = 14(2) μm and 120(40) μm for SRM-676a and α-Al_2O_3 respectively. These numbers were calculated from Al_2O_3 quantity behaviour obtained with QPA in function of particle size applied in Brindley approach, they are average sizes that quantify exactly 50/50 for (SRM-676a and α-Al_2O_3)/LiF mixtures.

The Brindley correction could be failing for many reasons including crystallite agglomeration or the presence of a range of crystallite sizes. The SRM-676a data suggest that it is safe to assume 100% crystallinity when working with pharmaceutical samples. So, the Brindley approach was not considered in this case and LiF is assumed to be 100(1)% crystalline. To estimate the error value on this crystallinity assumption, the particle size of SRM-676a and Al_2O_3 were related, in Figure 2.4c, with respective difference between LiF quantified and weighted (% LiF_{calc} - % LiF_{weig}). Assuming all three materials are 100% crystalline, these two points should have a straight line passing through zero point and the linear coefficient of this equation estimates an error for this consideration.

Figure 2.4: Microabsorption effect on mixtures of: a) LiF/SRM-676a (errors bars are smaller than plotted points); b) LiF/Al_2O_3; c) Error on assuming LiF 100% crystalline.

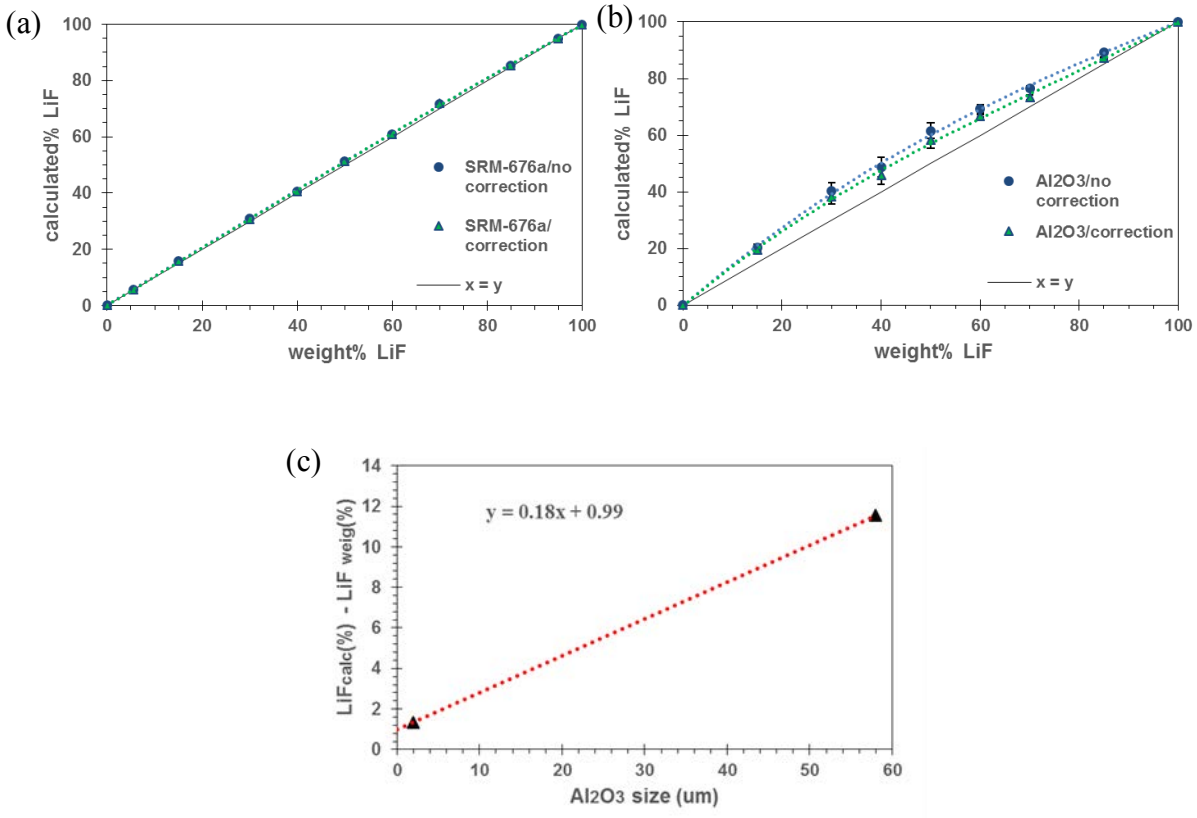

Source: Created by the author.

For mixtures between Li_2CO_3 and SRM-676a (Figure 2.5a), the QPA underestimates the amount of Li_2CO_3 present. If that is due to amorphous material, it is possible extract an amorphous content of. 12(2)%.

The data for ratios 30/70, 50/50 and 70/30, collected using the RINT2000 and LNLS, presented in Figure 2.5b and Table 2.2 give similar values

Figure 2.5: a) QPA behaviour of mixtures SRM-676a/Li_2CO_3 (errors bars are smaller than plotted points); b) Amorphous quantity in 100% of Li_2CO_3 for each ratio of mixtures with SRM-676a collected in D8, RINT2000 and LNLS.

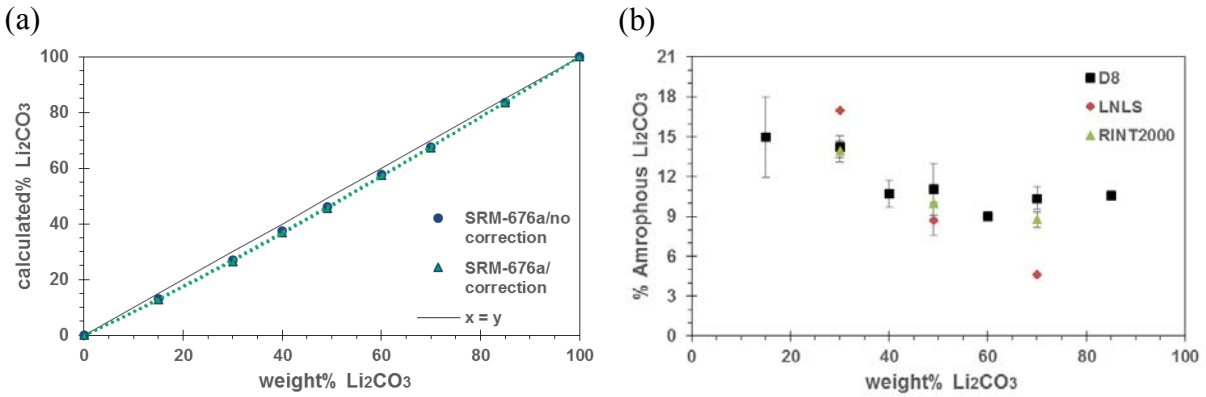

Source: Created by the author.

Table 2.2. Amorphous (%) quantification for Li_2CO_3 in three different set-ups with average values of R_{wp} (%) and *g.o.f.*, for data collected in D8, RINT2000 and LNLS.

	Amorphous	**Amorphous (Brindley correction)**
D8	12(2)	14(2)
LNLS	10(5)	12(5)
RINT2000	11(2)	13(3)

Source: Created by the author.

This is a lower estimate for the quantity of amorphous material as there are likely to be microabsorption effects similar to the LiF case. A Brindley correction applied to those seven

mixtures, collected in D8, gives an amorphous equal to 13(6)%; the same correction was applied to the extra data and are compared in Table 2.2.

LiF is a better candidate to be an internal standard for pharmaceuticals products than Li_2CO_3 due the higher crystallinity added to the higher symmetry what means less overlap.

2.2.2. Amorphous quantification of pharmaceutical products

The MBZ sample used in this study contains MBZA and MBZC polymorphs which have characteristic peaks at 7.7° and 4.9° (2θ), respectively. In order to check that the sample and the polymorphic ratio remained unchanged in contact with the internal standard, room temperature data collections were performed as a function of time, over 10 hours (Figure 2.4), in RINT2000. No alterations, like minor changes in relative intensities or FWHM were observed for either mixture (LiF/MBZ and Li_2CO_3/MBZ). The lack of change in the diffraction data also confirms that there are no issues associated with moisture uptake from the atmosphere. Either LiF or Li_2CO_3 can therefore be used as internal standard for MBZ, for at least 10 hours. A similar interaction test is recommended when using a new pharmaceutical product.

Figure 2.6. Interaction test at room temperature, for mixtures: (a) MBZ/LiF (50/50) and (b) MBZ/Li_2CO_3 (50/50) using XRD in function of time collected over 10 hours.

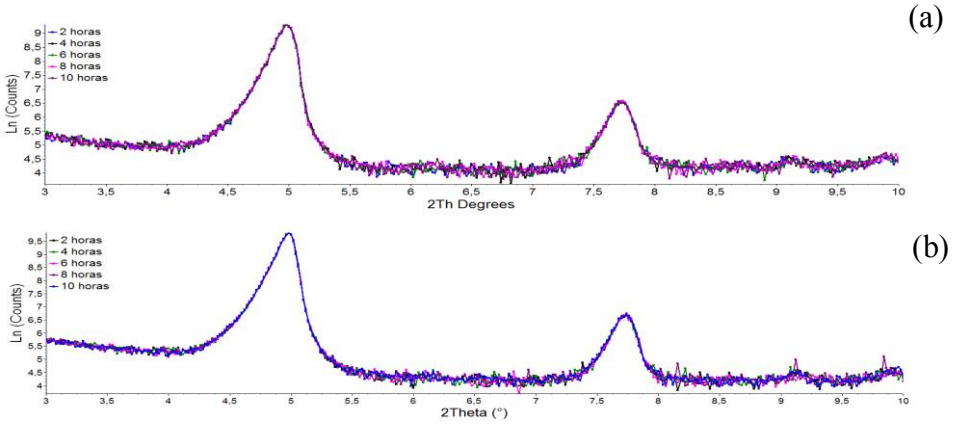

Source: Created by the author.

With SRM-676a, LiF (100% crystalline) and Li_2CO_3 (88% crystalline) as internal standard, the amorphous content of MBZ was quantified; Table 2.3 presents the amount calculated for each internal standard, for each experimental set-up. Values using Li_2CO_3 were corrected for its amorphous content.

Table 2.3 shows that the amorphous amount quantified follows the trend: LiF > Li_2CO_3 > SRM-676a. For mixtures LiF/MBZ and Li_2CO_3/MBZ, there are not microabsorption effects presence, but there were present in previous Li_2CO_3 amorphous quantification as in the mixture SRM-676a/MBZ. For this reason, amorphous quantification from LiF was considered the best value.

Table 2.3. Amorphous (%) in Mebendazole, quantified using three different internal standards, Al_2O_3, LiF and Li_2CO_3, with respectively Rwp (%) and g.o.f., obtained in each set-up (*Brindley correction).

	Al_2O_3	Al_2O_3 *	Rwp	*g.o.f.*	LiF	Rwp	*g.o.f.*	Li_2CO_3	Rwp	*g.o.f.*
D8	9(2)	10(2)	6.39	2.054	12.1(14)	6.45	2.478	10.61(16)	5.65	2.336
LNLS	9.11(7)	10.03(1)	5.23	1.446	12.00(7)	7.39	1.354	10.22(11)	6.79	1.620
RINT2000	8.8(3)	9.6(3)	15.68	2.994	12.23(9)	16.98	2.721	9.9(4)	15.03	2.486

Source: Created by the author.

To provide additional confidence in the 12% amorphous content determined using the LiF internal standard and to investigate how significantly small absorption effects influence this values a series of experiments were performed in which the 50/50 LiF/MBZ sample was deliberately diluted with an amorphous material. For this purpose amorphous polystyrene was chose to use since it is expected to have an absorption coefficient similar to MBZ and other pharmaceuticals.

From Rietveld refinement, the overestimation of the LiF weight % gives the amorphous quantity in MBZ plus the $(C_8H_8)_n$ added. The average value calculated for MBZ amorphous is 13.0(6)%; these quantities are presented in Table 2.4 and Figure 2.7.

In Figure 2.7, the amorphous quantity of each sample is presented as a function of $(C_8H_8)_n$ added. A least squares straight line fit an intersection with y-of 6.3% corresponding to an amorphous content of 12.6%. The consistent amorphous content across a wide range of LiF/organic material suggests that effects of microabsorption are small.

Table 2.4. Amorphous (%) quantified in each sample LiF/MBZ/$(C_8H_8)_n$ and the respective MBZ amorphous (%) calculate.

LiF	MBZ	$(C_8H_8)_n$	Amorphous Total	MBZ Amorphous
50	**50**	**0**	6.1(4)	12.1(14)
50	**45**	**5**	10.6(3)	12.4(7)
50	**40**	**10**	14.4(8)	13.0(4)
50	**35**	**15**	19.6(2)	13.2(5)
50	**30**	**20**	24.12(7)	13.7(2)
50	**25**	**25**	28.31(3)	13.22(13)
50	**20**	**30**	32.6(2)	13.0(8)
50	**15**	**35**	36.96(6)	13.1(4)
50	**10**	**40**	41.28(6)	12.8(6)
50	**5**	**45**	45.66(4)	13.2(9)
50	**0**	**50**	50	-

Source: Created by the author.

Figure 2.7. a) Amorphous quantification from internal standard method in samples with 50% LiF + x% $(C_8H_8)_n$ + (50 – x)% MBZ (error bars are smaller than plotted points); b) MBZ amorphous quantified in each mixture.

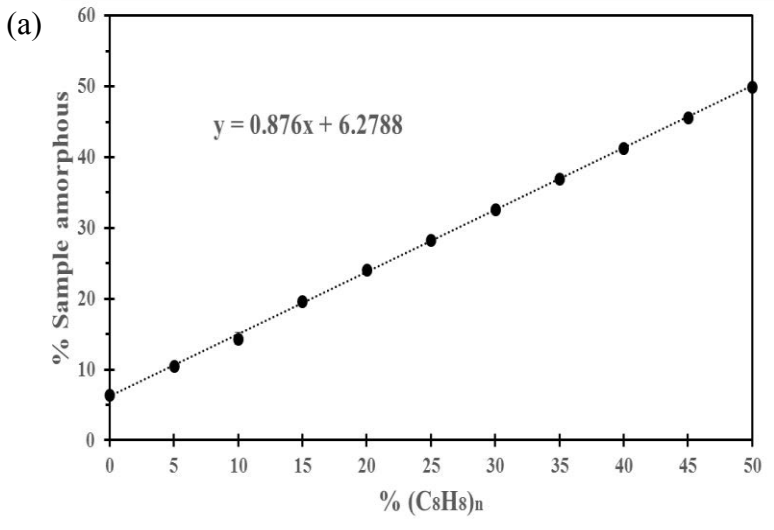

(b)

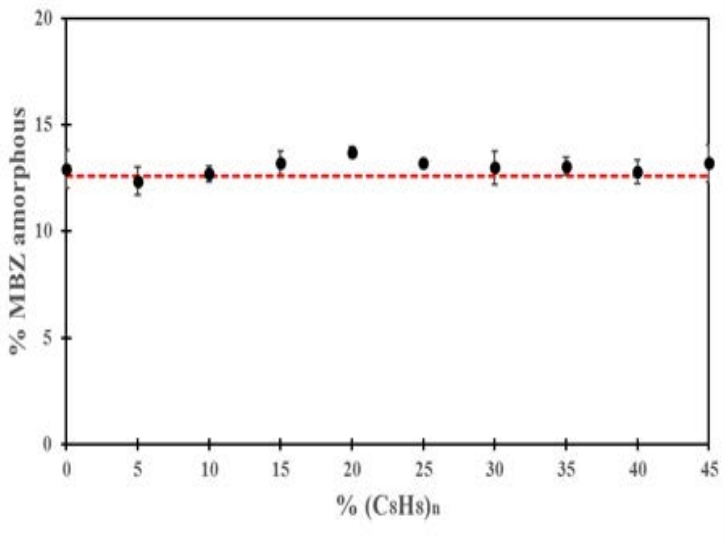

Source: Created by the author.

2.3. Summary

The crystallinity of LiF and Li_2CO_3 were quantified using SRM-676a as internal standard suggesting microabsorption effects limit the accuracy of this procedure, but this work estimate the % crystallinity as 100 and 88% respectively.

We recommend the use of LiF, which calculates 12% amorphous content in MBZ. Systematic errors in this value were investigated by further quantitative dilution with amorphous polystyrene giving confidence in this value.

Chapter 3

TUCANO: *in situ* experiments using x-ray powder diffraction at LNLS with temperature and relative humidity control

Several classes of inorganic and organic materials change their physical, chemical and/or biological features due to relative humidity (RH) and temperature variations (Mono & Schober, 1996; Kishi *et al.*, 2002; Arii & Kishi, 2003; Furuki *et al.*, 2005). These important changes motivated the development of a thermal-humidity controlled sample environment furnace for the synchrotron beamlines at LNLS.

Many pharmaceuticals products are very susceptible to environmental conditions and the process of dehydration/rehydration is a common occurrence (Emery *et al.*, 2009). In many cases, it is a reversible or time dependent process such that *ex situ* measurements is not effective. Another pharmaceutically relevant process is crystallization from the amorphous solid (Byard *et al.*, 2005). The quantification of amorphous content from *in situ* x-ray diffraction data with controlled temperature and relative humidity can facilitate the understanding of the kinetics of this transformation. Both these type of structural changes alters the therapeutic effect of the drug. The stability of drugs in the solid state under moist atmosphere also dictates the behaviour of the pharmaceutical industry from processing to the storage of the product (Trask, 2005; Baratta *et al.*, 2012). Understanding the process of dehydration/rehydration can help to prevent this type of transformation during a product's shelf-life (Ticehurst, 2002). Since a drug's structural behaviour will vary depending on the local climatic conditions, the World Health Organization (WHO) subdivided the planet into four zones according to temperature and relative humidity: zones III (hot and dry) and IV (hot and humid) need particular attention for conducting stability tests (ICH, 2006). This chapter reports the design, construction and

application of a furnace, called TUCANO, to access the relevant conditions at the beamline D10B at LNLS. This chamber permits *in situ* characterization of materials, using synchrotron X-ray powder diffraction, under RH varying from 0.1% to 95% at room temperature (28 °C) and RH from 0.1% to 86% at 50°C. In a dry environment (nitrogen atmosphere), it is possible to heat the sample from room temperature to 250 °C. The design was developed from a number of chambers previously reported (Hashizume et al., 1996; Oetzel et al., 2000; Katsaras & Watson, 2000; Caracciolo et al., 2005; Miura et al., 2011).

X-ray powder diffraction experiments as a function of temperature were performed, on NIST SRM-676a (Al_2O_3) and the temperature profile of the chamber was obtained by Parametric Rietveld refinement (Stinton & Evans, 2007), see Appendix C for more SRM-676a cell parameter behaviour.

Parametric Rietveld refinement allows to work with *"an ensemble of diffraction data collected as a function of time, temperature, pressure or any other variable are fitted to a single evolving structural model. Parametric refinement offers a number of potential benefits over independent or sequential analysis. It can lead to higher precision of refined parameters, offers the possibility of applying physically realistic models during data analysis, allows the refinement of 'non-crystallographic' quantities such as temperature or rate constants directly from diffraction data, and can help avoid false minima"* (Stinton & Evans, 2007).

A careful control of gas temperature and gas flux determined the maximum RH possible for each temperature up to 50°C. The deliquescence effect of NaCl demonstrates the furnace efficiency for RH *in situ* XRPD experiments.

3.1. Beamline set-up

The X-ray powder diffraction beamline (XPD) at Brazilian Synchrotron Light Source (LNLS), Campinas-Brazil, is located at exit B of the 1.67 T bending magnet, D10 (Ferreira *et al.*, 2006). This beamline allows the use of energy over a range of $5 - 14$ KeV with an energy resolution better than 0.2 eV. The maximum flux is approximately 8.5×10^{10} photons/s with the current ring of 200 mA obtained with a beam's cross section of approximately 2 mm (H) - 0.8 mm (V) and wavelength at 1.8 Å. The experimental hutch has a slit to reduce the background, a scintillator detector to monitor and normalize the direct beam, a 4+2 circle Huber diffractometer and an ionization chamber to align the sample into the beam. Experiments are in reflection

geometry with a linear Mythen detector placed at 1 meter from the sample (equivalent to 3 degrees)

3.2. Chamber's design

Experiments involving materials sensitive to RH require sample temperature control, water vapour flux control as well as control of the atmosphere temperature inside the chamber. The sample temperature needs to be close to the atmosphere temperature in order to have RH on the sample close to that of the atmosphere. For this purpose, TUCANO has heating systems on the chamber feed gas tubes and on the furnace external wall, provided by thermal conduction from heating strips (Figure 3.1) as well as local heating on the sample.

A mixed gas flow of dry N_2 and wet N_2, produce and control the relative humidity inside the chamber, the wet flow is created by passing dry N_2 through a vessel containing water at controlled temperature (Figure 3.1). The sample temperature must be carefully controlled, because if it is equal or less than dew point temperature, the system becomes a liquid-sample interaction and not a vapour-sample interaction.

Figure 3.1: Schematic of the TUCANO furnace with its electronic and gas flow connections.

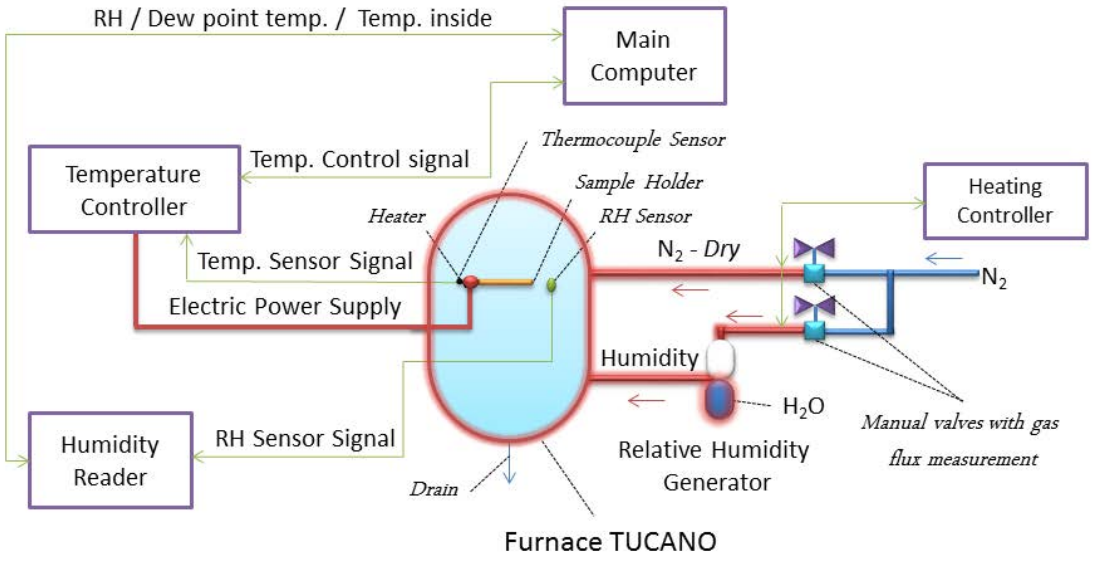

Source: Created by Adalberto Fontoura.

The design of the sample holder support provides homogeneous temperature on the sample. Figure 3.2a shows all constituents of the sample holder support; a heater support and sample holder made from copper, a cartridge resistance heater constructed from a small Kanthal A1 spiral wound element inserted in a tube of ceramic porous alumina 25 mm long with 6 mm diameter, a ceramic base and a goniometric head. Figure 3.2b presents a schematic drawing of TUCANO to explain the components' disposition inside the chamber and Table 3.1 contains the main characteristics of the furnace.

Table 3.1: Summary of the specifications for the TUCANO chamber.

Feature	Specification	Feature	Specification
Maximum temperature under dry N_2 atmosphere	250 °C	Min. *RH* at 25°C	0.1%
		Max. *RH* at 25°C	95%
Maximum temperature with relative humidity control	50 °C	Min. *RH* at 50°C	0.1%
		Max. *RH* at 50°C	86%
Temperature control	±1 °C	Sensor accuracy *RH*	±1.8%

Source: Created by the author.

Figure 3.2: (a) Schematic drawing of constituents of TUCANO sample holder support; (b) schematic drawing of components inside the chamber.

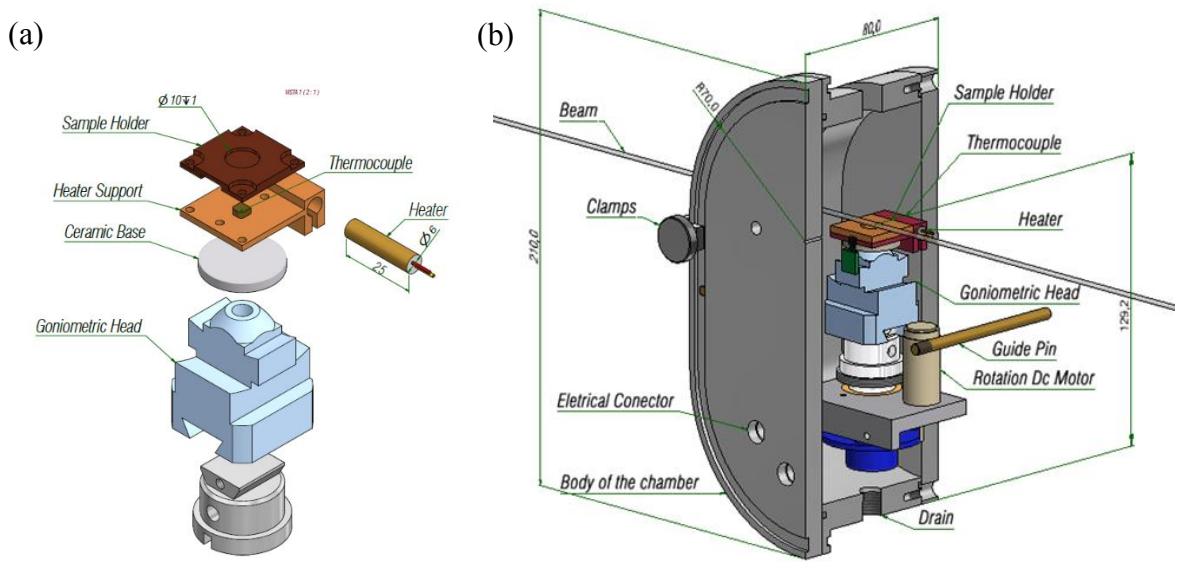

Source: Created by Adalberto Fontoura.

3.3. Results

3.3.1. Heating simulation of the sample holder

To show the effects of the sample holder support (sample holder, resistance, copper and ceramic base) on heating during an experiment, we carried out a simulation with COMSOL Multiphysics® software. This considered parameters such as sample holder material (copper), resistance of ferritic iron-chromium-aluminium alloy (FeCrAl alloy), copper and ceramic base (Figure 3.3).

In this simulation, the system heated from 25 °C to 250 °C and takes 3.7 seconds for sample holder and the copper base temperatures to thermalize with the resistance. The heating occurs gradually and due to a large temperature gradient almost evenly as shown in Figure 3.3. As expected, no large heat transfer to the ceramic base modelled thus avoiding heating the goniometric head. With this result, it is possible to say that at a given temperature, the entire sample surface is equally heated.

Figure 3.3. Heating simulation of the sample holder from 25 °C to 250 °C: (a) time = 0.0 s; (b) time = 1.5 s; (c) time = 3.0 s; (d) time= 7.0 s.

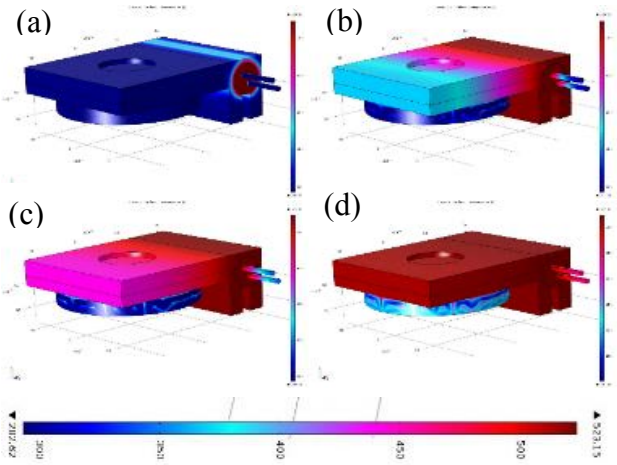

Source: Created by Adalberto Fontoura.

3.3.2. Sample temperature behaviour in TUCANO

Figure 3.4 shows the quality of data obtainable in this chamber for a sample of NIST Al_2O_3 at LNLS. Data were collected from 20-120° 2θ over 3.5 minutes. Rietveld refinement (Rietveld, 1969) was performed using TOPAS-Academic v.5 software (Coelho, 2012). The Rietveld

analysis achieved Rwp = 4.22% with g.o.f. = 1.132, refining 14 terms of a Chebychev background polynomial, cell parameters, zero error, scale factor, peak shape parameters and two atomic displacement parameters (cell parameters refined to a = 4.7593 Å and c = 12.9921 Å).

Figure 3.4: Rietveld refinement of Al_2O_3 recorded at 28 °C from TUCANO's set-up. Observed data is in black, calculated in red, difference in grey.

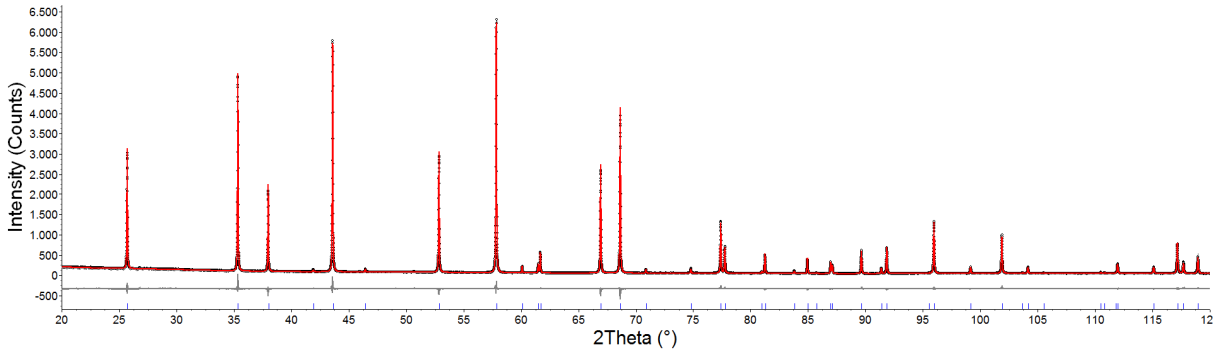

Source: Created by the author.

The temperature calibration of the furnace was checked by heating SRM-676a from 30°C to 250°C, at a heating rate of 5°C min^{-1} with 14 diffraction patterns collected over 23-70° 2θ. Sequential Rietveld refinement and Parametric Rietveld refinement (Stinton & Evans, 2007) were applied to this set data.

Sequential Rietveld refinement is an automating Rietveld refinement, sequentially applied for each pattern starting the next refinement with parameters previously calculated, available in TOPAS-Academic (Topas, 2014).

Figure 3.5a compares cell volume behaviour calculated by both refinement strategies and they have a good agreement with each other. Therefore, the actual temperature of SRM-676a was determined from Parametric Rietveld refinement with polynomial coefficients to describe thermal expansion of Al_2O_3 lattice parameters as reported by Taylor (Taylor, 1984), $X(T) = X_0(1 + X_1T + X_2T^2)$, where X's values correspond to lattice parameters a and c (temperature must be used in degree Celsius), which for temperatures between 20°C and 1232°C, they are: a_0 = 4.7568 Å, a_1 = 6.55×10^{-6} Å°C^{-1}, a_2 =1.82×10^{-9} Å°C^{-2}, c_0 = 12.9886 Å, c_1 = 6.54×10^{-6}Å°C^{-1} and c_2 = 2.60×10^{-9} Å·°C^{-2}; and a calibration polynomial, equation 3.1, to correct true sample temperature,

$$\Delta T = b_1 + b_2T + b_3T^2 + b_4T^3, \quad (3.1)$$

where b_1, b_2, b_3 and b_4 are refined from the whole data simultaneously (Stinton & Evans, 2007). *"To reduce correlations, equations are often expressed with temperature or other quantities rescaled onto a -1 to +1 scale using T* = (2T$_A$ - T$_{MAX}$ - 3T$_{MIN}$)/(T$_{MAX}$ - T$_{MIN}$) during refinement"* (Stinton & Evans, 2007).

The polynomial coefficients were used to calculate the difference between applied temperature (T_A) and sample temperature (T_S), $\Delta T = T_A - T_S$, presented in Figure 3.5b. Figure 3.5b shows that the sample temperature is within 2°C of the set temperature up to 180°C. Above this temperature, the sample temperature increase faster than applied temperature and at 250°C the real sample temperature is approximately 20°C higher. We presume that this is caused by temperature gradients in the apparatus or poor contact between the thermocouple and the sample holder.

Figure 3.5: (a) Comparison between cell volume behaviour determined by sequential Rietveld refinement and Parametric Rietveld refinement with Taylor volume expected for each temperature; (b) Difference of temperature (T_A - T_S) behaviour due temperature applied.

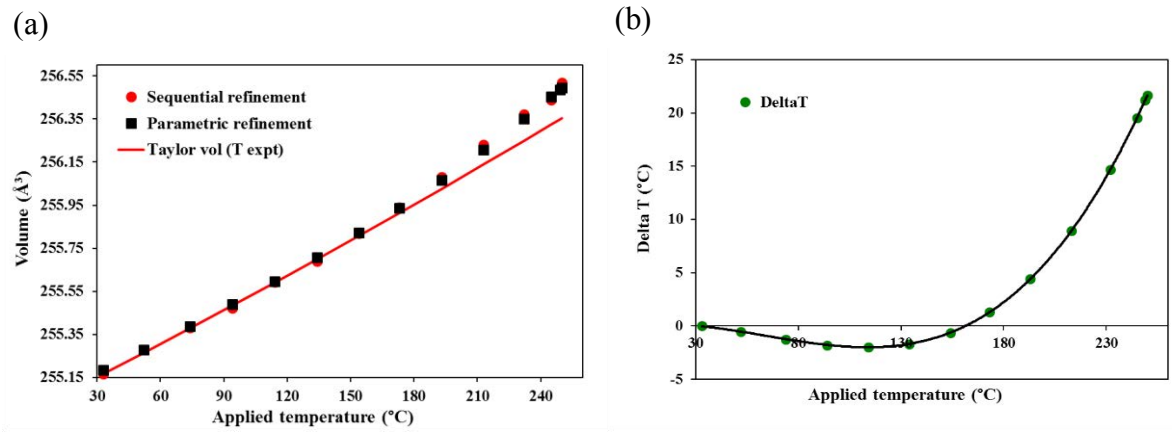

Source: Created by the author.

3.3.3. Humidity behaviour

Relative humidity at a given temperature is defined as the ratio between water vapour pressure, Pw, and saturation water vapour pressure, Pws, as given in equation 3.2,

$$RH = \frac{P_w}{P_{ws}} \times 100\%. \quad (3.2)$$

Saturation water vapour pressure depends exponentially on the gas temperature (Wagner & Pruß, 1995).

To explore the limitation on maximum RH applicable, with good stability (±1%), it is necessary to control the gas flux, gas temperature and applied temperature to the sample holder.

3.3.3. Humidity behaviour

As Pws varies exponentially with gas temperature inside the chamber, a good control of RH depends of the stability of this parameter.

An experiment controlling simultaneously these three parameters was made taking the gas temperature (wet N_2) to the value of the sample temperature (from thermocouple) and the RH behaviour analysed in function of time. If the RH oscillation is not higher than ±1%, it is considered a RH applicable.

Figure 3.6 shows a linear behaviour of the maximum RH achievable as a function of sample temperature up to 50°C; after that RH was not stable due the instability of gas temperature caused by the high gas flux applied and perhaps also due to a limitation on the heating systems on the chamber feed gas tubes and on the furnace external wall. Therefore, TUCANO allows us to work with RH over 0.1% - 95% at room temperature and over 0.1% - 86% at 50°C (Figure 3.6 and Table 3.2).

Figure 3.6: Maximum RH achievable as a function of true sample temperature.

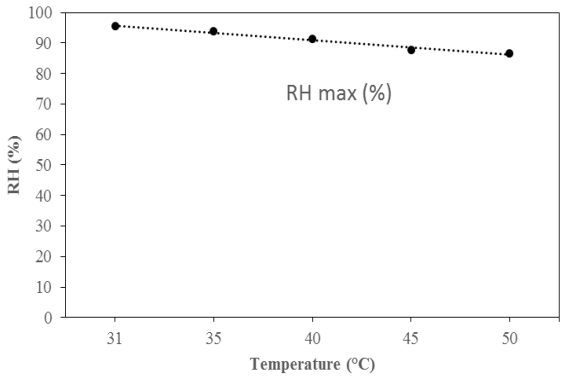

Source: Created by the author.

Table 3.2: Gas temperature (T_G), maximum relative humidity (RH), applied temperature (T_A) and sample temperature (T_S).

T_G (°C)	RH (%)	T_A (°C)	T_S (°C)
31	96	31	31.0
35	95	35	34.9
41	91	40	39.8
47	89	45	44.7
50	87	50	49.5

Source: Created by the author.

3.3.3. Humidity behaviour

As NaCl presents deliquescencent properties, which will depend on the RH, it was chosen to test the efficiency of this set-up. 17 powder diffraction patterns of NaCl were collected over 25-100° 2θ range with sample temperature at 28 °C and RH equal to 90% on the sample. Each pattern was collected for 7 minutes giving an overall experiment time of 2 hours. Data are plotted in Figure 3.7, using the Powder3D software (Hinrichsen, 2004). Rietveld analysis of each data set (mean R_{wp} equal to 8.91% with *g.o.f.* equal to 1.864) refined the zero error, 13 terms of a Chebychev background polynomial, cell parameter, peak shape parameters, scale factor and atomic displacement parameters; it was also necessary to fit weak peaks (at 43.5° and 50.6° 2θ) due to copper sample holder using the Pawley method (Pawley, 1981), these peaks remain throughout the experiment.

In Figure 3.7, all NaCl peaks decrease in intensity as a function of time until they disappear completely in the last pattern, when NaCl fully dissolves. The pattern background (Figure 3.8a), rises during the experiment as NaCl dissolves. The scale factor (Figure 3.8b) becomes smaller for each data set as this process occurs.

The short time of NaCl exposure to set RH of 90% until it becomes liquid, shows the high level of water vapour present in the atmosphere inside the chamber.

Figure 3.7: Deliquescence of NaCl observed at RH = 90%, T = 28 °C.

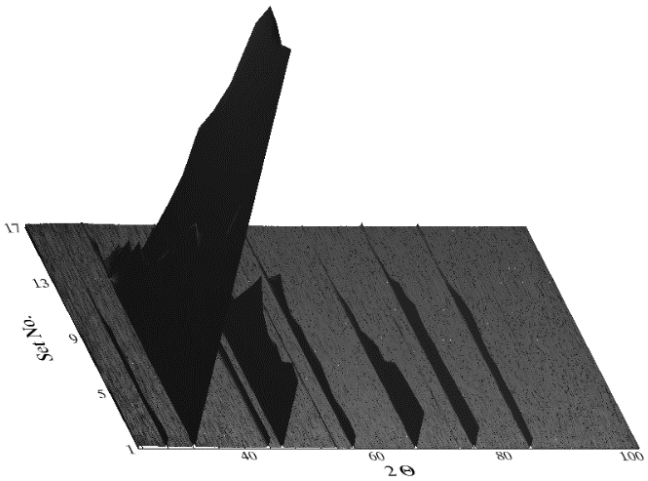

Source: Created by the author.

Figure 3.8. a) Deliquescence of NaCl observed from rise in background; b) NaCl scale factor behaviour from Rietveld refinement.

(a) (b)

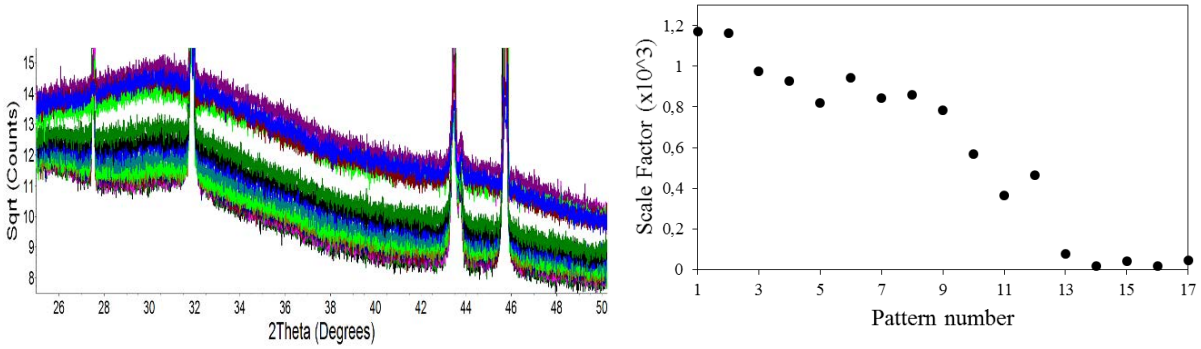

Source: Created by the author.

3.4. Summary

This chapter presents a chamber to perform *in situ* x-ray powder diffraction experiments with temperature and relative humidity control. Parametric Rietveld refinement characterized the sample temperature behaviour and showed that TUCANO's heating system is very good up to 180°C, with an accuracy of ±2°C, but the actual sample temperature at 250°C is around 20°C higher than set. A linear behaviour describes the maximum RH applicable up to 50°C with ±1% stability. The fast NaCl deliquescence effect observed confirms the production of a very humid environment within the chamber, when RH was set to 90%.

Chapter 4

Norfloxacin crystal structure behaviour on relative humidity effect

Structure of solid drugs can be affected by many external parameters, from these, temperature and relative humidity are highlighted by World Health Organization (WHO), that recognize climatic conditions (temperature + relative humidity) as a crucial previous information to a good storage of medicines (ICH, 2006), due the large number of pharmaceuticals sensible to these two parameters (Trask *et al.*, 2005).

Solvate forms or pseudo-polymorphs is a very common phenomenon present in pharmaceutical products such polymorphism. The main solvate form of solid pharmaceutical is hydrate form (water as solvate), where *n* molecules of water can be present in different packing ways inside the crystal structure. In general, hydrate forms reduce the velocity of dissolution compared to their anhydrous forms (Morris & Rodríguez-Homedo, 1993).

For each hydrate packing, the interactions between water molecule and organic compound determine their physical-chemistry properties. There are three main classes: isolated site hydrates, without contact between water molecules and they have van der Waals interaction with the organic compound, channel hydrates, with chains along symmetry directions of water molecules from hydrogen bonds, and ion-associated hydrates, with strong bonds between water molecule and the compound (Tian *et al.*, 2010).

As hydration/dehydration can be a sensible and reversible process (dehydration temperature depends of hydrate packing), *in situ* XRPD experiments with temperature and/or relative humidity controlled are useful to study this process as make possible to study how RH affects a hydrate crystal structure compound (Tian *et al.*, 2010).

This chapter explores the structural behaviour of Norfloxacin sesquihydrate (NF, $C_{16}H_{18}FN_3O_3$) in function of RH variation, using TUCANO (see chapter 3).

For the first time, Parametric Rietveld refinement, applied relative humidity as a 'non crystallography' parameter.

NF, Figure 4.1a, is a fluoroquinolone antibacterial agent used in several infectious diseases, such as urinary tract infection. NF has three anhydrous polymorphs, Form A (Basavoju *et. al.,* 2006), Form B (Sustar *et al.*, 1993; Barbas *et al.*, 2006) and Form C (Barbas *et al.*, 2007), but only polymorph A has its crystal structure solved. Form B and Form C are enantiotropically related to Form A (Barbas *et al.*, 2006; Barbas *et al.*, 2007), while Form C is monotropically related to Form B (Barbas *et al.*, 2007).

NF is very sensitive to relative humidity and presents several hydrate forms, such as 1.125 and 1.25 hydrates (Roy et al., 2008), sesquihydrate Form I (Ravindra et al., 2009), sesquihydrate Form II (Puigjaner *et al.*, 2010), dihydrate (Florence et al., 2000), hemipentahydrate, trihydrate and pentahydrate (Chongcharoen et al., 2008). During hydration process, the interaction neutral molecule anhydrous transforms into a zwitterionic conformation, a neutral molecule with a positive and a negative electrical charge, (Hu *et al.*, 2002).

Figure 4.1: a) Neutral anhydrous Norfloxacin; b) Zwitterionic hydrate Norfloxacin.

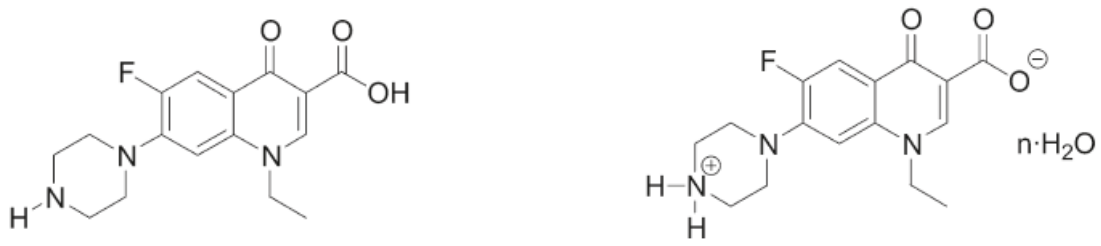

Source: Created by the author.

Sesquihydrate Form I transforms to another polymorph, sesquihydrate Form II, at low temperature, 150 K. All hydrates reported were obtained and then partially and/or completely transformed into Form A (Puigjaner *et al.*, 2010; Chongcharoen *et al.*, 2008).

This chapter presents the first hydration process from NF Form C. This anhydrous form transforms into a sesquihydrate Form I and, from RH = 90%, a new hydrate form appears. The new hydrate has an enantiotropic relationship with NF sesquihydrate Form I. The structural behaviour of NF was studied by Parametric Rietveld refinement. In addition, a tablet of NF was studied under the same conditions.

4.1. Experimental section

4.1.1. Sample preparation

All materials analysed are industrially produced. LiF (Êxodo Científica, 99.5%) and NIST standard SRM-676a (Al_2O_3) are the same previous utilized. NF API was sourced by Nortec and NF tablet bought in a conventional pharmacy.

Mixtures 50/50 were carefully prepared for NF API and tablet materials with LiF and a sample with same ratio made for SRM-676a/NF API.

4.1.2. Data collection

The measurements were performed at XPD beamline. All samples were submitted to a maximum relative humidity (~90-95%) until the hydrate form appears and then the RH was take down to a minimum and so on, to analyse the structure behaviour of sesquihydrate form of NF. For this strategy, it was used TUCANO chamber setup and detector MYTHEN 1K in one Huber diffractometer.

4.1.3. Analysis Methods

Parametric Rietveld refinement (Stinton & Evans, 2007), performed in TOPAS-Academic software (Coelho, 2012), use crystal structures of inorganic materials, obtained from the ICSD (ICSD, 2009) with numbers 31548 (Al_2O_3) and 53839 (LiF). The crystal structure of sesquihydrate form of NF obtained from Ravindra and co-workers paper (2009).

In all refinements (sequential and surface) were calculated independently for each scan, linear absorption correction for adjusting the peak shape due to sample transparency, 14 terms in Chebychev background polynomial, specimen displacement. For each phase, scale factor, peak shapes, lattice parameters and atomic displacement parameter were refined. P, the preferred orientation in NF were corrected by March Dollase model. For NF hydrate form, the lattice parameters are parameterized by a 3rd order polynomial in function of relative humidity rescaled between ±1 (chapter 3). In this way, the parameters refined to calculate the best cell parameter configuration are the coefficients of theses polynomials and the correction (ΔRH) for RH applied; that correction is calculated freely for each scan (the RH's behaviour in TUCANO is still not estimated during the gas flux variation), where $0 \leq RH + \Delta RH \leq 1$. The coefficients of polynomials X_1, X_2 and X_3, calculated in the surface refinement are used as

constant on sequential Rietveld refinement, but the coefficient X_0 is refined to keep the RH as measured.

4.2. Results

The first data set of SRM-676a/NF API sample was collect at RH = 0%. The Rietveld refinement was applied (Figure 4.2) and it is not possible identify any polymorph or hydrate form, with crystal structure already known. From this result, it is possible to affirm that the sesquihydrate form present in future analysis is due RH effect (the parameter that will be variable).

Figure 4.2: Rietveld analysis of SRM676a/NF-API. It is not possible to identify any NF form which crystal structure is already known.

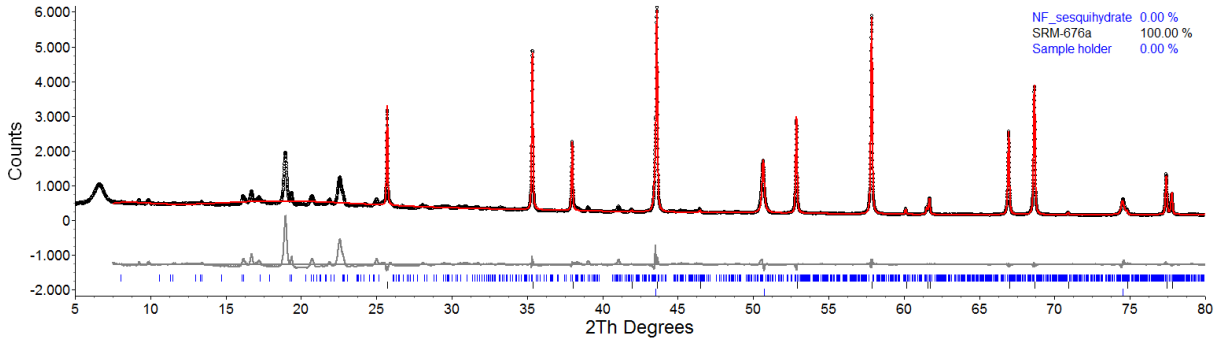

Source: Created by the author.

For this sample, 37 scans were collected under different environment conditions (T = 28°C, RH_{MIN} = 2% and RH_{MAX} = 97%). As the sample does not have sesquihydrate form initially, the refinement is done only from 4th scan, when it is noticeable. At high RH, the sesquihydrate is formed and a peak at 6.5° is observed. The presence of this peak depends of RH, when RH is high the peak appears and when lowered it disappears (Figure 4.3 and Figure 4.4). At this moment, it is not possible explains what the presence of this peak means. But according literature it is possible that had appeared a new hydrate (Chongcharoen *et al.*, 2008; Puigjaner *et al.*, 2010; Hu *et al.*, 2002; Roy *et al.*, 2008; Florence *et al.*, 2000; Ravindra *et al.*, 2009; Katdare *et al.*, 1986; Yuasa *et al.*, 1981).

Figure 4.3: SRM-676a/NF data set plotted in: a) 2D-film and b) 3D.

(a)

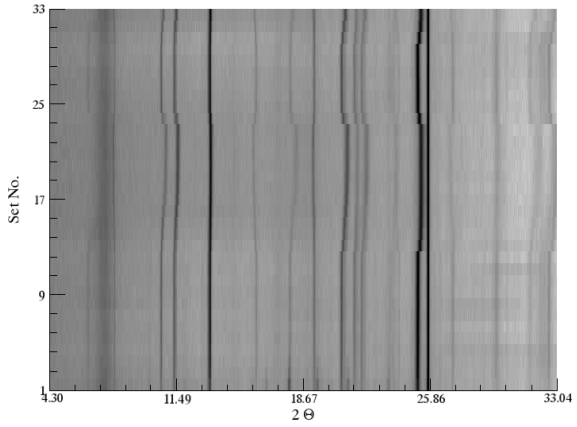

(b)

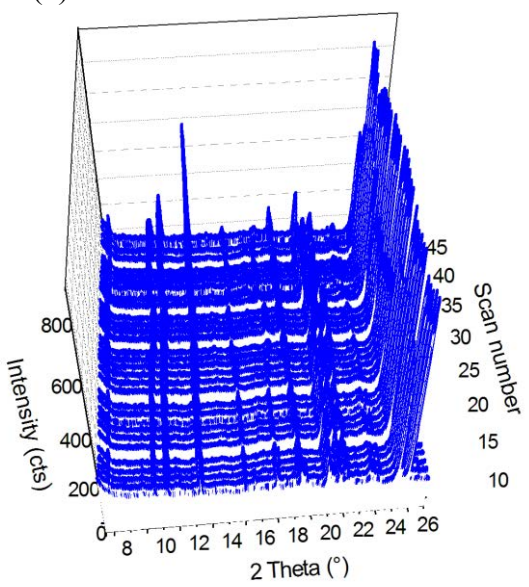

Source: Created by the author.

Figure 4.4: Comparison between first scan and the last scan of each cycle during RH variation (RH going up and going down), in sequence.

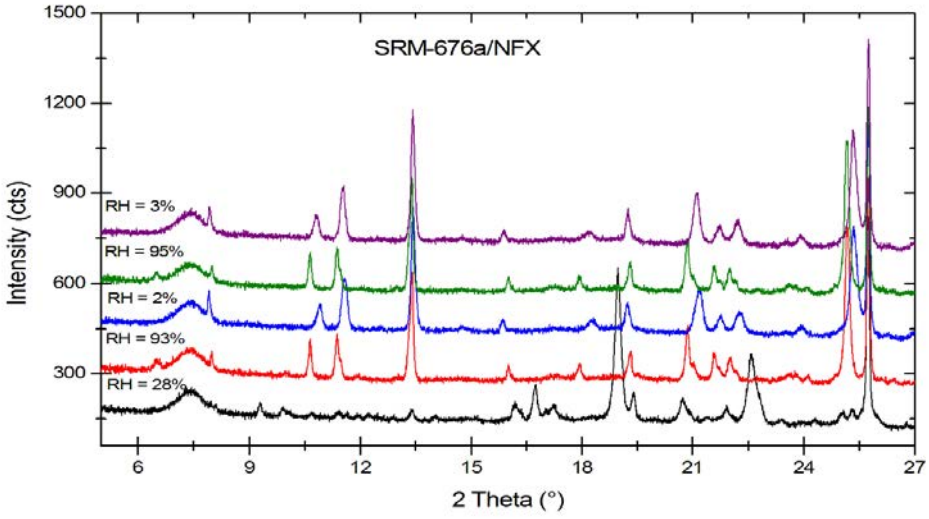

Source: Created by the author.

The volume of NF hydrate is calculated from sequential and surface Rietveld refinement, but the RH is corrected by parametric refinement. Figure 4.5a presents the volume behaviour from these two ways and the volume calculated from sequential is presented in function of RH corrected (RH_C). The good agreement between both volumes calculated (sequential and surface) in function of RH_C means that the parametric Rietveld refinement is reliable. This correction makes the cell parameters have a behaviour more physically possible (see Appendix D).

The main reason for such difference between RH applied (RH_A) and RH_C is the transition from a minimum to a maximum and vice-verse. This happens because in this system is not possible have a careful control of gas flux in this mid-time and the sample takes a while longer than the sensor to answer structurally to this variation. Figure 4.5b is the RH_C behaviour in function of RH_A shows the bigger difference on these 'RH of transition' and the behaviour can be fitted by a natural logarithm function.

Figure 4.5: a) Comparison between NF sesquihydrate volumes calculated by sequential Rietveld refinement (in function of RH_A and RH_C) and surface Rietveld refinement; b) RH_C behaviour in function of RH_A fitted by a natural logarithm function.

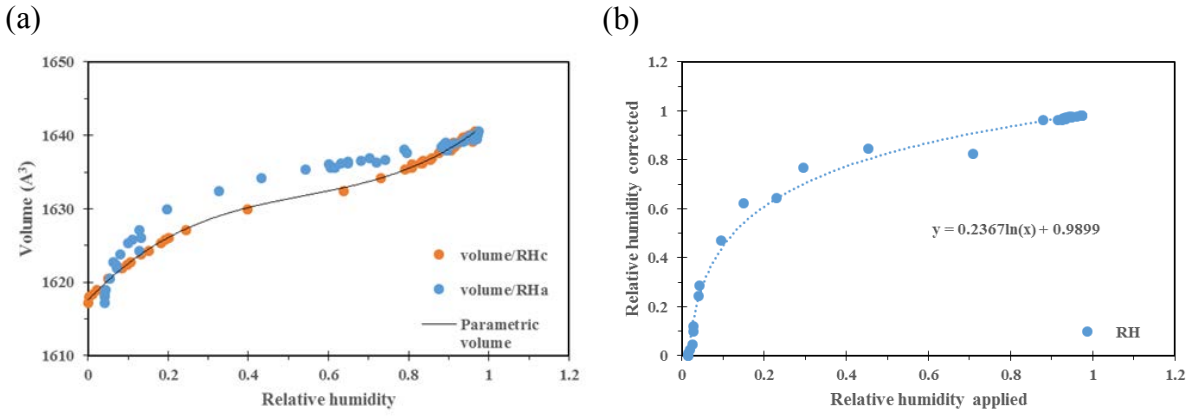

Source: Created by the author.

The mixture LiF/NF API was submitted to two different interval of RH. Firstly to an interval of 8% ≤ RH ≤ 88% with 41 scans and the second interval on 4% ≤ RH ≤ 97% with 55 scans.

For the first interval (Figure 4.6) it is not observable the peak at 6.5°, however there are more peaks, perhaps referent to others crystallographic forms of NF, between 17.5° and 25°

(Figure 4.7). This different transformation is neglected in this analysis, where only the NF hydrate structure is explored in function of RH.

Figure 4.6: LiF/NF API data set plotted in: a) 2D-film and b) 3D.

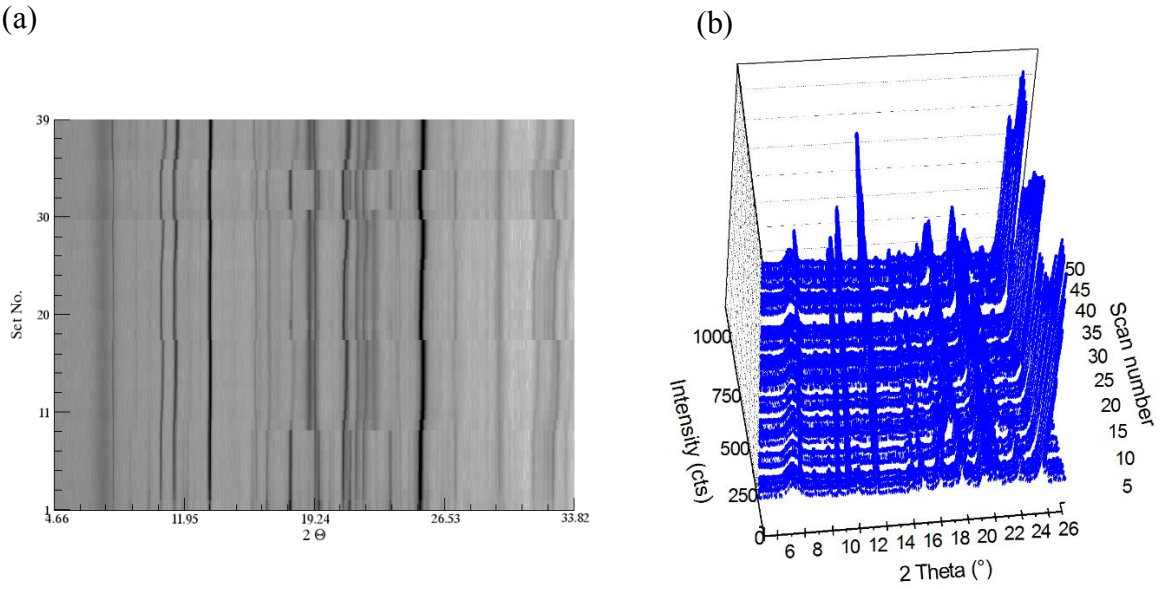

Source: Created by the author.

Figure 4.7: Comparison between first scan and the last scan of each cycle during RH variation (RH going up and going down), in sequence.

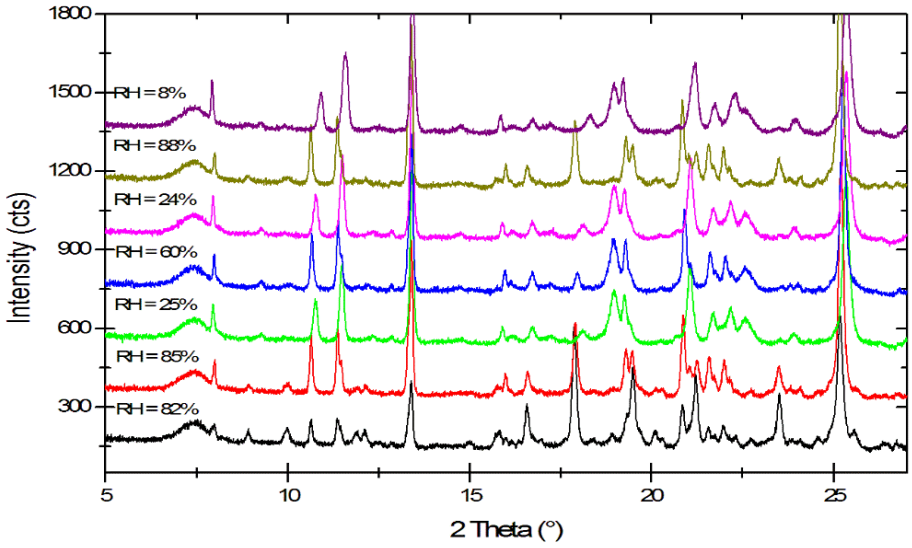

Source: Created by the author.

The same strategy already discussed for Rietveld refinements were applied and Figure 4.8a shows the difference on volumes calculated from sequential refinement (in function of

RH_A and RH_C) and surface Rietveld refinement. In this case, there is not a big difference between the volume in function of RH_C and RH_A and the behaviour presented in Figure 4.8b has a discontinuity where is expected to be bigger the RH correction (on 'RH of transition') and does not seems to fit well to a natural logarithm function, but the reason for this is still unclear.

Figure 4.8: a) Comparison between NF sesquihydrate volumes calculated by sequential Rietveld refinement (in function of RH_A and RH_C) and surface Rietveld refinement; b) RH_C behaviour in function of RH_A fitted by a natural logarithm function.

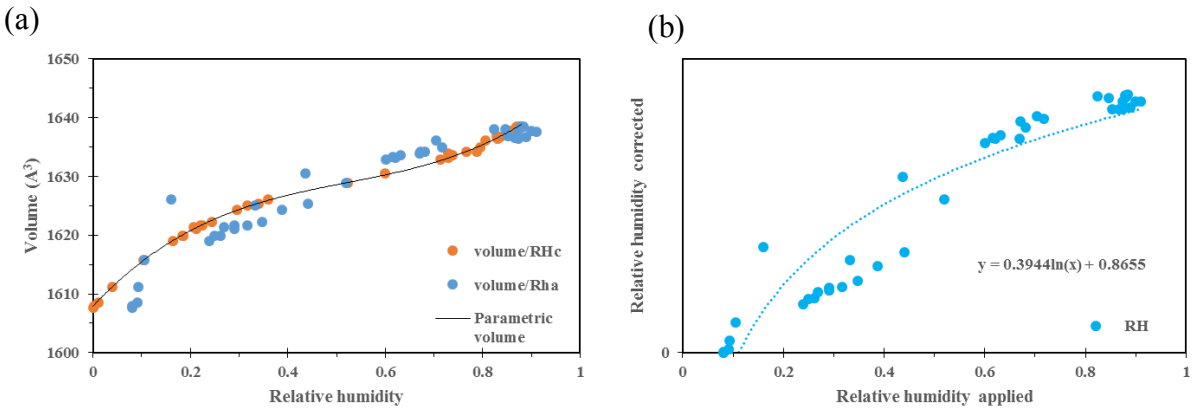

Source: Created by the author

Figure 4.9: LiF/NF API data set (4% ≤ RH ≤ 97%) plotted in: a) 2D-film and b) 3D.

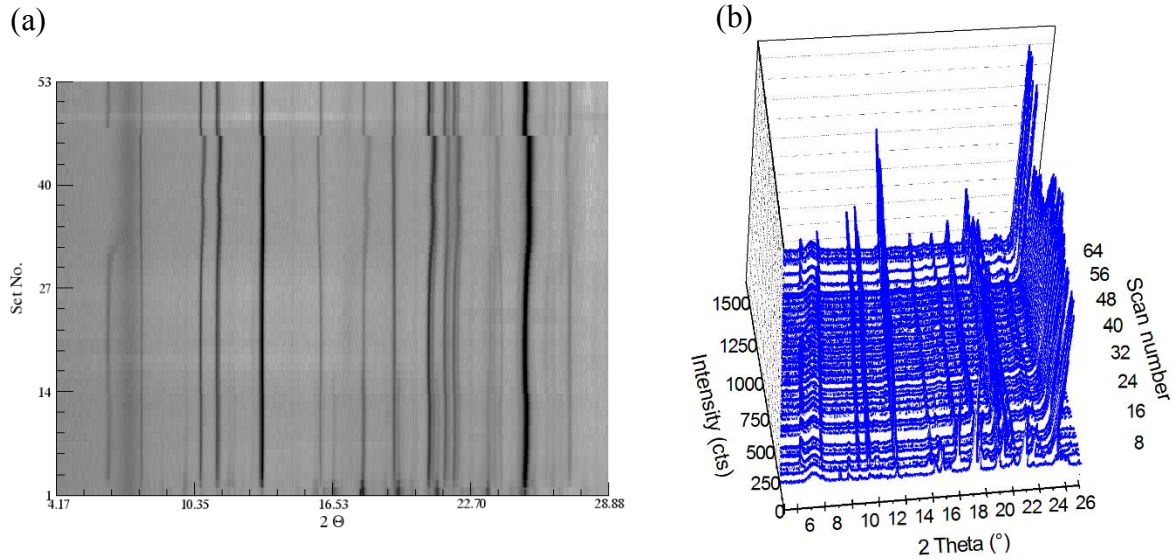

Source: Created by the author.

In second interval, 4% ≤ RH ≤ 97% (Figure 4.9), the peak at 6.5° is not present up to the second scan at 90% and it appears in the third at 96%. Its behaviour is exactly as mentioned above, i.e., its presence is depends of percentage of RH applied (Figure 4.10) and it is possible that the RH of activation is around 90%.

Figure 4.10: Comparison between first scan and the last scan of each cycle during RH variation (RH going up and going down), in sequence. for LiF/NF API data set (4% ≤ RH ≤ 97%).

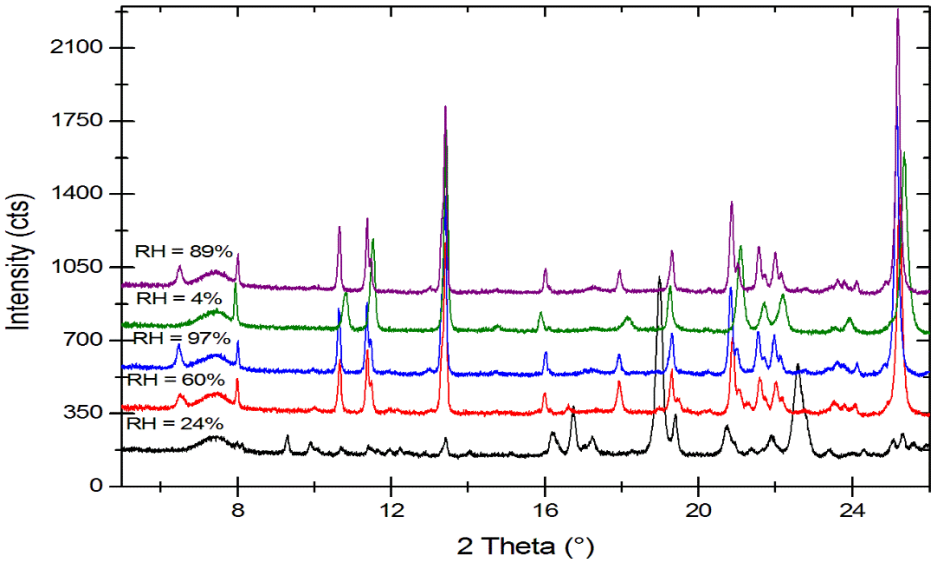

Source: Created by the author.

Figure 4.11: a) Comparison between NF sesquihydrate volumes calculated by sequential Rietveld refinement (in function of RH_A and RH_C) and surface Rietveld refinement; b) RH_C behaviour in function of RH_A fitted by a natural logarithm function.

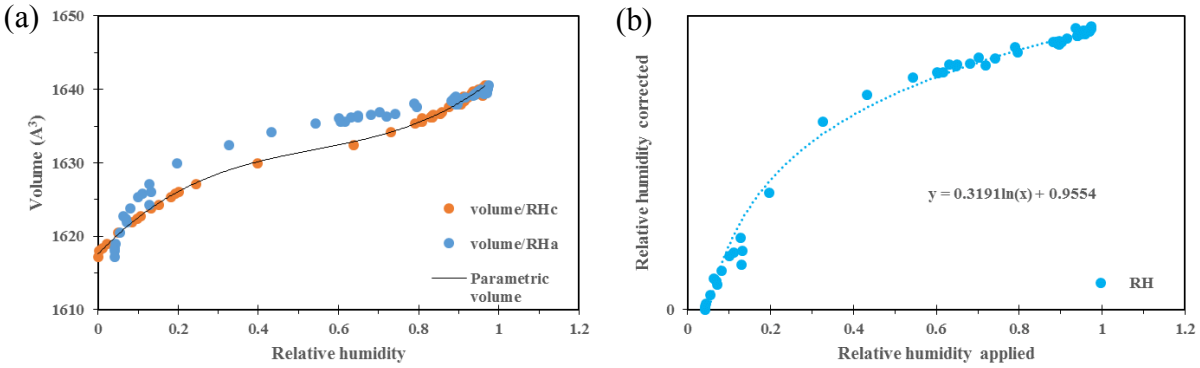

Source: Created by the author.

For this interval (4% ≤ RH ≤ 97%), there is a situation very similar of sample SRM-676a/NF API. Beyond this peak RH dependent, the RH correction during the experiment has a behaviour close to it as well. Figure 4.10a shows the good agreement between the volume calculated from sequential refinement in function of RH_C and the volume calculated from surface refinement. Therefore, the RH_C behaviour in function of RH_A has the biggest correction at 'RH of transition' because of same reason explained above and consequently it can be fitted by a natural logarithm function.

A very interesting question about the structural behaviour of a certain API is when it is in a medicine with the presence of excipients. For this reason, a tablet of NF medicine was mixture to the internal standard LiF and applied to a RH interval between 0 % ≤ RH ≤ 96% (Figure 4.12).

Figure 4.12: LiF/NF tablet data set plotted in: a) 2D-film and b) 3D.

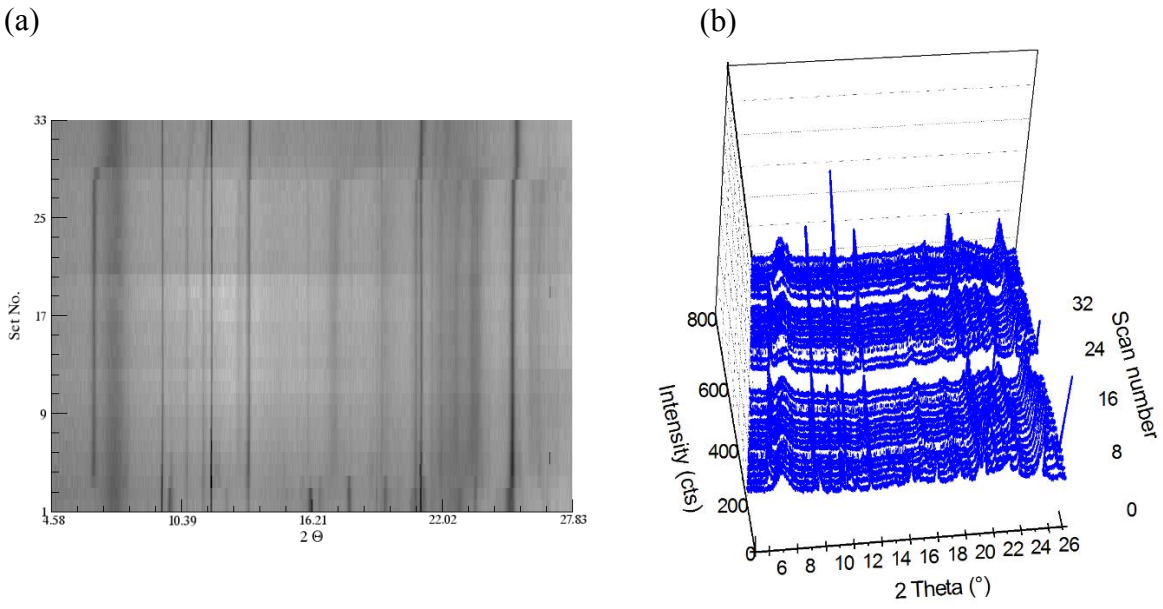

Source: Created by the author.

With a qualitative analysis, is observable that there are extra peaks (perhaps excipients peaks) also disappearing during the RH increase. As expected, the peak at 6.5° is present, but curiously, its relative intensity seems to be stronger than in previous experiments with NF API (Figure 4.13). It was not made an excipient structure identification and even with a lower percentage of NF present to the medicine, it was possible to quantify the sesquihydrate form during the experiment using the sequential and surface Rietveld refinement.

Figure 4.13: Comparison between first scan and the last scan of each cycle during RH variation (RH going up and going down), in sequence.for LiF/NF tablet data set.

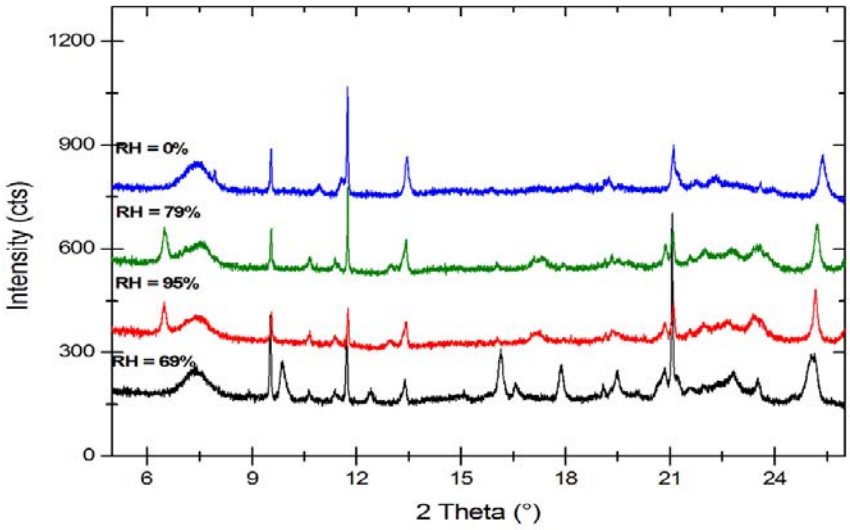

Source: Created by the author.

In Figure 4.14, shows that for this sample there was a strong correction at high RH and the highest RH_C is now around 80%, however almost no correction was made to the 'RH of transition', then the behaviour of RH_C in function of RH_A does not fit well to the reasonable function of a natural logarithm.

For this case, it is a bit more complicate find the answer obtained in these calculus because there are not only the RH control, but also the presence of excipients and if they are interfering, somehow needs a very careful analysis.

Figure 4.14: a) Comparison between NF sesquihydrate volumes calculated by sequential Rietveld refinement (in function of RH_A and RH_C) and surface Rietveld refinement; b) RH_C behaviour in function of RH_A fitted by a natural logarithm function.

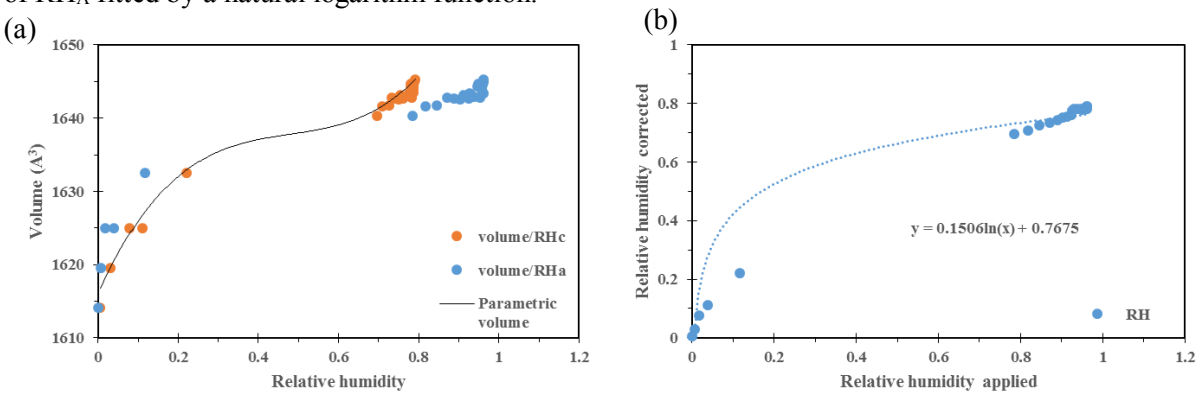

Source: Created by the author.

4.3. Summary

It is the first time that RH is applied as a 'non-crystallographic' parameter during the parametric Rietveld refinement. Its correction during the refinements improved physically all cell parameters for each sample. However, still there are few points to understand about the RH control in TUCANO furnace.

A peak at 6.5° was observed and its presence depends if the RH is high or low, but for it first appears, is necessary get a RH of activation around 90%. As most of NF (pseudo)polymorphs have no crystal structure known, understand what this peak means is not an easy work.

The LiF standard application was satisfactory when applied the interval $4\% \leq RH \leq 97\%$, with a result very similar to the obtained with NIST standard SRM-676a and the structural behaviour under the interval $8\% \leq RH \leq 88\%$ could be credit to the RH control.

For structural behaviour of NF sesquihydrate form in medicines no aberration (different polymorphs) was detected, but as the RH correction was not as expected, it is complicate to affirm that this happened due excipients interaction or again due the RH control.

Chapter 5

Kinetic study of Mebendazole by parametric Rietveld refinement, MBZ form B recrystallization and phase transition

The thermodynamic relations determine whether enantiotropic transition (reversible transition) or monotropic transition (irreversible transition) occurs. There are several combination of thermo-analytical techniques to explore kinetic studies of pharmaceutical products (Giron, 2001). Studies by *in situ* x-ray powder diffraction have stimulated investigations of phase transitions for a variety of materials (Evans & Evans, 2004) and the parametric Rietveld refinement can improve a kinetic study made by this technique (Stiton & Evans, 2007).

Mebendazole or MBZ (Figure 5.1), $C_{16}H_{13}N_3O_3$, is an anthelmintic with three polymorphs known as: Form A, Form B and Form C (Himmelreich *et al*., 1977). Form C is the pharmaceutically recommended; Form B is the most soluble of them; and form A the least soluble.

Figure 5.1: Flat isomerism between Mebendazole form C and Mebendazole form A.

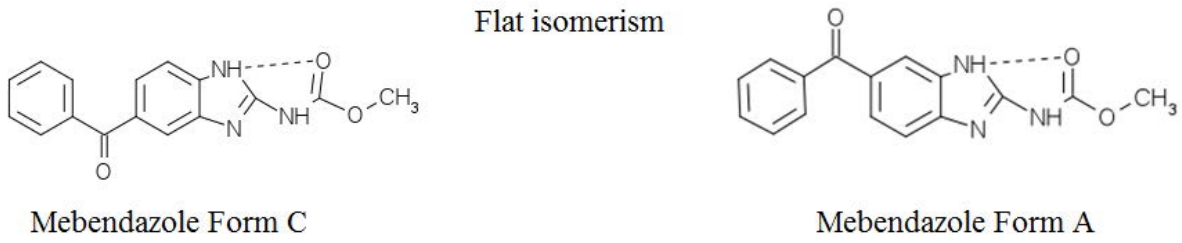

Source: Created by the author.

Table 5.1: Cell parameters of form C (Martins *et al.,* 2009) and form A (Ferreira *et al.,* 2010).

Form	a (Å)	b (Å)	c (Å)	α (°)	β (°)	γ (°)	Volume (Å^3)
MBZ C	5.1480(9)	7.8779(15)	17.907(3)	82.425(6)	82.743(7)	71.091(13)	678.3(2)
MBZ A	5.5044(2)	11.2872(2)	12.5276(5)	66.694(2)	82.959(2)	78.443(2)	699.52(5)

Source: Created by the author.

Figure 5.2: Mebendazole packing: a) form C along a axis; b) form A along a axis.

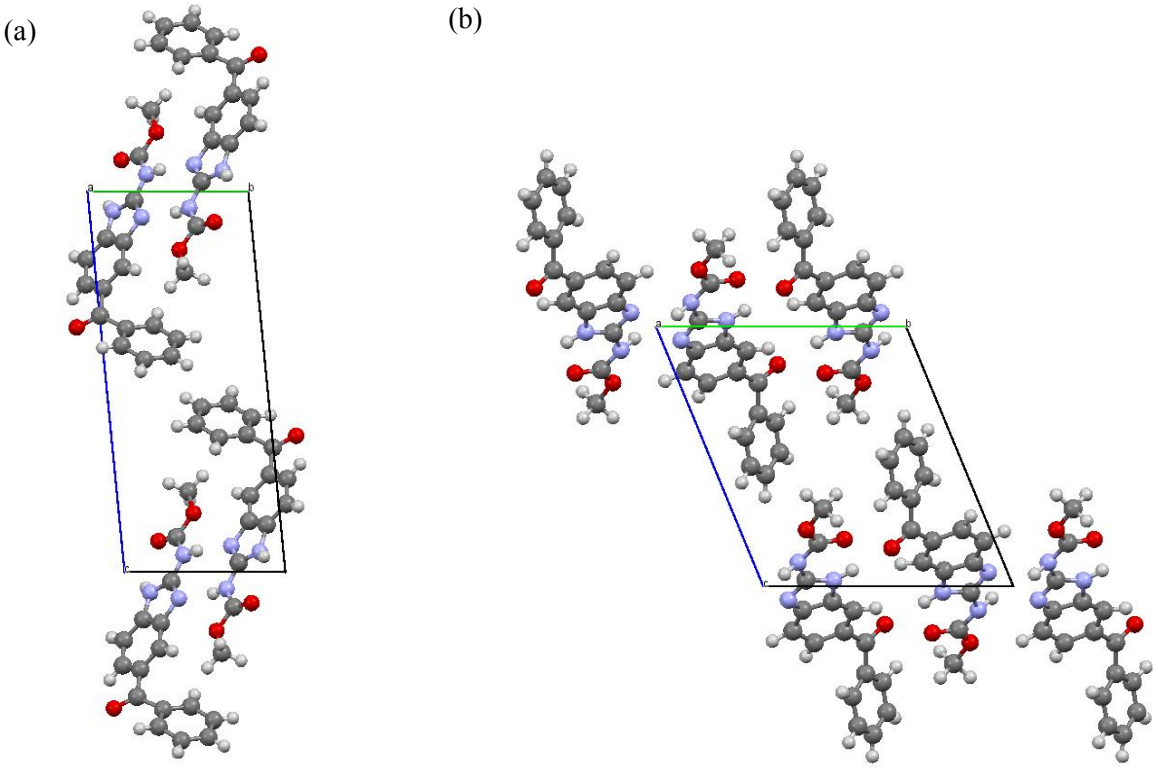

Source: Created by the author.

Form C (Martins *et al.,* 2009) and form A (Ferreira *et al.,* 2010) have the same space group ($P\bar{1}$) and the unit cell of both forms are in Table 5.1. Figure 5.2 shows difference between the form C packing (along a axis) and the form A packing (along a axis).

Figure 5.1 presents a flat isomerism between this two molecules, i.e. the benzoyl is attached to a different carbon of benzene from benzimidazole. The torsion angle between benzene and carbonyl decreases from 27° in form C to 11° in form A. A third classical intermolecular hydrogen bond appears in MBZA (N−H···O), and all hydrogen bonds non-

classic are different. Tables 5.2 and 5.3 provides information about hydrogen bonds geometry in form C and form A, respectively.

Table 5.2: Mebendazole form C hydrogen bond geometry (Å, °).

D−H···Á	D−H	H···A	D···A	D−H···Á
N−H···O	0.82(9)	2.31(7))	2.720(9)	112(6)
N−H···N	0.81(7)	2.09(7)	2.877(9)	165(6)
C−H···O (1)	0.95	2.51	3.35(1)	147
C−H···O (2)	0.98	2.70	3.56(1)	147

Source: Created by the author.

Table 5.3: Mebendazole form A hydrogen bond geometry (Å, °).

D−H···Á	D−H	H···A	D···A	D−H···Á
N−H···O (1)	1.00(7)	2.13(10)	2.69(3)	114(6)
N−H···N	0.99(13)	2.09(14)	2.86(3)	133(11)
N−H···O (2)	1.00(7)	2.30(8)	3.05(2)	131(7)
C−H···O	1.01(8)	2.39(8)	3.40(3)	175(6)

Source: Created by the author.

The crystal structure of the Form B is not known, and distinct powder diffraction patterns are assigned to it. Figure 5.3 shows a comparison between the XRPD patterns, simulated in TOPAS-Academic, according they are presented in respective works.

In this chapter, several strategies were tried until the recrystallization of a pure Form B was possible (at this moment, pure means no presence of peaks of known (pseudo)polymorphs). In addition, a study of the MBZB phase transition make possible to explore the polymorphic map of Mebendazole.

But still there are challenges as: verify if this sample is a pure MBZ compound from complementary techniques and to solve its crystal structure. In Table 5.4, there are a list of solvents capable to recrystallize the MBZ (Kumar *et al.,* 2008; Brusau *et al.,* 2007).

Figure 5.3: Comparison between XRD patterns of form B.

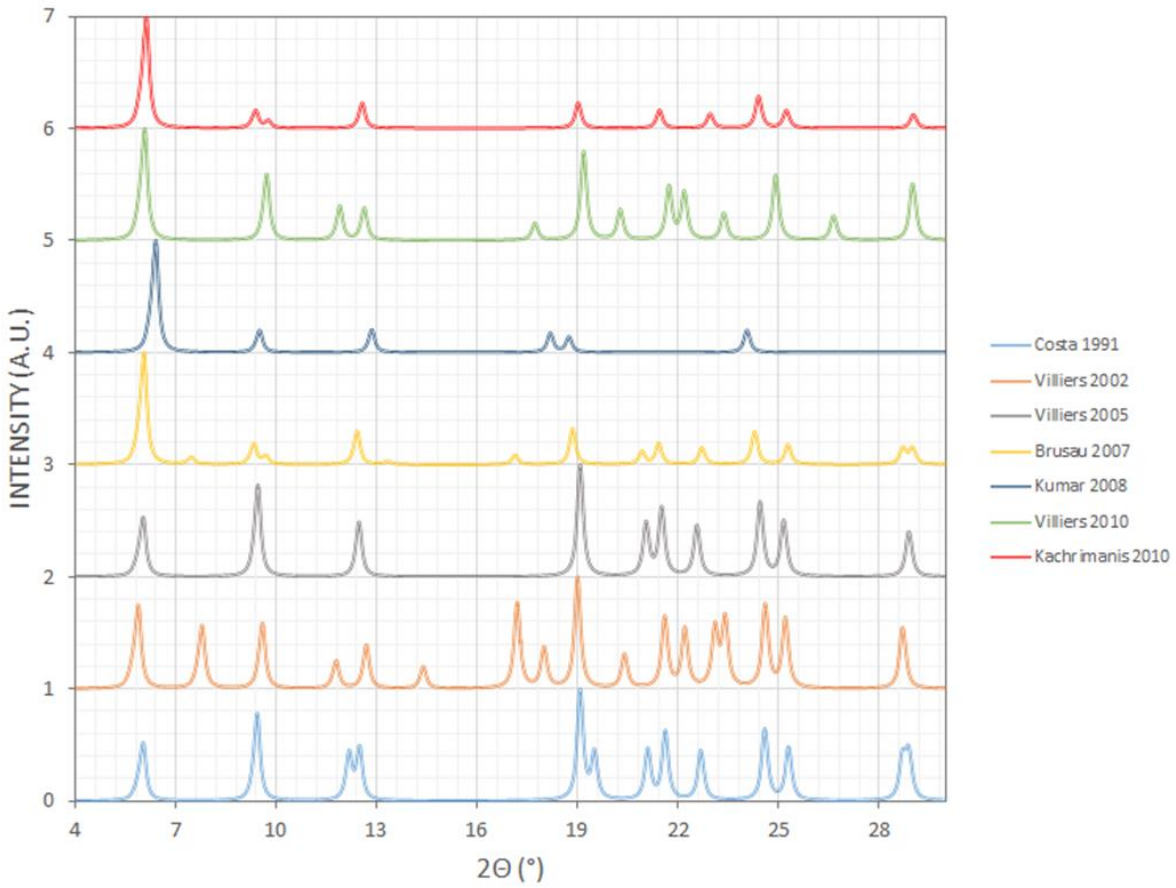

Source: Created by the author.

According Himmelreich and co-workers (1977) demonstrated, from DTA data, transformation of form B and form C to form A are at 210 °C and 170 °C, respectively. A kinetic study of transformation form C → form A, by qualitatively analysis of *in situ* x-ray powder diffraction (without the knowledge of the crystal structures), determine the stability of the form C up to 179 °C and the transformation form C → form A as a first order process with activation energy equal to 238 KJ/mol (Villiers et al. 2005). A simple study about form B transformation showed that it transforms to form C and then to form A (Brits et al., 2010).

Table 5.4: Solubility values of MBZ in different solvents and respective (pseudo)polymorph recrystallized.

Solvents	Solubility	Forms	Solvents	Solubility	Forms
N,N-Dimethyl acetamide	20	Salt	**Acetonitrile**	-	B
N,N-Dimethyl formamide	20	Salt	**Methanol**	10	A, C
Methanol:Ethyl acetate	-	A, B	**Ethyl acetate**	5	A, B, C
Acetic acid:Methanol	5	A			

Source: Created by the author.

5.1 Experimental section

5.1.1 Sample preparation

The internal standard used in this study is LiF (Êxodo Científica, 99.5%); MBZ containing MBZA and MBZC was sourced by Formil Química Ltda.. MBZ sample with pure form A and pure form C. MBZ form B, recrystallized from MBZ sample in Ethyl acetate solvent, dissolved M/V = 5 mg/ml at 23°C., filtered and then evaporate at room temperature by 15 days.

Mixtures 50/50 were carefully prepared for LiF/MBZ, and LiF/MBZB.

5.1.2 Data collection

Thermal analysis were collected in NETZSCH STA 409C equipment, at Material Engineer Department (DEMa) of São Carlos Federal University (UFSCar). Data were collected in Argon atmosphere (flux: 60 mL/min) and heat ratio of 10 °C/min from 35 °C up to 290 °C for all pure materials and mixtures with mass: pure LiF (3.4 mg), pure MBZA (6.6 mg) and pure MBZC (1.8 mg), LiF/MBZA (4.3 mg) and LiF/MBZC (3.0 mg).

In situ x-ray powder diffraction data, in function of time, were collected for LiF/MBZ sample, 2705 patterns in total for isotherm condition at each 5°C from 130°C up to 160°C, using Anton Paar HTK1200 furnace (300-1500 K) coupled to the D8 diffractometer over 4-85° 2θ with a 0.02° step using variable divergence slit 6 mm in 5 minutes scan.

For MBZB the same Anton Paar set-up was used, but the data collection was made in function of temperature, 20 patterns from 31°C to 220°C, 10°C per scan (isotherm) over 4-85° 2θ with a 0.02° step using variable divergence slit 6 mm in 6 minutes scan. A second set-up

using a capillary mode with an Oxford Cryostream Cooler to control the temperature from 27°C to 207°C in a heating ratio of 7.5°C/h, collected 72 patterns over 2-40° 2θ with a 0.01° step using divergence slit 0.6 mm and capillary 0.7 mm in 20 minutes scan.

At room temperature, MBZB had data collected in D8 diffractometer over 2-40° 2θ with a 0.01° step using variable divergence slit 6 mm and 1 second per step.

5.1.3 Analysis Methods

A comparison of thermogravimetry (TG) data between pure sample and mixture sample and a comparison of differential scanning calorimetry (DSC) data verify whether any interaction occurs. TG and DSC cannot have changes their curves behaviour, e.g. decomposition temperature. (Freire *et al.,* 2009).

Parametric Rietveld refinement, use same crystal structures already used for LiF, MBZA and MBZC. For all refinements (sequential and surface) were calculated independently for each scan, linear absorption correction for adjusting the peak shape due to sample transparency and 14 terms in Chebychev background polynomial. For each phase, scale factor, peak shapes, lattice parameters and atomic displacement parameter were refined. The preferred orientation in MBZA and MBZC were corrected by March Dollase model and the amorphous quantification was proceed from internal standard method. These two MBZ polymorphs had their lattice parameters parameterized by a 2nd order polynomial in function of time, rescaled between ±1 (chapter 3).

The behaviour of the natural logarithm of MBZC phase quantity, corrected and uncorrected by amorphous quantification, from sequential and surface refinement, for each temperature in function of time determined as a first order transition and the activation energy was calculated from Arrhenius' equation.

The indexation attempt of Mebendazole Form B made in TOPAS-Academic from lattice parameter search (lp_search), *"a new indexing algorithm that is independent of d-spacing extraction; (...) minimizes on a new figure of merit function that gives a measure of correctness for a particular set of lattice parameters. More specifically the figure of merit function assigns parts of the diffraction pattern to peaks and then sums the absolute values of the products of the diffraction intensities multiplied by the distance to the peaks:*

$$FOM = \sum_j \sum_i I(2\theta_i)\left|2\theta_i - 2\theta_{0,j}\right| \qquad (5.1)$$

where the summation in 'j' is over the calculated Bragg positions $2\theta_0$ and the summation in 'i' is over part of the diffraction pattern such that $(2\theta_{0,j-1} + 2\theta_{0,j})/2 < 2\theta_i < (2\theta_{0,j+1} + 2\theta_{0,j})/2$. The method avoids difficulties associated with extracting d-spacings from complex patterns comprising heavily overlapped lines; the primary difficulty being that of ascertaining the number of lines present" (Topas, 2012). For a good result from lattice parameter search the Pawley method was applied.

5.2Results

5.2.1 LiF/MBZ interaction test from TG and DSC curves

As LiF does not have any thermic event bellow 360 °C (region of temperature where, usually, pharmaceutical products present phase transition and decomposition), TG curve for MBZ Form A, shows no event until the decomposition process, 225-274 °C, with loss of 14% of initial mass (Figure 5.4a). Form C has decomposition starting at 208 °C and ending at 260 °C, with loss of 10% of initial mass (Figure 5.4b). When MBZA is mixture with LiF, there is no change on temperature which decomposition begins (225 °C), but the final temperature now is equal to 262 °C and the mass loss is 6.4% (Figure 5.4a). For LiF/MBZC mixture, the decomposition initiate at 202 °C and finish at 260 °C) and mass loss of 6.4% (Figure 5.4b).

Figure 5.4: Comparison between TG curves of pure samples and mixture samples: (a) MBZA; (b) MBZC.

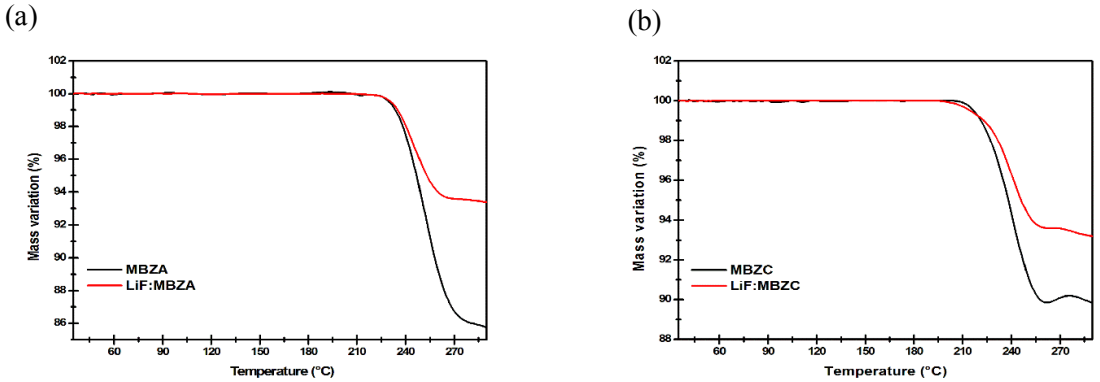

Source: Created by the author.

Pure Form A presents an endothermic peak at 256.59 °C and enthalpy variation, ΔH, equal to -36.20 μJ/mg (Figure 5.5a), while mixture LiF/MBZA has the endothermic peak at T

= 249.56 °C and ΔH = -15.36 µJ/mg (Figure 5.5a). Form C pure contains an exothermic peak at 206.09 C with ΔH = 0.82 µJ/mg and two endothermic peaks in sequence at 226.96 °C and 246.09 °C with total enthalpy variation ΔH = -25.42 µJ/mg (Figure 5.5b). These three events of form C curve are phase transition of first order to form A, melting point and decomposition, respectively. For LiF/MBZC sample, there is no difference observed of temperature, the exothermic enthalpy keeps the same value and the endothermic enthalpy decrease proportionally (Figure 5.5b). According Figure 5.5 and Table 5.5, no significant changes happen on this system.

Table 5.5: Thermal events observed from DSC for MBZA pure, LiF/MBZA, MBZC pure and LiF/MBZC (T_i – intial temperature of thermal event, T_f – final temperature of thermal event, T_m – peak position, ΔH – Entalpy variation).

Sample	Ti-Tf (°C)	Tm (°C)	ΔH (µJ/mg)
MBZA	222,15 – 272,02	256,59	-36,20
LiF/MBZA	222,17 – 266,05	249,56	-15,36
MBZC	193,85-211,59	206,09	0,83
	211,59-255,36	226,96	
		246,09	-25,43
LiF/ MBZC	194,19-215,00	207,47	0,85
	215,00-259,04	227,28	
		245,95	-11,26

Source: Created by the author.

Figure 5.5: Comparison between DSC curves of pure samples and mixture samples: (a) MBZA; (b) MBZC.

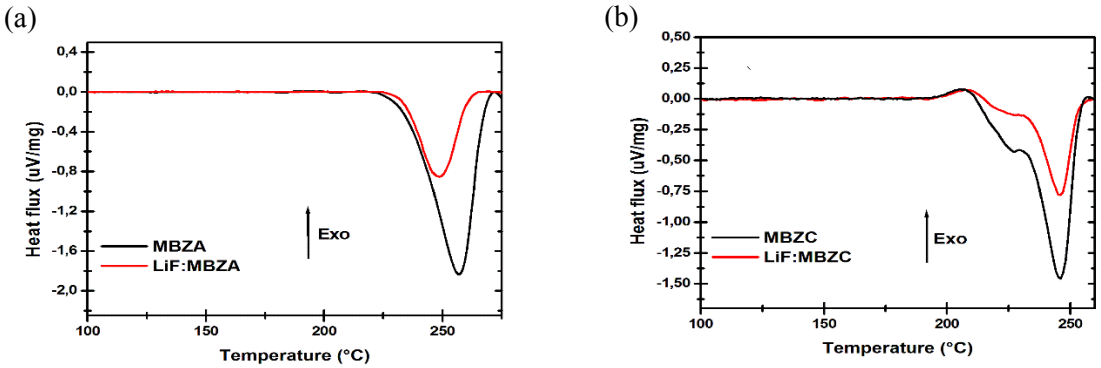

Source: Created by the author.

5.2.2 MBZ kinetic study from in situ XRPD

A kinetic study made for the first time from XRPD, there was not knowledge about crystal structure and the concentration was determined from intensity behaviour in function of time. With this situation, without consider any correction for preferred orientation, the activation energy of transformation from Form C to Form A, calculated from Arrhenius plot, is equal to 238±16 KJ/mole (Villiers *et al.*, 2005).

The actual study does not differ only by the crystal structure knowledge and preferred orientation correction, but it also considers a concentration correction by amorphous quantification and a QPA from parametric Rietveld refinement with time as 'non-crystallographic' parameter.

The first two situations compare a QPA made by sequential Rietveld refinement with and without amorphous quantification. Figure 5.6a shows how the transformation from Form C to Form A occurs in function of time at 130°C, in Figure 5.6b this behaviour is corrected by the consideration of amorphous quantity generated.

Figure 5.6: Comparison between quantitative phase analysis by sequential Rietveld refinement: a) without amorphous quantification; b) with amorphous quantification.

(a) (b)

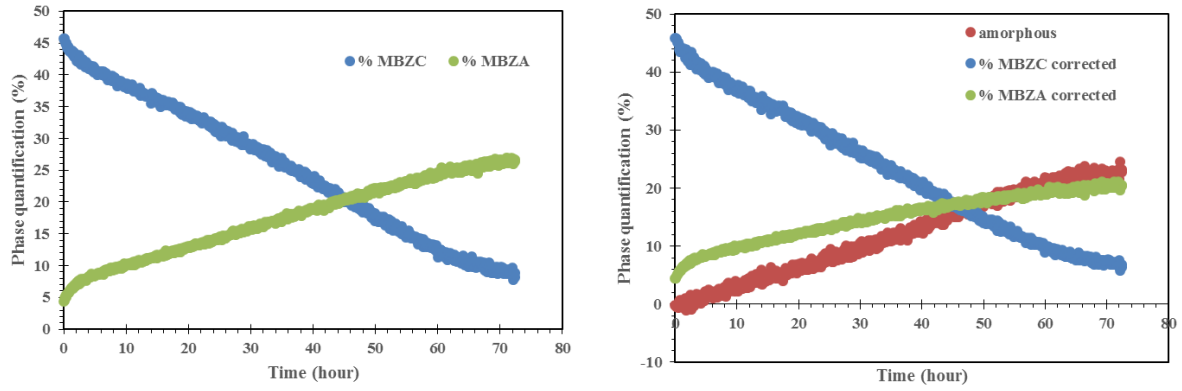

Source: Created by the author.

The natural logarithm of MBZC quantity (%) in function of time (hour), for each temperature from 130°C to 160°C (Figure 5.7), have an average linearity factor $R^2 > 0.900$, in both situations of phase quantification. These R^2 factor confirms the first order transition already expected (Villiers et al., 2005). The rate constant, k, of phase transformation is the angular coefficient of linear equation calculated from this linear behaviour.

Figure 5.7: Natural logarithm of MBZC quantity in function of time for temperatures from 130°C to 160°C with respective linearity factor, R^2: a) MBZC without correction; b) MBZC corrected by amorphous quantification.

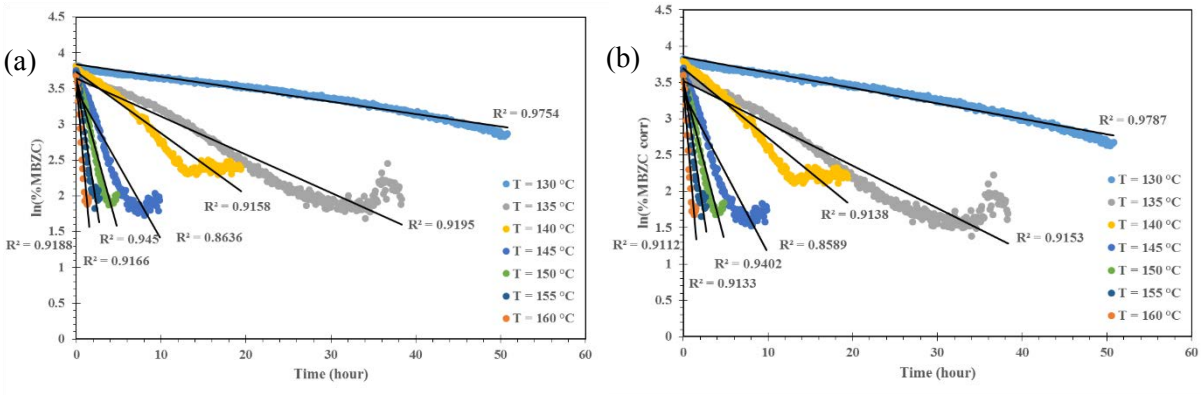

Source: Created by the author.

The natural logarithm of k, determined for each temperature, in these two cases, have a linear behaviour in function of 1/T (K^{-1}), as expected for Arrhenius plot (Figure 5.8) and the activation energy for MBZC transformation is calculated according the equation,

$$\ln(k) = \frac{-E_a}{R}\frac{1}{T} + \ln(A),$$

where E_a is activation energy (J/mole), R is the universal gas constant (8.31 J/mol.K) and A is the prefactor.

The activation energy is equal to 206(6) KJ/mole without correction in MBZC quantity and 200(4) KJ/mole for MBZC corrected by internal standard method.

Figure 5.8: Arrhenius plot for transformation of Mebendazole form C corrected (black) or not (red), by the amorphous quantity.

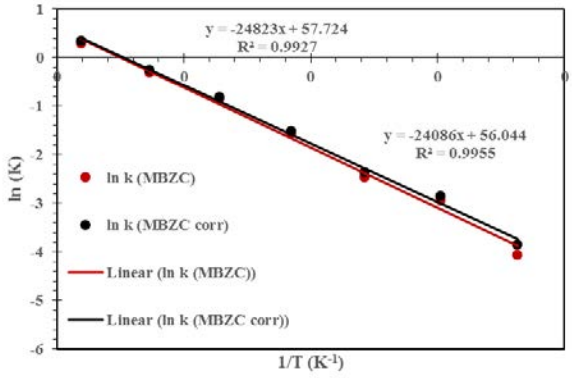

Source: Created by the author.

These two follow situations compare a QPA made by parametric Rietveld refinement with and without amorphous quantification. Figure 5.9a shows how the transformation from

Form C to Form A occurs in function of time at 130°C, in Figure 5.9b this behaviour is corrected by the consideration of amorphous quantity generated.

Figure 5.9: Comparison between quantitative phase analysis by parametric Rietveld refinement: a) without amorphous quantification; b) with amorphous quantification.

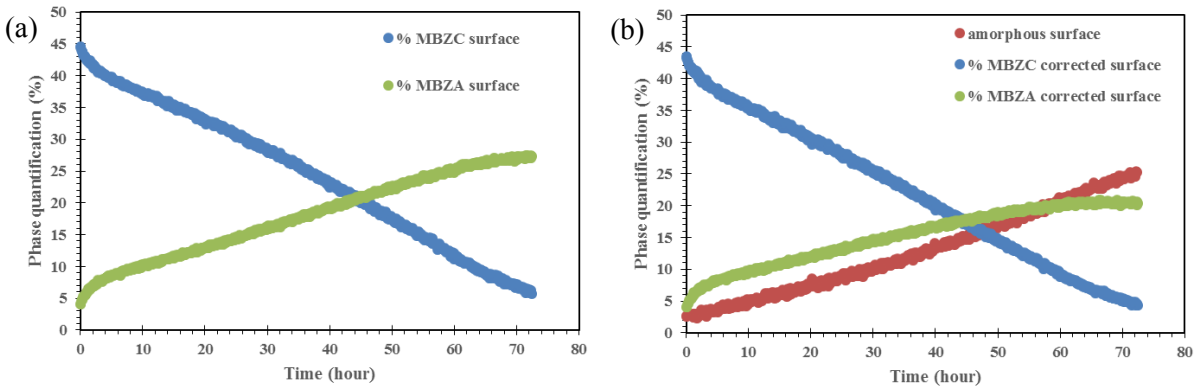

Source: Created by the author.

The natural logarithm of MBZC quantity (%) in function of time (hour), for each temperature from 130°C to 160°C (Figure 5.10), have an average linearity factor $R^2 > 0.900$, in both situations of phase quantification. Again, a first order transition is confirmed, but all R^2 factors obtained for phase quantification from parametric Rietveld refinement are higher than obtained by sequential Rietveld refinement.

Figure 5.10: Natural logarithm of MBZC quantity (from parametric Rietveld refinement) in function of time for temperatures from 130°C to 160°C with respective linearity factor, R^2: a) MBZC without correction; b) MBZC corrected by amorphous quantification.

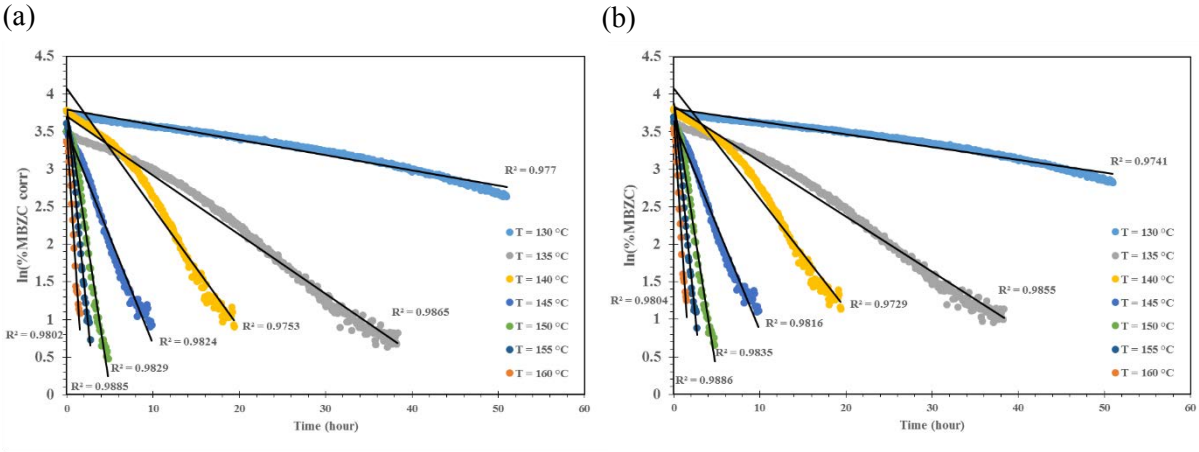

Source: Created by the author.

That higher linearity for phase quantification from parametric Rietveld refinement shows the quality of this result even when the intensity of form C still present in the sample difficult the QPA from a simple Rietveld refinement, as it is easy to observe comparing Figures 5.6 and 5.9.

From the natural logarithm of k, in function of 1/T (K^{-1}), the Arrhenius plot (Figure 5.11) determines the activation energy for MBZC transformation equal to 218(13) KJ/mole without correction in MBZC quantity and 211(11) KJ/mole for MBZC corrected by internal standard method.

Figure 5.11: Arrhenius plot for transformation of Mebendazole form C, quantified from parametric Rietveld refinement, corrected (black) or not (red), by the amorphous quantity.

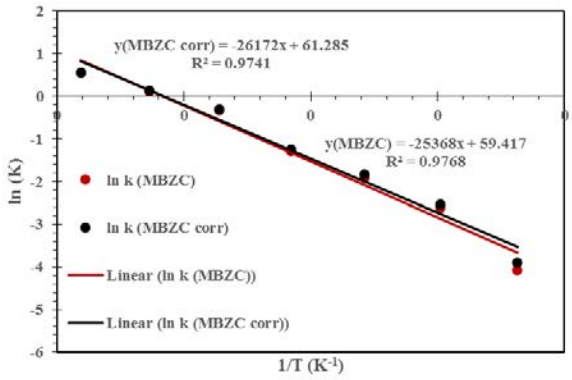

Source: Created by the author.

The activation energy calculated by Villiers and co-workers (2005) is higher than the energy calculated in all situations used in this thesis. Without consider the natural limitation of this previous result, due no crystal structure knowledge or preferred orientation correction, the reduction in energy calculated from Rietveld refinement shows that the internal standard does not work as a catalyst.

The kinetic study from parametric Rietveld refinement is clearly more reliable, once the phase quantification has more physical/chemical meaning. The difference between activation energy calculated from MBZC corrected and uncorrected by amorphous quantification is not big (~ 7 KJ) and could be considered only a fine adjustment value.

5.2.3 Mebendazole form B recrystallization and phase transition study

The sample recrystallized from Ethyl acetate (Figure 5.12), presents a characteristic peak at 6.4° (form B characteristic peak) and no peaks at 4.9° and 7.7°, peaks of form C and A, respectively. Assuming that there is only form B present in this sample and observing the peak at 3.2°, MBZB has a bigger volume than MBZA and MBZC.

Figure 5.12: Mebendazole form B recrystallized from Ethyl acetate at room temperature.

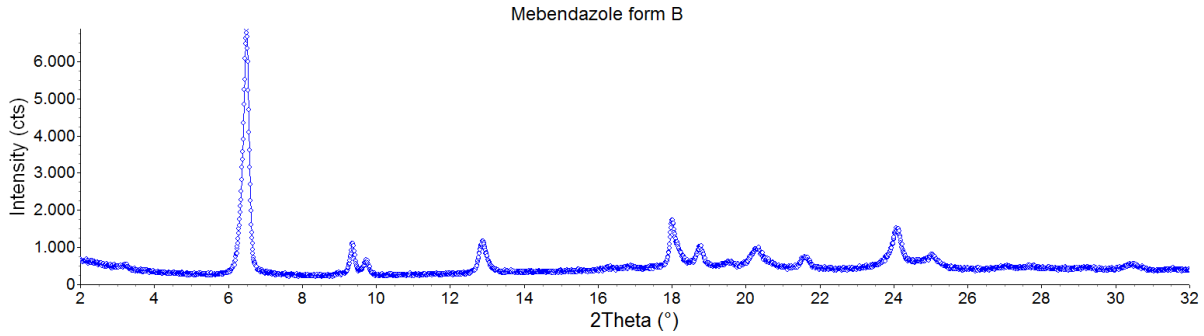

Source: Created by the author.

The indexation attempt from powder pattern obtained three possible space groups with good Pawley fits (Table 5.6, see Annex F). Triclinic and Monoclinic are the two crystal systems with best adjust and all volumes calculated are bigger than 2500 Å^3, a very big volume as discussed above.

Table 5.6: Space groups indexed with respective lattice parameters, Rwp(%) and gof values calculated from Pawley method.

Space group	P-1(1)	P-1(2)	P2
a (Å)	28.738894	29.989282	9.545668
b (Å)	9.489889	9.933344	27.465567
c (Å)	11.002775	10.746676	9.962272
alpha (°)	92.65931	96.31460	90
beta (°)	84.45296	72.55161	98.13515
gamma (°)	106.03827	75.02921	90
Volume (Å^3)	2869.864	2888.733	2585.597
Rwp (%)	4.87	4.90	5.91
gof	1.426	1.434	1.661

Source: Created by the author.

Form B was submitted to two experiments with temperature controlled, using two different geometries. The first geometry is in transmission mode with the sample in a capillary. Figure 5.13 shows MBZB phase transformation to an unknown (pseudo)polymorph, after to form A and finally decomposition.

Figure 5.13: Form B phase transformation with geometry in transmission mode.

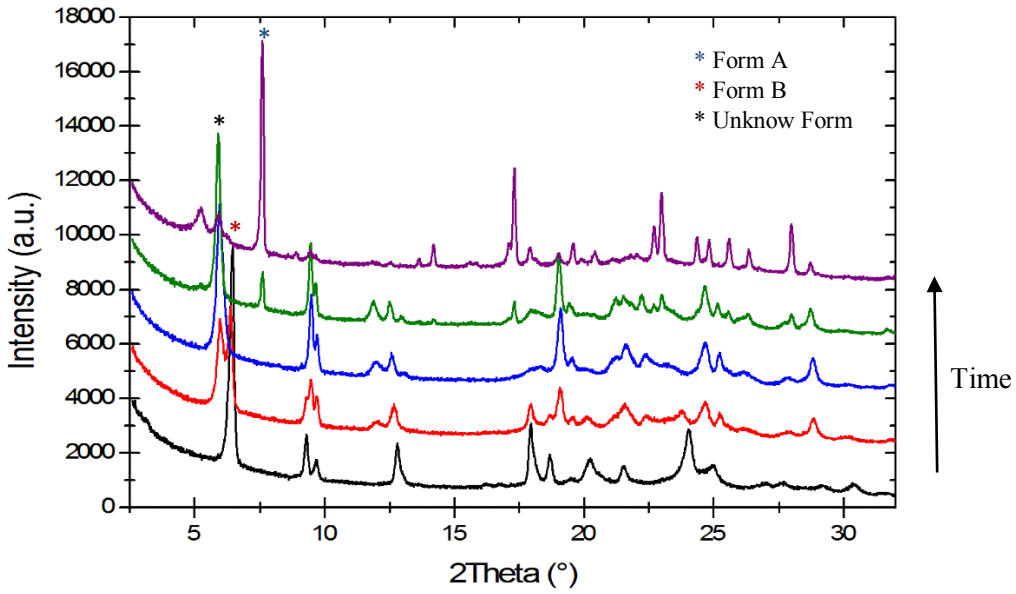

Source: Created by the author.

The second geometry is in flat mode. Figure 5.14 shows MBZB phase transformation to an unknown (pseudo)polymorph and then straight to decomposition, no Form A is formed during this experiment.

Beyond the geometry, these two experiments have different temperature control. For transmission mode, the temperature has heating rate of 7.5 °C/hour and for flat mode the pattern is collected in isotherms each 10 °C.

Figures 5.15 shows a possible polymorphic map for MBZ according the previous MBZC phase transformation study and experiment with MBZB using geometry in transmission mode, where the unknown form transforms to form A before decompose. However, Figure 5.16 propose a second possibility of polymorphic map, considering the experiment with MBZB using flat mode geometry. In this map, no transformation from that unknown form to Form A occurs. These two polymorphic maps can be compared with polymorphic map proposed by

Villiers and co-workers, in Figure 5.17. This last map does not consider the amorphous generation and Form B transforms to Form C before transform in Form A.

Figure 5.14: Form B phase transformation with geometry in flat mode.

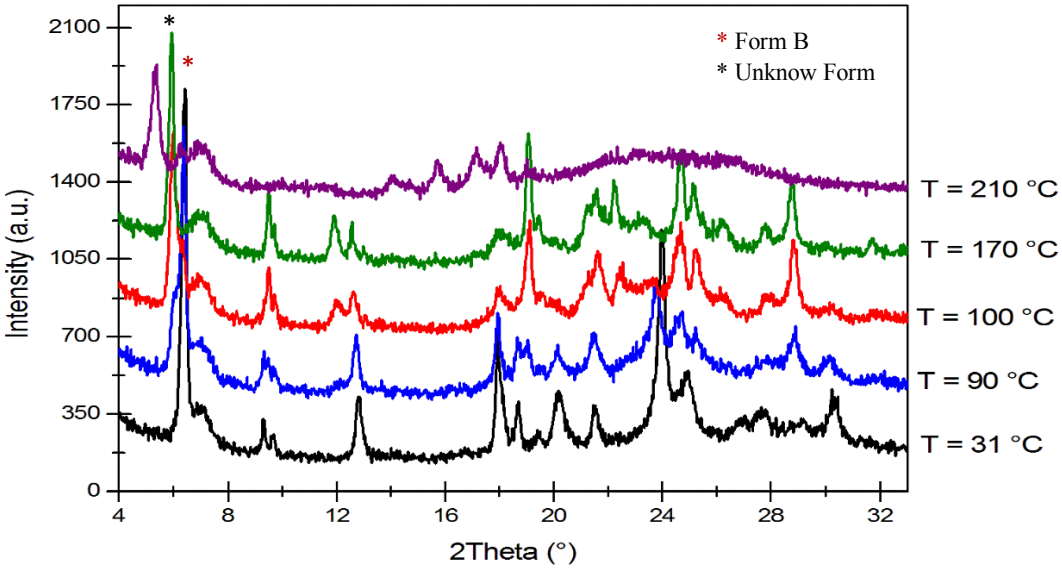

Source: Created by the author.

Figure 5.15: MBZ polymorphic map according MBZB phase transition obtained in experiment with transmission mode.

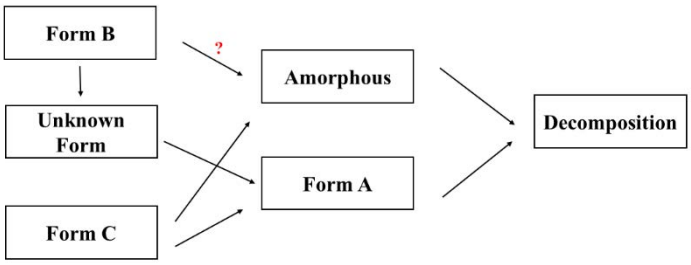

Source: Created by the author.

Figure 5.16: MBZ polymorphic map according MBZB phase transition obtained in experiment with flat mode.

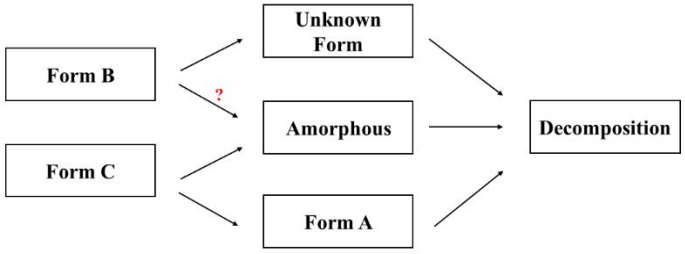

Source: Created by the author.

Figure 5.17: MBZ polymorphic map according MBZB phase transition obtained by Villiers and co-workers.

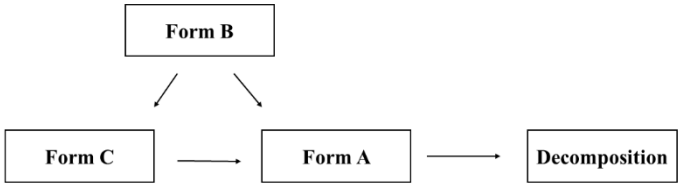

Source: Created by the author.

5.3Summary

The interaction test between LiF/MBZ, from DSC and TG data, showed LiF has no influence on MBZ behaviour in function of temperature.

The kinetic study made by *in situ* XRPD experiment, showed a good agreement with literature and demonstrate the better efficiency of parametric Rietveld refinement in comparison with a simple sequential Rietveld refinement. The difference between activation energy considering or not, the amorphous content, for Mebendazole, is not expressive, but could means a result with better accuracy.

Form B has been recrystallized in Ethyl acetate solution and three possible space groups obtained satisfactory Pawley fits (see Appendix F). Its phase transition, explored by *in situ* XRPD with different geometries (transmission and reflection mode), shows two different

pathways for Form B to decomposition. Therefore, two polymorphic maps are proposed as an alternative of previous polymorphic map present in literature.

Chapter 6
Final considerations and perspectives

This project explored different points past four years. The characterization of an internal standard showed how important is to consider the microabsorption effect between two materials with very different linear coefficient absorption. The successful amorphous quantification with LiF as internal standard demonstrate that it is as possible as cheap to add the method to a large-scale application.

TUCANO chamber, that applies different environment conditions (temperature and relative humidity control), developed in collaboration with LNLS, can be used to explore drug's crystal structure under variation of these two parameters. Parametric Rietveld refinement was applied with temperature as 'non-crystallographic' parameter to correct the sample temperature during heating process.

Norfloxacin sesquihydrate form had its crystal structure behaviour, in function of relative humidity, analysed by Parametric Rietveld refinement. This was the first time that RH is used as a 'non-crystallographic' parameter and showed a coherent correction fitted by a natural logarithm. However, there are some points to better explore, as the reason of a natural logarithm function to describe RH felt by the sample, resulting this 'RH of transition', or why each experiment had different coefficients of RH equation correction. Molecular dynamics simulation, for example, can be used to compare expected cell parameters behaviour.

The kinetic study made by *in situ* XRPD experiment demonstrated the better efficiency of Parametric Rietveld refinement in comparison with a simple sequential Rietveld refinement. To verify the difference between activation energy considering or not, the amorphous content, for Mebendazole, the same study will be proceed to a sample SRM-676a/MBZ.

Form B, recrystallized in Ethyl acetate solution and its phase transition, need to be explored by complementary spectroscopic and thermic techniques to determine molecular

properties of this initial crystalline phase (called Form B) and the second unknown crystalline phase that appears during the *in situ* XRPD experiment.

Appendix

Appendix A

Values calculated and graphical fits for internal standards characterization (LiF and Li_2CO_3)

Seven different mixtures (15/85; 30/70; 40/60; 50/50; 60/40; 70/30; 85/15 by weight) for α-Al_2O_3/LiF, SRM-676a/LiF, and SRM-676a/Li_2CO_3 were prepared. In SRM-676a/LiF case, two more ratios (5/95; 95/5) were added to these seven different mixtures.

They had data collected three times each, in the D8 diffractometer over 10-140° 2θ with a 0.02° step using variable divergence slit 6 mm and 1 second per step. For three of these ratios (30/70; 50/50; 70/30), of LiF/SRM-676a and Li_2CO_3/SRM-676a data were collected on the RINT2000 and at LNLS.

For Rietveld refinements the crystal structures of inorganic materials, were obtained from the ICSD (ICSD, 2009) with numbers 31548 (Al_2O_3), 53839 (LiF) and 9009641 (Li_2CO_3).

In all refinements were applied linear absorption correction for adjusting the peak shape due to sample transparency, 14 terms in Chebychev background polynomial, and refined scale factor for each phase, lattice parameters, peak shapes and one general atomic displacement parameter.

For data from D8, the refinement applied corrections for: axial divergence, specimen displacement, tube tails correction, variable divergence intensity and a modelled small portion of K_β radiation; with data from RINT2000, only simple axial model and specimen displacement has been applied; and in data collected at LNLS, simple axial model and zero error.

A.1. Al_2O_3/LiF mixtures

A.1.1. Bruker D8 equipment

A.1.1.1. Values calculated

1st Data set

Table A.1: 1st data set for Al_2O_3/LiF mixture, from Bruker D8 equipment, with values calculated from Rietveld refinement, for LiF phase quantification (%) and respective e.s.d. (%), *gof* and Rwp (%) obtained.

data code	%LiF	%LiF calc	e.s.d. (%)	*gof*	Rwp (%)
d7_03348	15.00	20.57	0.21	2.567	4.17
d7_03350	30.00	43.03	1.88	2.551	4.00
d7_03352	40.00	45.72	2.05	2.472	4.10
d7_03344	50.00	60.38	0.83	2.350	3.53
d7_03354	60.00	69.66	0.24	2.559	3.74
d7_03356	70.00	77.64	0.71	2.256	3.21
d7_03358	85.00	89.41	0.03	2.380	3.21

Source: Created by the author.

After apply Brindley correction to Rietveld refinement strategy.

Table A.2: 1st data set for Al_2O_3/LiF mixture, from Bruker D8 equipment, with values calculated from Rietveld refinement with Brindley correction, for LiF phase quantification (%) and respective e.s.d. (%) obtained.

data code	%LiF	%LiF calc	e.s.d. (%)
d7_03348	15.00	19.81	0.20
d7_03350	30.00	40.69	1.75
d7_03352	40.00	43.20	1.92
d7_03344	50.00	57.07	0.81
d7_03354	60.00	66.23	0.37
d7_03356	70.00	74.43	0.74
d7_03358	85.00	87.28	0.03

Source: Created by the author.

2nd Data set

Table A.3: 2nd data set for Al_2O_3/LiF mixture, from Bruker D8 equipment, with values calculated from Rietveld refinement, for LiF phase quantification (%) and respective e.s.d. (%), *gof* and Rwp (%) obtained.

data code	%LiF	%LiF calc	e.s.d. (%)	*g.o.f.*	Rwp (%)
d7_03832	15.00	21.60	0.94	2.912	5.77
d7_03405	30.00	41.57	0.85	2.428	3.82
d7_03407	40.00	53.50	3.45	2.437	3.76
d7_03834	50.00	58.86	1.90	2.885	5.23
d7_03836	60.00	67.51	1.28	2.709	4.80
d7_03935	70.00	75.56	0.76	2.517	4.41
d7_03937	85.00	89.71	0.25	2.572	4.21

Source: Created by the author.

After apply Brindley correction to Rietveld refinement strategy.

Table A.4: 2nd data set for Al_2O_3/LiF mixture, from Bruker D8 equipment, with values calculated from Rietveld refinement with Brindley correction, for LiF phase quantification (%) and respective e.s.d. (%) obtained.

data code	%LiF	%LiF calc	e.s.d. (%)
d7_03832	15.00	20.77	0.88
d7_03405	30.00	39.32	0.78
d7_03407	40.00	50.51	3.24
d7_03834	50.00	55.60	1.85
d7_03836	60.00	67.38	0.45
d7_03935	70.00	72.26	0.79
d7_03937	85.00	87.63	0.28

Source: Created by the author.

3rd Data set

Table A.5: 3rd data set for Al_2O_3/LiF mixture, from Bruker D8 equipment, with values calculated from Rietveld refinement, for LiF phase quantification (%) and respective e.s.d. (%), *gof* and Rwp (%) obtained.

data code	%LiF	%LiF calc	e.s.d. (%)	*g.o.f.*	Rwp (%)
d7_04424	15.00	18.64	1.15	2.33	6.69
d7_04425	30.00	36.51	2.73	2.07	5.77
d7_04451	40.00	46.63	1.40	1.82	4.08
d7_04453	50.00	65.41	2.73	1.79	3.82
d7_04455	60.00	70.80	1.05	1.74	3.64
d7_04555	70.00	76.70	0.05	1.69	3.63
d7_04557	85.00	88.97	0.28	1.75	3.55

Source: Created by the author.

After apply Brindley correction to Rietveld refinement strategy.

Table A.6: 3rd data set for Al_2O_3/LiF mixture, from Bruker D8 equipment, with values calculated from Rietveld refinement with Brindley correction, for LiF phase quantification (%) and respective e.s.d. (%) obtained.

data code	%LiF	%LiF calc	e.s.d. (%)
d7_04424	15.00	18.00	1.08
d7_04425	30.00	34.64	2.53
d7_04451	40.00	44.05	1.32
d7_04453	50.00	61.99	2.66
d7_04455	60.00	66.64	0.08
d7_04555	70.00	73.44	0.05
d7_04557	85.00	86.79	0.31

Source: Created by the author.

Average values calculated from Rietveld refinements of these three data sets

Table A.7: Average values for Al_2O_3/LiF mixture, from Bruker D8 equipment, with values calculated from Rietveld refinement, for LiF phase quantification (%) and respective e.s.d. (%), *gof* and Rwp (%) obtained.

%LiF	%LiF calc	e.s.d. (%)	*g.o.f.*	Rwp (%)
15.00	20.27	1.23	2.603	5.54
30.00	40.37	2.79	2.350	4.53
40.00	48.61	3.47	2.244	3.98
50.00	61.55	2.80	2.341	4.19
60.00	69.32	1.37	2.334	4.06
70.00	76.63	0.85	2.155	3.75
85.00	89.36	0.30	2.232	3.66

Source: Created by the author.

Average values calculated after apply Brindley correction to Rietveld refinement strategy.

Table A.8: Average values for Al_2O_3/LiF mixture, from Bruker D8 equipment, with values calculated from Rietveld refinement with Brindley correction, for LiF phase quantification (%) and respective e.s.d. (%) obtained.

%LiF	%LiF calc	e.s.d. (%)
15.00	19.52	1.15
30.00	38.22	2.59
40.00	45.92	3.26
50.00	58.22	2.73
60.00	66.75	0.48
70.00	73.38	0.89
85.00	87.23	0.34

Source: Created by the author.

A.1.1.2. Graphical fits

Figure A.1: Graphical Rietveld refinement obtained on data 'd7_03348' for mixture Al_2O_3/LiF (85/15). Blue dots – observed data; red curve – calculated data; grey curve – residual curve.

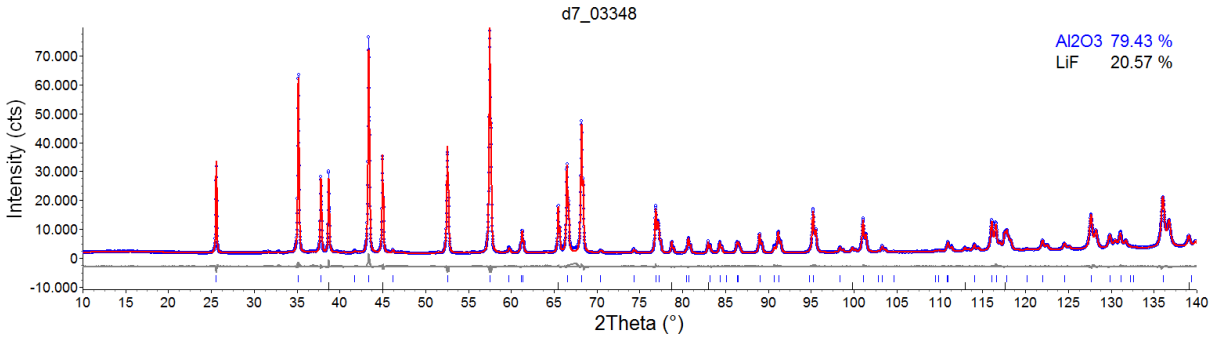

Source: Created by the author.

Figure A.2: Graphical Rietveld refinement obtained on data 'd7_03350' for mixture Al_2O_3/LiF (70/30). Blue dots – observed data; red curve – calculated data; grey curve – residual curve.

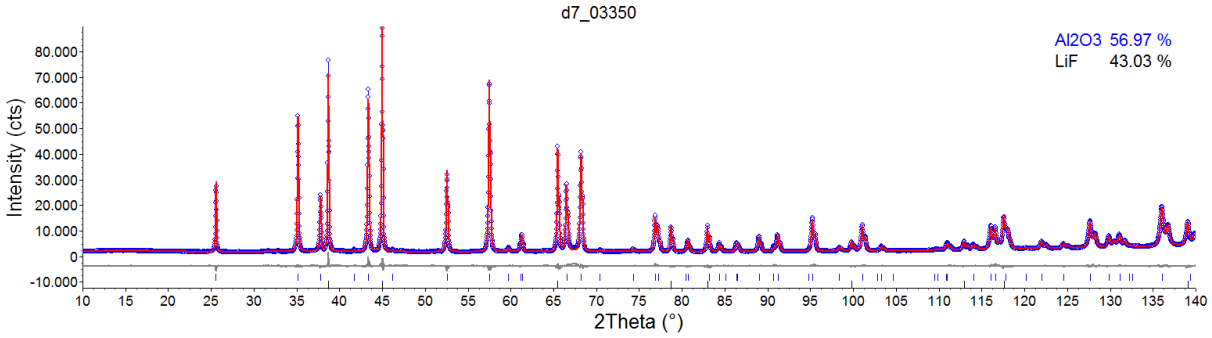

Source: Created by the author.

Figure A.3: Graphical Rietveld refinement obtained on data 'd7_03352' for mixture Al_2O_3/LiF (60/40). Blue dots – observed data; red curve – calculated data; grey curve – residual curve.

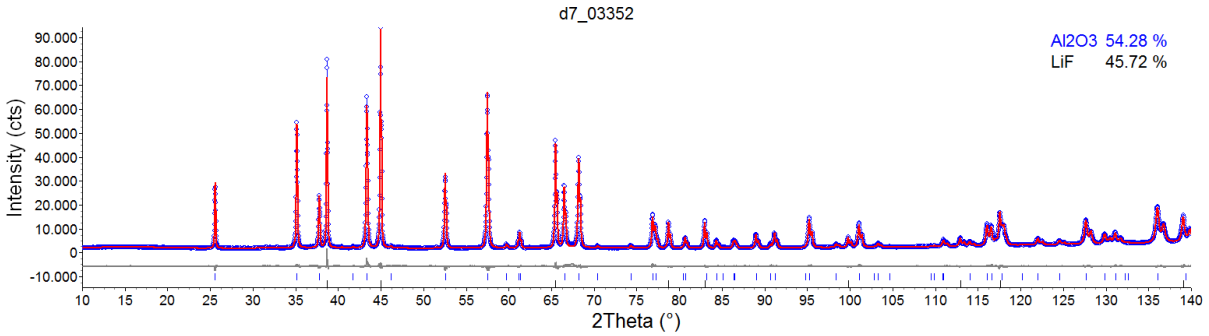

Source: Created by the author.

Figure A.4: Graphical Rietveld refinement obtained on data 'd7_03344' for mixture Al_2O_3/LiF (50/50). Blue dots – observed data; red curve – calculated data; grey curve – residual curve.

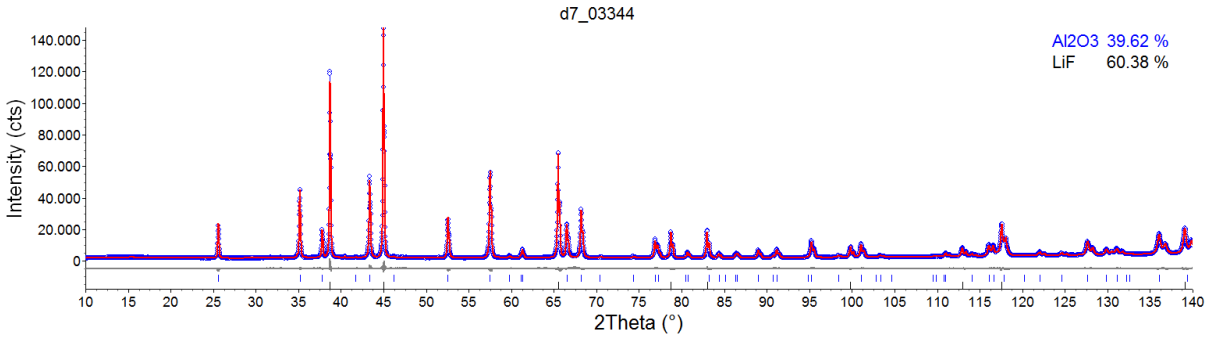

Source: Created by the author.

Figure A.5: Graphical Rietveld refinement obtained on data 'd7_03354' for mixture Al_2O_3/LiF (40/60). Blue dots – observed data; red curve – calculated data; grey curve – residual curve.

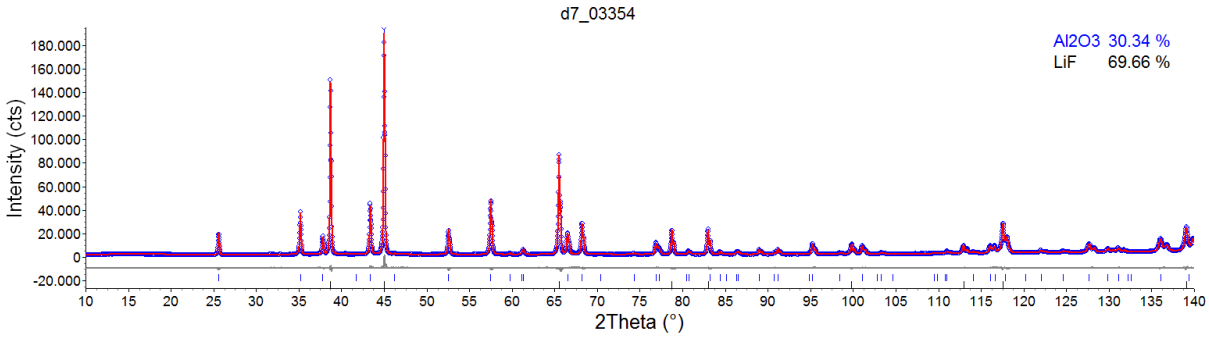

Source: Created by the author.

Figure A.6: Graphical Rietveld refinement obtained on data 'd7_03356' for mixture Al_2O_3/LiF (30/70). Blue dots – observed data; red curve – calculated data; grey curve – residual curve.

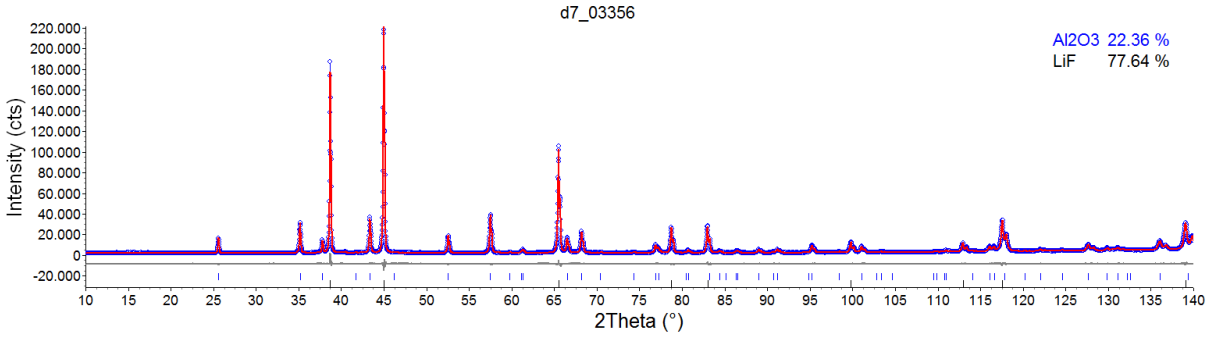

Source: Created by the author.

Figure A.7: Graphical Rietveld refinement obtained on data 'd7_03358' for mixture Al_2O_3/LiF (15/85). Blue dots – observed data; red curve – calculated data; grey curve – residual curve.

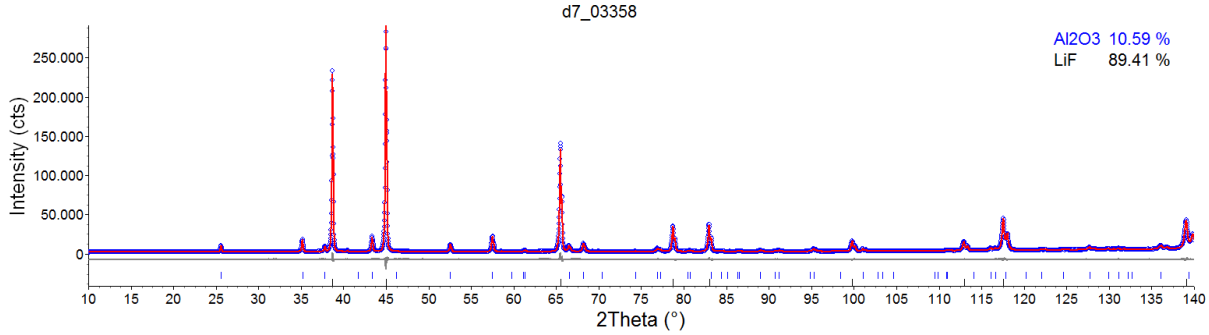

Source: Created by the author.

A.2. SRM-676a/LiF mixtures

A.2.1. Bruker D8 equipment

A.2.1.1. Values calculated

1st Data set

Table A.9: 1st data set for SRM-676a/LiF mixture, from Bruker D8 equipment, with values calculated from Rietveld refinement, for LiF phase quantification (%) and respective e.s.d. (%), *gof* and Rwp (%) obtained.

data code	%LiF	%LiF calc	e.s.d. (%)	*g.o.f.*	Rwp (%)
d7_04585	5.47	5.97	0.14	1.610	4.32
d7_04920	15.00	15.05	0.58	1.563	4.08
d7_04625	30.01	30.84	0.02	1.606	4.14
d7_04997	40.00	40.64	0.01	1.623	4.05
d7_04655	50.00	51.54	0.14	1.677	3.98
d7_05016	60.00	61.00	0.02	1.565	3.75
d7_04658	70.00	71.70	0.07	1.577	3.58
d7_05040	85.00	85.38	0.04	1.650	3.66
d7_05044	95.00	95.00	0.01	1.661	3.56

Source: Created by the author.

After apply Brindley correction to Rietveld refinement strategy.

Table A.10: 1st data set for SRM-676a/LiF mixture, from Bruker D8 equipment, with values calculated from Rietveld refinement with Brindley correction, for LiF phase quantification (%) and respective e.s.d. (%) obtained.

data code	%LiF	%LiF calc	e.s.d. (%)
d7_04585	5.47	5.68	0.02
d7_04920	15.00	14.99	0.54
d7_04625	30.01	30.73	0.02
d7_04997	40.00	40.51	0.01
d7_04655	50.00	51.40	0.14
d7_05016	60.00	60.85	0.02
d7_04658	70.00	71.98	0.04
d7_05040	85.00	85.29	0.04
d7_05044	95.00	94.96	0.01

Source: Created by the author.

2nd Data set

Table A.11: 2nd data set for SRM-676a/LiF mixture, from Bruker D8 equipment, with values calculated from Rietveld refinement, for LiF phase quantification (%) and respective e.s.d. (%), *gof* and Rwp (%) obtained.

data code	%LiF	%LiF calc	e.s.d. (%)	*g.o.f.*	Rwp (%)
d7_04599	5.47	5.82	0.04	1.616	4.32
d7_04931	15.00	15.78	0.07	1.589	4.11
d7_04639	30.01	30.78	0.07	1.627	4.02
d7_05012	40.00	40.85	0.13	1.586	3.95
d7_04656	50.00	51.18	0.12	1.632	3.89
d7_05017	60.00	60.88	0.07	1.468	3.73
d7_04665	70.00	71.72	0.05	1.776	4.42
d7_05041	85.00	85.37	0.03	1.651	3.69
d7_05072	95.00	95.021	0.004	1.650	3.54

Source: Created by the author.

After apply Brindley correction to Rietveld refinement strategy.

Table A.12: 2nd data set for SRM-676a/LiF mixture, from Bruker D8 equipment, with values calculated from Rietveld refinement with Brindley correction, for LiF phase quantification (%) and respective e.s.d. (%) obtained.

data code	%LiF	%LiF calc	e.s.d. (%)
d7_04599	5.47	5.80	0.10
d7_04931	15.00	15.56	0.14
d7_04639	30.01	30.67	0.06
d7_05012	40.00	40.72	0.13
d7_04656	50.00	51.04	0.12
d7_05017	60.00	60.73	0.06
d7_04665	70.00	72.32	0.20
d7_05041	85.00	85.28	0.04
d7_05072	95.00	94.98	0.00

Source: Created by the author.

3rd Data set

Table A.13: 3rd data set for SRM-676a/LiF mixture, from Bruker D8 equipment, with values calculated from Rietveld refinement, for LiF phase quantification (%) and respective e.s.d. (%), *gof* and Rwp (%) obtained.

data code	%LiF	%LiF calc	e.s.d. (%)	*g.o.f.*	Rwp (%)
d7_04612	5.47	5.51	0.18	1.629	4.35
d7_04938	15.00	16.79	0.65	1.571	4.08
d7_04652	30.01	30.99	0.09	1.745	5.1
d7_05015	40.00	40.49	0.12	1.579	3.94
d7_04657	50.00	51.33	0.02	1.673	3.96
d7_05039	60.00	61.04	0.05	1.598	3.81
d7_04666	70.00	71.96	0.12	1.633	3.69
d7_05042	85.00	85.21	0.08	1.651	3.68
d7_05074	95.00	95.02	0.01	1.669	3.59

Source: Created by the author.

After apply Brindley correction to Rietveld refinement strategy.

Table A.14: 3rd data set for SRM-676a/LiF mixture, from Bruker D8 equipment, with values calculated from Rietveld refinement with Brindley correction, for LiF phase quantification (%) and respective e.s.d. (%) obtained.

data code	%LiF	%LiF calc	e.s.d. (%)
d7_04612	5.47	5.49	0.12
d7_04938	15.00	16.73	0.69
d7_04652	30.01	30.88	0.08
d7_05015	40.00	40.36	0.12
d7_04657	50.00	51.18	0.02
d7_05039	60.00	60.88	0.04
d7_04666	70.00	71.82	0.16
d7_05042	85.00	85.12	0.08
d7_05074	95.00	94.99	0.01

Source: Created by the author.

Average values calculated from Rietveld refinements of these three data sets.

Table A.15: Average values for SRM-676a/LiF mixture, from Bruker D8 equipment, with values calculated from Rietveld refinement, for LiF phase quantification (%) and respective e.s.d. (%), *gof* and Rwp (%) obtained.

%LiF	%LiF calc	e.s.d. (%)	*g.o.f.*	Rwp (%)
5.47	5.77	0.12	1.618	4.33
15.00	15.87	0.43	1.574	4.09
30.01	30.87	0.06	1.659	4.42
40.00	40.66	0.09	1.596	3.98
50.00	51.35	0.09	1.661	3.94
60.00	60.97	0.04	1.544	3.76
70.00	71.79	0.08	1.662	3.90
85.00	85.32	0.05	1.651	3.68
95.00	95.02	0.01	1.660	3.56

Source: Created by the author.

Average values calculated after apply Brindley correction to Rietveld refinement strategy.

Table A.16: Average values for SRM-676a/LiF mixture, from Bruker D8 equipment, with values calculated from Rietveld refinement with Brindley correction, for LiF phase quantification (%) and respective e.s.d. (%) obtained.

%LiF	%LiF calc	e.s.d. (%)
5.47	5.66	0.13
15.00	15.76	0.72
30.01	30.76	0.09
40.00	40.53	0.15
50.00	51.21	0.15
60.00	60.82	0.06
70.00	72.04	0.21
85.00	85.23	0.08
95.00	94.98	0.01

Source: Created by the author.

A.2.1.2. Graphical fits

Figure A.8: Graphical Rietveld refinement obtained on data 'd7_04585' for mixture SRM-676a/LiF (95/5). Blue dots – observed data; red curve – calculated data; grey curve – residual curve.

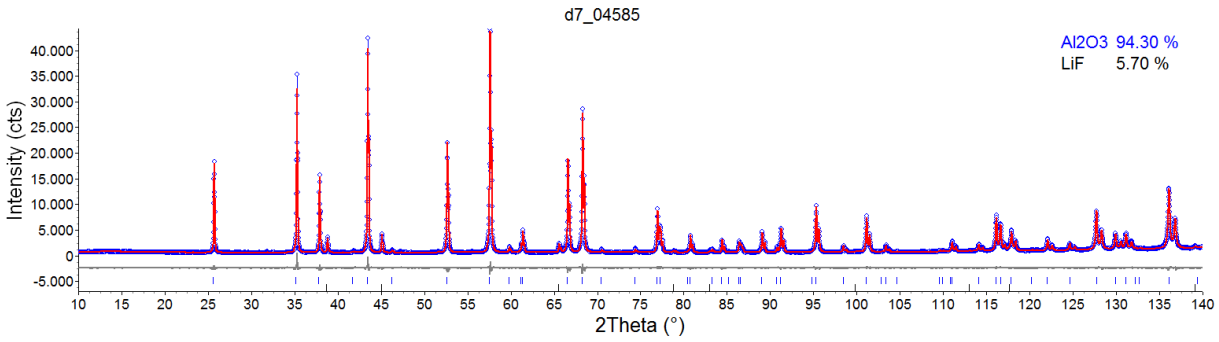

Source: Created by the author.

Figure A.9: Graphical Rietveld refinement obtained on data 'd7_04920' for mixture SRM-676a/LiF (85/15). Blue dots – observed data; red curve – calculated data; grey curve – residual curve.

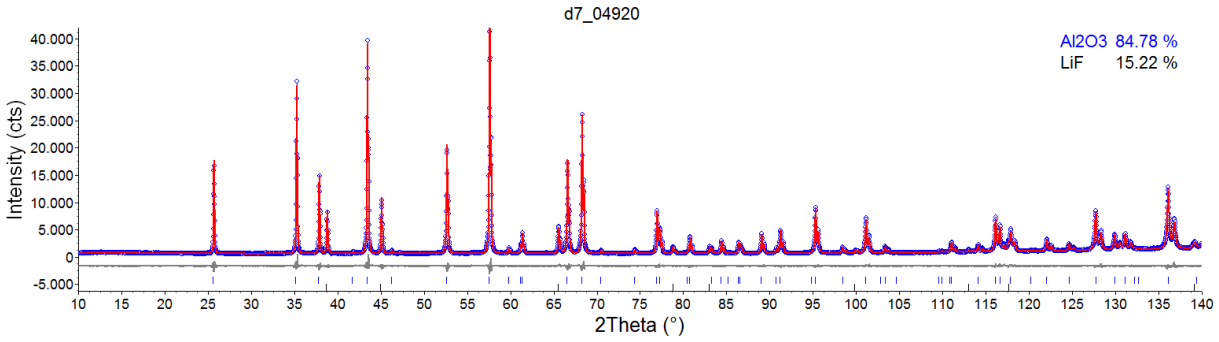

Source: Created by the author.

Figure A.10: Graphical Rietveld refinement obtained on data 'd7_04625' for mixture SRM-676a/LiF (70/30). Blue dots – observed data; red curve – calculated data; grey curve – residual curve.

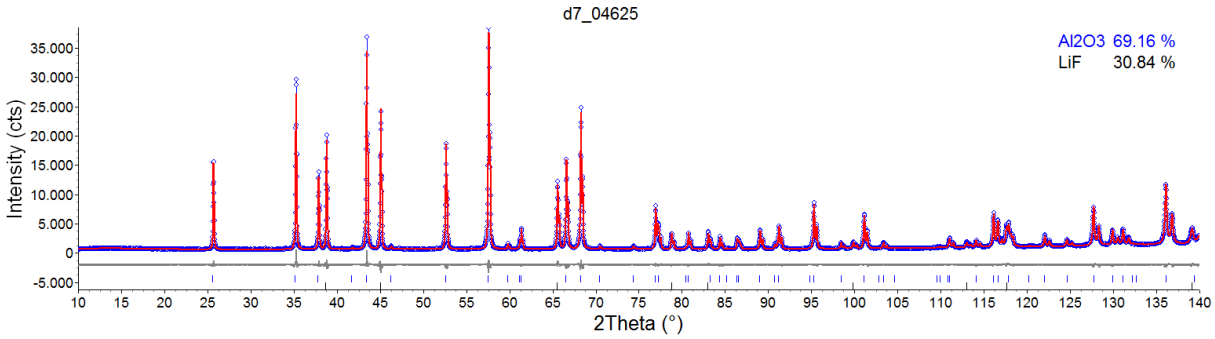

Source: Created by the author.

Figure A.11: Graphical Rietveld refinement obtained on data 'd7_04997' for mixture SRM-676a/LiF (60/40). Blue dots – observed data; red curve – calculated data; grey curve – residual curve.

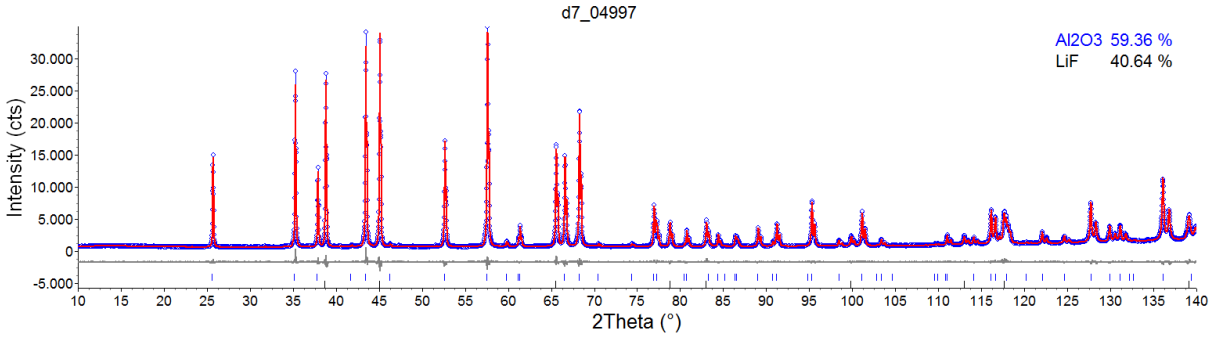

Source: Created by the author.

Figure A.12: Graphical Rietveld refinement obtained on data 'd7_04656' for mixture SRM-676a/LiF (50/50). Blue dots – observed data; red curve – calculated data; grey curve – residual curve.

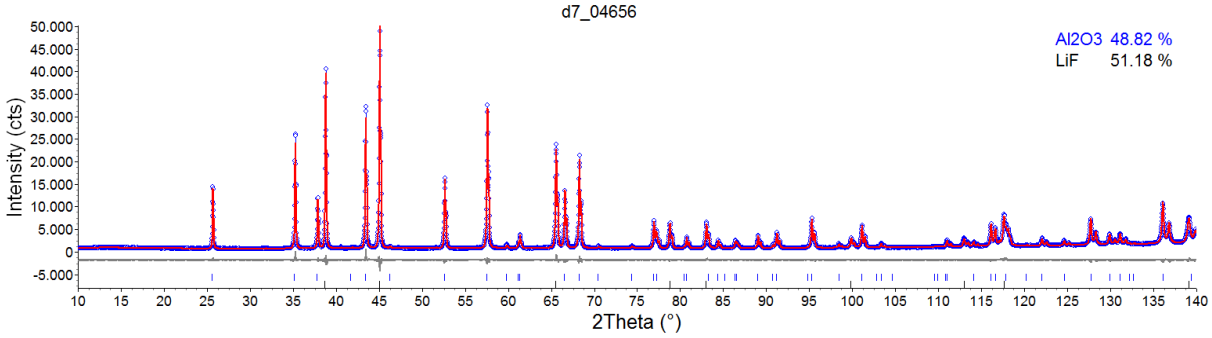

Source: Created by the author.

Figure A.13: Graphical Rietveld refinement obtained on data 'd7_05016' for mixture SRM-676a/LiF (40/60). Blue dots – observed data; red curve – calculated data; grey curve – residual curve.

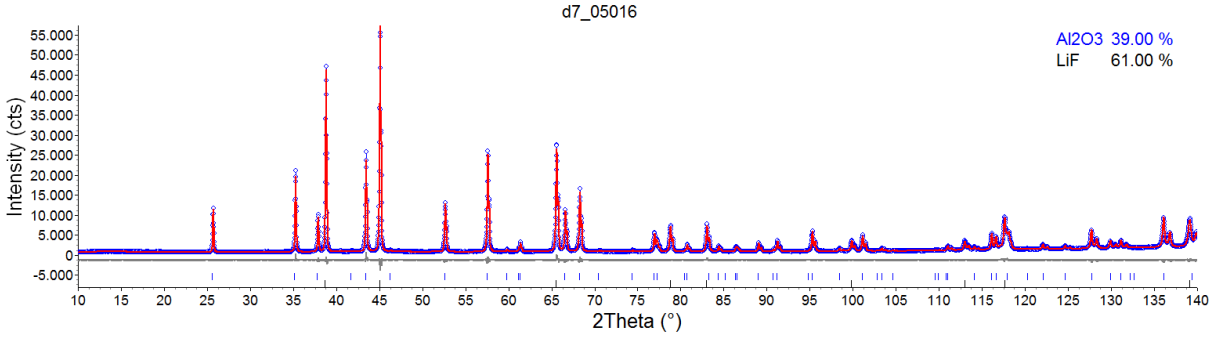

Source: Created by the author.

Figure A.14: Graphical Rietveld refinement obtained on data 'd7_04658' for mixture SRM-676a/LiF (30/70). Blue dots – observed data; red curve – calculated data; grey curve – residual curve.

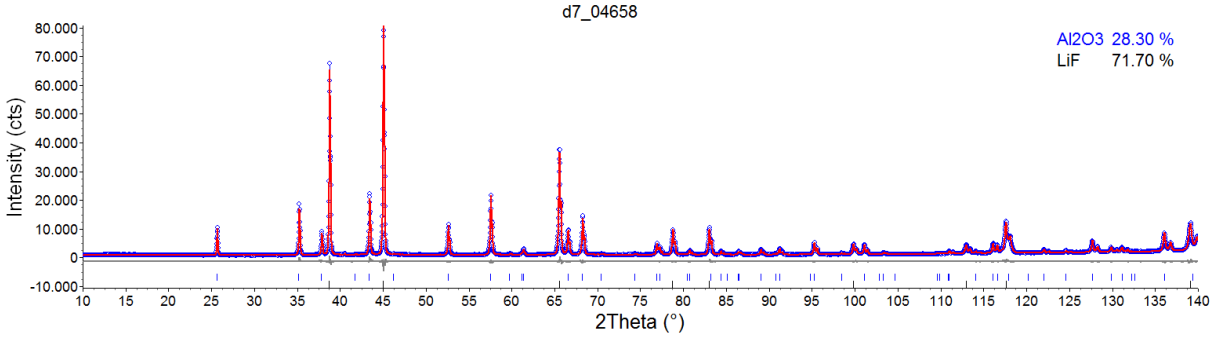

Source: Created by the author.

Figure A.15: Graphical Rietveld refinement obtained on data 'd7_05040' for mixture SRM-676a/LiF (15/85). Blue dots – observed data; red curve – calculated data; grey curve – residual curve.

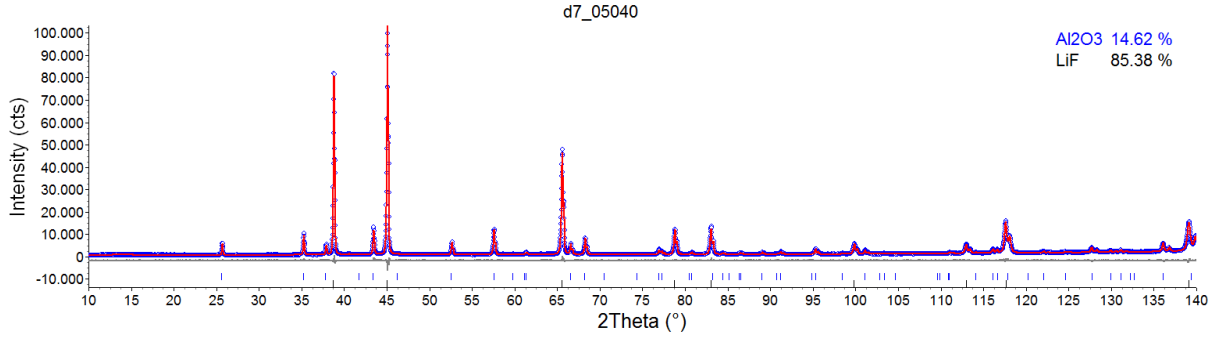

Source: Created by the author.

Figure A.16: Graphical Rietveld refinement obtained on data 'd7_05044' for mixture SRM-676a/LiF (5/95). Blue dots – observed data; red curve – calculated data; grey curve – residual curve.

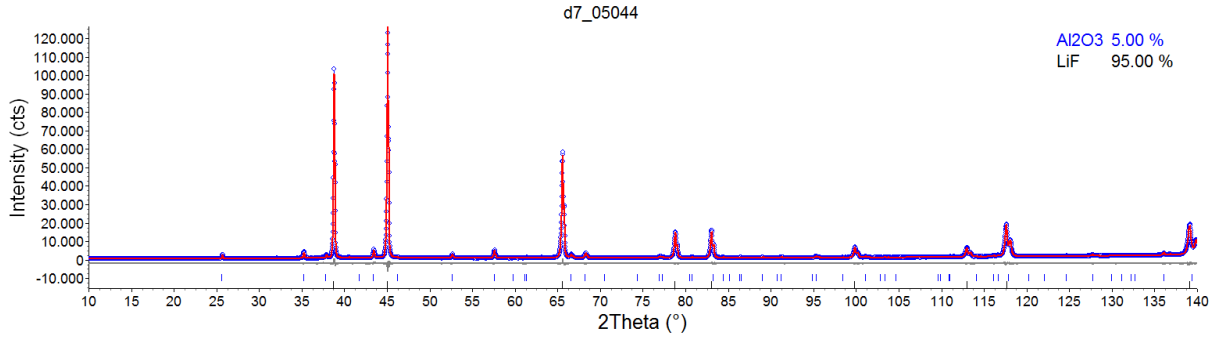

Source: Created by the author.

A.2.2. Huber equipment – LNLS

A.2.2.1 Arara furnace – atmospheric pressure

Table A.17: Data set for SRM-676a/LiF mixture, from LNLS (Arara furnace) – atmospheric pressure, with values calculated from Rietveld refinement, for LiF phase quantification (%) and respective e.s.d. (%), *gof* and Rwp (%) obtained.

data code	%LiF	%LiF calc	e.s.d. (%)	*g.o.f.*	Rwp (%)
70Al_2O_3_30LiF	30.01	31.48	0.24	0.888	6.59
50Al_2O_3_50LiF	50.00	51.92	0.23	0.974	7.12
30Al_2O_3_70LiF	70.00	73.33	0.05	1.033	7.21

Source: Created by the author.

After apply Brindley correction to Rietveld refinement strategy.

Table A.18: Data set for SRM-676a/LiF mixture, from LNLS (Arara furnace) – atmospheric pressure, with values calculated from Rietveld refinement with Brindley correction, for LiF phase quantification (%) and respective e.s.d. (%) obtained.

data code	%LiF	%LiF calc	e.s.d. (%)
70Al_2O_3_30LiF	30.01	31.38	0.24
50Al_2O_3_50LiF	50.00	51.77	0.15
30Al_2O_3_70LiF	70.00	73.19	0.05

Source: Created by the author.

A.2.2.2 Arara furnace – vaccum

Table A.19: Data set for SRM-676a/LiF mixture, from LNLS (Arara furnace) – vaccum, with values calculated from Rietveld refinement, for LiF phase quantification (%) and respective e.s.d. (%), *gof* and Rwp (%) obtained.

data code	%LiF	%LiF calc	e.s.d. (%)	*g.o.f.*	Rwp (%)
70Al_2O_3_30LiF_vac	30.01	31.19	0.45	0.962	7.43
50Al_2O_3_50LiF_vac	50.00	51.47	0.55	1.044	7.84
30Al_2O_3_70LiF_vac	70.00	73.33	0.05	1.060	7.63

Source: Created by the author.

After apply Brindley correction to Rietveld refinement strategy.

Table A.20: Data set for SRM-676a/LiF mixture, from LNLS (Arara furnace) – vaccum, with values calculated from Rietveld refinement with Brindley correction, for LiF phase quantification (%) and respective e.s.d. (%) obtained.

data code	%LiF	%LiF calc	e.s.d. (%)
70Al_2O_3_30LiF_vac	30.01	31.08	0.45
50Al_2O_3_50LiF_vac	50.00	51.32	0.47
30Al_2O_3_70LiF_vac	70.00	73.20	0.06

Source: Created by the author.

A.2.2.3. Tucano furnace

Table A.21: Data set for SRM-676a/LiF mixture, from LNLS (Tucano furnace), with values calculated from Rietveld refinement, for LiF phase quantification (%) and respective e.s.d. (%), *gof* and Rwp (%) obtained.

data code	%LiF	%LiF calc	e.s.d. (%)	*g.o.f.*	Rwp (%)
70Al_2O_3_30LiF_tu	30.01	32.80	0.69	1.366	5.08
50Al_2O_3_50LiF_tu	50.00	53.36	0.78	1.497	5.42
30Al_2O_3_70LiF_tu	70.00	73.10	0.11	1.630	5.74

Source: Created by the author.

After apply Brindley correction to Rietveld refinement strategy.

Table A.22: Data set for SRM-676a/LiF mixture, from LNLS (Tucano furnace), with values calculated from Rietveld refinement with Brindley correction, for LiF phase quantification (%) and respective e.s.d. (%) obtained.

data code	%LiF	%LiF calc	e.s.d. (%)
70Al_2O_3_30LiF_tu	30.01	32.69	0.69
50Al_2O_3_50LiF_tu	50.00	52.86	0.62
30Al_2O_3_70LiF_tu	70.00	72.96	0.11

Source: Created by the author.

Average values calculated from Rietveld refinements of these LNLS data sets.

Table A.23: Average values for SRM-676a/LiF mixture, from LNLS data sets, with values calculated from Rietveld refinement, for LiF phase quantification (%) and respective e.s.d. (%), *gof* and Rwp (%) obtained.

%LiF	%LiF calc	e.s.d. (%)	*g.o.f.*	Rwp (%)
30.01	31.82	0.70	1.072	6.367
50.00	52.25	0.81	1.172	6.793
70.00	73.25	0.11	1.241	6.86

Source: Created by the author.

Average values calculated after apply Brindley correction to Rietveld refinement strategy.

Table A.24: Average values for SRM-676a/LiF mixture, from LNLS data sets, with values calculated from Rietveld refinement with Brindley correction, for LiF phase quantification (%) and respective e.s.d. (%) obtained.

%LiF	%LiF calc	e.s.d. (%)
30.01	31.72	0.68
50.00	51.98	0.63
70.00	73.12	0.16

Source: Created by the author.

A.2.3. Rigaku RINT2000 equipment

Table A.25: Data set for SRM-676a/LiF mixture, from Rigaku RINT2000 equipment, with values calculated from Rietveld refinement, for LiF phase quantification (%) and respective e.s.d. (%), *gof* and Rwp (%) obtained.

data code	%LiF	%LiF calc	e.s.d. (%)	*g.o.f.*	Rwp (%)
s1105	30.01	30.50	0.40	1.289	12.70
s1104	50.00	51.07	0.34	1.221	10.92
s1106	70.00	72.03	0.23	1.230	10.39

Source: Created by the author.

After apply Brindley correction to Rietveld refinement strategy.

Table A.26: Data set for SRM-676a/LiF mixture, from Rigaku RINT2000 equipment, with values calculated from Rietveld refinement with Brindley correction, for LiF phase quantification (%) and respective e.s.d. (%) obtained.

data code	%LiF	%LiF calc	e.s.d. (%)
s1105	30.01	30.38	0.43
s1104	50.00	50.56	0.49
s1106	70.00	71.89	0.33

Source: Created by the author.

A.3. SRM-676a/Li_2CO_3 mixtures

A.3.1. Bruker D8 equipment

A.3.1.1. Values calculated

1st Data set

Table A.27: 1st data set for SRM-676a/Li_2CO_3 mixture, from Bruker D8 equipment, with values calculated from Rietveld refinement, for Li_2CO_3 phase quantification (%) and respective e.s.d. (%), *gof* and Rwp (%) obtained.

data code	%Li_2CO_3	% calc	e.s.d. (%)	Amor. (%)	e.s.d. (%)	g.o.f.	R_{wp} (%)
d7_05177	15.00	12.88	0.11	16.16	0.85	2.047	5.06
d7_04730	30.02	26.82	0.05	14.54	0.20	1.855	4.58
d7_05116	40.02	36.97	0.25	12.07	0.96	2.233	5.46
d7_04733	49.05	45.90	0.16	11.87	0.58	2.584	6.35
d7_05132	60.01	57.68	0.03	9.19	0.13	2.700	6.23
d7_04740	70.01	67.47	0.14	11.18	0.57	3.175	6.95
d7_05159	85.02	83.52	0.02	10.71	0.11	3.603	7.22

Source: Created by the author.

After apply Brindley correction to Rietveld refinement strategy.

Table A.28: 1st data set for SRM-676a/Li_2CO_3 mixture, from Bruker D8 equipment, with values calculated from Rietveld refinement with Brindley correction, for Li_2CO_3 phase quantification (%) and respective e.s.d. (%) obtained.

data code	%Li_2CO_3	% calc	e.s.d. (%)	Amor. (%)	e.s.d. (%)
d7_05177	15.00	12.52	0.12	18.90	0.90
d7_04730	30.02	26.29	0.05	16.82	0.20
d7_05116	40.02	36.42	0.25	14.15	0.94
d7_04733	49.05	45.36	0.16	13.74	0.57
d7_05132	60.01	57.23	0.04	10.85	0.13
d7_04740	70.01	67.11	0.14	12.58	0.54
d7_05159	85.02	83.35	0.02	11.80	0.12

Source: Created by the author.

2nd Data set

Table A.29: 2nd data set for SRM-676a/Li_2CO_3 mixture, from Bruker D8 equipment, with values calculated from Rietveld refinement, for Li_2CO_3 phase quantification (%) and respective e.s.d. (%), *gof* and Rwp (%) obtained.

data code	%Li_2CO_3	% calc	e.s.d. (%)	Amor. (%)	e.s.d. (%)	g.o.f.	R_{wp} (%)
d7_05178	15.00	12.65	0.28	17.91	2.09	1.995	4.95
d7_04731	30.02	26.70	0.13	15.08	0.58	2.144	5.26
d7_05117	40.02	37.45	0.09	10.25	0.33	2.206	5.40
d7_04734	49.05	45.59	0.37	12.94	1.33	2.46	6.25
d7_05136	60.01	57.72	0.01	9.05	0.03	2.805	6.47
d7_04741	70.01	67.58	0.06	10.73	0.25	3.212	7.00
d7_05173	85.02	83.53	0.01	10.61	0.04	3.594	7.18

Source: Created by the author.

After apply Brindley correction to Rietveld refinement strategy.

Table A.30: 2nd data set for SRM-676a/Li_2CO_3 mixture, from Bruker D8 equipment, with values calculated from Rietveld refinement with Brindley correction, for Li_2CO_3 phase quantification (%) and respective e.s.d. (%) obtained.

data code	%Li_2CO_3	% calc	e.s.d. (%)	Amor. (%)	e.s.d. (%)
d7_05178	15.00	12.31	0.27	20.46	2.00
d7_04731	30.02	26.17	0.13	17.35	0.58
d7_05117	40.02	36.90	0.09	12.36	0.32
d7_04734	49.05	45.06	0.37	14.80	1.32
d7_05136	60.01	57.27	0.01	10.71	0.03
d7_04741	70.01	67.23	0.05	12.14	0.23
d7_05173	85.02	83.36	0.01	11.71	0.05

Source: Created by the author.

3rd Data set

Table A.31: 3rd data set for SRM-676a/Li_2CO_3 mixture, from Bruker D8 equipment, with values calculated from Rietveld refinement, for Li_2CO_3 phase quantification (%) and respective e.s.d. (%), *gof* and Rwp (%) obtained.

data code	%Li_2CO_3	% calc	e.s.d. (%)	Amor. (%)	e.s.d. (%)	g.o.f.	R_{wp} (%)
d7_05196	15.00	13.60	0.39	10.81	2.93	1.965	4.86
d7_04732	30.02	27.14	0.18	13.15	0.78	2.180	5.36
d7_05124	40.02	37.57	0.17	9.81	0.64	2.199	5.39
d7_04739	49.05	46.87	0.53	8.35	1.91	3.037	7.05
d7_05143	60.01	57.79	0.04	8.78	0.16	2.711	6.01
d7_05082	70.01	67.95	0.20	9.2	0.83	3.021	6.77
d7_05175	85.02	83.57	0.02	10.35	0.15	3.559	7.13

Source: Created by the author.

After apply Brindley correction to Rietveld refinement strategy.

Table A.32: 3rd data set for SRM-676a/Li_2CO_3 mixture, from Bruker D8 equipment, with values calculated from Rietveld refinement with Brindley correction, for Li_2CO_3 phase quantification (%) and respective e.s.d. (%) obtained.

data code	%Li_2CO_3	% calc	e.s.d. (%)	Amor. (%)	e.s.d. (%)
d7_05196	15.00	13.24	0.39	13.53	2.90
d7_04732	30.02	26.61	0.18	15.44	0.78
d7_05124	40.02	37.01	0.16	11.94	0.62
d7_04739	49.05	46.34	0.53	10.28	1.88
d7_05143	60.01	57.34	0.04	10.45	0.16
d7_05082	70.01	67.58	0.19	10.71	0.78
d7_05175	85.02	83.41	0.03	11.4	0.17

Source: Created by the author.

Average values calculated from Rietveld refinements of these three data sets.

Table A.33: Average values for SRM-676a/Li_2CO_3 mixture, from Bruker D8 equipment, with values calculated from Rietveld refinement, for Li_2CO_3 phase quantification (%) and respective e.s.d. (%), *gof* and Rwp (%) obtained.

%Li_2CO_3	% calc	e.s.d. (%)	Amor. (%)	e.s.d. (%)	g.o.f.	R_{wp} (%)
15.00	13.04	0.40	14.96	3.02	2.002	4.96
30.02	26.89	0.19	14.26	0.81	2.060	5.07
40.02	37.33	0.26	10.71	0.98	2.213	5.42
49.05	46.12	0.54	11.05	1.96	2.694	6.55
60.01	57.73	0.05	9.01	0.17	2.739	6.24
70.01	67.66	0.21	10.37	0.85	3.136	6.91
85.02	83.54	0.02	10.56	0.15	3.585	7.18

Source: Created by the author.

Average values calculated after apply Brindley correction to Rietveld refinement strategy.

Table A.34: Average values for SRM-676a/Li_2CO_3 mixture, from Bruker D8 equipment, with values calculated from Rietveld refinement with Brindley correction, for Li_2CO_3 phase quantification (%) and respective e.s.d. (%) obtained.

%Li_2CO_3	% calc	e.s.d. (%)	Amor. (%)	e.s.d. (%)
15.00	12.69	0.40	17.63	2.97
30.02	26.36	0.19	16.54	0.81
40.02	36.78	0.26	12.82	0.96
49.05	45.59	0.55	12.94	1.93
60.01	57.28	0.05	10.67	0.17
70.01	67.31	0.20	11.81	0.80
85.02	83.37	0.03	11.64	0.17

Source: Created by the author.

A.3.1.2. Graphical fits

Figure A.17: Graphical Rietveld refinement obtained on data 'd7_05177' for mixture SRM-676a/Li_2CO_3 (85/15). Blue dots – observed data; red curve – calculated data; grey curve – residual curve.

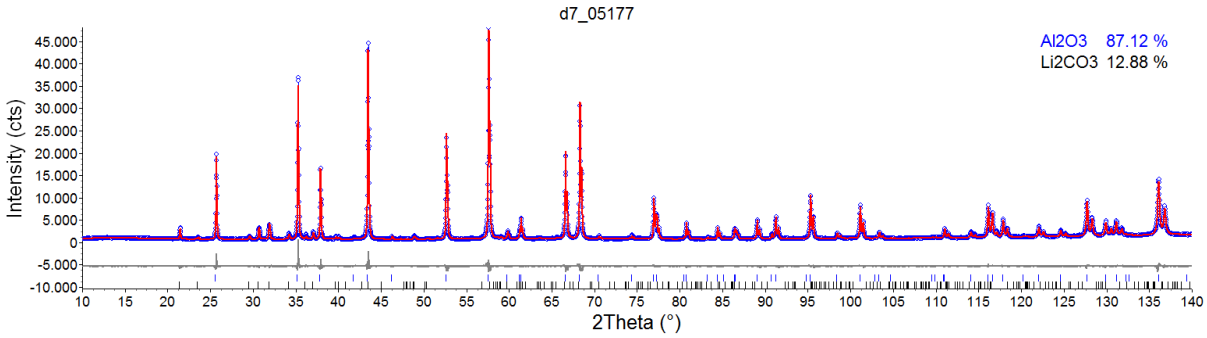

Source: Created by the author.

Figure A.18: Graphical Rietveld refinement obtained on data 'd7_04730' for mixture SRM-676a/Li_2CO_3 (70/30). Blue dots – observed data; red curve – calculated data; grey curve – residual.

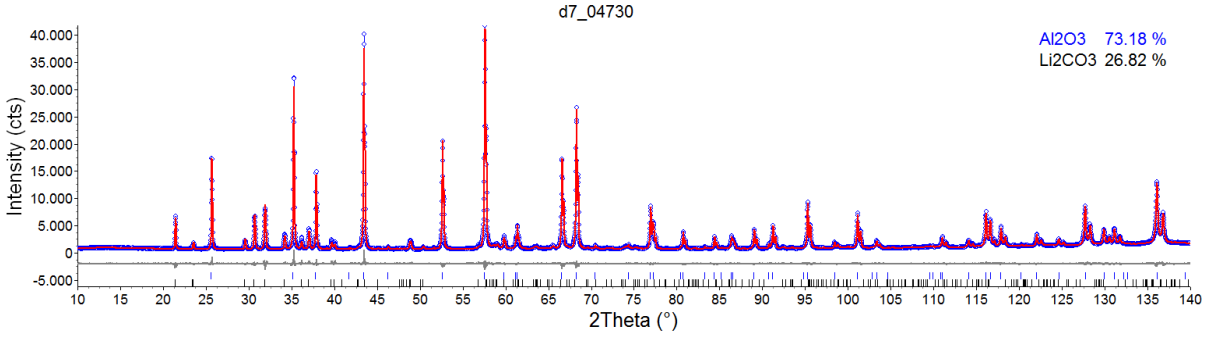

Source: Created by the author.

Figure A.19: Graphical Rietveld refinement obtained on data 'd7_05116' for mixture SRM-676a/Li_2CO_3 (60/40). Blue dots – observed data; red curve – calculated data; grey curve – residual.

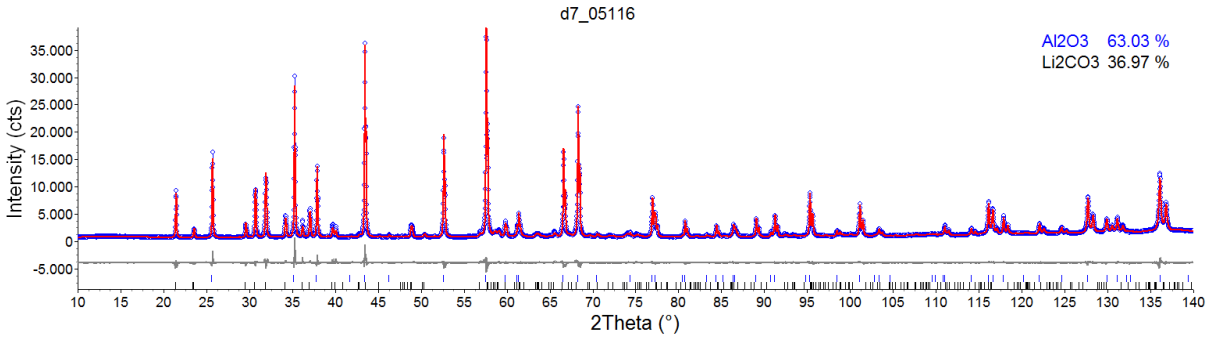

Source: Created by the author.

Figure A.20: Graphical Rietveld refinement obtained on data 'd7_04733' for mixture SRM-676a/Li_2CO_3 (50/50). Blue dots – observed data; red curve – calculated data; grey curve – residual.

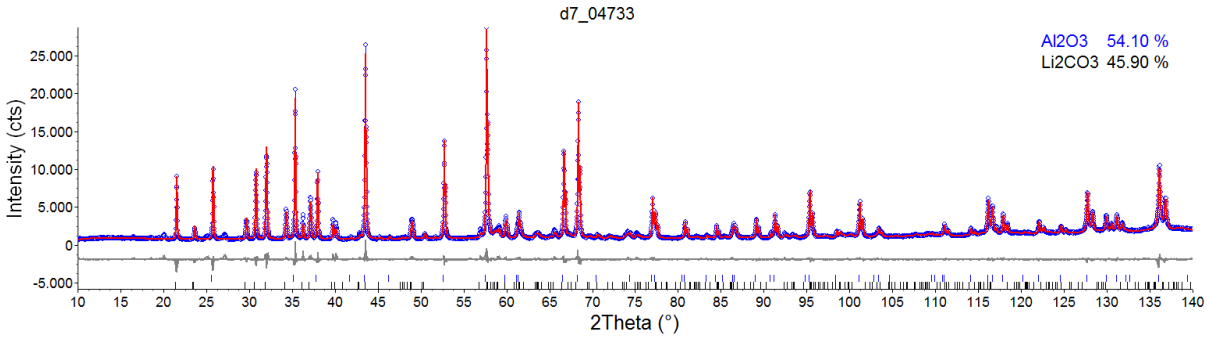

Source: Created by the author.

Figure A.21: Graphical Rietveld refinement obtained on data 'd7_05132' for mixture SRM-676a/Li_2CO_3 (40/60). Blue dots – observed data; red curve – calculated data; grey curve – residual.

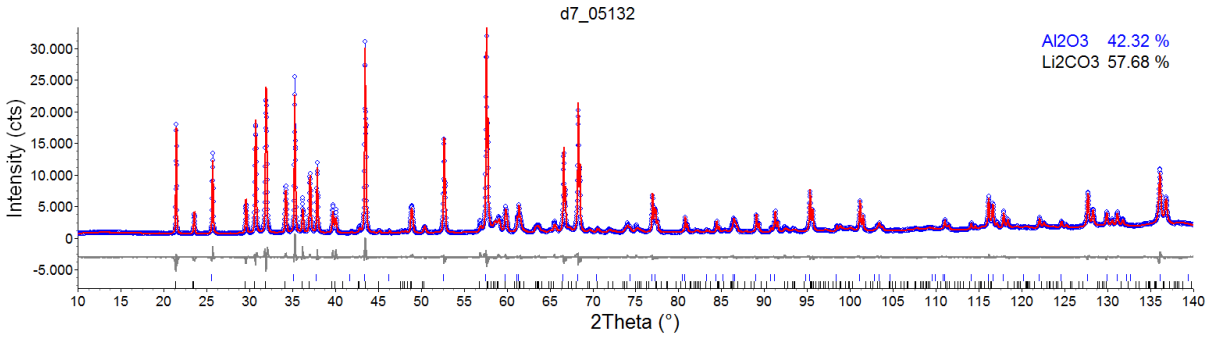

Source: Created by the author.

Figure A.22: Graphical Rietveld refinement obtained on data 'd7_04740' for mixture SRM-676a/Li_2CO_3 (30/70). Blue dots – observed data; red curve – calculated data; grey curve – residual.

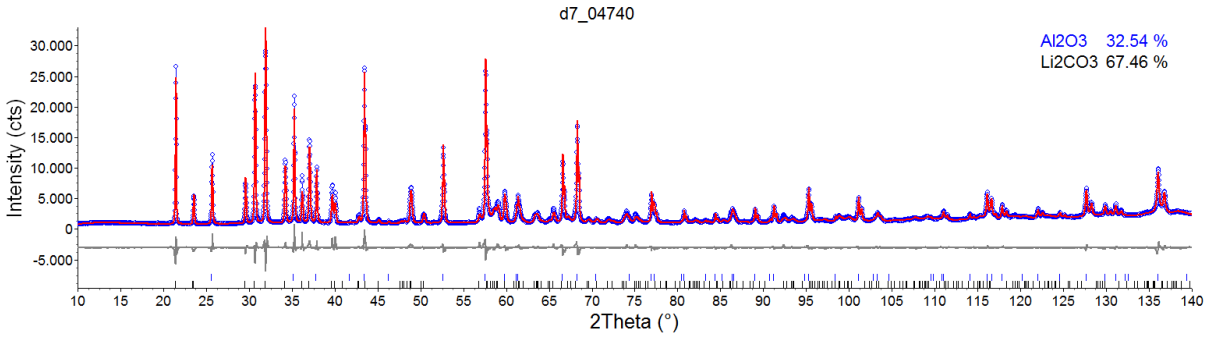

Source: Created by the author.

Figure A.23: Graphical Rietveld refinement obtained on data 'd7_05159' for mixture SRM-676a/Li_2CO_3 (15/85). Blue dots – observed data; red curve – calculated data; grey curve – residual.

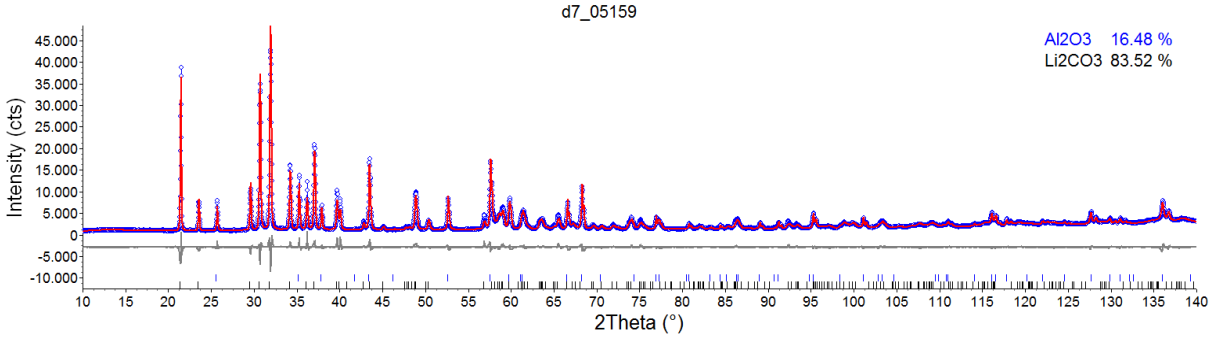

Source: Created by the author.

A.3.2. Huber equipment – LNLS

A.3.2.1 Arara furnace – atmospheric pressure

Table A.35: Data set for SRM-676a/Li_2CO_3 mixture, from LNLS (Arara furnace) – atmospheric pressure, with values calculated from Rietveld refinement, for LiF phase quantification (%) and respective e.s.d. (%), *gof* and Rwp (%) obtained.

Data code	%Li_2CO_3	%calc	e.s.d. (%)	Amor. (%)	e.s.d. (%)	*gof*	R_{wp} (%)
70Al_2O_3_30Li_2CO_3	30.02	26.24	0.02	17.07	0.07	0.997	5.79
50Al_2O_3_50Li_2CO_3	49.05	46.51	0.42	9.67	0.68	1.077	5.96
30Al_2O_3_30Li_2CO_3	70.01	69.02	0.01	4.58	0.03	1.158	5.98

Source: Created by the author.

After apply Brindley correction to Rietveld refinement strategy.

Table A.36: Data set for SRM-676a/Li_2CO_3 mixture, from LNLS (Arara furnace) – atmospheric pressure, with values calculated from Rietveld refinement with Brindley correction, for LiF phase quantification (%) and respective e.s.d. (%) obtained.

Data code	%Li_2CO_3	% calc	e.s.d. (%)	Amor. (%)	e.s.d. (%)
70Al_2O_3_30Li_2CO_3	30.02	25.71	0.02	19.30	0.07
50Al_2O_3_50Li_2CO_3	49.05	45.97	0.43	11.61	0.67
30Al_2O_3_30Li_2CO_3	70.01	68.68	0.01	6.05	0.04

Source: Created by the author.

A.3.2.2. Arara furnace – vaccum

Table A.37: Data set for SRM-676a/Li_2CO_3 mixture, from LNLS (Arara furnace) – vaccum, with values calculated from Rietveld refinement, for LiF phase quantification (%) and respective e.s.d. (%), *gof* and Rwp (%) obtained.

Data code	%Li_2CO_3	% calc	e.s.d. (%)	Amor. (%)	e.s.d. (%)	*gof*	R_{wp} (%)
70Al_2O_3_vac	30.02	26.29	0.02	16.86	0.07	1.243	7.63
50Al_2O_3_vac	49.05	46.67	0.31	8.98	0.20	1.154	6.74
30Al_2O_3_vac	70.01	69.00	0.01	4.67	0.03	1.292	6.85

Source: Created by the author.

After apply Brindley correction to Rietveld refinement strategy.

Table A.38: Data set for SRM-676a/Li_2CO_3 mixture, from LNLS (Arara furnace) – vaccum, with values calculated from Rietveld refinement with Brindley correction, for LiF phase quantification (%) and respective e.s.d. (%) obtained.

Data code	%Li_2CO_3	% calc	e.s.d. (%)	Amor. (%)	e.s.d. (%)
70Al_2O_3_30Li_2CO_3_vac	30.02	25.76	0.02	19.10	0.07
50Al_2O_3_50Li_2CO_3_vac	49.05	46.16	0.30	10.93	0.19
30Al_2O_3_30Li_2CO_3_vac	70.01	68.66	0.01	6.15	0.04

Source: Created by the author.

A.3.2.3. Tucano furnace

Table A.39: Data set for SRM-676a/Li_2CO_3 mixture, from LNLS (Tucano furnace), with values calculated from Rietveld refinement, for LiF phase quantification (%) and respective e.s.d. (%), *gof* and Rwp (%) obtained.

Data code	%Li_2CO_3	% calc	e.s.d. (%)	Amor. (%)	e.s.d. (%)	*gof*	R_{wp} (%)
50Al_2O_3_tu	49.05	48.15	0.74	7.46	0.88	1.664	4.81

Source: Created by the author.

After apply Brindley correction to Rietveld refinement strategy.

Table A.40: Data set for SRM-676a/Li_2CO_3 mixture, from LNLS (Tucano furnace), with values calculated from Rietveld refinement with Brindley correction, for LiF phase quantification (%) and respective e.s.d. (%) obtained.

Data code	%Li_2CO_3	% calc	e.s.d. (%)	Amor. (%)	e.s.d. (%)
50Al_2O_3_50Li_2CO_3_tu	49.05	47.62	0.73	9.45	0.86

Source: Created by the author.

Average values calculated from Rietveld refinements of these LNLS data sets.

Table A.41: Average values for SRM-676a/Li_2CO_3 mixture, from LNLS, with values calculated from Rietveld refinement, for LiF phase quantification (%) and respective e.s.d. (%) obtained.

%Li_2CO_3	% calc	e.s.d. (%)	Amor. (%)	e.s.d. (%)
30.02	26.27	0.03	16.97	0.11
49.05	47.11	0.74	8.70	1.13
70.01	69.01	0.01	4.63	0.04

Source: Created by the author.

After apply Brindley correction to Rietveld refinement strategy.

Table A.42: Average values for SRM-676a/Li_2CO_3 mixture, from LNLS, with values calculated from Rietveld refinement with Brindley correction, for LiF phase quantification (%) and respective e.s.d. (%) obtained.

%Li_2CO_3	% calc	e.s.d. (%)	Amor. (%)	e.s.d. (%)
30.02	25.74	0.03	19.20	0.10
49.05	46.58	0.74	10.66	0.90
70.01	68.67	0.01	6.10	0.05

Source: Created by the author.

A.3.3. Rigaku RINT2000 equipment

Table A.43: Data set for SRM-676a/Li_2CO_3 mixture, from Rigaku RINT2000 equipment, with values calculated from Rietveld refinement, for LiF phase quantification (%) and respective e.s.d. (%), *gof* and Rwp (%) obtained.

Data code	%Li_2CO_3	% calc	e.s.d. (%)	Amor. (%)	e.s.d. (%)	*gof*	R_{wp} (%)
S1068	30.02	26.97	0.19	13.91	0.8	1.535	18.25
S1066	49.05	47.47	0.40	9.99	0.1	1.402	15.01
S1067	70.01	68.06	0.13	8.74	0.6	1.482	13.42

Source: Created by the author.

After apply Brindley correction to Rietveld refinement strategy.

Table A.44: Data set for SRM-676a/Li_2CO_3 mixture, from Rigaku RINT2000 equipment, with values calculated from Rietveld refinement with Brindley correction, for LiF phase quantification (%) and respective e.s.d. (%) obtained.

Data code	%Li_2CO_3	% calc	e.s.d. (%)	Amor. (%)	e.s.d. (%)
S1068	30.02	26.44	0.19	16.19	0.79
S1066	49.05	46.95	0.41	11.91	0.05
S1067	70.01	67.71	0.13	10.17	0.57

Source: Created by the author.

Appendix B

Values calculated and graphical fits for Mebendazol amorphous quantification

MBZ was carefully mixed in a 50/50 weight ratio, with each internal standard (LiF, Li_2CO_3 and SRM-676a) and more nine mixtures of LiF/MBZ/$(C_8H_8)_n$, 50/(45/5; 40/10; 35/15; 30/20; 25/25; 20/30; 15/35; 10/40; 5/45; 0/50).

All samples with MBZ (LiF/MBZ, Li_2CO_3/MBZ, SRM-676a/MBZ and LiF/MBZ/$(C_8H_8)_n$) were collected three times over 3-85° 2θ on the D8 and the samples LiF/MBZ, Li_2CO_3/MBZ and SRM-676a/MBZ were also collected in RINT2000 and at LNLS.

For Rietveld refinements the crystal structures of inorganic materials, were obtained from the ICSD (ICSD, 2009) with numbers 31548 (Al_2O_3), 53839 (LiF) and 9009641 (Li_2CO_3); for MBZ polymorphs, the crystal structures were obtained from literature MBZA (Ferreira *et al.*, 2010) and MBZC (Martins *et al.*, 2009).

In all refinements were applied linear absorption correction for adjusting the peak shape due to sample transparency, 14 terms in Chebychev background polynomial, and refined scale factor for each phase, lattice parameters, peak shapes and one general atomic displacement parameter; for MBZA and MBZC, the preferred orientation were corrected by March Dollase model. For data from D8, the refinement applied corrections for: axial divergence, specimen displacement, tube tails correction, variable divergence intensity and a modelled small portion of K_β radiation; with data from RINT2000, only simple axial model and specimen displacement has been applied; and in data collected at LNLS, simple axial model and zero error.

B.1. SRM-676a/MBZ, LiF/MBZ and Li_2CO_3/MBZ mixtures

B.1.1. Bruker D8 Equipment

B.1.1.1. Values calculated

Table B.1: Data set for SRM-676a/MBZ mixture, from Bruker D8 equipment, with values calculated from Rietveld refinement, for MBZA, MBZC and amorphous quantification (%) and respective e.s.d. (%), *gof* and Rwp (%) obtained.

Data code	%MBZ	%MBZA	e.s.d.	%MBZC	e.s.d.	Amor. (%)	e.s.d.	*gof*	Rwp (%)
d7_04785	49.70	2.57	0.005	45.42	0.53	6.64	1.94	2.117	6.55
d7_04792	49.70	3.01	0.32	43.96	0.50	10.39	0.71	1.975	6.15
d7_04801	49.70	2.11	0.32	44.64	0.02	11.12	1.23	2.070	6.48

Source: Created by the author.

After apply Brindley correction to Rietveld refinement strategy.

Table B.2: Data set for SRM-676a/MBZ mixture, from Bruker D8 equipment, with values calculated from Rietveld refinement with Brindley correction, for MBZA, MBZC and amorphous quantification (%) and respective e.s.d. (%) obtained.

Data code	%MBZ	%MBZA	e.s.d.	%MBZC	e.s.d.	Amor. (%)	e.s.d.
d7_04785	49.70	2.56	0.005	45.22	0.53	7.42	1.93
d7_04792	49.70	2.99	0.31	43.76	0.51	11.16	0.72
d7_04801	49.70	2.11	0.31	44.45	0.02	11.86	1.21

Source: Created by the author.

Table B.3: Data set for LiF/MBZ mixture, from Bruker D8 equipment, with values calculated from Rietveld refinement with Brindley correction, for MBZA, MBZC and amorphous quantification (%) and respective e.s.d. (%), *gof* and Rwp (%) obtained.

Data code	%MBZ	%MBZA	e.s.d.	%MBZC	e.s.d.	Amor. (%)	e.s.d.	*gof*	Rwp (%)
d7_04875	50.16	2.89	0.05	44.12	0.005	11.85	0.17	2.331	6.05
d7_04876	50.16	2.70	0.09	44.69	0.41	10.51	1.13	2.430	6.30
d7_04894	50.16	2.88	0.04	43.53	0.41	13.94	1.30	2.674	7.00

Source: Created by the author.

B.1.1.1. Values calculated

Table B.4: Data set for Li_2CO_3/MBZ mixture, from Bruker D8 equipment, with values calculated from Rietveld refinement with Brindley correction, for MBZA, MBZC and amorphous quantification (%) and respective e.s.d. (%), *gof* and Rwp (%) obtained.

Data code	%MBZ	%MBZA	e.s.d.	%MBZC	e.s.d.	Amor. (%)	e.s.d.	*gof*	Rwp (%)
d7_04902	49.77	2.89	0.13	47.28	0.13	10.58	0.02	2.274	5.50
d7_04908	49.77	2.43	0.19	47.67	0.15	10.82	0.15	2.396	5.80
d7_04913	49.77	2.79	0.06	47.43	0.02	10.42	0.13	2.337	5.64

Source: Created by the author.

After consider Li_2CO_3 amorphous from Brindley correction

Table B.5: Data set for Li_2CO_3/MBZ mixture, from Bruker D8 equipment, with values calculated from Rietveld refinement with Li_2CO_3 amorphous from Brindley correction, for MBZA, MBZC and amorphous quantification (%) and respective e.s.d. (%) obtained.

Data code	%MBZ	%MBZA	e.s.d.	%MBZC	e.s.d.	Amor. (%)	e.s.d.
d7_04902	49.77	2.89	0.13	47.28	0.13	11.59	0.02
d7_04908	49.77	2.43	0.19	47.67	0.15	11.83	0.15
d7_04913	49.77	2.79	0.06	47.43	0.02	11.44	0.13

Source: Created by the author.

Average values calculated from Rietveld refinements of these data sets.

Table B.6: Average values for SRM-676a/MBZ, LiF/MBZ and Li_2CO_3/MBZ mixtures, from Bruker D8 equipment, with values calculated from Rietveld refinement, for MBZA, MBZC and amorphous quantification (%) and respective e.s.d. (%), *gof* and Rwp (%) obtained.

Int. stand.	%MBZ	%MBZA	e.s.d.	%MBZC	e.s.d.	Amor. (%)	e.s.d.	*gof*	Rwp (%)
SRM-676a	49.70	2.56	0.37	44.67	0.60	9.38	1.96	2.054	6.39
LiF	50.16	2.82	0.09	44.11	0.47	12.10	1.41	2.478	6.45
Li_2CO_3	49.77	2.70	0.20	47.46	0.16	10.61	0.16	2.336	5.65

Source: Created by the author.

After apply Brindley correction to Rietveld refinement strategy.

Table B.7: Average values for SRM-676a/MBZ and Li_2CO_3/MBZ mixtures, from Bruker D8 equipment, with values calculated from Rietveld refinement with Brindley correction, for MBZA, MBZC and amorphous quantification (%) and respective e.s.d. (%) obtained.

Int. stand.	%MBZ	%MBZA	e.s.d.	%MBZC	e.s.d.	Amor. (%)	e.s.d.
SRM-676a	49.70	2.55	0.36	44.48	0.60	10.15	1.95
Li_2CO_3	49.77	2.70	0.20	47.46	0.16	11.62	0.16

Source: Created by the author.

B.1.1.2. Graphical fits

Figure B.1: Graphical Rietveld refinement obtained on data 'd7_04801' for mixture SRM-676a/MBZ. Blue dots – observed data; red curve – calculated data; grey curve – residual curve.

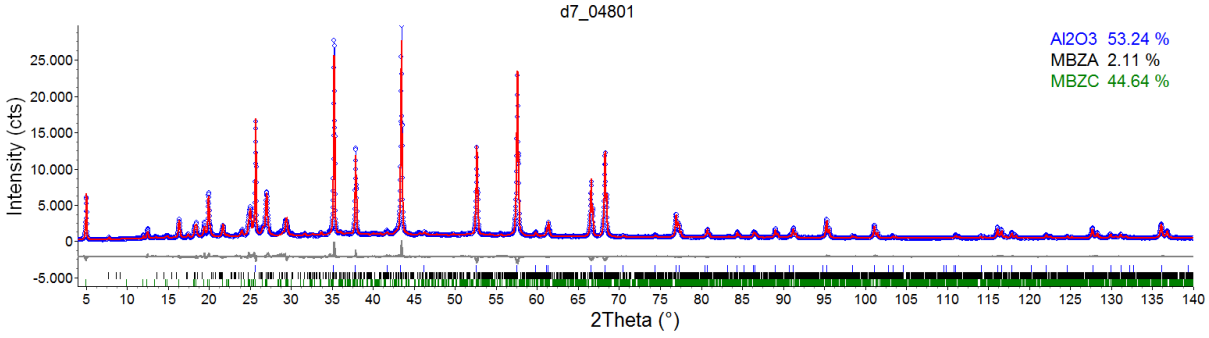

Source: Created by the author.

Figure B.2: Graphical Rietveld refinement obtained on data 'd7_04902' for mixture Li_2CO_3/MBZ. Blue dots – observed data; red curve – calculated data; grey curve – residual curve.

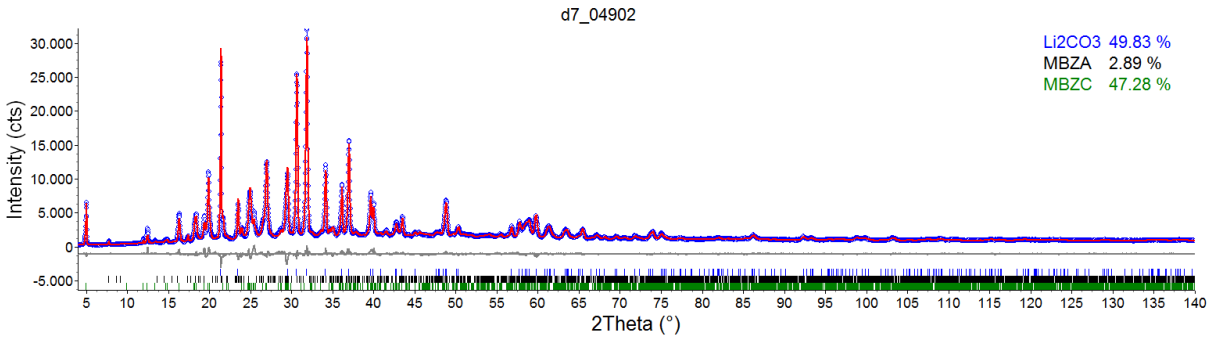

Source: Created by the author.

Figure B.3: Graphical Rietveld refinement obtained on data 'd7_04894' for mixture LiF/MBZ. Blue dots – observed data; red curve – calculated data; grey curve – residual curve.

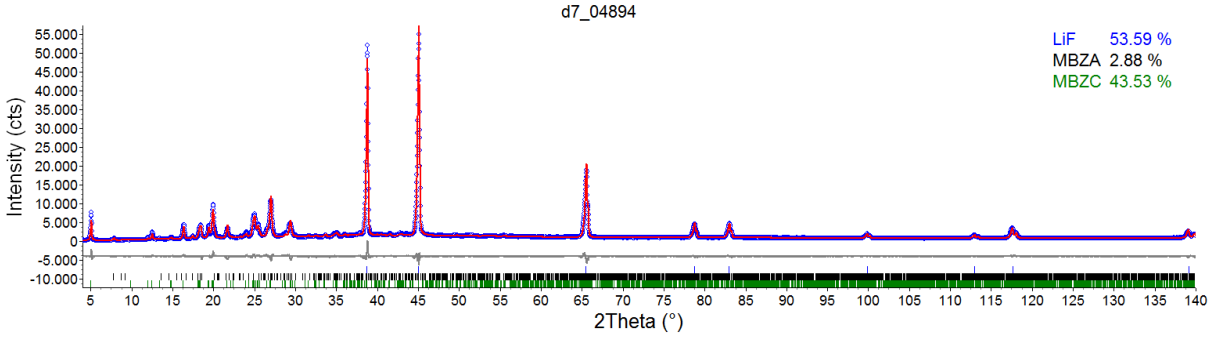

Source: Created by the author.

B.1.2. Huber equipment – Tucano furnace – LNLS

Table B.8: Data set for SRM-676a/MBZ, LiF/MBZ and Li_2CO_3/MBZ mixture, from LNLS (Tucano furnace), with values calculated from Rietveld refinement, for MBZA, MBZC and amorphous quantification (%) and respective e.s.d. (%), *gof* and Rwp (%) obtained.

Data code	%MBZ	%MBZA	e.s.d.	%MBZC	e.s.d.	Amor. (%)	e.s.d.	g.o.f.	Rwp (%)
50Al_2O_3_50MBZ	49.70	2.46	0.028	44.82	0.03	9.11	0.077	1.446	5.23
50LiF_50MBZ	50.16	2.58	0.11	44.39	0.14	12.00	0.07	1.354	7.39
50Li_2CO_3_50MBZ	49.77	2.42	0.33	47.86	0.37	10.22	0.112	1.620	6.79

Source: Created by the author.

After apply Brindley correction to Rietveld refinement strategy.

Table B.9: Data set for SRM-676a/MBZ and Li_2CO_3/MBZ mixture, from LNLS (Tucano furnace), with values calculated from Rietveld refinement with Brindley correction, for MBZA, MBZC and amorphous quantification (%) and respective e.s.d. (%) obtained.

Data code	%MBZ	%MBZA	e.s.d.	%MBZC	e.s.d.	Amor. (%)	e.s.d.
50Al_2O_3_50MBZ	49.70	2.45	0.028	44.62	0.03	10.03	0.01
50Li_2CO_3_50MBZ	49.77	2.42	0.33	47.86	0.36	11.28	0.07

Source: Created by the author.

B.1.3. Rigaku RINT2000 equipment

Table B.10: Data set for SRM-676a/MBZ, LiF/MBZ and Li_2CO_3/MBZ mixture, from Rigaku RINT2000 equipment, with values calculated from Rietveld refinement, for MBZA, MBZC and amorphous quantification (%) and respective e.s.d. (%), *gof* and Rwp (%) obtained.

Int. stand.	%MBZ	%MBZA	e.s.d.	%MBZC	e.s.d.	Amor. (%)	e.s.d.	g.o.f.	Rwp (%)
SRM-676a	49.70	2.35	0.11	45.04	0.19	8.84	0.267	2.994	15.68
LiF	50.16	2.64	0.07	44.26	0.04	12.23	0.09	2.721	16.98
Li_2CO_3	49.77	3.91	0.72	46.47	0.62	9.85	0.37	2.486	15.03

Source: Created by the author.

After apply Brindley correction to Rietveld refinement strategy.

Table B.11: Data set for SRM-676a/MBZ and Li_2CO_3/MBZ mixture, from Rigaku RINT2000 equipment, with values calculated from Rietveld refinement with Brindley correction, for MBZA, MBZC and amorphous quantification (%) and respective e.s.d. (%) obtained.

Int. stand.	%MBZ	%MBZA	e.s.d.	%MBZC	e.s.d.	Amor. (%)	e.s.d.
SRM-676a	49.70	2.34	0.11	44.85	0.19	9.58	0.304
Li_2CO_3	49.77	3.91	0.72	46.49	0.61	10.79	0.421

Source: Created by the author.

B.2. LiF/MBZ/$(C_8H_8)_n$ mixtures

B.2.1. Bruker D8 Equipment

B.2.1.1. Values calculated

1st Data set

Table B.12: 1st data set for SRM-676a/MBZ/$(C_8H_8)_n$ mixture, from Bruker D8 equipment, with values calculated from Rietveld refinement, for sample amorphous, MBZ amorphous quantification (%) and respective e.s.d. (%), *gof* and Rwp (%) obtained.

Data code	C_8H_8 (%)	Amor. (%)	Amor. MBZ	R_{wp} (%)	gof
d7_04875	0	6.899	13.753	8.19	3.154
d7_05197	5	10.243	11.652	9.41	4.413
d7_05198	10	14.995	12.489	7.97	3.731
d7_05202	15	19.359	12.454	7.66	3.600
d7_05205	20	24.045	13.483	7.19	3.361
d7_05212	25	28.324	13.295	6.82	3.230
d7_05213	30	32.815	14.073	5.45	2.585
d7_05219	35	36.879	12.526	4.62	2.187
d7_05220	40	41.298	12.978	4.37	2.099
d7_05221	45	45.605	12.102	4.19	1.99

Source: Created by the author.

2nd Data set

Table B.13: 2nd data set for SRM-676a/MBZ/$(C_8H_8)_n$ mixture, from Bruker D8 equipment, with values calculated from Rietveld refinement, for sample amorphous, MBZ amorphous quantification (%) and respective e.s.d. (%), *gof* and Rwp (%) obtained.

Data code	C_8H_8 (%)	Amor. (%)	Amor. MBZ	R_{wp} (%)	*gof*
d7_04876	0	6.667	13.291	7.98	3.075
d7_05199	5	10.483	12.184	9.01	4.203
d7_05200	10	14.948	12.371	7.67	3.59
d7_05210	15	19.702	13.435	6.55	3.07
d7_05211	20	24.212	14.041	7.38	3.469
d7_05217	25	28.333	13.332	6.17	2.895
d7_05218	30	32.456	12.278	5.55	2.639
d7_05222	35	36.968	13.118	4.67	2.219
d7_05223	40	41.204	12.039	4.12	1.909
d7_05227	45	45.663	13.266	3.82	1.815

Source: Created by the author.

3rd Data set

Table B.14: 3rd data set for SRM-676a/MBZ/$(C_8H_8)_n$ mixture, from Bruker D8 equipment, with values calculated from Rietveld refinement, for sample amorphous, MBZ amorphous quantification (%) and respective e.s.d. (%), *gof* and Rwp (%) obtained.

Data code	C_8H_8 (%)	Amor. (%)	Amor. MBZ	R_{wp} (%)	*gof*
d7_04894	0	5.861	11.686	8.08	3.085
d7_05204	5	10.966	13.257	9.36	4.382
d7_05206	10	13.236	13.236	7.58	3.524
d7_05214	15	19.809	13.740	6.56	3.055
d7_05216	20	24.095	13.650	7.19	3.383
d7_05224	25	28.261	13.043	5.73	2.722
d7_05225	30	32.523	12.614	5.24	2.478
d7_05226	35	37.033	13.551	4.57	2.175
d7_05301	40	41.338	13.377	4.13	1.909
d7_05302	45	45.711	14.23	3.73	1.719

Source: Created by the author.

Average values calculated from Rietveld refinements of these data sets.

Table B.15: Average values for SRM-676a/MBZ/$(C_8H_8)_n$ mixture, from Bruker D8 equipment, with values calculated from Rietveld refinement, for sample amorphous, MBZ amorphous quantification (%) and respective e.s.d. (%), *gof* and Rwp (%) obtained.

C_8H_8 (%)	Amor. (%)	e.s.d.	Amor. MBZ	R_{wp} (%)	gof
0	6.476	0.44	12.910	8.08	3.105
5	10.564	0.30	12.364	9.26	4.333
10	14.393	0.82	12.699	7.74	3.615
15	19.623	0.19	13.210	6.92	3.242
20	24.117	0.07	13.725	7.25	3.404
25	28.306	0.03	13.223	6.24	2.949
30	32.598	0.16	12.988	5.41	2.567
35	36.960	0.06	13.065	4.62	2.194
40	41.280	0.06	12.798	4.21	1.972
45	45.660	0.04	13.199	3.91	1.841

Source: Created by the author.

B.2.1.2. Graphical fits

Figure B.4: Graphical Rietveld refinement obtained on data 'd7_05197' for mixture LiF/MBZ/$(C_8H_8)_n$ (50/45/5). Blue dots – observed data; red curve – calculated data; grey curve – residual curve.

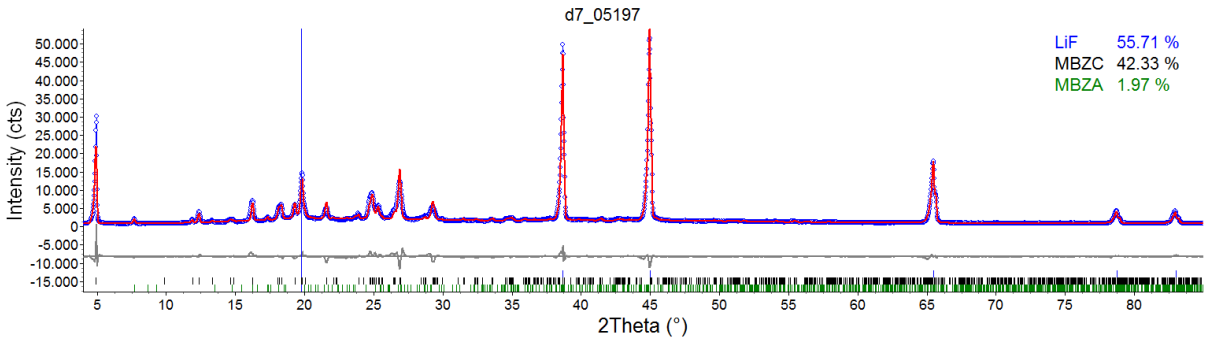

Source: Created by the author.

Figure B.5: Graphical Rietveld refinement obtained on data 'd7_05198' for mixture LiF/MBZ/$(C_8H_8)_n$ (50/40/10). Blue dots – observed data; red curve – calculated data; grey curve – residual curve.

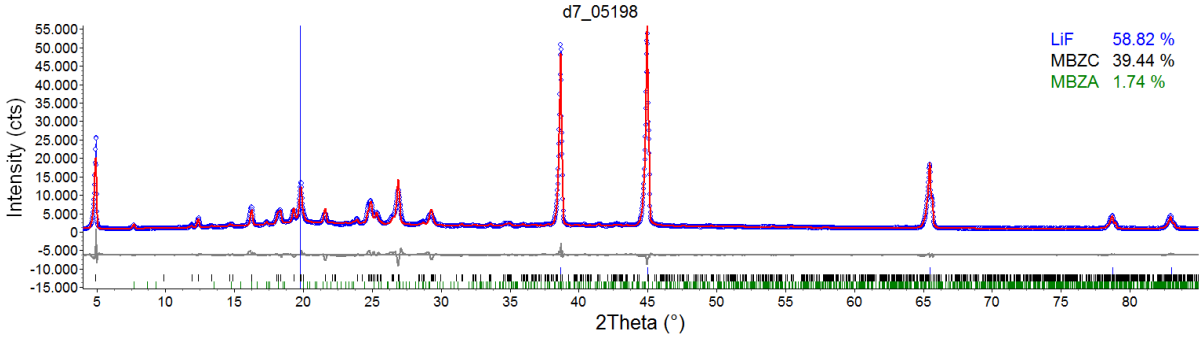

Source: Created by the author.

Figure B.6: Graphical Rietveld refinement obtained on data 'd7_05202' for mixture LiF/MBZ/$(C_8H_8)_n$ (50/35/15). Blue dots – observed data; red curve – calculated data; grey curve – residual curve.

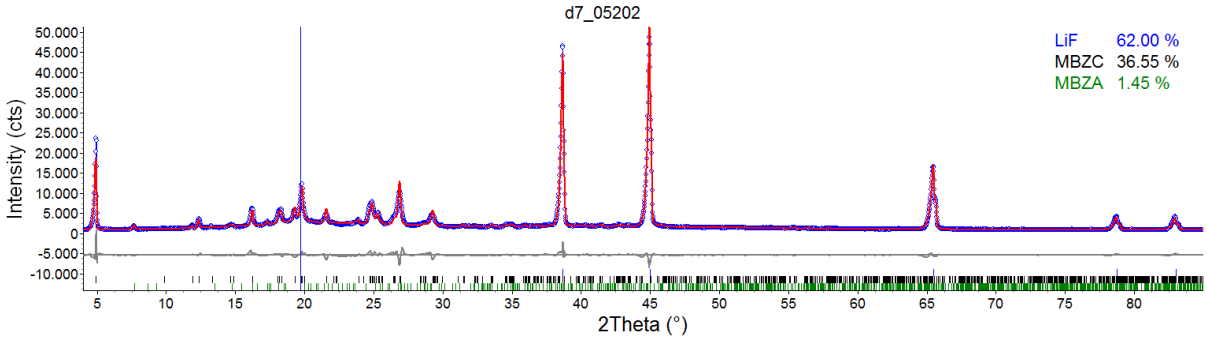

Source: Created by the author.

Figure B.7: Graphical Rietveld refinement obtained on data 'd7_05205' for mixture LiF/MBZ/$(C_8H_8)_n$ (50/30/20). Blue dots – observed data; red curve – calculated data; grey curve – residual curve.

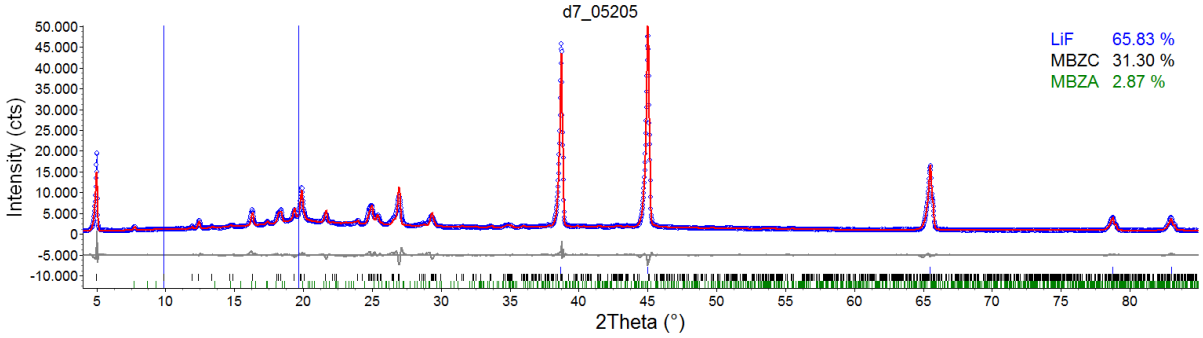

Source: Created by the author.

Figure B.8: Graphical Rietveld refinement obtained on data 'd7_05212' for mixture LiF/MBZ/$(C_8H_8)_n$ (50/25/25). Blue dots – observed data; red curve – calculated data; grey curve – residual curve.

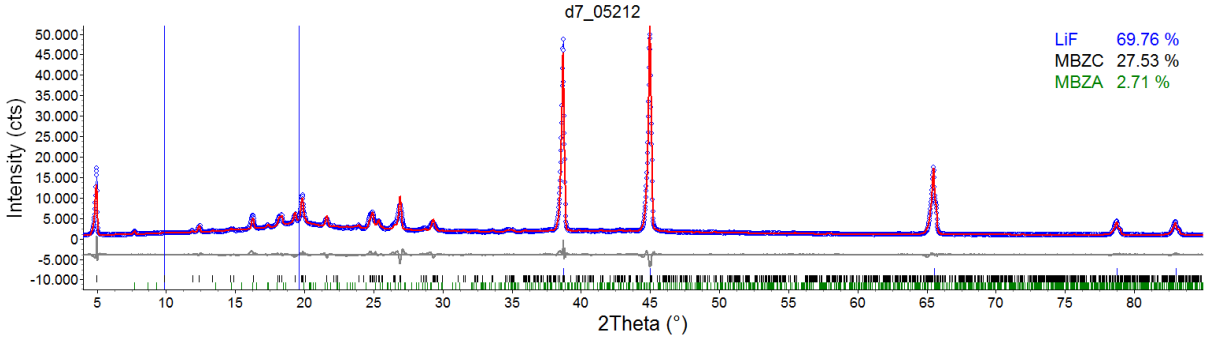

Source: Created by the author.

Figure B.9: Graphical Rietveld refinement obtained on data 'd7_05213' for mixture LiF/MBZ/$(C_8H_8)_n$ (50/20/30). Blue dots – observed data; red curve – calculated data; grey curve – residual curve.

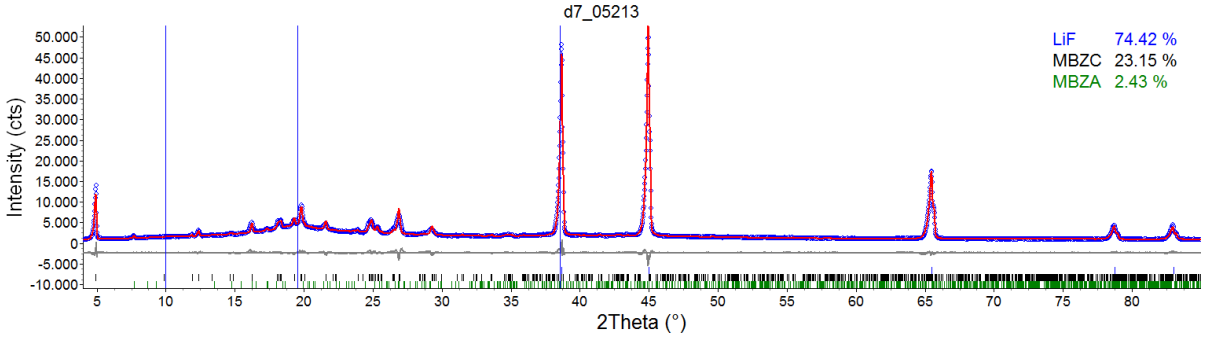

Source: Created by the author.

Figure B.10: Graphical Rietveld refinement obtained on data 'd7_05219' for mixture LiF/MBZ/$(C_8H_8)_n$ (50/15/35). Blue dots – observed data; red curve – calculated data; grey curve – residual curve.

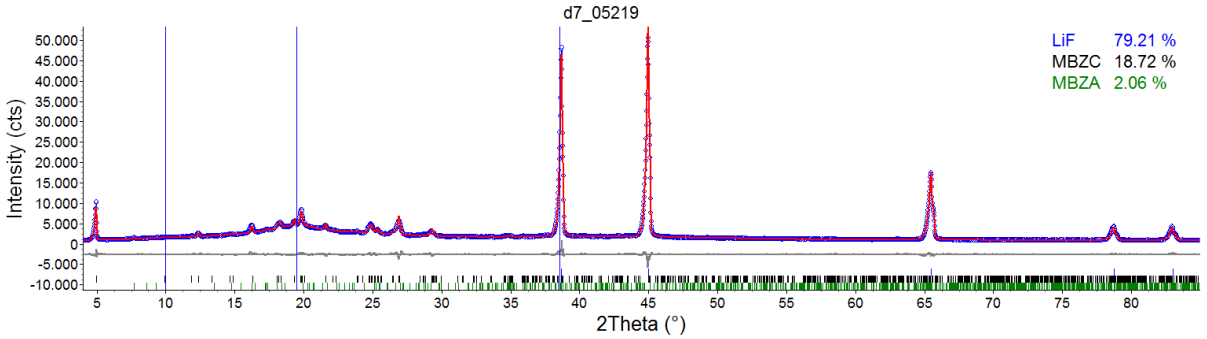

Source: Created by the author.

Figure B.11: Graphical Rietveld refinement obtained on data 'd7_05220' for mixture LiF/MBZ/$(C_8H_8)_n$ (50/10/40). Blue dots – observed data; red curve – calculated data; grey curve – residual curve.

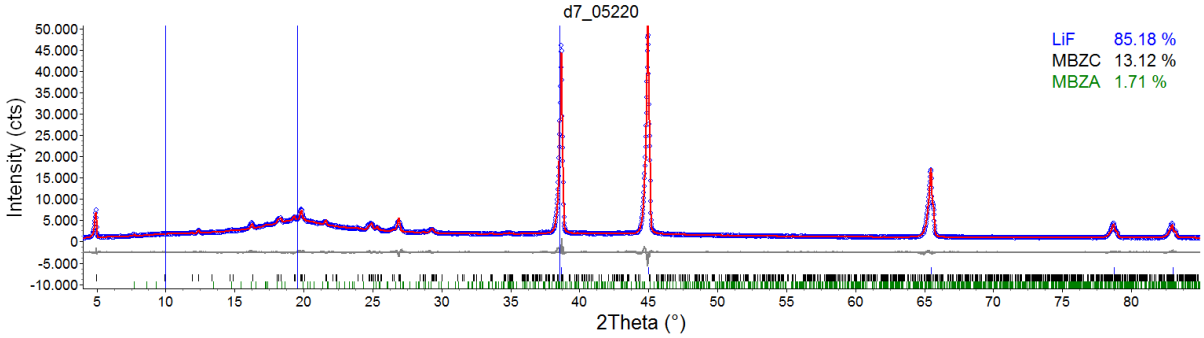

Source: Created by the author.

Figure B.12: Graphical Rietveld refinement obtained on data 'd7_05221' for mixture LiF/MBZ/$(C_8H_8)_n$ (50/5/45). Blue dots – observed data; red curve – calculated data; grey curve – residual curve.

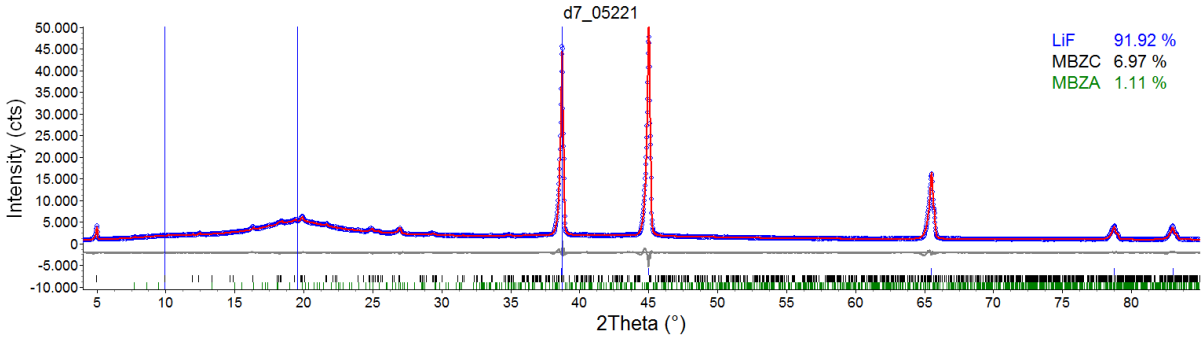

Source: Created by the author.

Appendix C

SRM-676a parameters behaviour and graphical fits in function of Temperature

The temperature calibration of the furnace was checked by heating SRM-676a from 30 °C to 250 °C, at a heating rate of 5 °C min^{-1} with 14 diffraction patterns were collected over 23-70° 2θ.

The Rietveld analysis achieved Rwp = 4.22% with g.o.f. = 1.132, refining 14 terms in Chubychev background polynomial, cell parameters, zero error, scale factor, peak shape parameters and two atomic displacement parameters.

Sequential Rietveld refinement and the Parametric Rietveld refinement (Stinton & Evans, 2007) were applied to this set data.

Therefore, the actual temperature of SRM-676a was determined from Parametric Rietveld refinement with polynomial coefficients to describe thermal expansion of Al_2O_3 lattice parameters reported by Taylor (Taylor, 1984), a_0 = 4.7568 Å, a_1 = 6.55×10^{-6} Å·°C^{-1}, a_2 =1.82×10^{-9} Å·°C^{-2}, c_0 = 12.9886 Å , c_1 = 6.54×10^{-6}Å·°C^{-1} and c_2 = 2.60×10^{-9} Å·°C^{-2}; and a calibration polynomial, to correct true sample temperature.

C.1. SRM-676a pure

C.1.1. Huber equipment – Tucano furnace – LNLS

C.1.1.1. Values calculated

Figure C.1: a) Comparison between lattice parameter 'a' behaviour determined by sequential Rietveld refinement and surface Rietveld refinement with Taylor equation for each temperature; b) Comparison between lattice parameter 'c' behaviour determined by sequential Rietveld refinement and surface Rietveld refinement with Taylor equation for each temperature.

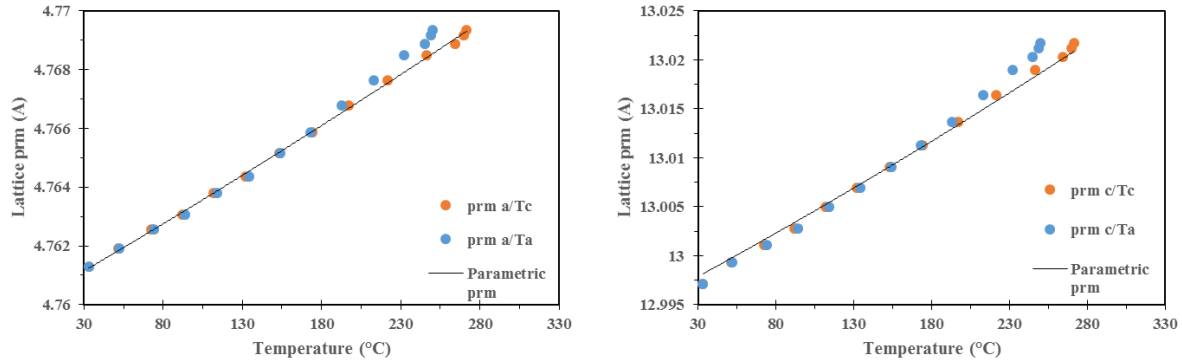

Source: Created by the author.

Figure C.2: a) Comparison between cell volume behaviour determined by sequential Rietveld refinement and surface Rietveld refinement with Taylor equation for each temperature; b) Comparison between Rwp (%) behaviour obtained by sequential Rietveld refinement and surface Rietveld refinement with Taylor equation.

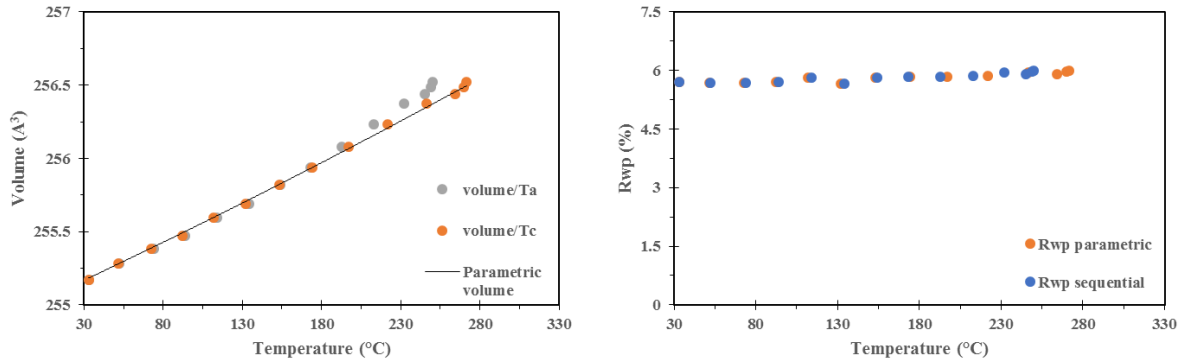

Source: Created by the author.

Figure C.3: Comparison between *gof* behaviour obtained by sequential Rietveld refinement and surface Rietveld refinement with Taylor equation.

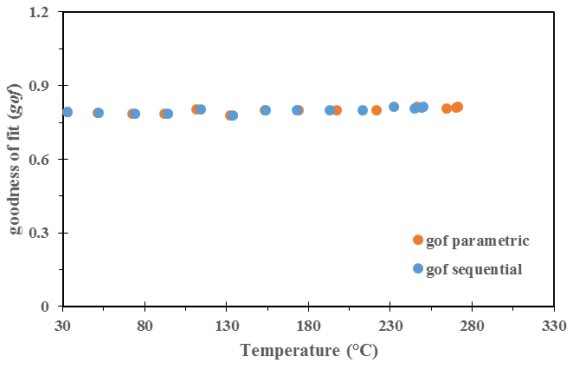

Source: Created by the author.

C.1.1.2. Graphical fits

Figure C.4: All graphical Rietveld refinements obtained on SRM-676a heating from 33 °C up to 25°C. Black curve– all observed data; red curve – all calculated data; grey curve – all residual curves.

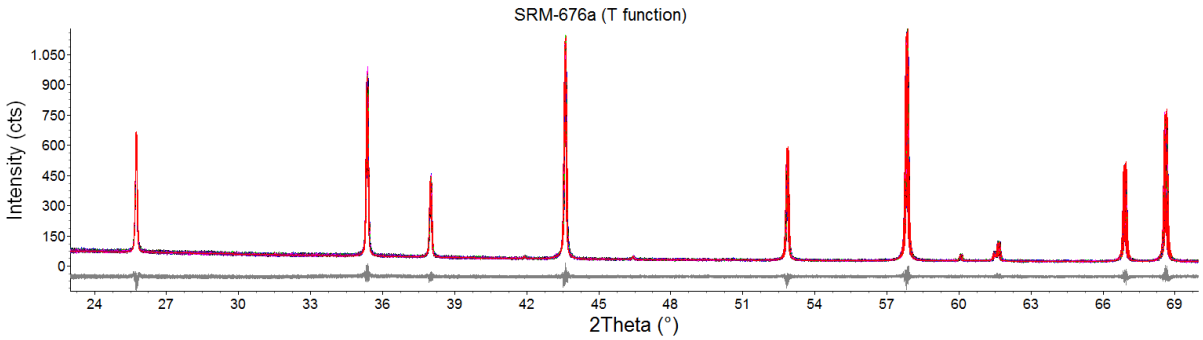

Source: Created by the author.

Figure C.5: Graphical Rietveld refinements obtained on SRM-676a at 33 °C. Blue curve – observed data; red curve – calculated data; grey curve – residual curves.

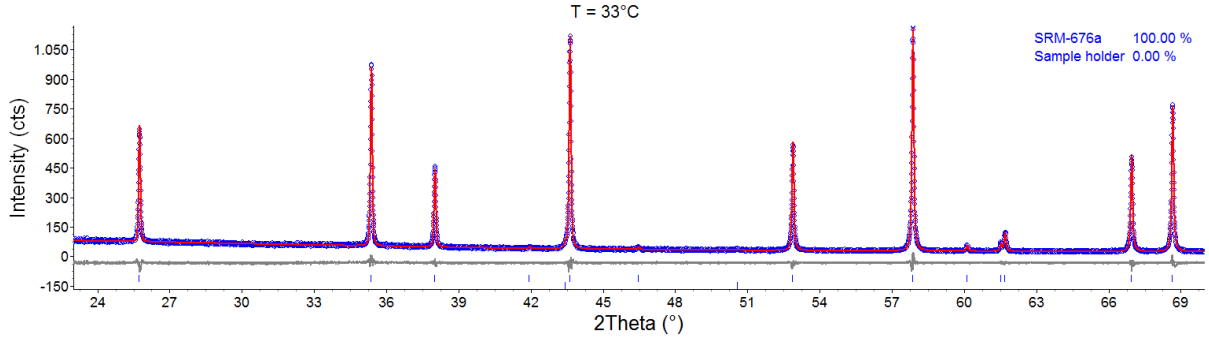

Source: Created by the author.

Figure C.6: Graphical Rietveld refinements obtained on SRM-676a at 114 °C. Blue curve – observed data; red curve – calculated data; grey curve – residual curves.

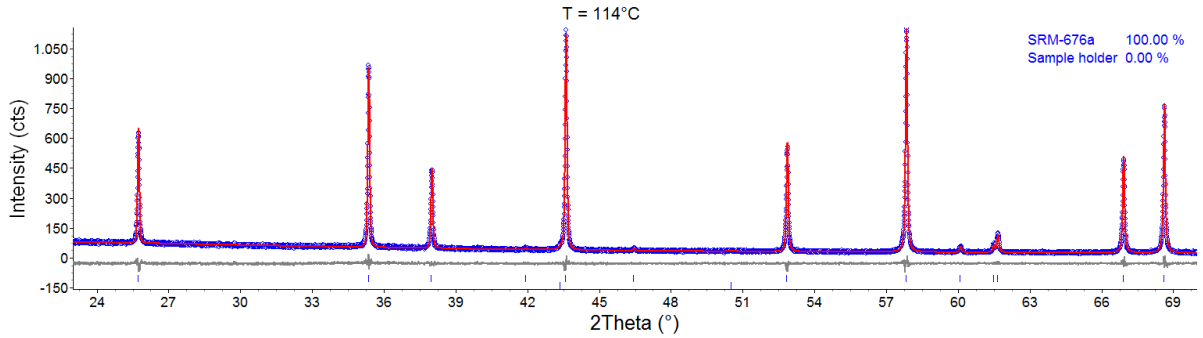

Source: Created by the author.

Figure C.7: Graphical Rietveld refinements obtained on SRM-676a at 173 °C. Blue curve – observed data; red curve – calculated data; grey curve – residual curves.

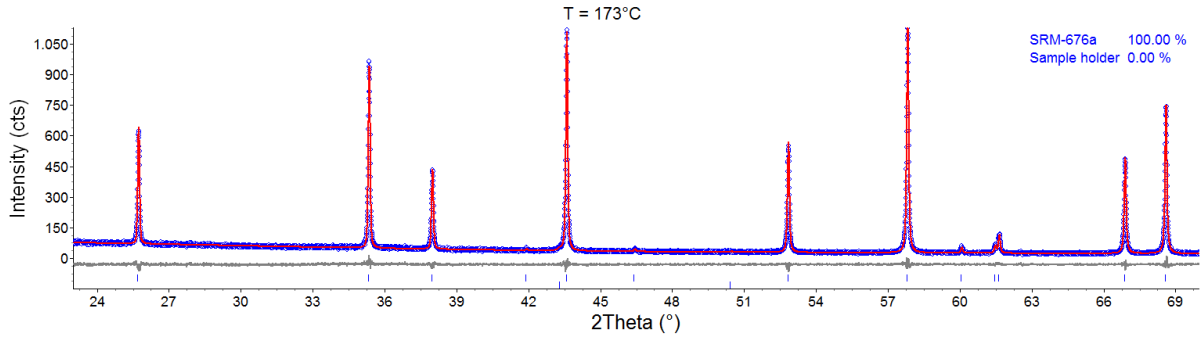

Source: Created by the author.

Figure C.8: Graphical Rietveld refinements obtained on SRM-676a at 232 °C. Blue curve – observed data; red curve – calculated data; grey curve – residual curves.

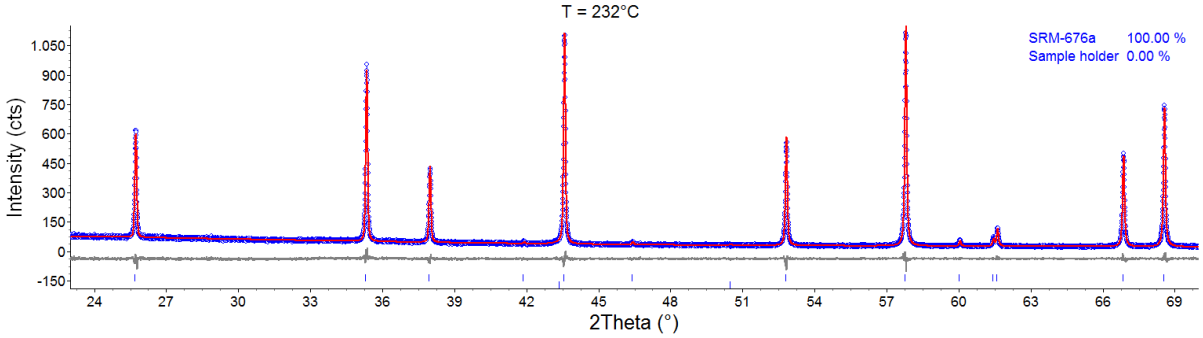

Source: Created by the author.

Figure C.9: Graphical Rietveld refinements obtained on SRM-676a at 250 °C. Blue curve – observed data; red curve – calculated data; grey curve – residual curves.

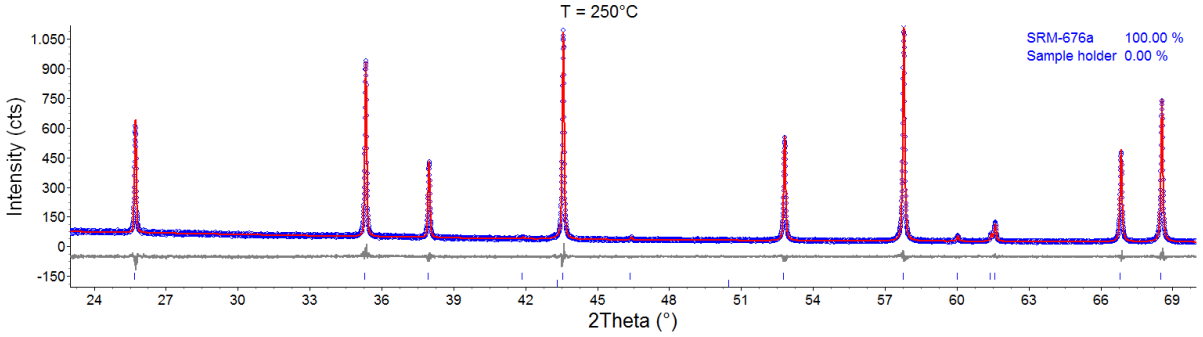

Source: Created by the author.

Appendix D

Norfloxacin parameters behaviour and graphical fits in function of Relative Humidity

Mixtures 50/50 were carefully prepared for NF API and tablet materials with LiF and a sample with same ratio made for SRM-676a/NF API.

All samples were submitted to a maximum relative humidity (~90-95%) until the hydrate form appears and then the RH is take down to a minimum and so on, to analyse the structure behaviour of sesquihydrate form of NF. For this strategy, it is used TUCANO chamber setup and detector MYTHEN 1K on diffractometer Huber.

Parametric Rietveld refinement (Stinton & Evans, 2007), performed in TOPAS-Academic software (Coelho, 2012), use crystal structures of inorganic materials, obtained from the ICSD (ICSD, 2009) with numbers 31548 (Al_2O_3) and 53839 (LiF). The crystal structure of sesquihydrate form of NF obtained from Ravindra and co-workers paper (2009).

In all refinements (sequential and surface) were calculated independently for each scan, linear absorption correction for adjusting the peak shape due to sample transparency, 14 terms in Chebychev background polynomial, specimen displacement, scale factor for each phase as well as peak shapes and atomic displacement parameter, the preferred orientation in NF were corrected by March Dollase model and the lattice parameters for internal standards.

The parameters refined to calculate the best cell parameter configuration are the coefficients of theses polynomials and the correction (ΔRH) for RH applied; that correction is calculated freely for each scan (the RH's behaviour in TUCANO is still not estimated during the gas flux variation), where $0 \leq RH + \Delta RH \leq 1$.

D.1. SRM-676a/NF sample

D.1.1. Huber equipment – Tucano furnace – LNLS

D.1.1.1. Values calculated

Figure D.1: a) Comparison between NF sesquihydrate lattice parameter 'a', in sample SRM-676a/NF, calculated by sequential Rietveld refinement (in function of RH_A and RH_C) and surface Rietveld refinement; b) Comparison between NF sesquihydrate lattice parameter 'b', in sample SRM-676a/NF, calculated by sequential Rietveld refinement (in function of RH_A and RH_C) and surface Rietveld refinement.

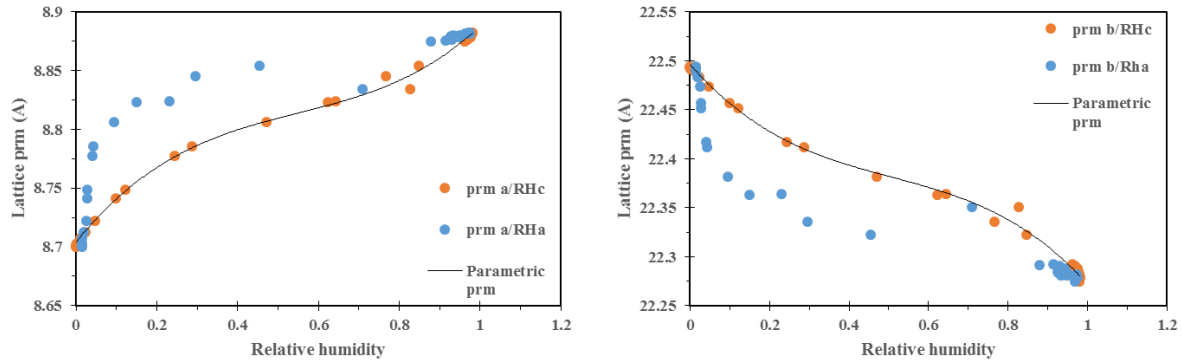

Source: Created by the author

Figure D.2: a) Comparison between NF sesquihydrate lattice parameter 'c', in sample SRM-676a/NF, calculated by sequential Rietveld refinement (in function of RH_A and RH_C) and surface Rietveld refinement; b) Comparison between NF sesquihydrate lattice parameter 'beta', in sample SRM-676a/NF, calculated by sequential Rietveld refinement (in function of RH_A and RH_C) and surface Rietveld refinement.

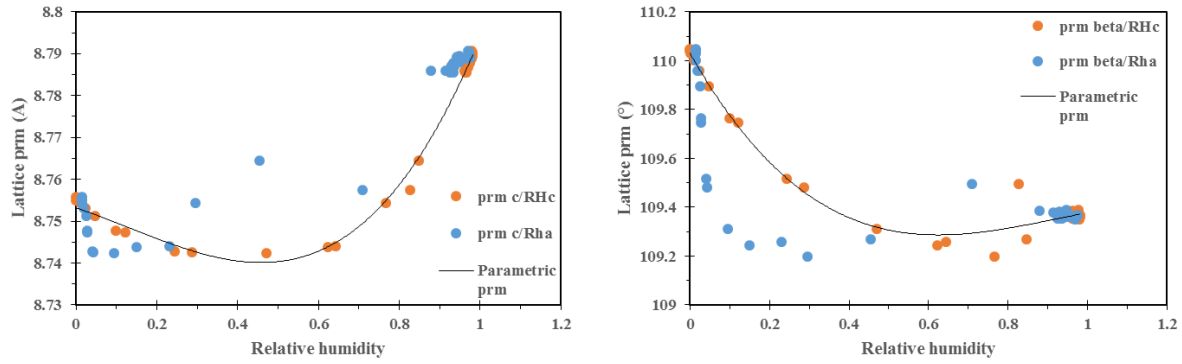

Source: Created by the author

Figure D.3: a) Comparison between NF sesquihydrate volume, in sample SRM-676a/NF, calculated by sequential Rietveld refinement (in function of RH_A and RH_C) and surface Rietveld refinement; b) Comparison between NF sesquihydrate phase, in sample SRM-676a/NF, calculated by sequential Rietveld refinement and surface Rietveld refinement.

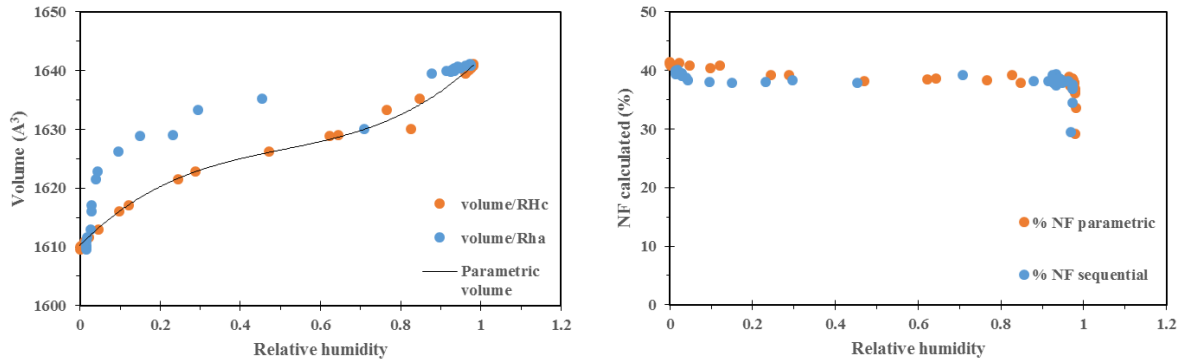

Source: Created by the author

Figure D.4: a) Comparison between Rwp (%) obtained, for SRM-676a/NF sample, by sequential Rietveld refinement and surface Rietveld refinement; b) Comparison between *gof* obtained, for SRM-676a/NF sample, by sequential Rietveld refinement and surface Rietveld refinement.

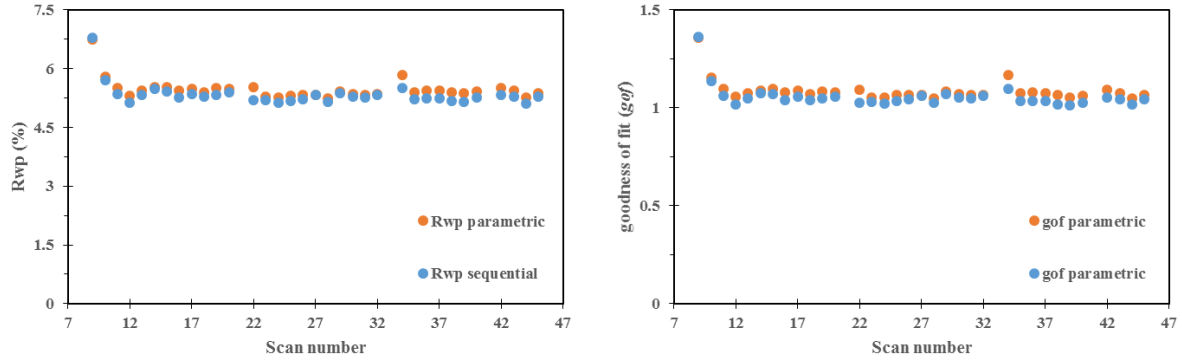

Source: Created by the author.

D.1.1.2. Graphical fits

Figure D.5: All graphical Rietveld refinements obtained for SRM-676a/NF during RH variation. Black curve– all observed data; red curve – all calculated data; grey curve – all residual curves.

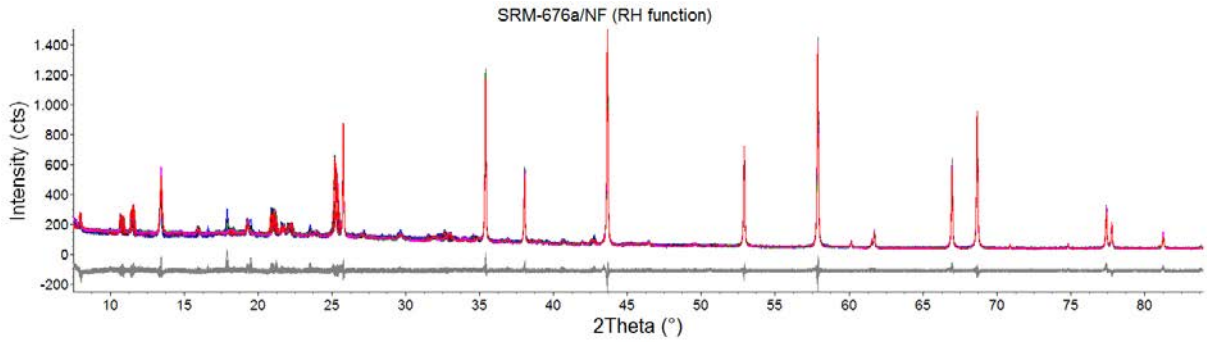

Source: Created by the author.

Figure D.6: Graphical Rietveld refinements obtained for SRM-676a/NF at RH = 97%. Blue curve – observed data; red curve – calculated data; grey curve – residual curve.

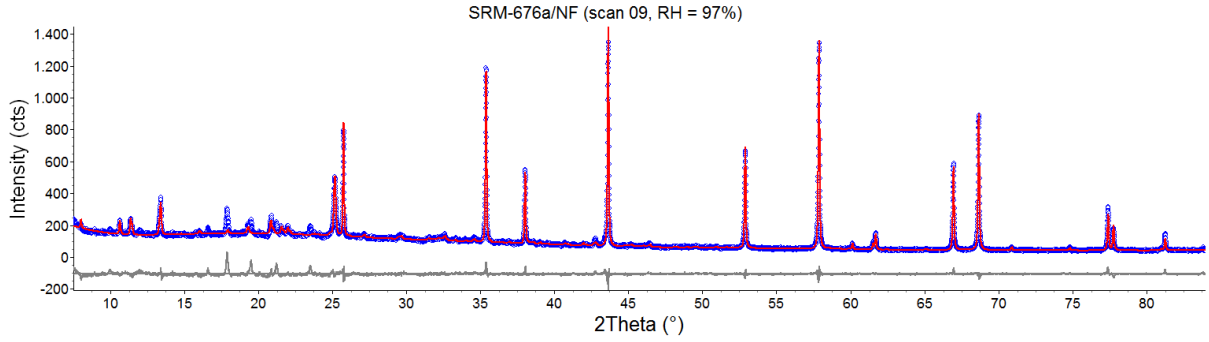

Source: Created by the author.

Figure D.7: Graphical Rietveld refinements obtained for SRM-676a/NF at RH = 95%. Blue curve – observed data; red curve – calculated data; grey curve – residual curve.

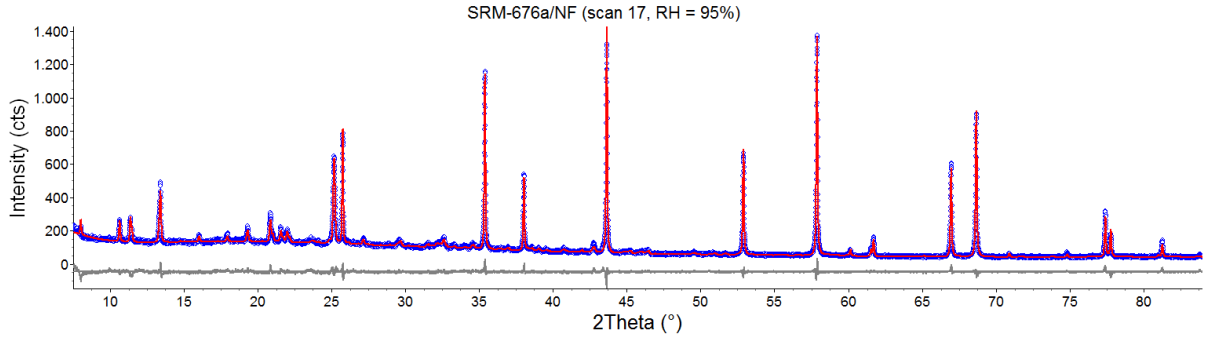

Source: Created by the author.

Figure D.8: Graphical Rietveld refinements obtained for SRM-676a/NF at RH = 3%. Blue curve – observed data; red curve – calculated data; grey curve – residual curves.

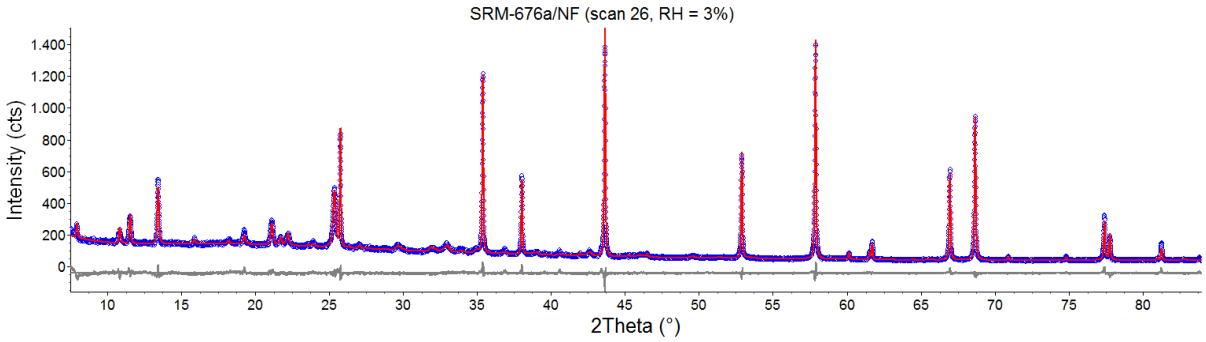

Source: Created by the author.

Figure D.9: Graphical Rietveld refinements obtained for SRM-676a/NF at RH = 91%. Blue curve – observed data; red curve – calculated data; grey curve – residual curves.

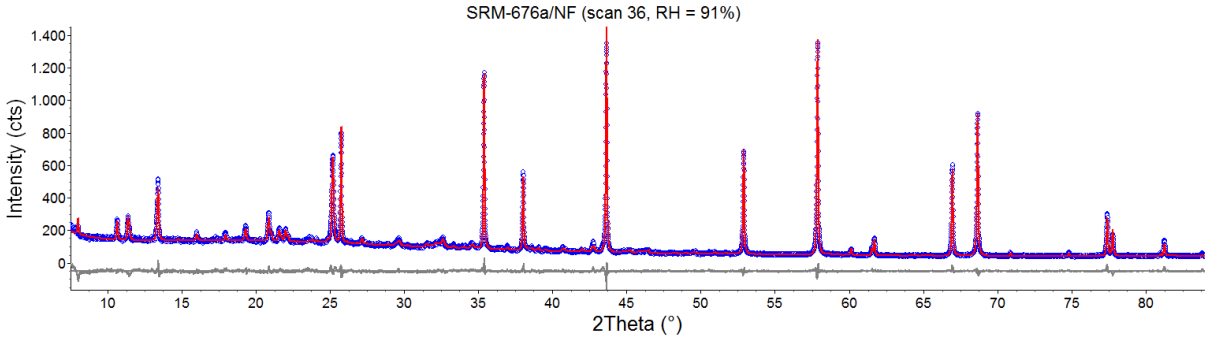

Source: Created by the author.

Figure D.10: Graphical Rietveld refinements obtained for SRM-676a/NF at RH = 3%. Blue curve – observed data; red curve – calculated data; grey curve – residual curves.

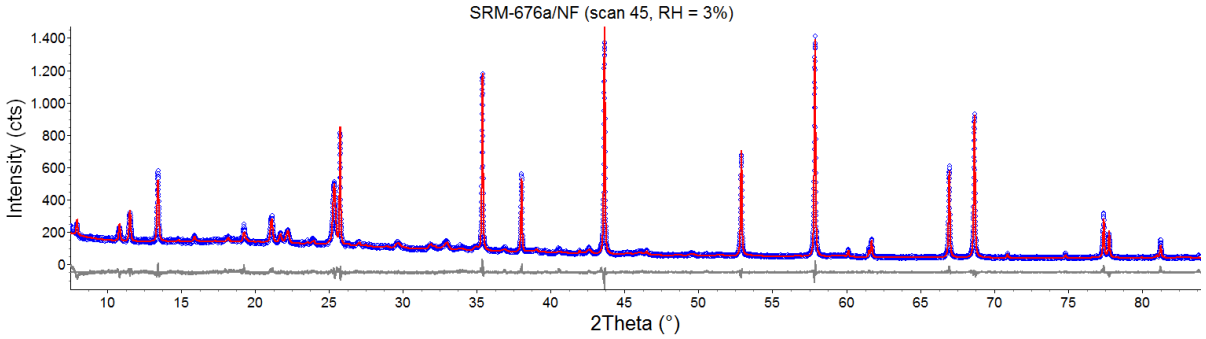

Source: Created by the author.

D.2. LiF/NF sample

D.2.1. Huber equipment – Tucano furnace – LNLS

D.2.1.1. Values calculated for 1st data set

Figure D.11: a) Comparison between NF sesquihydrate lattice parameter 'a', in sample LiF/NF, calculated by sequential Rietveld refinement (in function of RH_A and RH_C) and surface Rietveld refinement; b) Comparison between NF sesquihydrate lattice parameter 'b', in sample LiF/NF, calculated by sequential Rietveld refinement (in function of RH_A and RH_C) and surface Rietveld refinement.

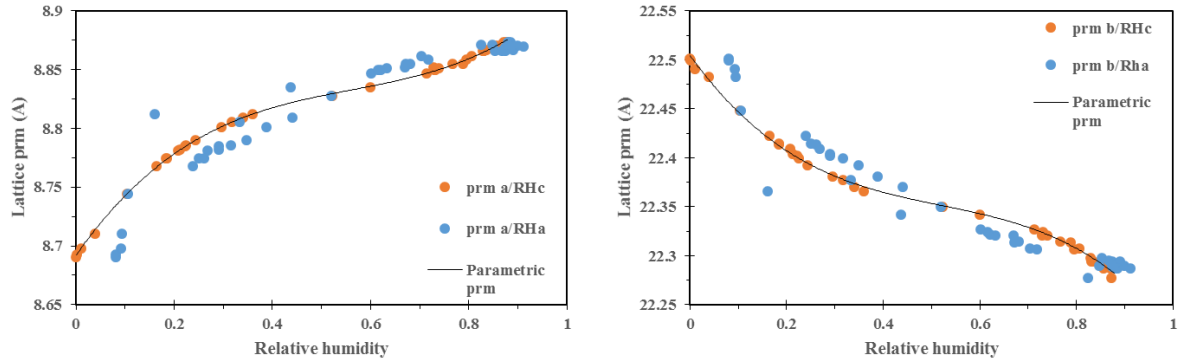

Source: Created by the author.

Figure D.12: a) Comparison between NF sesquihydrate lattice parameter 'c', in sample LiF/NF, calculated by sequential Rietveld refinement (in function of RH_A and RH_C) and surface Rietveld refinement; b) Comparison between NF sesquihydrate lattice parameter 'beta', in sample LiF/NF, calculated by sequential Rietveld refinement (in function of RH_A and RH_C) and surface Rietveld refinement.

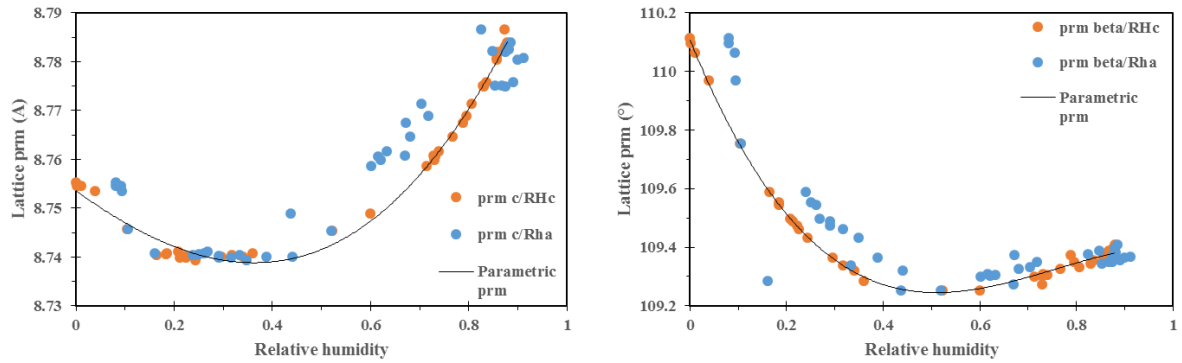

Source: Created by the author.

Figure D.13: a) Comparison between NF sesquihydrate volume, in sample LiF/NF, calculated by sequential Rietveld refinement (in function of RH_A and RH_C) and surface Rietveld refinement; b) Comparison between NF sesquihydrate phase, in sample LiF/NF, calculated by sequential Rietveld refinement and surface Rietveld refinement.

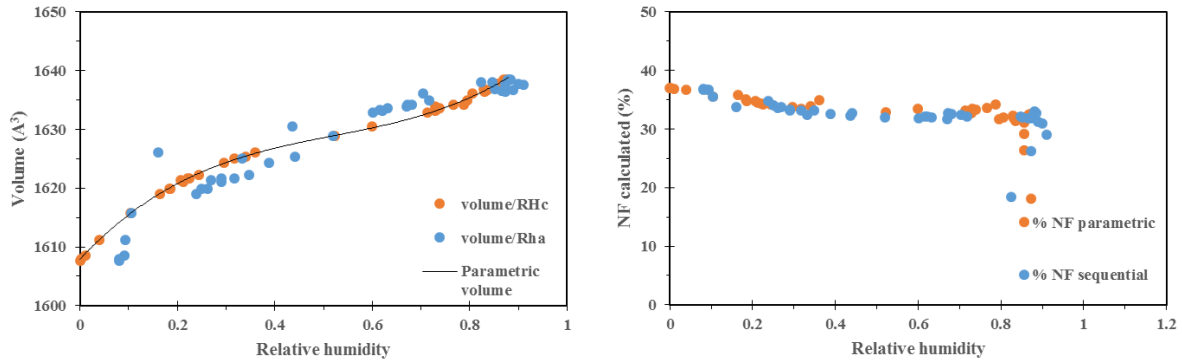

Source: Created by the author.

Figure D.14: a) Comparison between Rwp (%) obtained, for LiF/NF sample, by sequential Rietveld refinement and surface Rietveld refinement; b) Comparison between *gof* obtained, for LiF/NF sample, by sequential Rietveld refinement and surface Rietveld refinement.

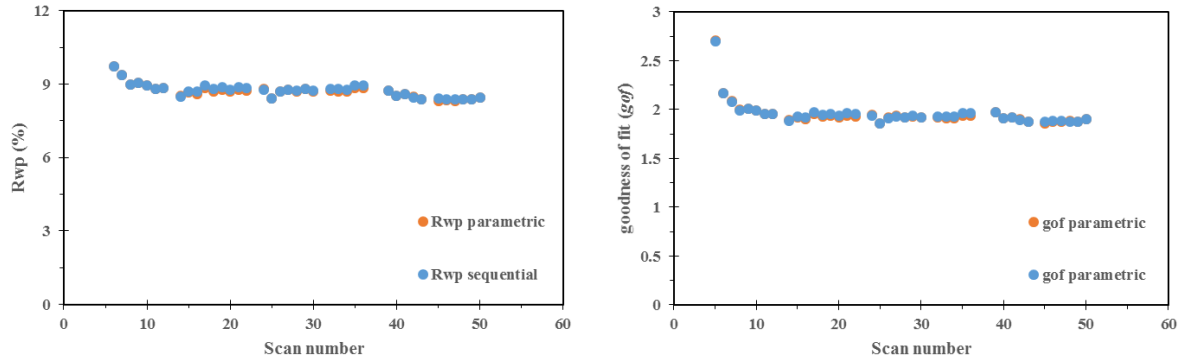

Source: Created by the author

D.2.1.2. Graphical fits for 1st data set

Figure D.15: All graphical Rietveld refinements obtained for LiF/NF during RH variation. Black curve– all observed data; red curve – all calculated data; grey curve – all residual curves.

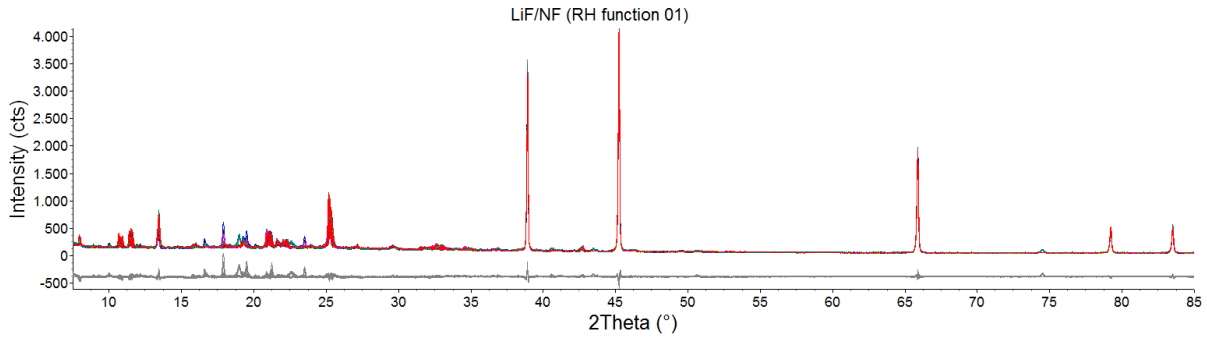

Source: Created by the author.

Figure D.16: Graphical Rietveld refinements obtained for LiF/NF at RH = 82%. Blue curve – observed data; red curve – calculated data; grey curve – residual curves.

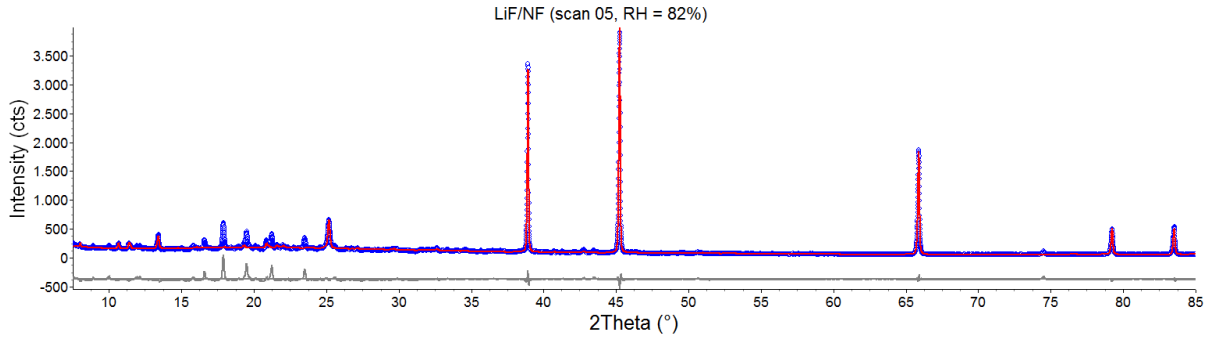

Source: Created by the author.

Figure D.17: Graphical Rietveld refinements obtained for LiF/NF at RH = 52%. Blue curve – observed data; red curve – calculated data; grey curve – residual curves.

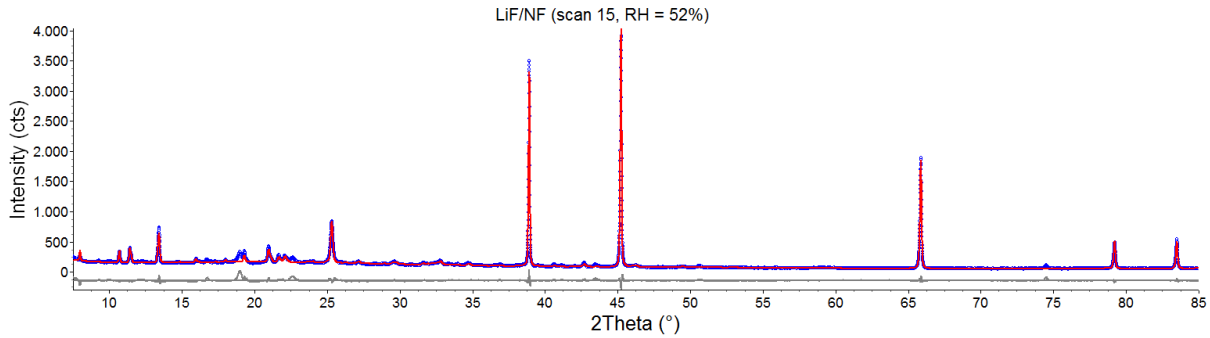

Source: Created by the author.

Figure D.18: Graphical Rietveld refinements obtained for LiF/NF at RH = 68%. Blue curve – observed data; red curve – calculated data; grey curve – residual curves.

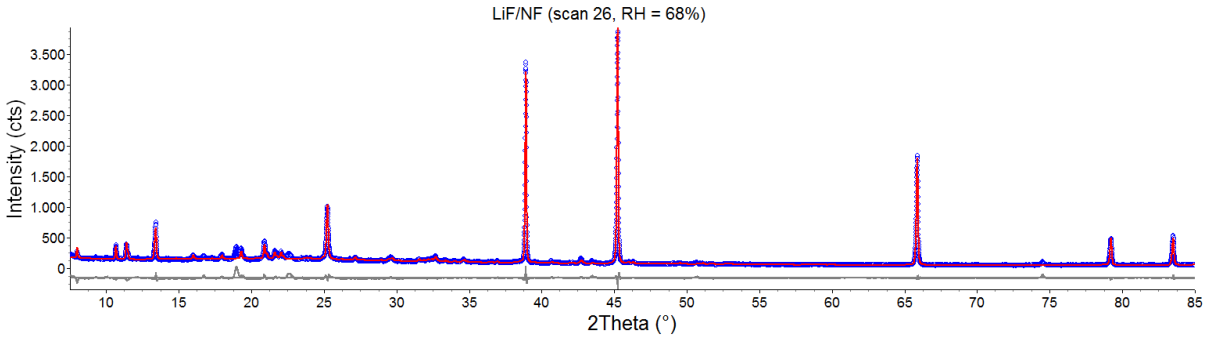

Source: Created by the author.

Figure D.19: Graphical Rietveld refinements obtained for LiF/NF at RH = 72%. Blue curve – observed data; red curve – calculated data; grey curve – residual curves.

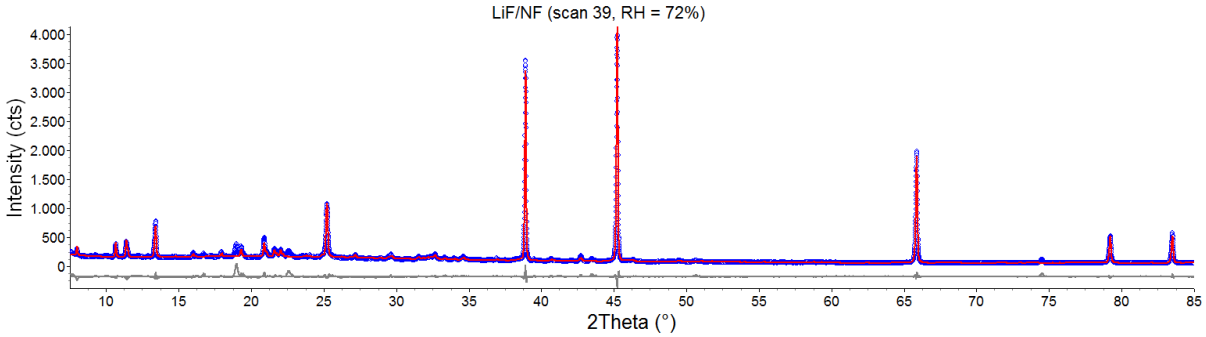

Source: Created by the author.

Figure D.20: Graphical Rietveld refinements obtained for LiF/NF at RH = 8%. Blue curve – observed data; red curve – calculated data; grey curve – residual curves.

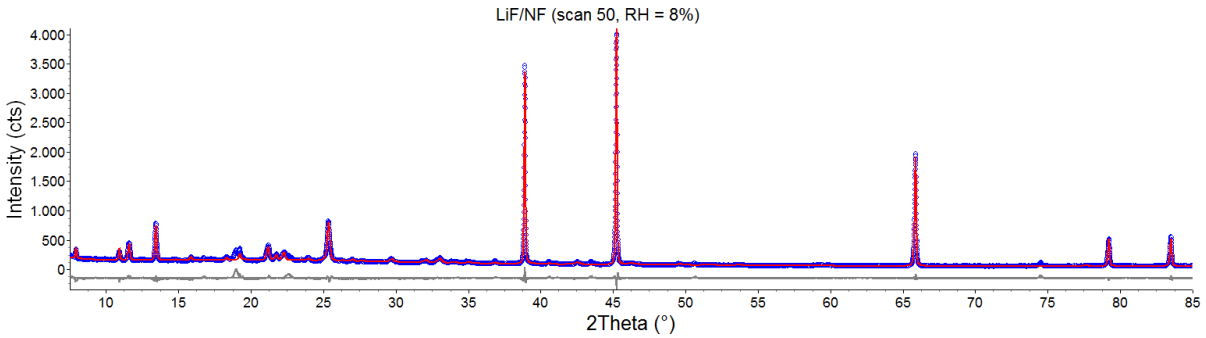

Source: Created by the author.

D.2.1.3. Values calculated for 2nd data set

Figure D.21: a) Comparison between NF sesquihydrate lattice parameter 'a', in sample LiF/NF, calculated by sequential Rietveld refinement (in function of RH_A and RH_C) and surface Rietveld refinement; b) Comparison between NF sesquihydrate lattice parameter 'b', in sample LiF/NF, calculated by sequential Rietveld refinement (in function of RH_A and RH_C) and surface Rietveld refinement.

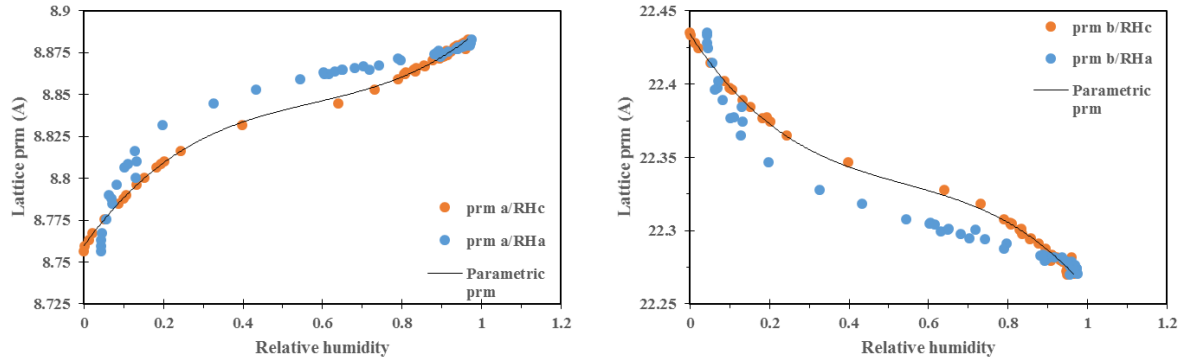

Source: Created by the author.

Figure D.22: a) Comparison between NF sesquihydrate lattice parameter 'c', in sample LiF/NF, calculated by sequential Rietveld refinement (in function of RH_A and RH_C) and surface Rietveld refinement; b) Comparison between NF sesquihydrate lattice parameter 'beta', in sample LiF/NF, calculated by sequential Rietveld refinement (in function of RH_A and RH_C) and surface Rietveld refinement.

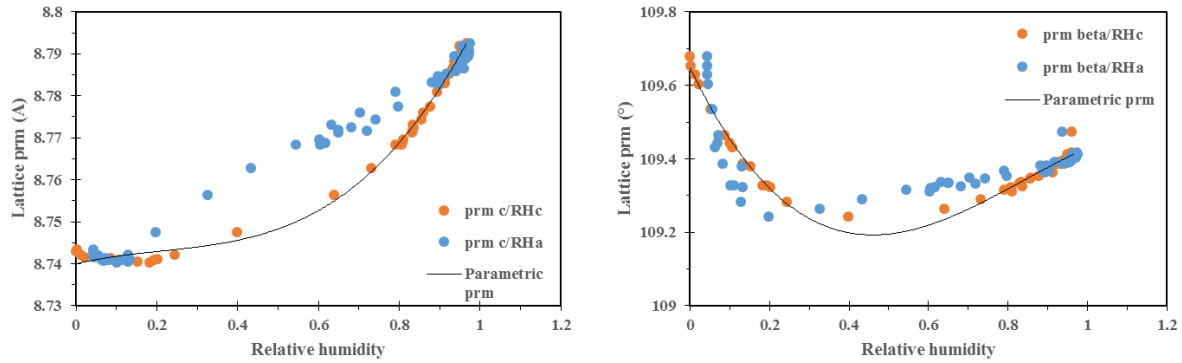

Source: Created by the author.

D.2.1.3. Values calculated for 2nd data set

Figure D.23: a) Comparison between NF sesquihydrate volume, in sample LiF/NF, calculated by sequential Rietveld refinement (in function of RH_A and RH_C) and surface Rietveld refinement; b) Comparison between NF sesquihydrate phase, in sample LiF/NF, calculated by sequential Rietveld refinement and surface Rietveld refinement.

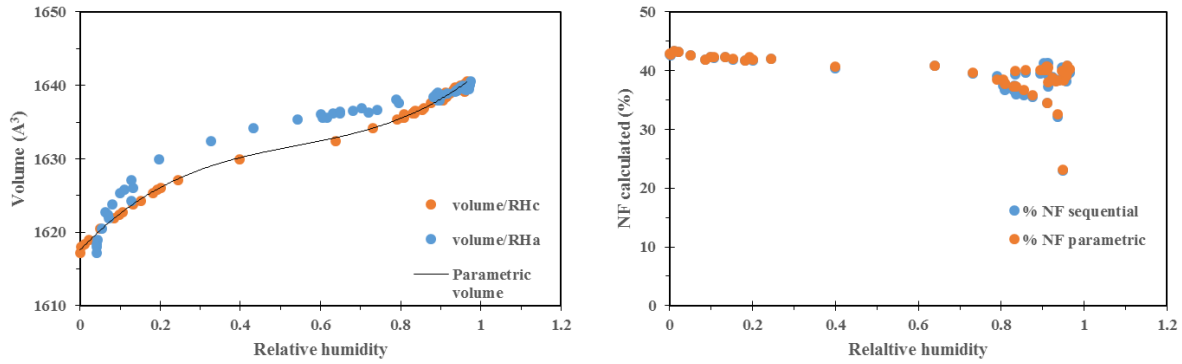

Source: Created by the author.

Figure D.24: a) Comparison between Rwp (%) obtained, for LiF/NF sample, by sequential Rietveld refinement and surface Rietveld refinement; b) Comparison between *gof* obtained, for LiF/NF sample, by sequential Rietveld refinement and surface Rietveld refinement.

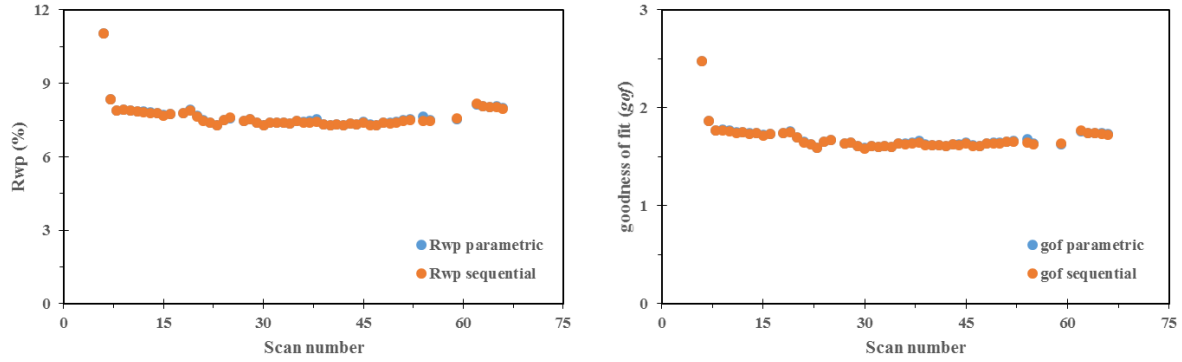

Source: Created by the author.

D.2.1.4. Graphical fits for 2nd data set

Figure D.25: All graphical Rietveld refinements obtained for LiF/NF during RH variation. Black curve– all observed data; red curve – all calculated data; grey curve – all residual curves.

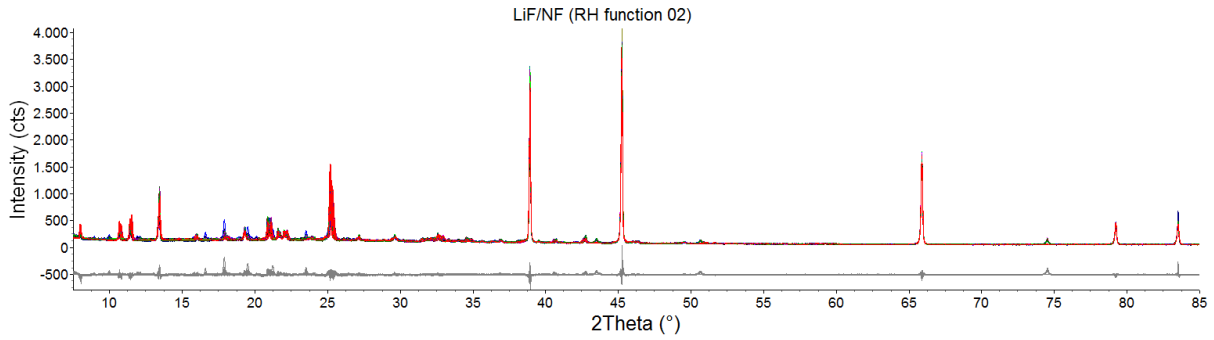

Source: Created by the author.

Figure D.26: Graphical Rietveld refinements obtained for LiF/NF at RH = 96%. Blue curve – observed data; red curve – calculated data; grey curve – residual curves.

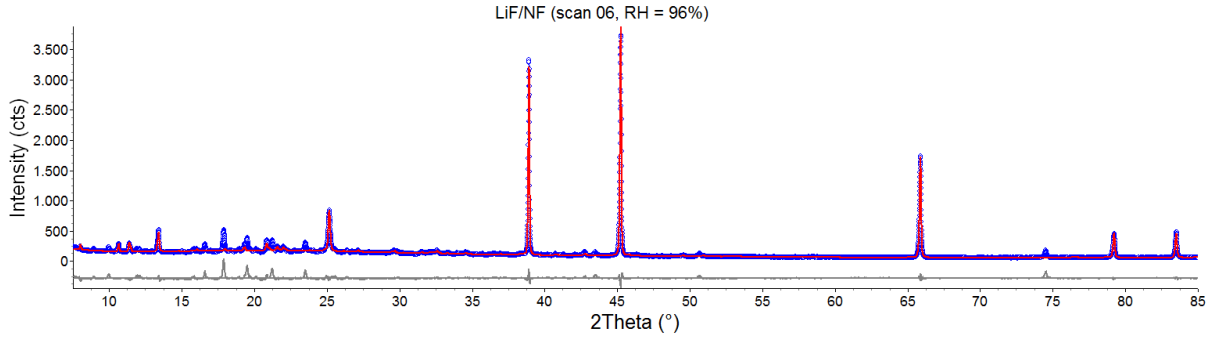

Source: Created by the author.

Figure D.27: Graphical Rietveld refinements obtained for LiF/NF at RH = 94%. Blue curve – observed data; red curve – calculated data; grey curve – residual curves.

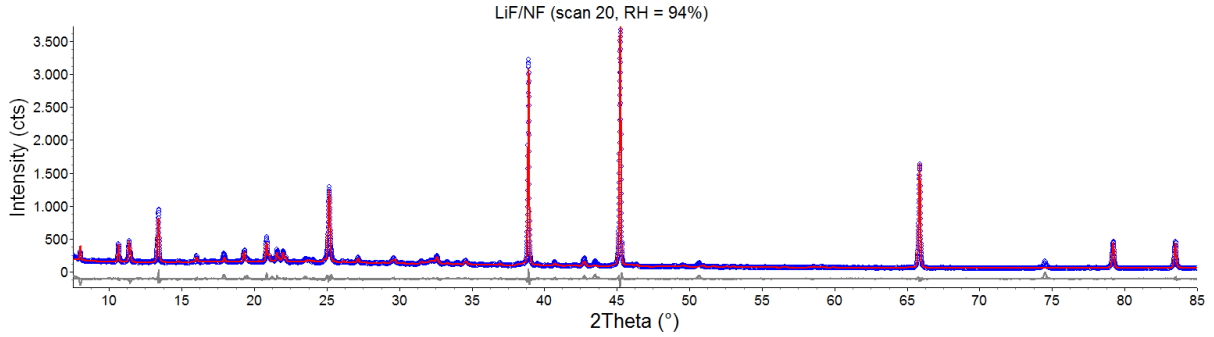

Source: Created by the author.

Figure D.28: Graphical Rietveld refinements obtained for LiF/NF at RH = 63%. Blue curve – observed data; red curve – calculated data; grey curve – residual curves.

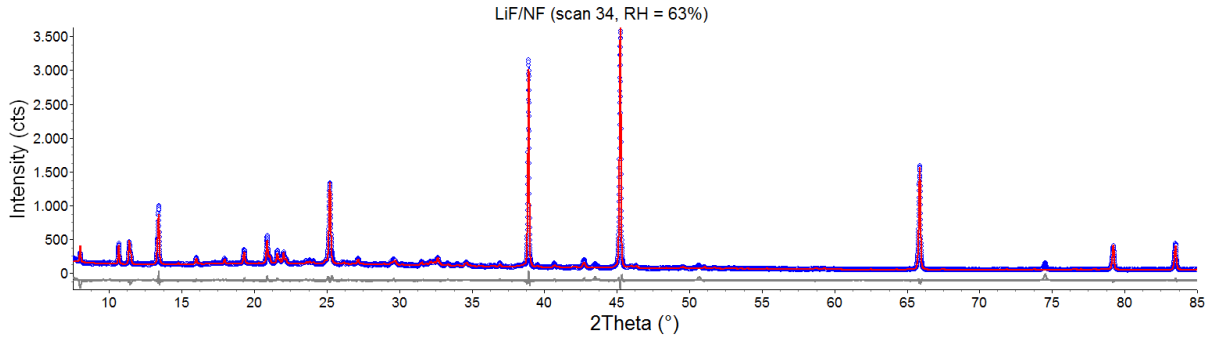

Source: Created by the author.

Figure D.29: Graphical Rietveld refinements obtained for LiF/NF at RH = 4%. Blue curve – observed data; red curve – calculated data; grey curve – residual curves.

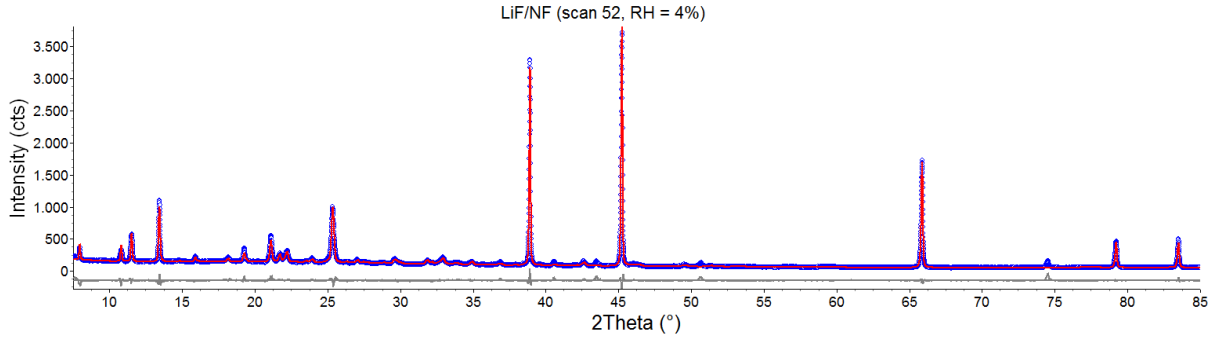

Source: Created by the author.

Figure D.30: Graphical Rietveld refinements obtained for LiF/NF at RH = 89%. Blue curve – observed data; red curve – calculated data; grey curve – residual curves.

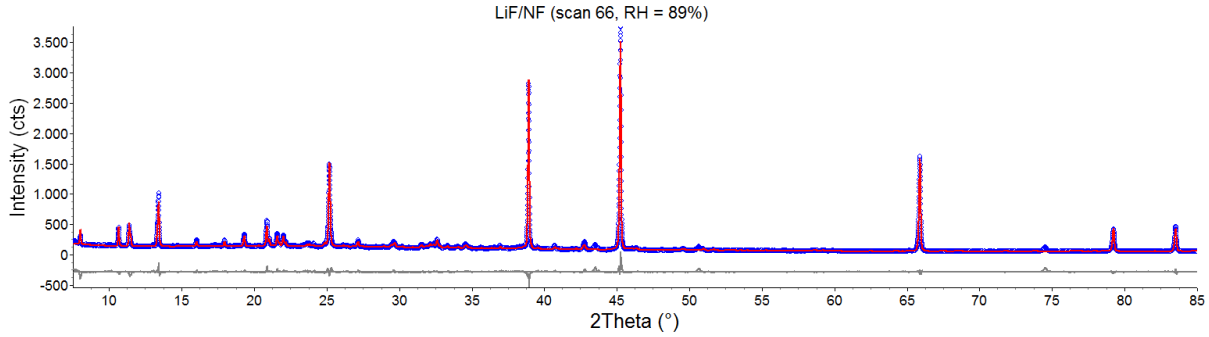

Source: Created by the author.

D.3. LiF/NF tablet sample

D.3.1. Huber equipment – Tucano furnace – LNLS

D.3.1.1. Values calculated

Figure D.31: a) Comparison between NF sesquihydrate lattice parameter 'a', in sample LiF/NF tablet, calculated by sequential Rietveld refinement (in function of RH_A and RH_C) and surface Rietveld refinement; b) Comparison between NF sesquihydrate lattice parameter 'b', in sample LiF/NF tablet, calculated by sequential Rietveld refinement (in function of RH_A and RH_C) and surface Rietveld refinement.

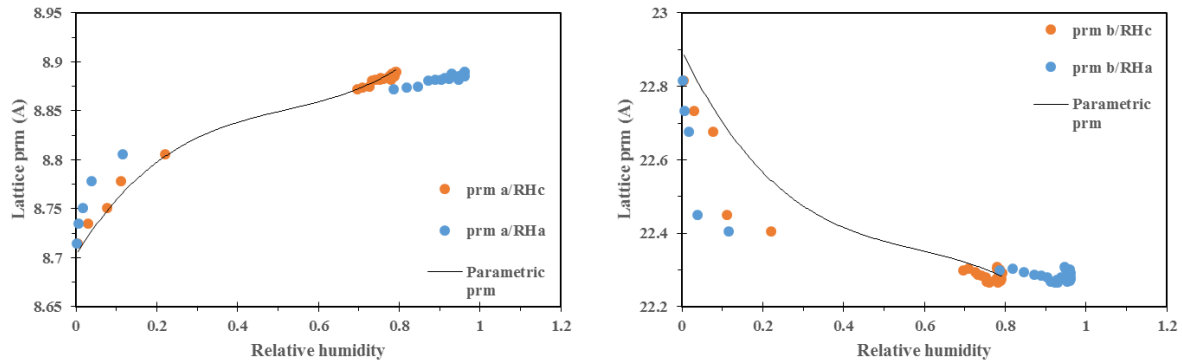

Source: Created by the author.

Figure D.32: a) Comparison between NF sesquihydrate lattice parameter 'c', in sample LiF/NF tablet, calculated by sequential Rietveld refinement (in function of RH_A and RH_C) and surface Rietveld refinement; b) Comparison between NF sesquihydrate lattice parameter 'beta', in sample LiF/NF tablet, calculated by sequential Rietveld refinement (in function of RH_A and RH_C) and surface Rietveld refinement.

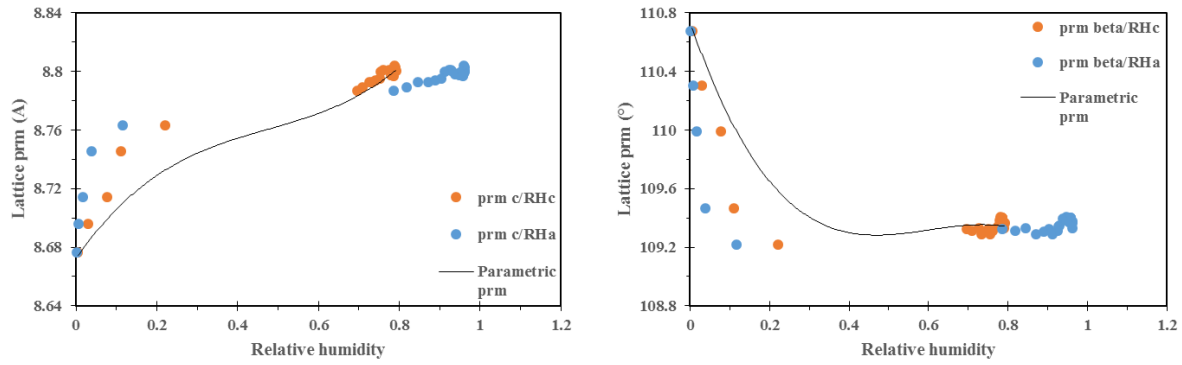

Source: Created by the author.

Figure D.33: a) Comparison between NF sesquihydrate volume, in sample LiF/NF tablet, calculated by sequential Rietveld refinement (in function of RH_A and RH_C) and surface Rietveld refinement; b) Comparison between NF sesquihydrate phase, in sample LiF/NF tablet, calculated by sequential Rietveld refinement and surface Rietveld refinement.

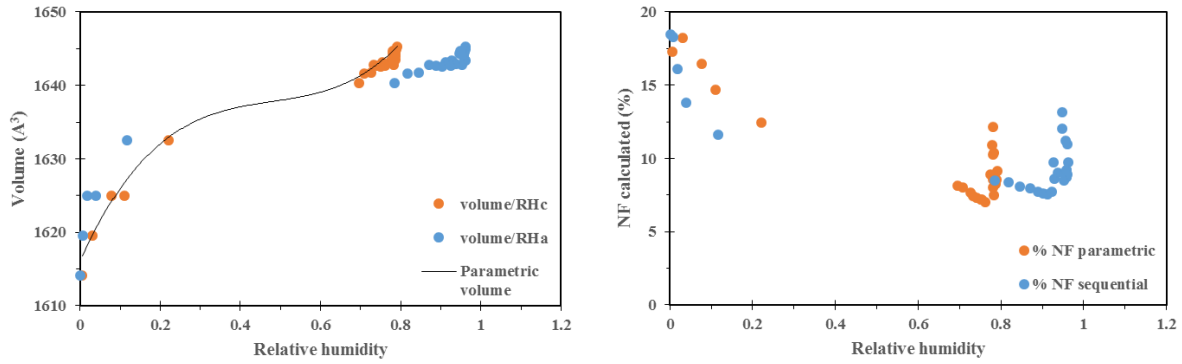

Source: Created by the author.

Figure D.34: a) Comparison between Rwp (%) obtained, for LiF/NF tablet sample, by sequential Rietveld refinement and surface Rietveld refinement; b) Comparison between *gof* obtained, for LiF/NF tablet sample, by sequential Rietveld refinement and surface Rietveld refinement.

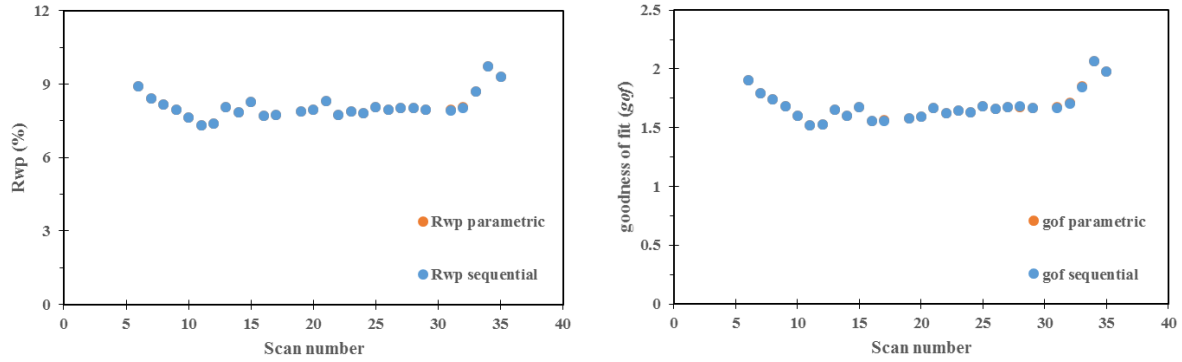

Source: Created by the author.

D.3.1.2. Graphical fits

Figure D.35: All graphical Rietveld refinements obtained for LiF/NF tablet, during RH variation. Black curve– all observed data; red curve – all calculated data; grey curve – all residual curves.

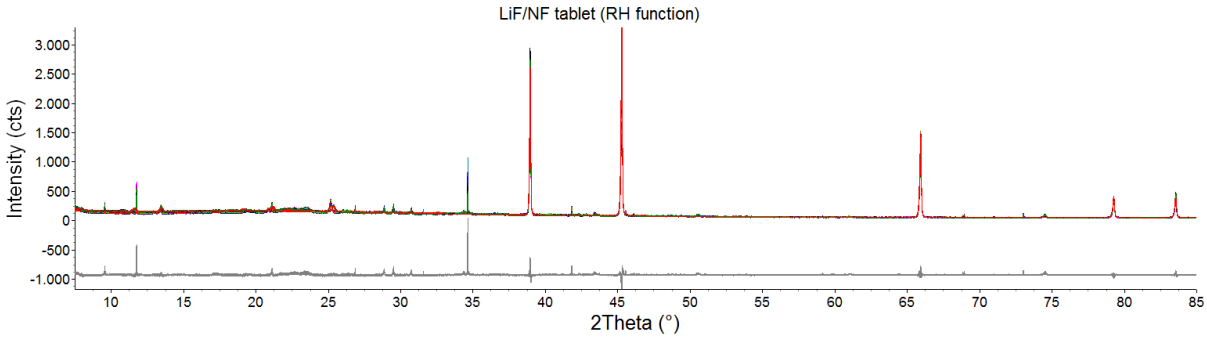

Source: Created by the author.

Figure D.36: Graphical Rietveld refinements obtained for LiF/NF tablet at RH = 95%. Blue curve – observed data; red curve – calculated data; grey curve – residual curves.

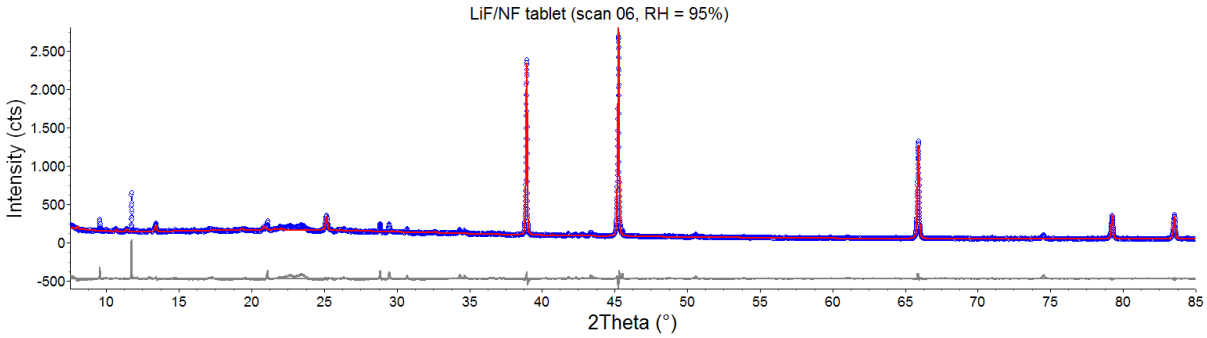

Source: Created by the author.

Figure D.37: Graphical Rietveld refinements obtained for LiF/NF tablet at RH = 96%. Blue curve – observed data; red curve – calculated data; grey curve – residual curves.

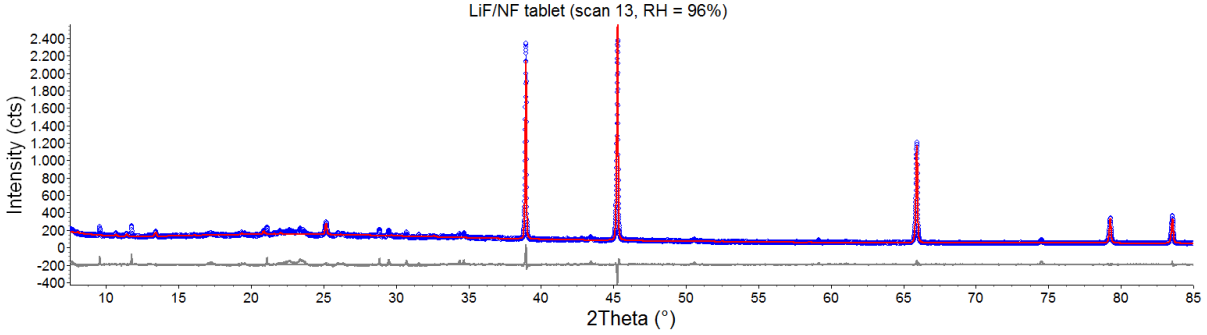

Source: Created by the author.

Figure D.38: Graphical Rietveld refinements obtained for LiF/NF tablet at RH = 93%. Blue curve – observed data; red curve – calculated data; grey curve – residual curves.

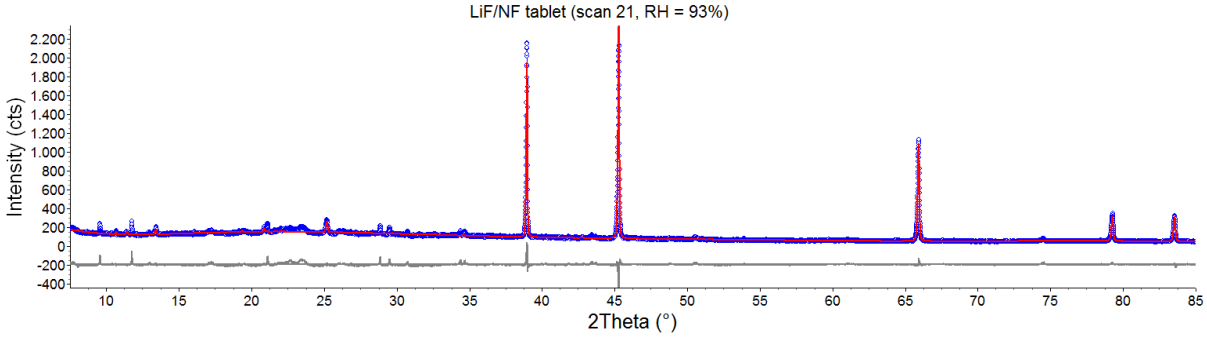

Source: Created by the author.

Figure D.39: Graphical Rietveld refinements obtained for LiF/NF tablet at RH = 79%. Blue curve – observed data; red curve – calculated data; grey curve – residual curves.

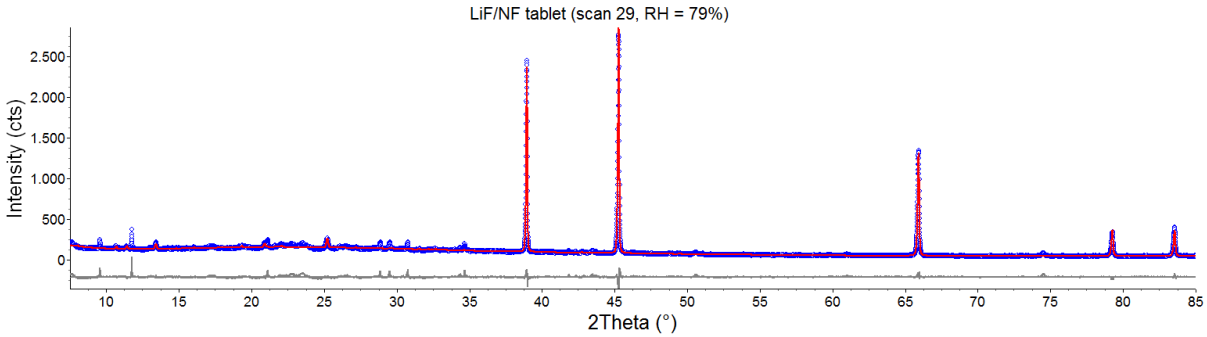

Source: Created by the author.

Figure D.40: Graphical Rietveld refinements obtained for LiF/NF tablet at RH = 0%. Blue curve – observed data; red curve – calculated data; grey curve – residual curves.

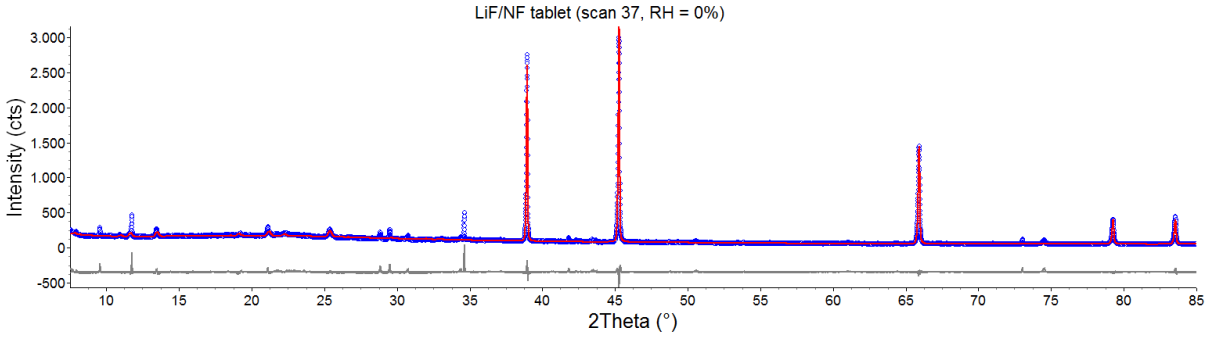

Source: Created by the author

Appendix E

Mebendazol parameters behaviour

Mixtures 50/50 were carefully prepared for LiF/MBZ. *In situ* powder diffraction data, in function of time, were collected for LiF/MBZ sample, 2705 patterns in total for isotherm condition at each 5°C from 130°C up to 160°C, using Anton Paar HTK1200 furnace (300-1500 K) coupled to the D8 diffractometer over 4-85° 2θ with a 0.02° step using variable divergence slit 6 mm in 5 minutes scan.

Parametric Rietveld refinement, use same crystal structures already used for LiF, MBZA and MBZC.

In all refinements (sequential and surface) were calculated independently for each scan, linear absorption correction for adjusting the peak shape due to sample transparency and 14 terms in Chebychev background polynomial. For each phase, scale factor, peak shapes, lattice parameters and atomic displacement parameter were refined. The preferred orientation in MBZA and MBZC were corrected by March Dollase model and the amorphous quantification was proceed from internal standard method. These two MBZ polymorphs had their lattice parameters parameterized by a 2^{nd} order polynomial in function of time, rescaled between ±1 (chapter 3).

E.1. LiF/MBZ sample

E.1.1. Bruker D8 Equipment

E.1.1.1. Values calculated at 130°C

Figure E.1: a) Comparison between Rwp (%) behaviour obtained by sequential Rietveld refinement and surface Rietveld refinement in function of time, for sample LiF/MBZ at 130°C; b) Comparison between *gof* behaviour obtained by sequential Rietveld refinement and surface Rietveld refinement in function of time, for sample LiF/MBZ at 130°C.

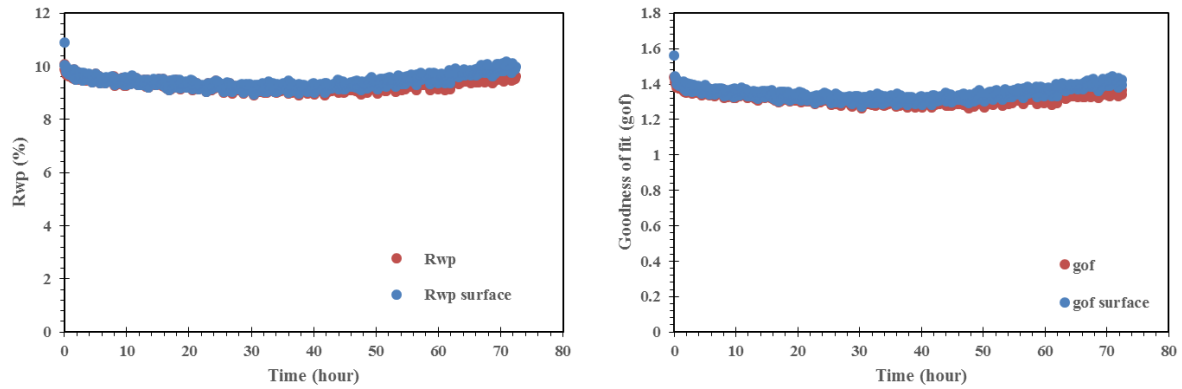

Source: Created by the author.

Figure E.2: a) Comparison between sample amorphous quantification calculated by sequential Rietveld refinement and surface Rietveld refinement in function of time, for sample LiF/MBZ at 130°C; b) Comparison between MBZ amorphous quantification calculated by sequential Rietveld refinement and surface Rietveld refinement in function of time, for sample LiF/MBZ at 130°C.

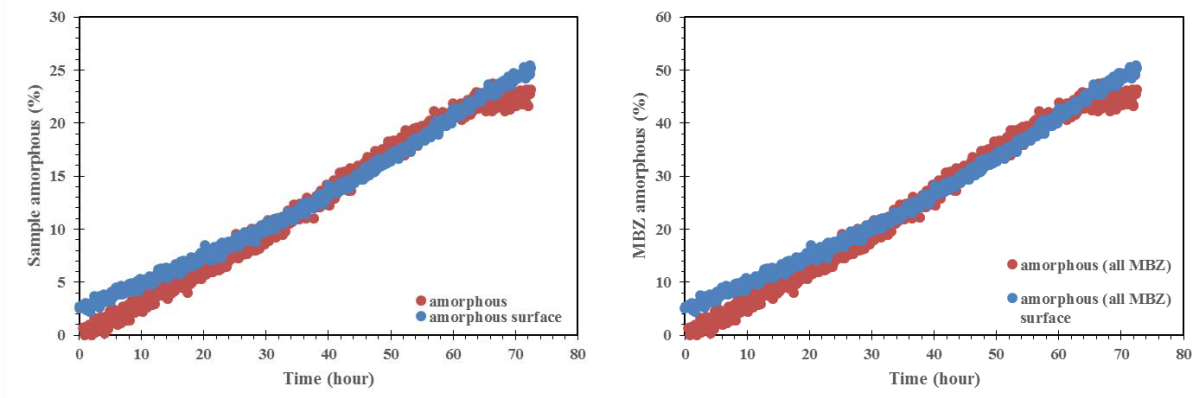

Source: Created by the author.

E.1.1.1. Values calculated at 130°C

Figure E.3: a) Comparison between LiF scale factor behaviour calculated by sequential Rietveld refinement and surface Rietveld refinement in function of time, for sample LiF/MBZ at 130°C; b) Comparison between LiF phase quantification calculated by sequential Rietveld refinement and surface Rietveld refinement in function of time, for sample LiF/MBZ at 130°C.

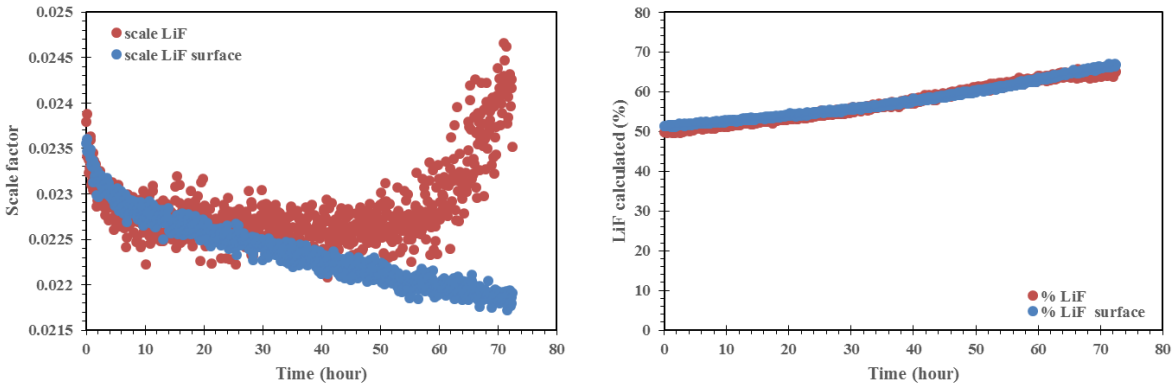

Source: Created by the author.

Figure E.4: a) Comparison between LiF lattice parameter 'a' behaviour determined by sequential Rietveld refinement and surface Rietveld refinement in function of time, for sample LiF/MBZ at 130°C; b) Comparison between LiF volume behaviour determined by sequential Rietveld refinement and surface Rietveld refinement in function of time, for sample LiF/MBZ at 130°C.

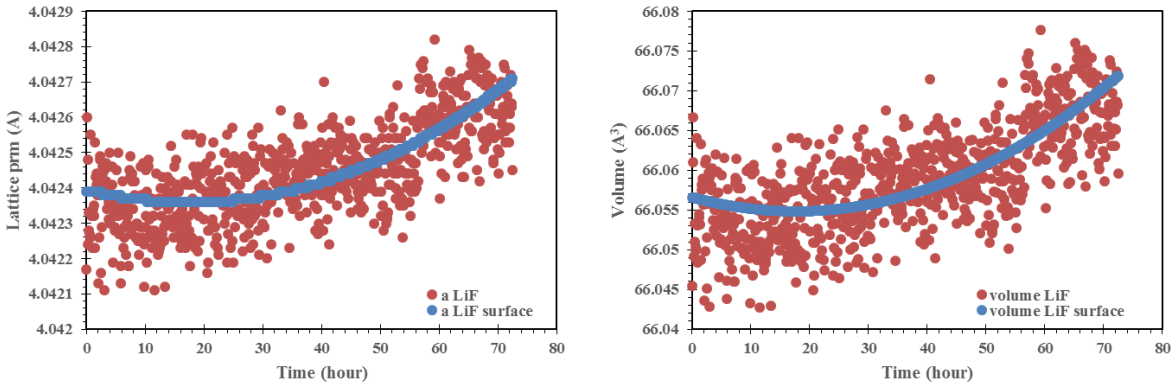

Source: Created by the author.

E.1.1.1. Values calculated at 130°C

Figure E.5: a) Comparison between MBZC scale factor behaviour calculated by sequential Rietveld refinement and surface Rietveld refinement in function of time, for sample LiF/MBZ at 130°C; b) Comparison between MBZC phase quantification calculated by sequential Rietveld refinement and surface Rietveld refinement in function of time, for sample LiF/MBZ at 130°C.

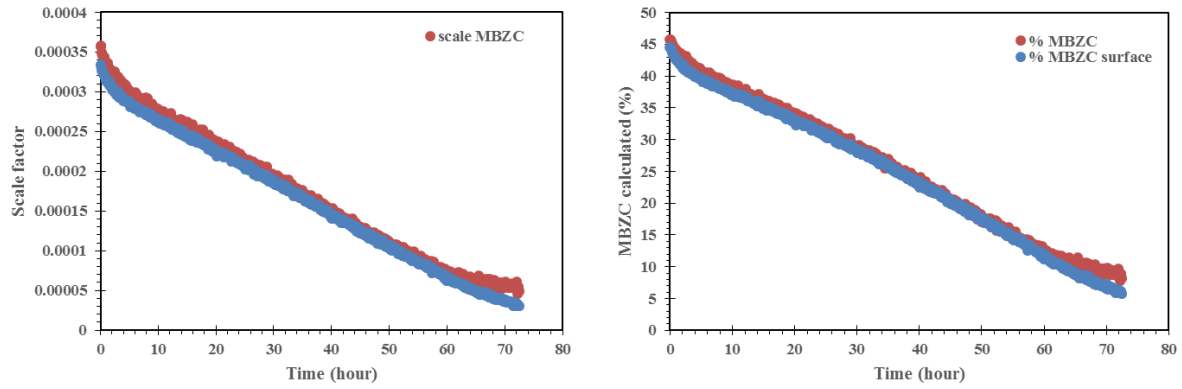

Source: Created by the author.

Figure E.6: a) Comparison between MBZC phase quantification corrected by internal standard method and calculated by sequential Rietveld refinement and surface Rietveld refinement in function of time, for sample LiF/MBZ at 130°C; b) Comparison between MBZC lattice parameter 'a' behaviour determined by sequential Rietveld refinement and surface Rietveld refinement in function of time, for sample LiF/MBZ at 130°C.

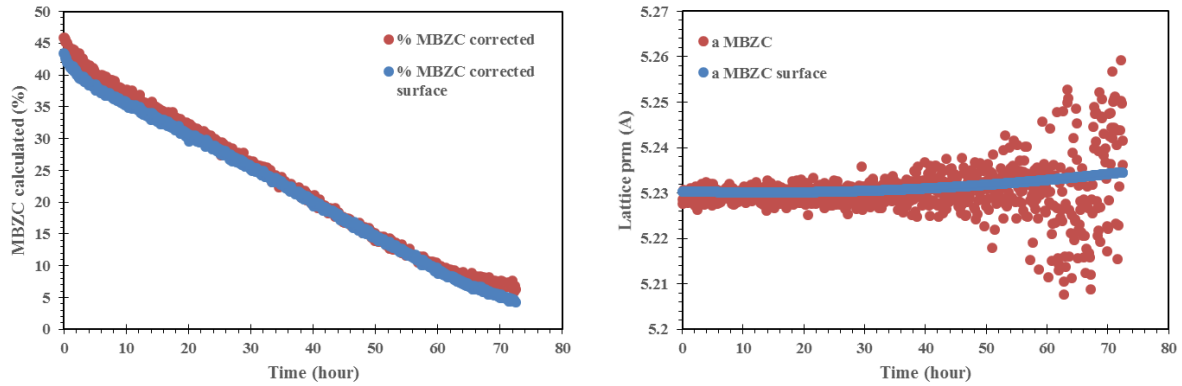

Source: Created by the author.

E.1.1.1. Values calculated at 130°C

Figure E.7: a) Comparison between MBZC lattice parameter 'b' behaviour determined by sequential Rietveld refinement and surface Rietveld refinement in function of time, for sample LiF/MBZ at 130°C.; b) Comparison between MBZC lattice parameter 'c' behaviour determined by sequential Rietveld refinement and surface Rietveld refinement in function of time, for sample LiF/MBZ at 130°C.

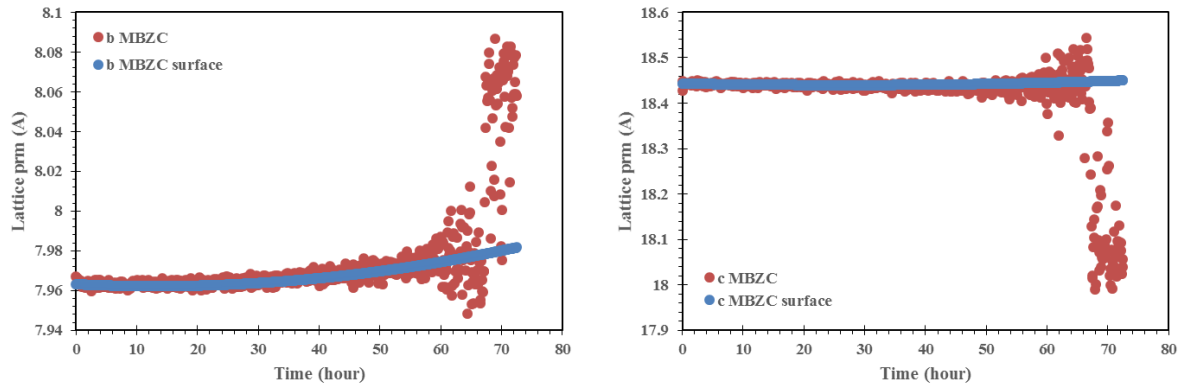

Source: Created by the author.

Figure E.8: a) Comparison between MBZC lattice parameter 'alpha' behaviour determined by sequential Rietveld refinement and surface Rietveld refinement in function of time, for sample LiF/MBZ at 130°C.; b) Comparison between MBZC lattice parameter 'beta' behaviour determined by sequential Rietveld refinement and surface Rietveld refinement in function of time, for sample LiF/MBZ at 130°C.

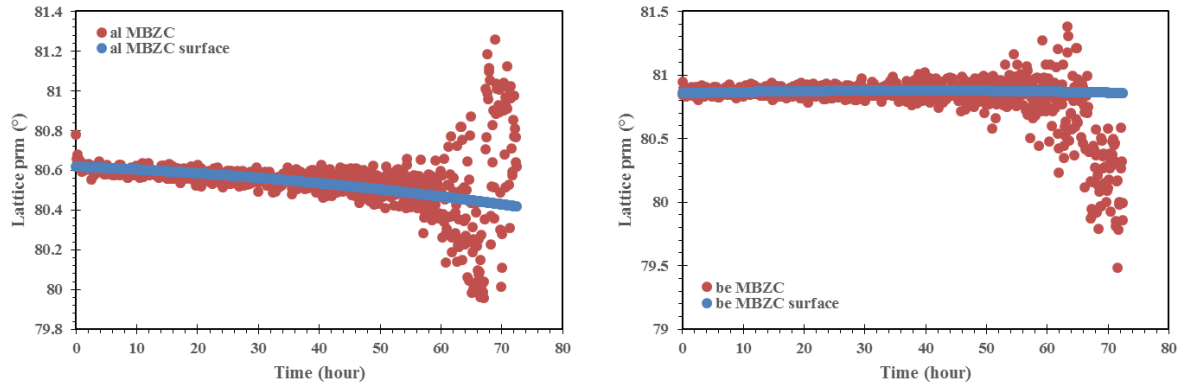

Source: Created by the author.

E.1.1.1. Values calculated at 130°C

Figure E.9: a) Comparison between MBZC lattice parameter 'gamma' behaviour determined by sequential Rietveld refinement and surface Rietveld refinement in function of time, for sample LiF/MBZ at 130°C.; b) Comparison between MBZC volume behaviour determined by sequential Rietveld refinement and surface Rietveld refinement in function of time, for sample LiF/MBZ at 130°C.

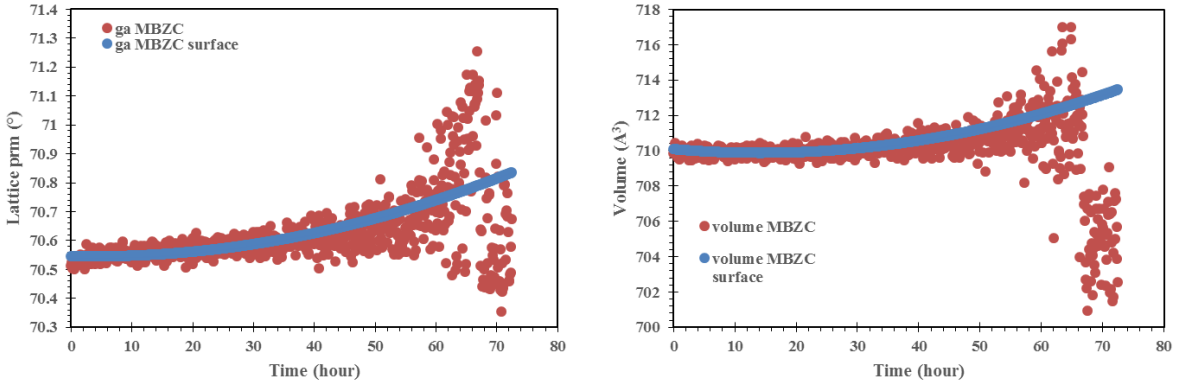

Source: Created by the author.

Figure E.10: a) Comparison between MBZA scale factor behaviour calculated by sequential Rietveld refinement and surface Rietveld refinement in function of time, for sample LiF/MBZ at 130°C; b) Comparison between MBZA phase quantification calculated by sequential Rietveld refinement and surface Rietveld refinement in function of time, for sample LiF/MBZ at 130°C.

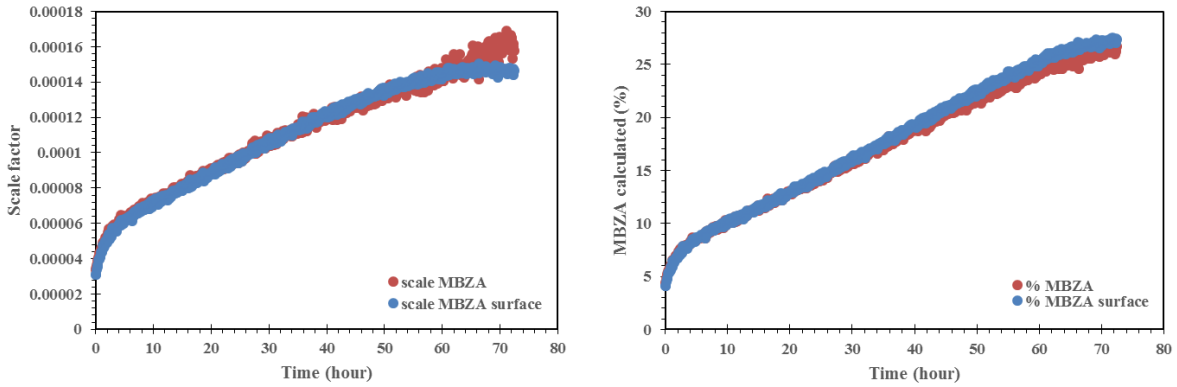

Source: Created by the author.

E.1.1.1. Values calculated at 130°C

Figure E.11: a) Comparison between MBZA phase quantification corrected by internal standard method and calculated by sequential Rietveld refinement and surface Rietveld refinement in function of time, for sample LiF/MBZ at 130°C; b) Comparison between MBZA lattice parameter 'a' behaviour determined by sequential Rietveld refinement and surface Rietveld refinement in function of time, for sample LiF/MBZ at 130°C.

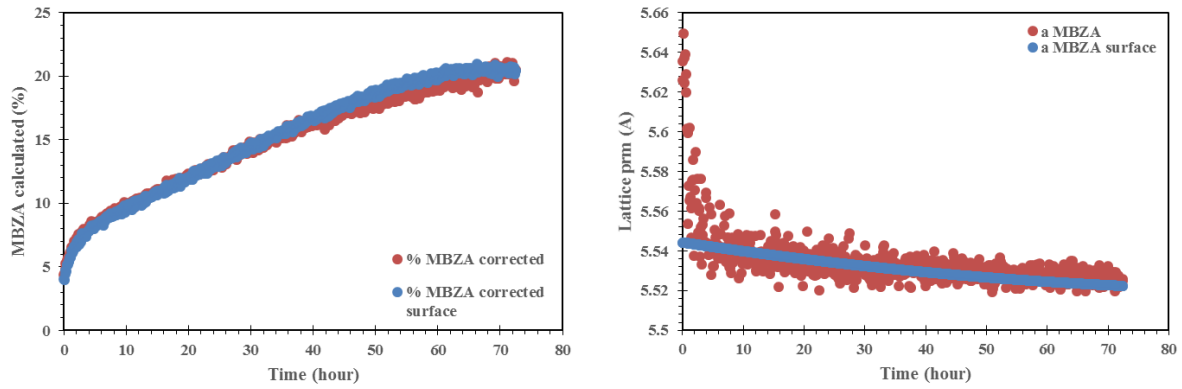

Source: Created by the author.

Figure E.12: a) Comparison between MBZA lattice parameter 'b' behaviour determined by sequential Rietveld refinement and surface Rietveld refinement in function of time, for sample LiF/MBZ at 130°C.; b) Comparison between MBZA lattice parameter 'c' behaviour determined by sequential Rietveld refinement and surface Rietveld refinement in function of time, for sample LiF/MBZ at 130°C.

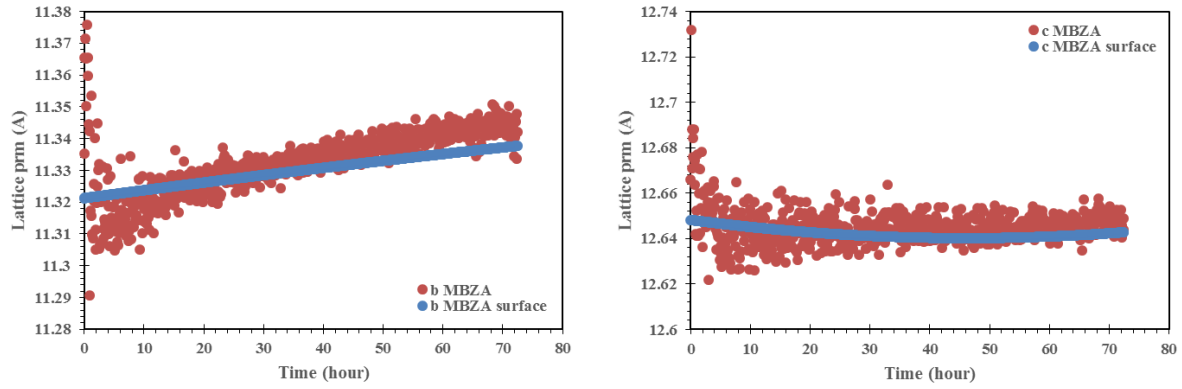

Source: Created by the author.

E.1.1.1. Values calculated at 130°C

Figure E.13: a) Comparison between MBZA lattice parameter 'alpha' behaviour determined by sequential Rietveld refinement and surface Rietveld refinement in function of time, for sample LiF/MBZ at 130°C.; b) Comparison between MBZA lattice parameter 'beta' behaviour determined by sequential Rietveld refinement and surface Rietveld refinement in function of time, for sample LiF/MBZ at 130°C.

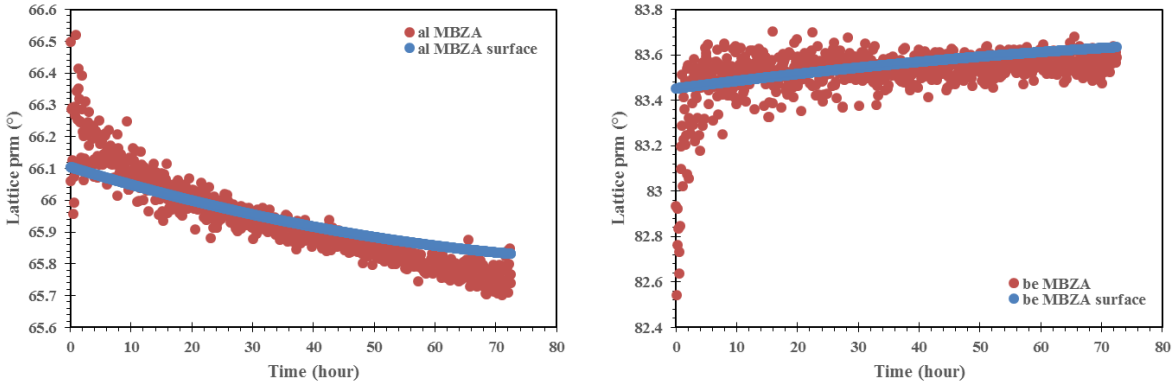

Source: Created by the author.

Figure E.14: a) Comparison between MBZA lattice parameter 'gamma' behaviour determined by sequential Rietveld refinement and surface Rietveld refinement in function of time, for sample LiF/MBZ at 130°C.; b) Comparison between MBZA volume behaviour determined by sequential Rietveld refinement and surface Rietveld refinement in function of time, for sample LiF/MBZ at 130°C.

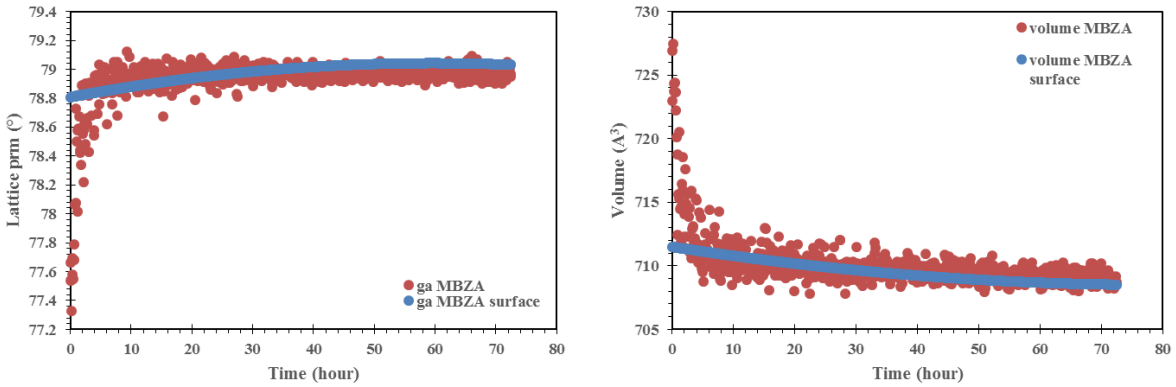

Source: Created by the author.

E.1.1.2. Graphical fits from surface Rietveld refinement at 130°C

Figure E.15: Graphical Rietveld refinements obtained for LiF/MBZ at T = 130 °C and t = 0 hour. Blue curve – observed data; red curve – calculated data; grey curve – residual curves.

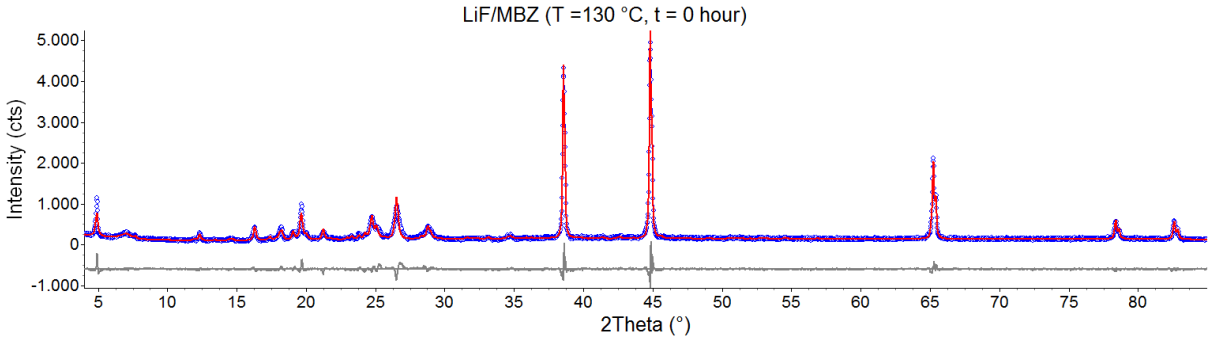

Source: Created by the author.

Figure E.16: Graphical Rietveld refinements obtained for LiF/MBZ at T = 130 °C and t = 14.5 hours. Blue curve – observed data; red curve – calculated data; grey curve – residual curves.

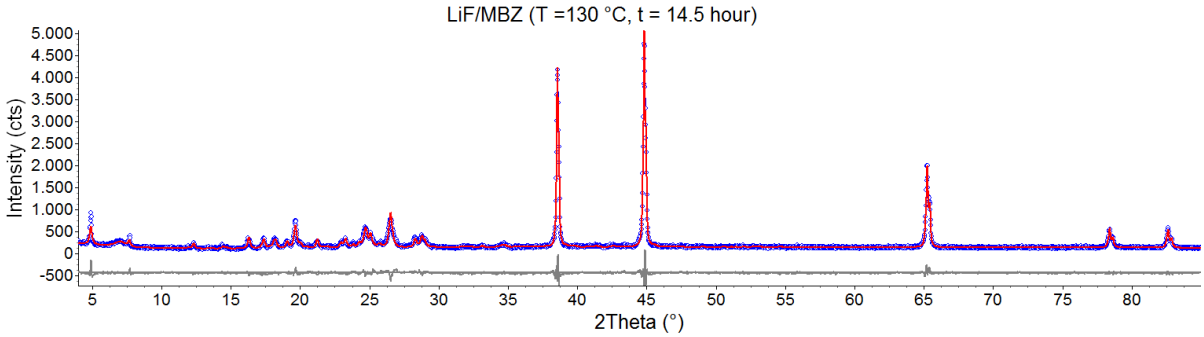

Source: Created by the author.

Figure E.17: Graphical Rietveld refinements obtained for LiF/MBZ at T = 130 °C and t = 29 hours. Blue curve – observed data; red curve – calculated data; grey curve – residual curves.

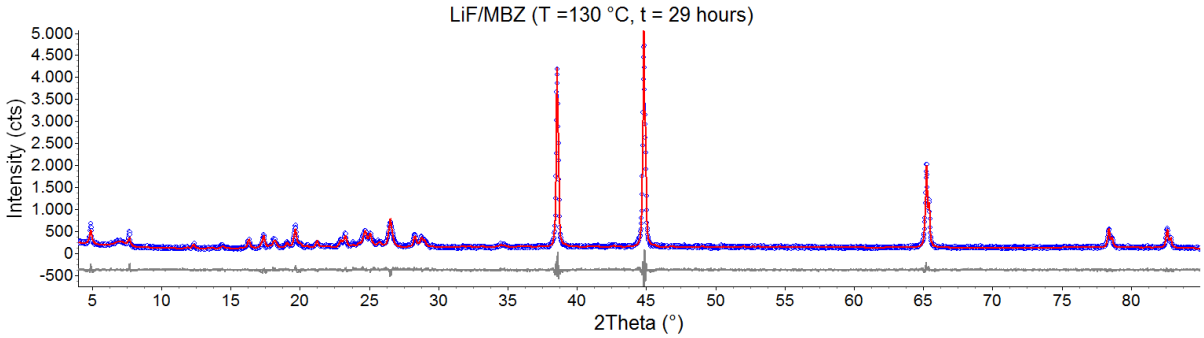

Source: Created by the author.

Figure E.18: Graphical Rietveld refinements obtained for LiF/MBZ at T = 130 °C and t = 43.5 hours. Blue curve – observed data; red curve – calculated data; grey curve – residual curves.

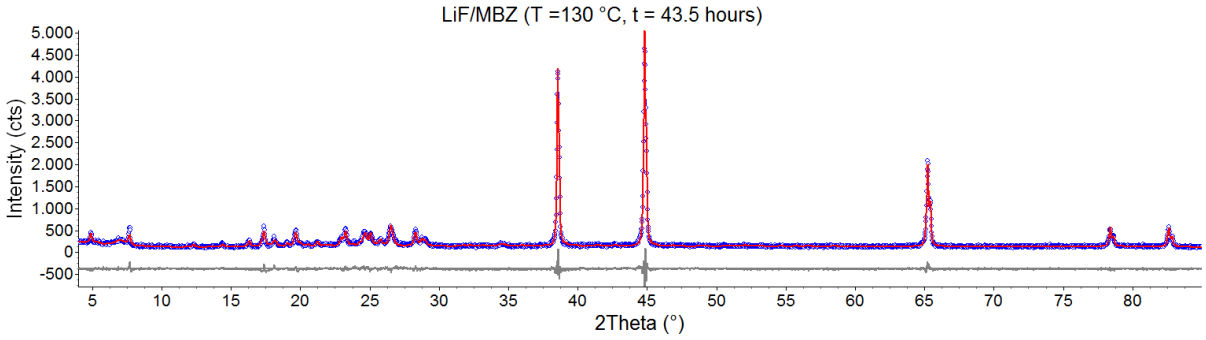

Source: Created by the author.

Figure E.19: Graphical Rietveld refinements obtained for LiF/MBZ at T = 130 °C and t = 58 hours. Blue curve – observed data; red curve – calculated data; grey curve – residual curves.

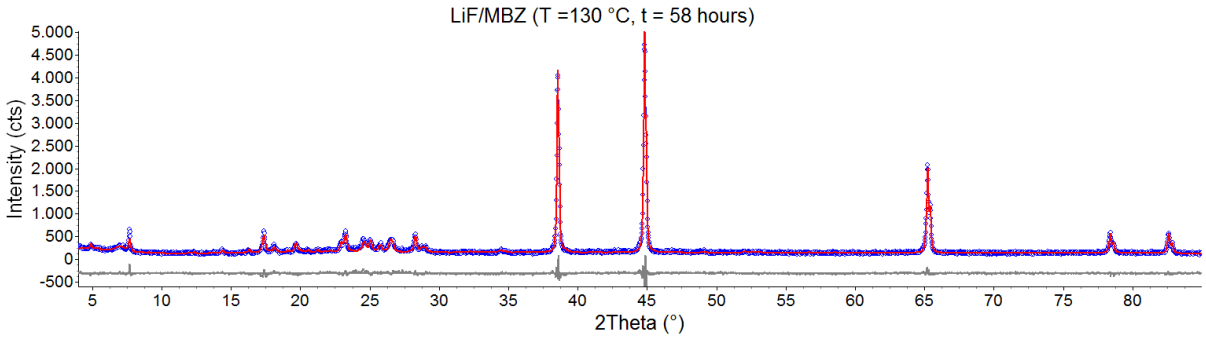

Source: Created by the author.

Figure E.20: Graphical Rietveld refinements obtained for LiF/MBZ at T = 130 °C and t = 72.5 hours. Blue curve – observed data; red curve – calculated data; grey curve – residual curves.

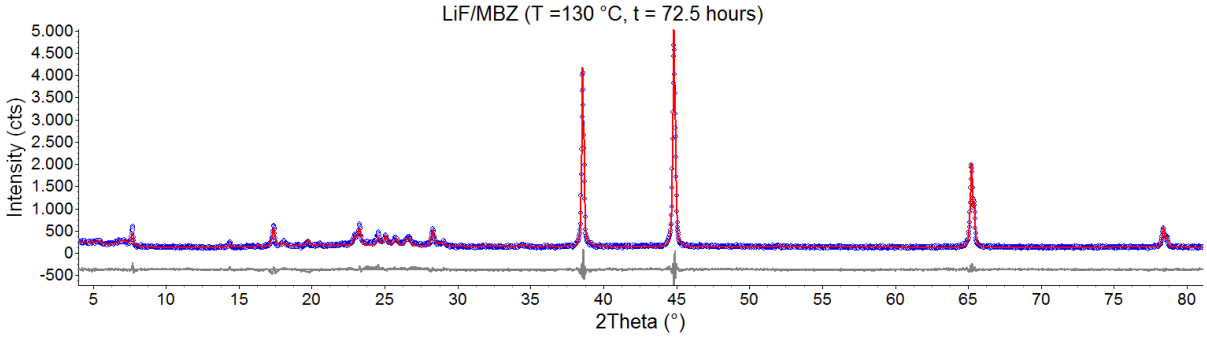

Source: Created by the author.

E.1.1.3. Values calculated at 135°C

Figure E.21: a) Comparison between Rwp (%) behaviour obtained by sequential Rietveld refinement and surface Rietveld refinement in function of time, for sample LiF/MBZ at 135°C; b) Comparison between *gof* behaviour obtained by sequential Rietveld refinement and surface Rietveld refinement in function of time, for sample LiF/MBZ at 135°C.

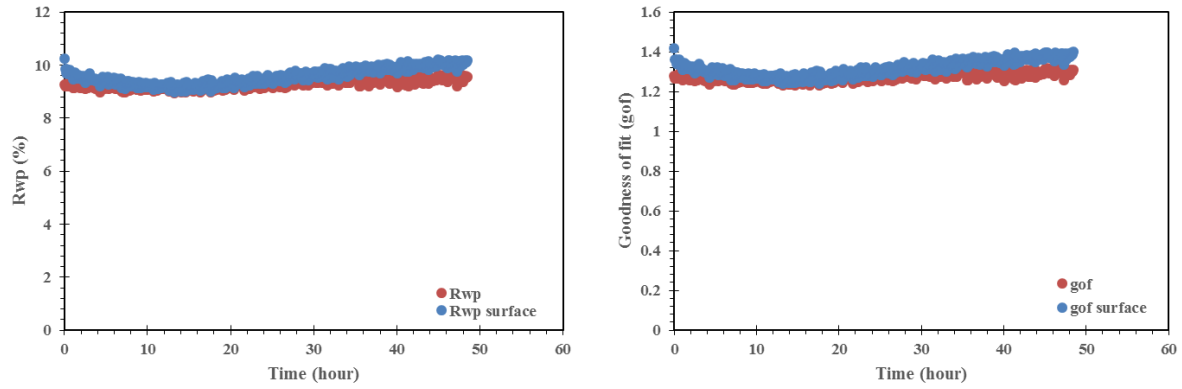

Source: Created by the author.

Figure E.22: a) Comparison between sample amorphous quantification calculated by sequential Rietveld refinement and surface Rietveld refinement in function of time, for sample LiF/MBZ at 135°C; b) Comparison between MBZ amorphous quantification calculated by sequential Rietveld refinement and surface Rietveld refinement in function of time, for sample LiF/MBZ at 135°C.

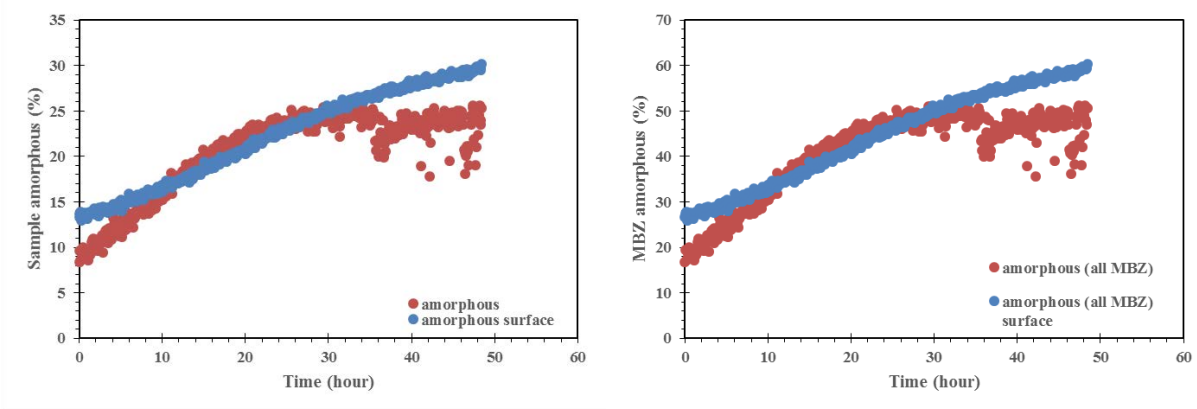

Source: Created by the author.

E.1.1.3. Values calculated at 135°C

Figure E.23: a) Comparison between LiF scale factor behaviour calculated by sequential Rietveld refinement and surface Rietveld refinement in function of time, for sample LiF/MBZ at 135°C; b) Comparison between LiF phase quantification calculated by sequential Rietveld refinement and surface Rietveld refinement in function of time, for sample LiF/MBZ at 135°C.

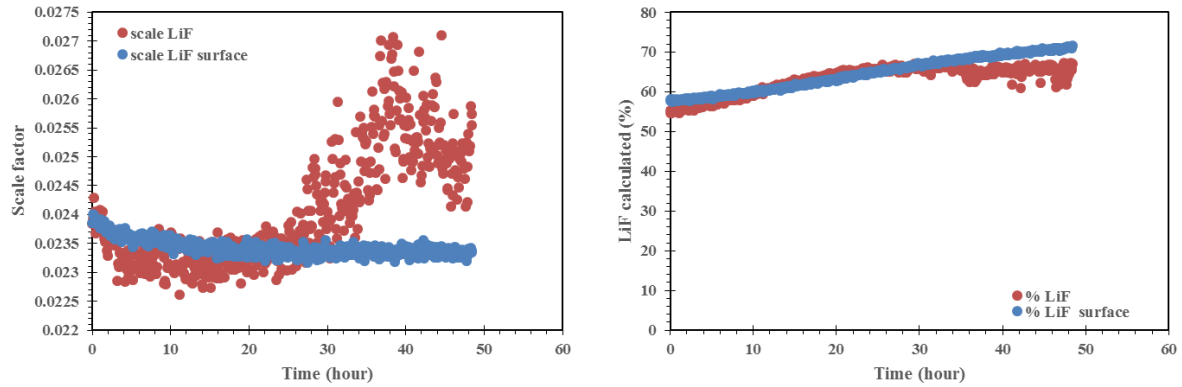

Source: Created by the author.

Figure E.24: a) Comparison between LiF lattice parameter 'a' behaviour determined by sequential Rietveld refinement and surface Rietveld refinement in function of time, for sample LiF/MBZ at 135°C; b) Comparison between LiF volume behaviour determined by sequential Rietveld refinement and surface Rietveld refinement in function of time, for sample LiF/MBZ at 135°C.

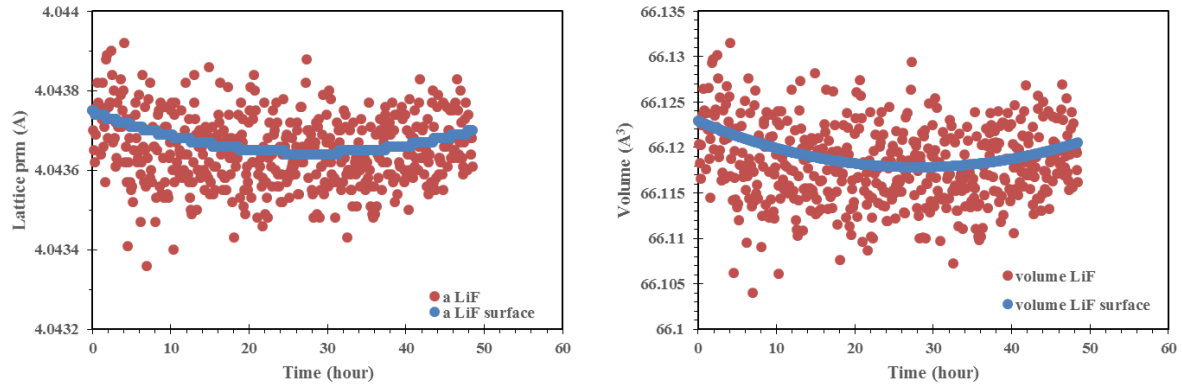

Source: Created by the author.

E.1.1.3. Values calculated at 135°C

Figure E.25: a) Comparison between MBZC scale factor behaviour calculated by sequential Rietveld refinement and surface Rietveld refinement in function of time, for sample LiF/MBZ at 135°C; b) Comparison between MBZC phase quantification calculated by sequential Rietveld refinement and surface Rietveld refinement in function of time, for sample LiF/MBZ at 135°C.

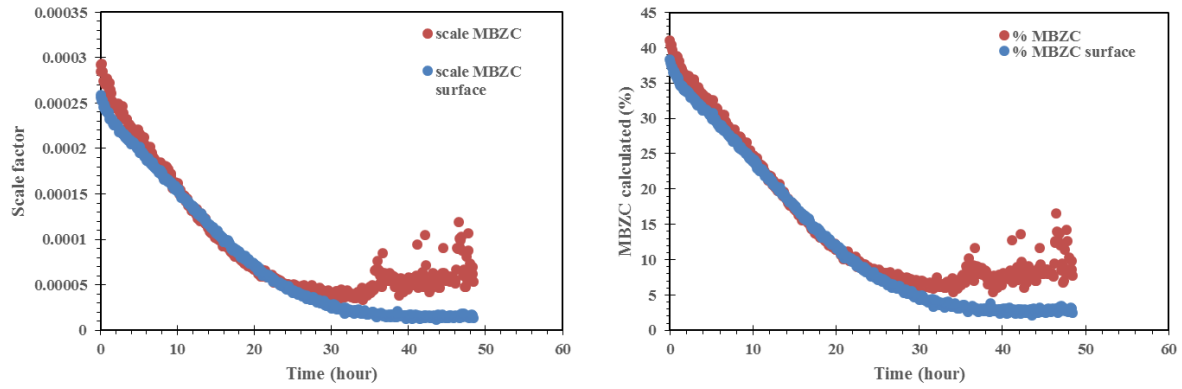

Source: Created by the author.

Figure E.26: a) Comparison between MBZC phase quantification corrected by internal standard method and calculated by sequential Rietveld refinement and surface Rietveld refinement in function of time, for sample LiF/MBZ at 135°C; b) Comparison between MBZC lattice parameter 'a' behaviour determined by sequential Rietveld refinement and surface Rietveld refinement in function of time, for sample LiF/MBZ at 135°C.

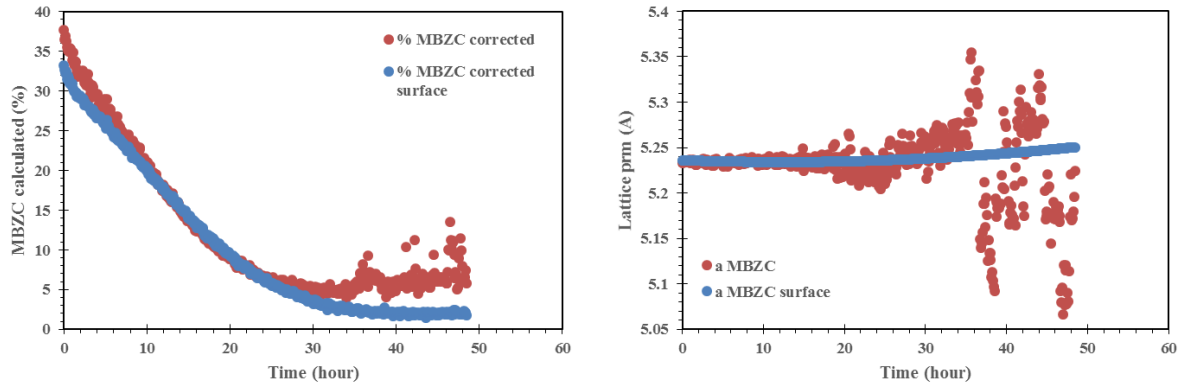

Source: Created by the author.

E.1.1.3. Values calculated at 135°C

Figure E.27: a) Comparison between MBZC lattice parameter 'b' behaviour determined by sequential Rietveld refinement and surface Rietveld refinement in function of time, for sample LiF/MBZ at 135°C.; b) Comparison between MBZC lattice parameter 'c' behaviour determined by sequential Rietveld refinement and surface Rietveld refinement in function of time, for sample LiF/MBZ at 135°C.

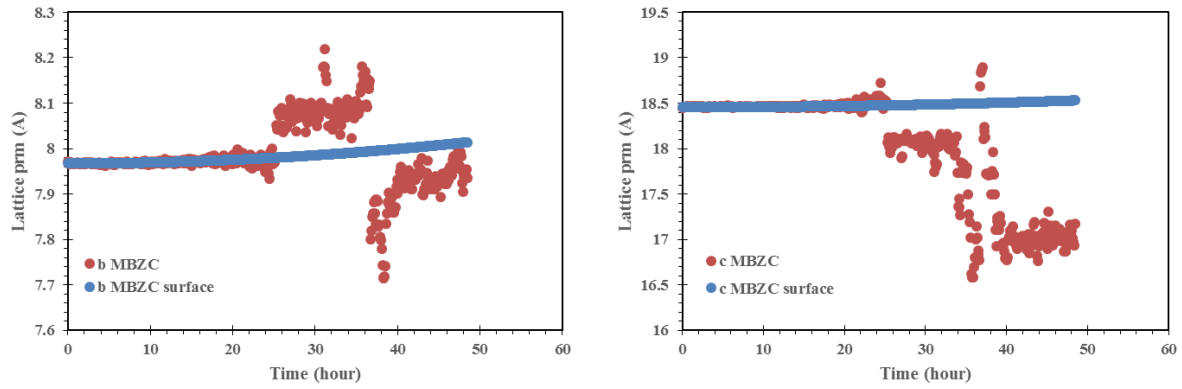

Source: Created by the author.

Figure E.28: a) Comparison between MBZC lattice parameter 'alpha' behaviour determined by sequential Rietveld refinement and surface Rietveld refinement in function of time, for sample LiF/MBZ at 135°C.; b) Comparison between MBZC lattice parameter 'beta' behaviour determined by sequential Rietveld refinement and surface Rietveld refinement in function of time, for sample LiF/MBZ at 135°C.

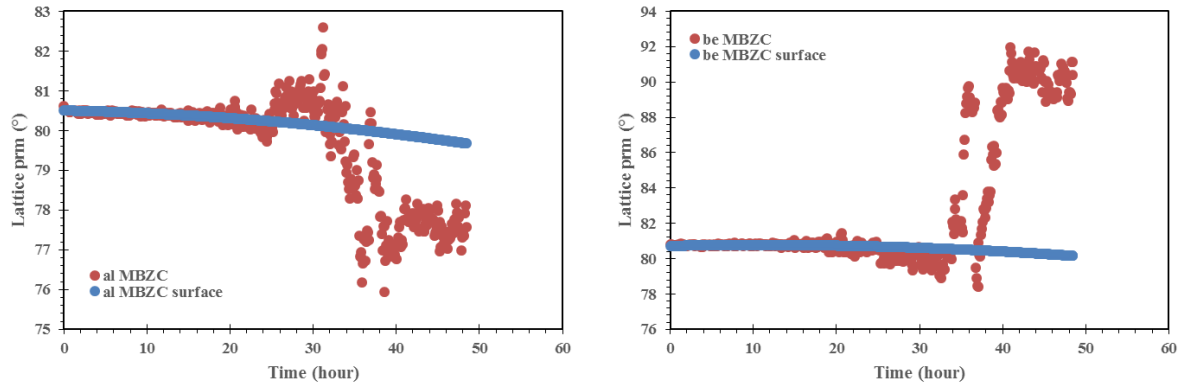

Source: Created by the author.

E.1.1.3. Values calculated at 135°C

Figure E.29: a) Comparison between MBZC lattice parameter 'gamma' behaviour determined by sequential Rietveld refinement and surface Rietveld refinement in function of time, for sample LiF/MBZ at 135°C.; b) Comparison between MBZC volume behaviour determined by sequential Rietveld refinement and surface Rietveld refinement in function of time, for sample LiF/MBZ at 135°C.

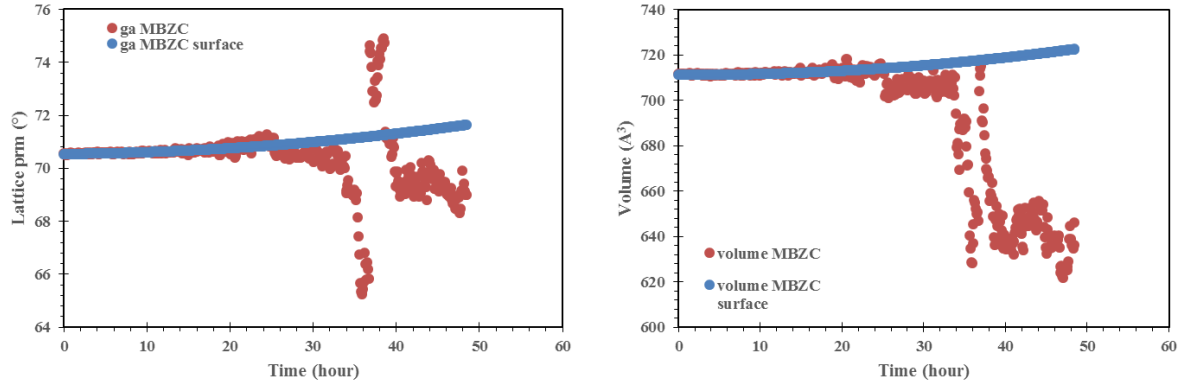

Source: Created by the author.

Figure E.30: a) Comparison between MBZA scale factor behaviour calculated by sequential Rietveld refinement and surface Rietveld refinement in function of time, for sample LiF/MBZ at 135°C; b) Comparison between MBZA phase quantification calculated by sequential Rietveld refinement and surface Rietveld refinement in function of time, for sample LiF/MBZ at 135°C.

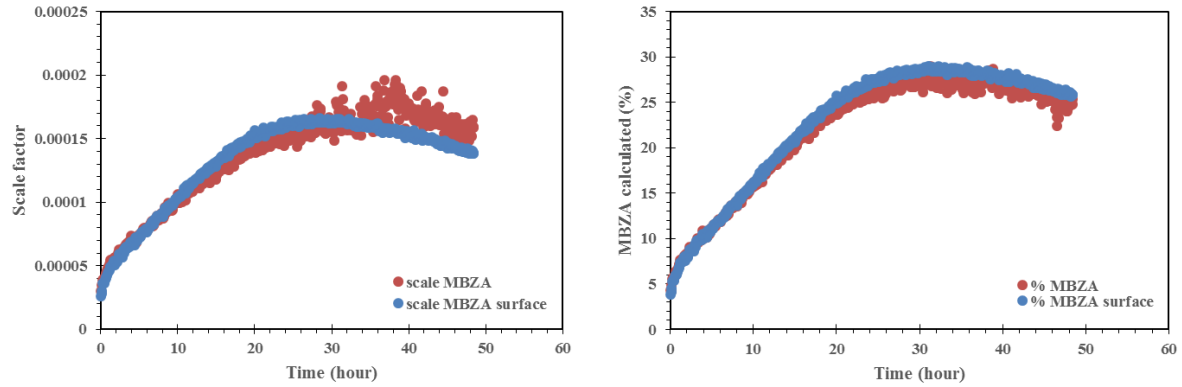

Source: Created by the author.

E.1.1.3. Values calculated at 135°C

Figure E.31: a) Comparison between MBZA phase quantification corrected by internal standard method and calculated by sequential Rietveld refinement and surface Rietveld refinement in function of time, for sample LiF/MBZ at 135°C; b) Comparison between MBZA lattice parameter 'a' behaviour determined by sequential Rietveld refinement and surface Rietveld refinement in function of time, for sample LiF/MBZ at 135°C.

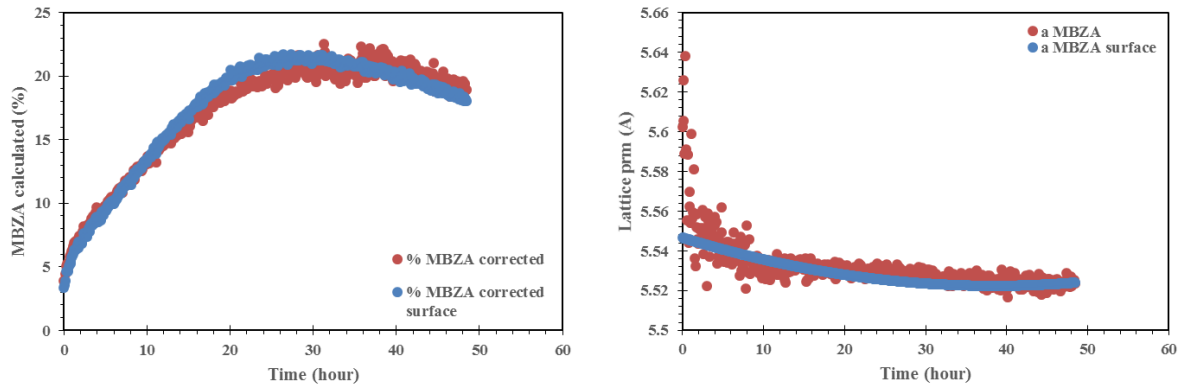

Source: Created by the author.

Figure E.32: a) Comparison between MBZA lattice parameter 'b' behaviour determined by sequential Rietveld refinement and surface Rietveld refinement in function of time, for sample LiF/MBZ at 135°C.; b) Comparison between MBZA lattice parameter 'c' behaviour determined by sequential Rietveld refinement and surface Rietveld refinement in function of time, for sample LiF/MBZ at 135°C.

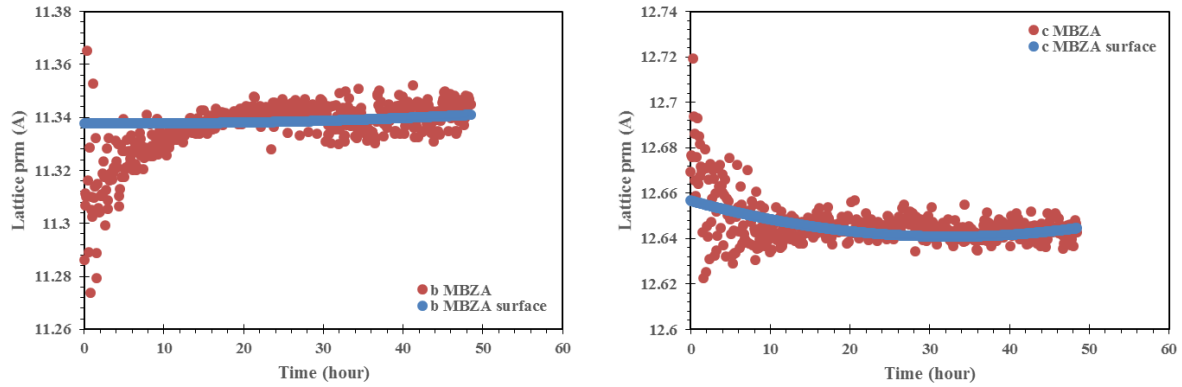

Source: Created by the author.

E.1.1.3. Values calculated at 135°C

Figure E.33: a) Comparison between MBZA lattice parameter 'alpha' behaviour determined by sequential Rietveld refinement and surface Rietveld refinement in function of time, for sample LiF/MBZ at 135°C.; b) Comparison between MBZA lattice parameter 'beta' behaviour determined by sequential Rietveld refinement and surface Rietveld refinement in function of time, for sample LiF/MBZ at 135°C.

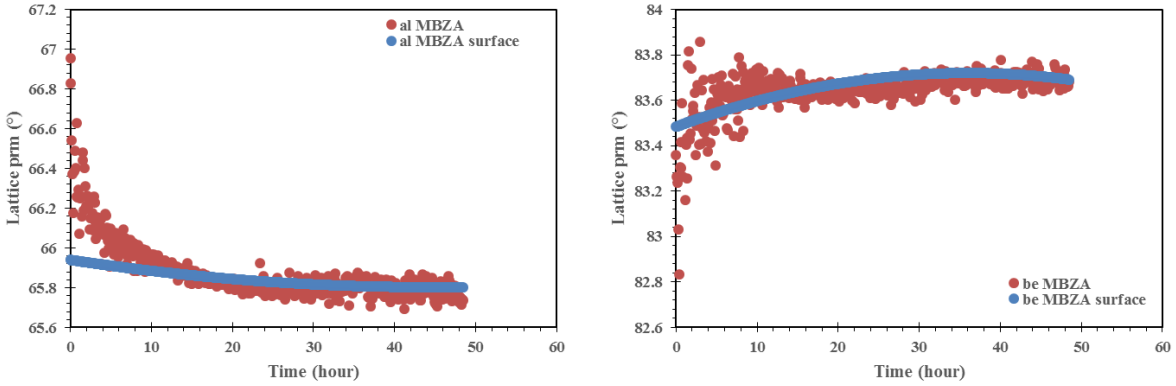

Source: Created by the author.

Figure E.34: a) Comparison between MBZA lattice parameter 'gamma' behaviour determined by sequential Rietveld refinement and surface Rietveld refinement in function of time, for sample LiF/MBZ at 135°C.; b) Comparison between MBZA volume behaviour determined by sequential Rietveld refinement and surface Rietveld refinement in function of time, for sample LiF/MBZ at 135°C.

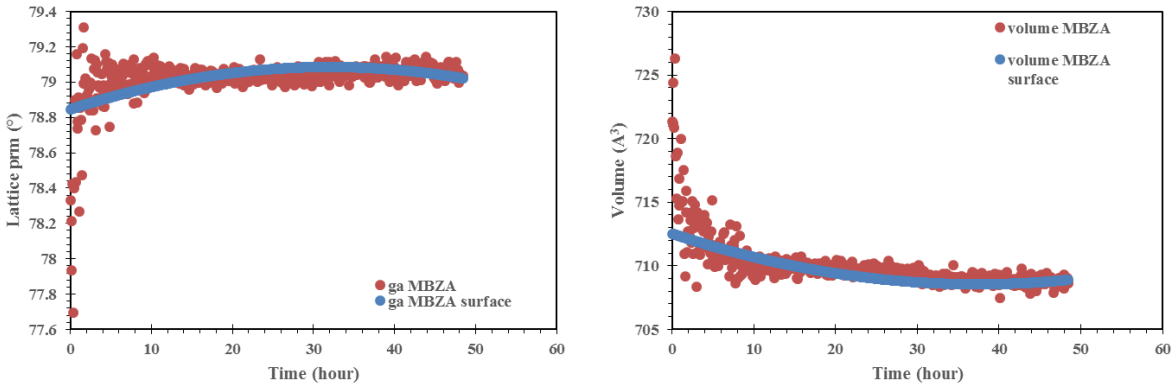

Source: Created by the author.

E.1.1.4. Graphical fits from surface Rietveld refinement at 135°C

Figure E.35: Graphical Rietveld refinements obtained for LiF/MBZ at T = 135 °C and t = 0 hour. Blue curve – observed data; red curve – calculated data; grey curve – residual curves.

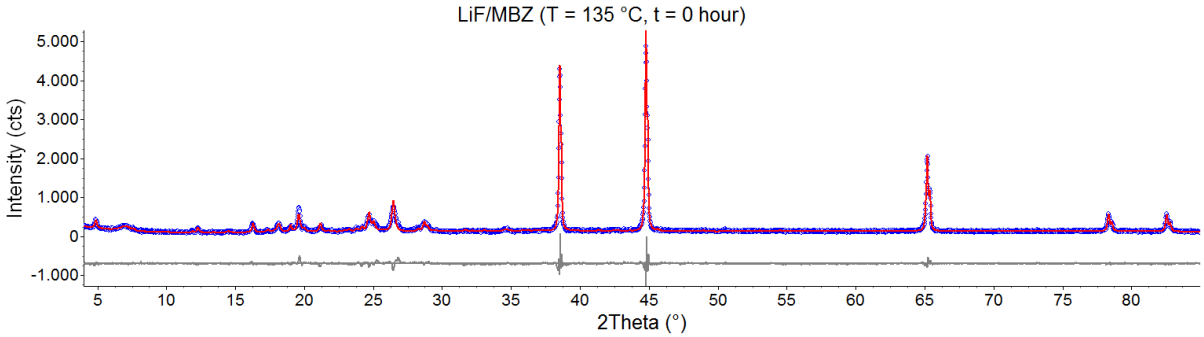

Source: Created by the author.

Figure E.36: Graphical Rietveld refinements obtained for LiF/MBZ at T = 135 °C and t = 10 hours. Blue curve – observed data; red curve – calculated data; grey curve – residual curves.

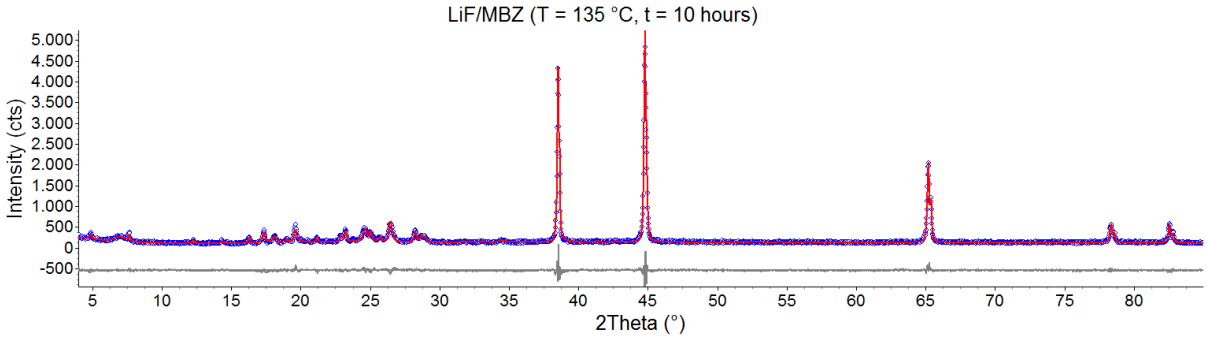

Source: Created by the author.

Figure E.37: Graphical Rietveld refinements obtained for LiF/MBZ at T = 135 °C and t = 19.5 hours. Blue curve – observed data; red curve – calculated data; grey curve – residual curves.

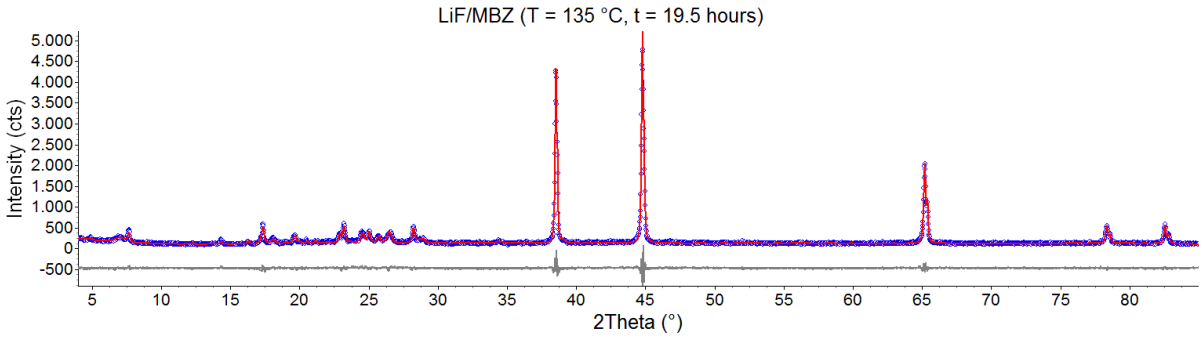

Source: Created by the author.

Figure E.38: Graphical Rietveld refinements obtained for LiF/MBZ at T = 135 °C and t = 29.5 hours. Blue curve – observed data; red curve – calculated data; grey curve – residual curves.

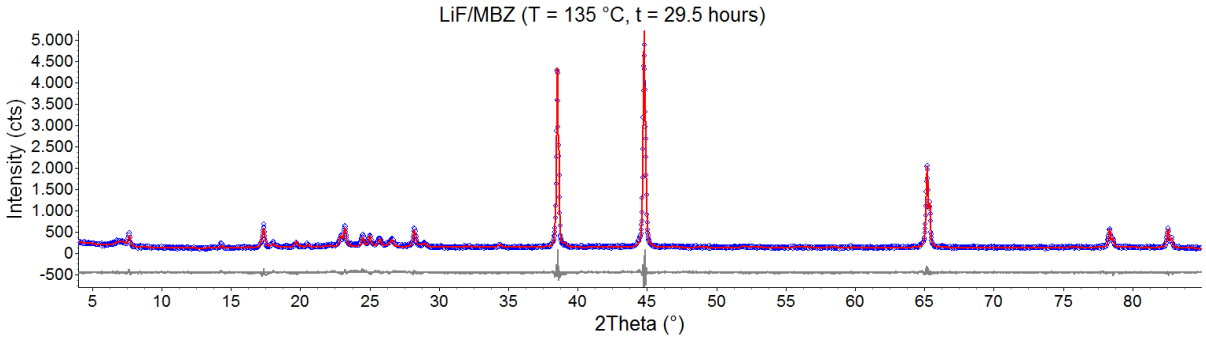

Source: Created by the author.

Figure E.39: Graphical Rietveld refinements obtained for LiF/MBZ at T = 135 °C and t = 39 hours. Blue curve – observed data; red curve – calculated data; grey curve – residual curves.

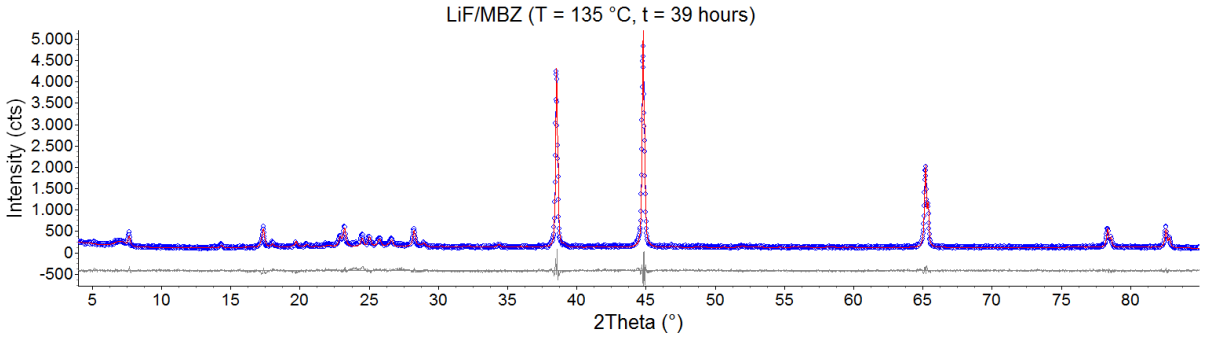

Source: Created by the author.

Figure E.40: Graphical Rietveld refinements obtained for LiF/MBZ at T = 135 °C and t = 48.5 hours. Blue curve – observed data; red curve – calculated data; grey curve – residual curves.

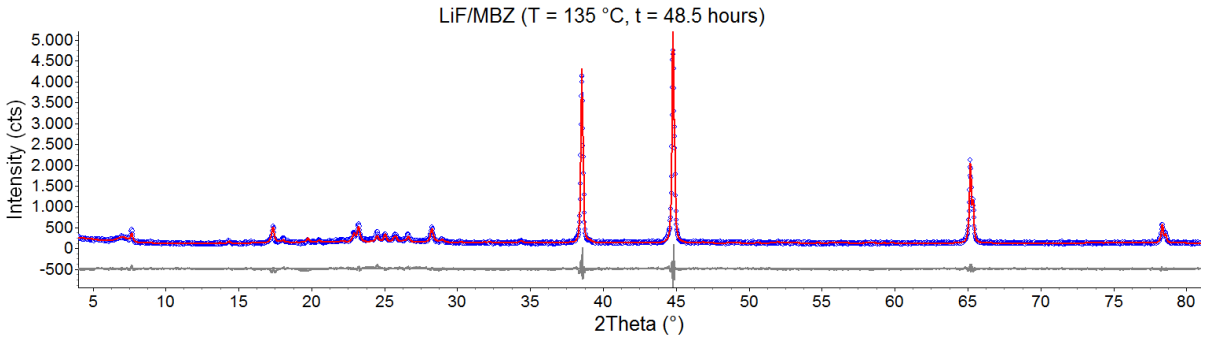

Source: Created by the author.

E.1.1.5. Values calculated at 140°C

Figure E.41: a) Comparison between Rwp (%) behaviour obtained by sequential Rietveld refinement and surface Rietveld refinement in function of time, for sample LiF/MBZ at 140°C; b) Comparison between *gof* behaviour obtained by sequential Rietveld refinement and surface Rietveld refinement in function of time, for sample LiF/MBZ at 140°C.

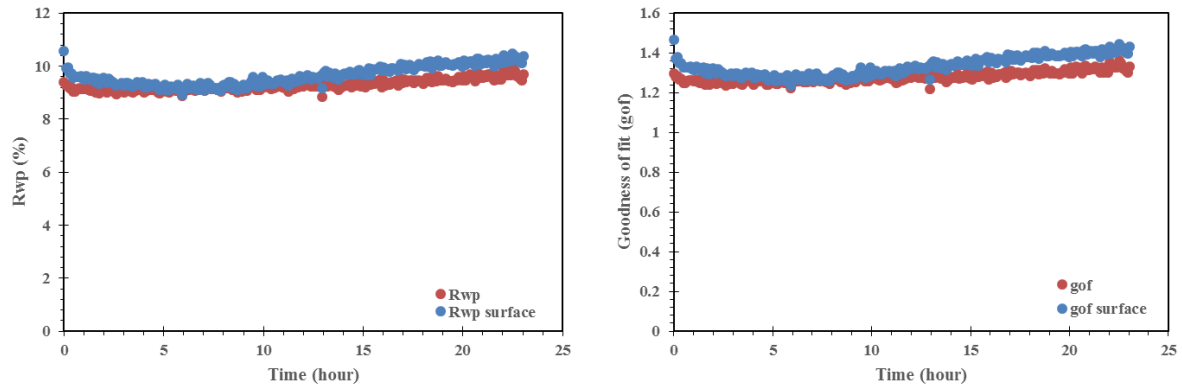

Source: Created by the author.

Figure E.42: a) Comparison between MBZ amorphous quantification calculated by sequential Rietveld refinement and surface Rietveld refinement in function of time, for sample LiF/MBZ at 140°C; b) Comparison between LiF phase quantification calculated by sequential Rietveld refinement and surface Rietveld refinement in function of time, for sample LiF/MBZ at 140°C.

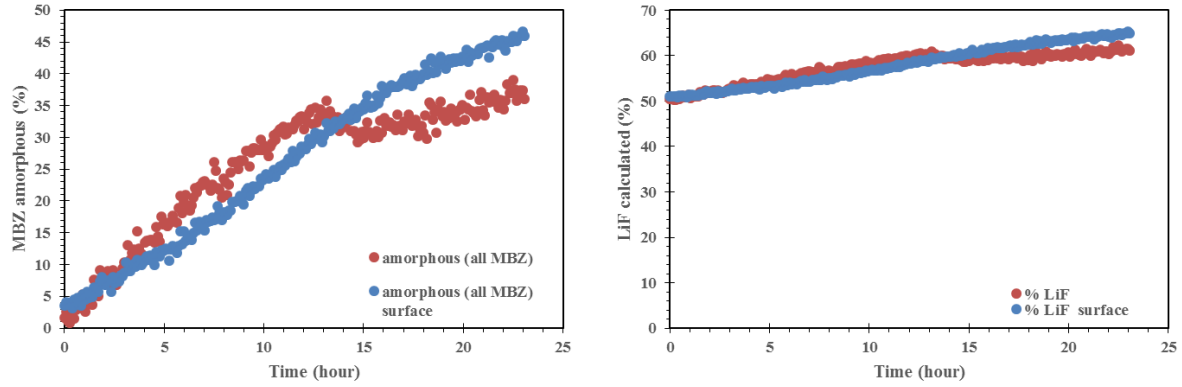

Source: Created by the author.

Figure E.43: a) Comparison between LiF lattice parameter 'a' behaviour determined by sequential Rietveld refinement and surface Rietveld refinement in function of time, for sample LiF/MBZ at 140°C; b) Comparison between LiF volume behaviour determined by sequential Rietveld refinement and surface Rietveld refinement in function of time, for sample LiF/MBZ at 140°C.

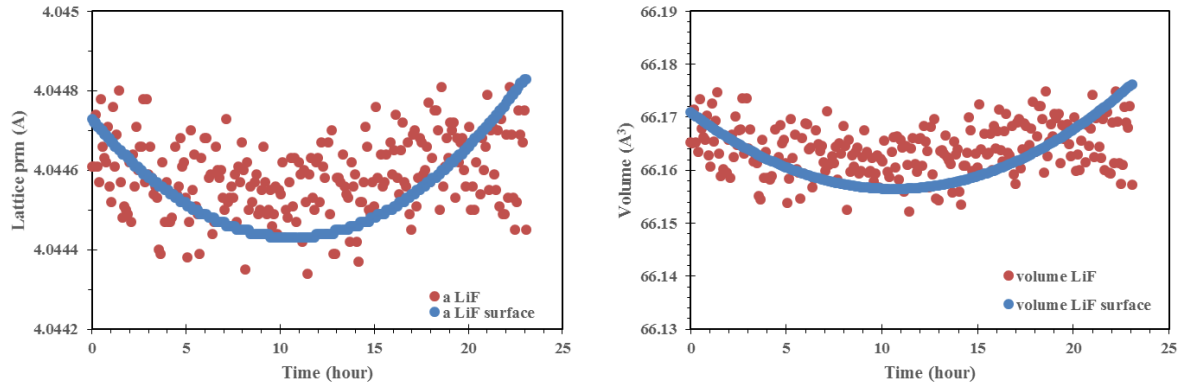

Source: Created by the author.

Figure E.44: a) Comparison between MBZC phase quantification calculated by sequential Rietveld refinement and surface Rietveld refinement in function of time, for sample LiF/MBZ at 140°C; b) Comparison between MBZC phase quantification corrected by internal standard method and calculated by sequential Rietveld refinement and surface Rietveld refinement in function of time, for sample LiF/MBZ at 140°C.

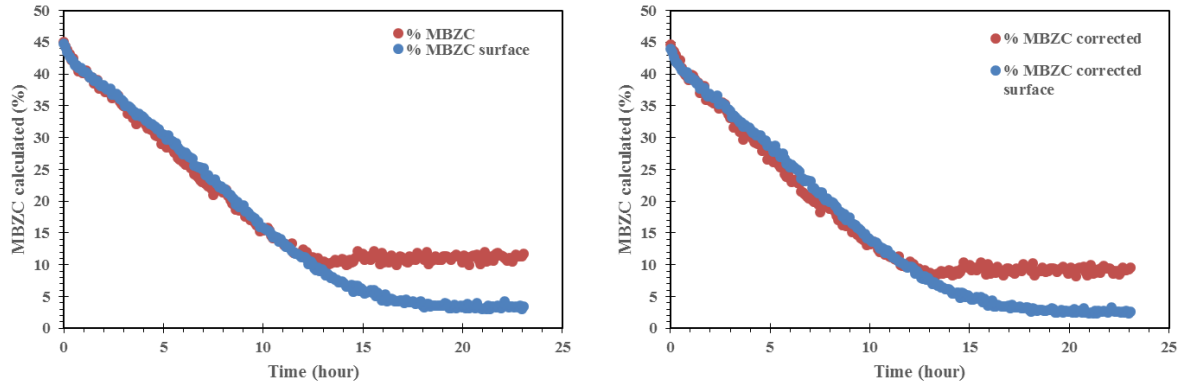

Source: Created by the author.

Figure E.45: a) Comparison between MBZC lattice parameter 'a' behaviour determined by sequential Rietveld refinement and surface Rietveld refinement in function of time, for sample LiF/MBZ at 140°C; b) Comparison between MBZC lattice parameter 'b' behaviour determined by sequential Rietveld refinement and surface Rietveld refinement in function of time, for sample LiF/MBZ at 140°C.

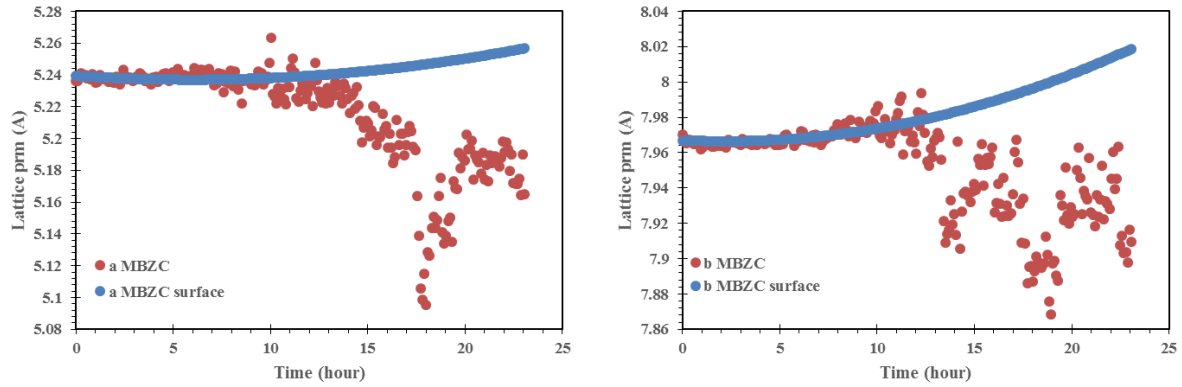

Source: Created by the author.

Figure E.46: a) Comparison between MBZC lattice parameter 'c' behaviour determined by sequential Rietveld refinement and surface Rietveld refinement in function of time, for sample LiF/MBZ at 140°C; b) Comparison between MBZC lattice parameter 'alpha' behaviour determined by sequential Rietveld refinement and surface Rietveld refinement in function of time, for sample LiF/MBZ at 140°C.

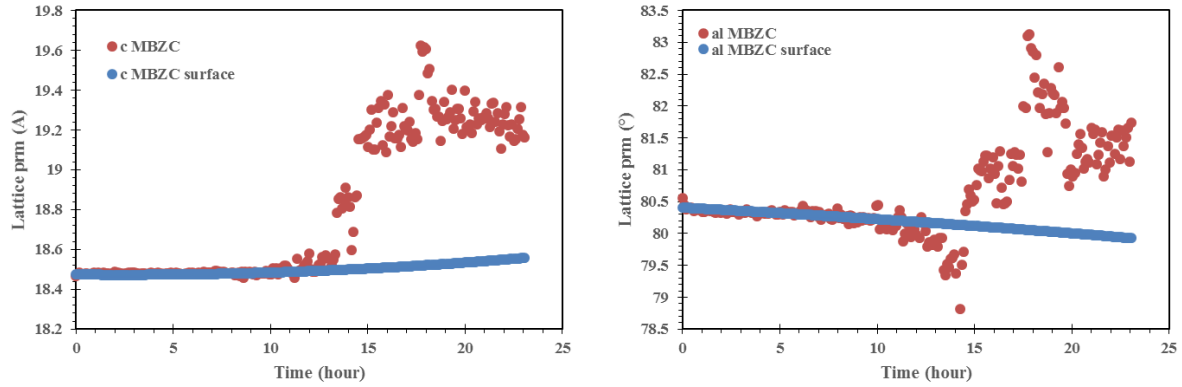

Source: Created by the author.

Figure E.47: a) Comparison between MBZC lattice parameter 'beta' behaviour determined by sequential Rietveld refinement and surface Rietveld refinement in function of time, for sample LiF/MBZ at 140°C; b) Comparison between MBZC lattice parameter 'gamma' behaviour determined by sequential Rietveld refinement and surface Rietveld refinement in function of time, for sample LiF/MBZ at 140°C.

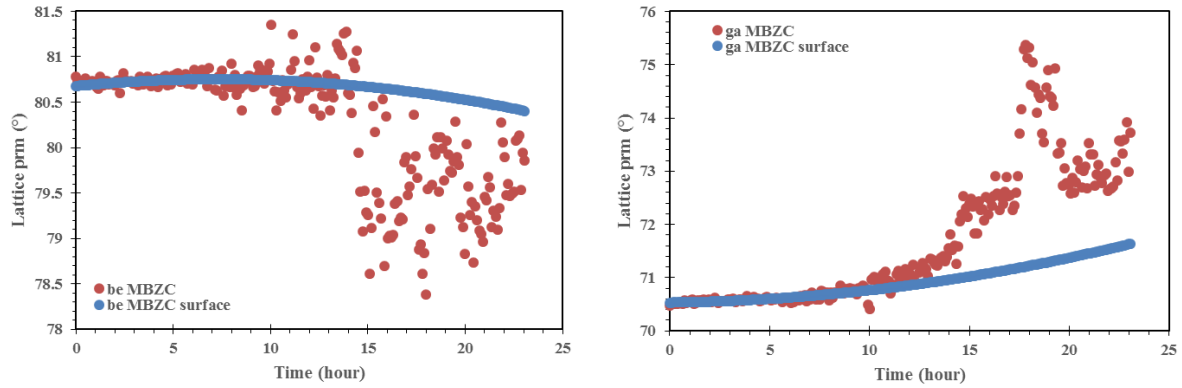

Source: Created by the author.

Figure E.48: a) Comparison between MBZC volume behaviour determined by sequential Rietveld refinement and surface Rietveld refinement in function of time, for sample LiF/MBZ at 140°C; b) Comparison between MBZA phase quantification calculated by sequential Rietveld refinement and surface Rietveld refinement in function of time, for sample LiF/MBZ at 140°C.

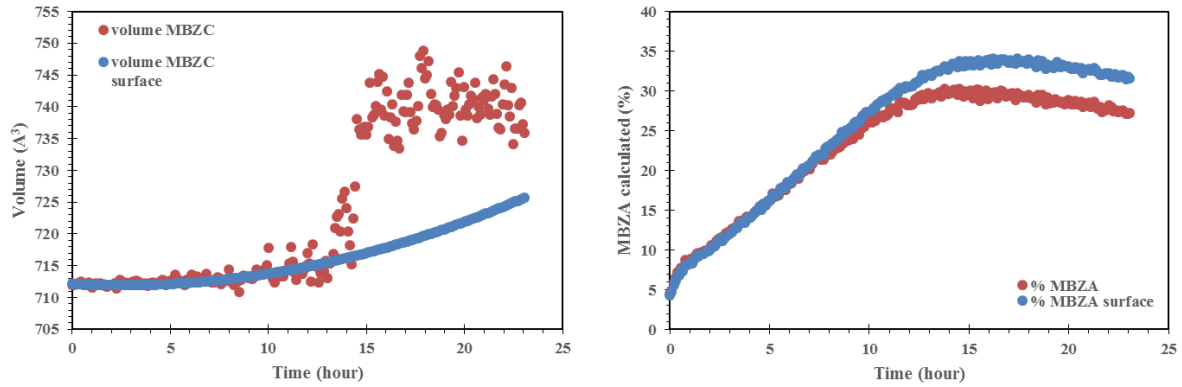

Source: Created by the author.

Figure E.49: a) Comparison between MBZA phase quantification corrected by internal standard method and calculated by sequential Rietveld refinement and surface Rietveld refinement in function of time, for sample LiF/MBZ at 140°C; b) Comparison between MBZA lattice parameter 'a' behaviour determined by sequential Rietveld refinement and surface Rietveld refinement in function of time, for sample LiF/MBZ at 140°C.

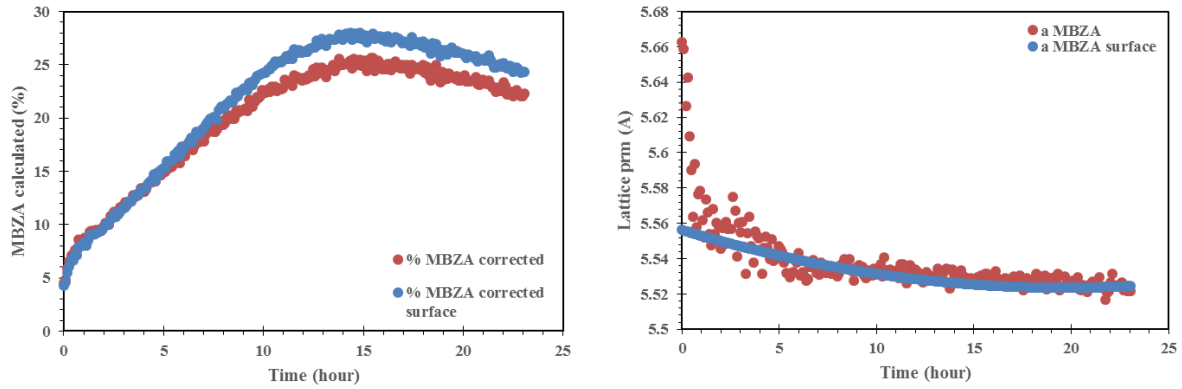

Source: Created by the author.

Figure E.50: a) Comparison between MBZA lattice parameter 'b' behaviour determined by sequential Rietveld refinement and surface Rietveld refinement in function of time, for sample LiF/MBZ at 140°C; b) Comparison between MBZA lattice parameter 'c' behaviour determined by sequential Rietveld refinement and surface Rietveld refinement in function of time, for sample LiF/MBZ at 140°C.

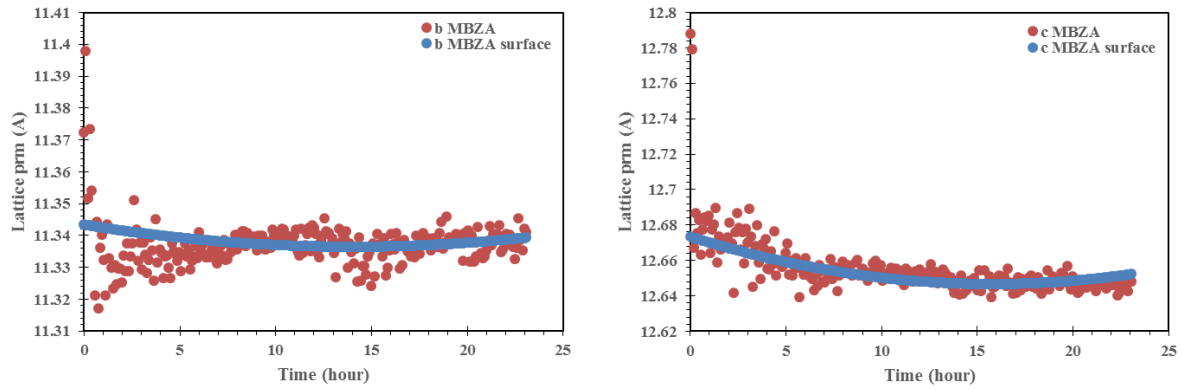

Source: Created by the author.

Figure E.51: a) Comparison between MBZA lattice parameter 'alpha' behaviour determined by sequential Rietveld refinement and surface Rietveld refinement in function of time, for sample LiF/MBZ at 140°C.; b) Comparison between MBZA lattice parameter 'beta' behaviour determined by sequential Rietveld refinement and surface Rietveld refinement in function of time, for sample LiF/MBZ at 140°C.

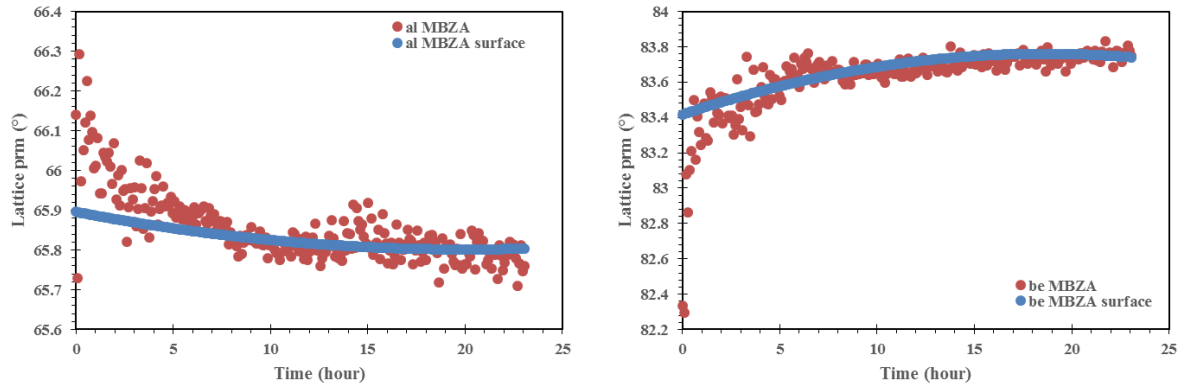

Source: Created by the author.

Figure E.52: a) Comparison between MBZA lattice parameter 'gamma' behaviour determined by sequential Rietveld refinement and surface Rietveld refinement in function of time, for sample LiF/MBZ at 140°C; b) Comparison between MBZA volume behaviour determined by sequential Rietveld refinement and surface Rietveld refinement in function of time, for sample LiF/MBZ at 140°C.

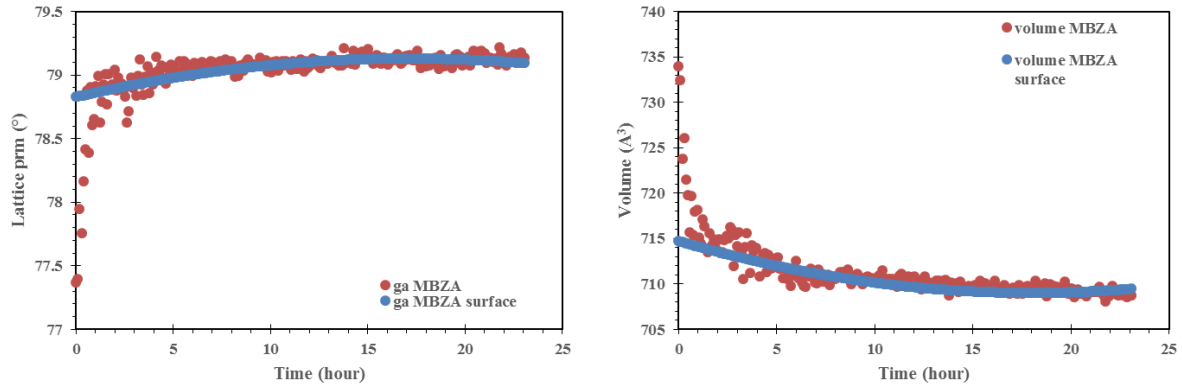

Source: Created by the author.

E.1.1.6. Graphical fits from surface Rietveld refinement at 140°C

Figure E.53: Graphical Rietveld refinements obtained for LiF/MBZ at T = 140 °C and t = 0 hour. Blue curve – observed data; red curve – calculated data; grey curve – residual curves.

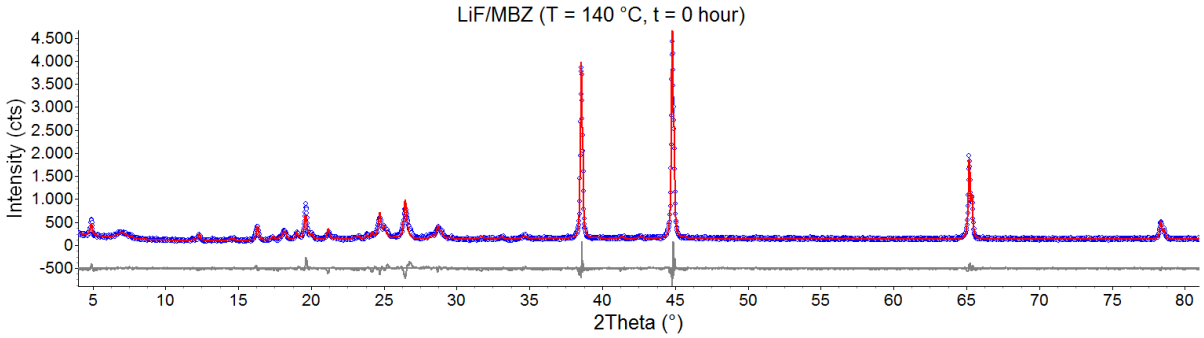

Source: Created by the author.

Figure E.54: Graphical Rietveld refinements obtained for LiF/MBZ at T = 140 °C and t =11.5 hours. Blue curve – observed data; red curve – calculated data; grey curve – residual curves.

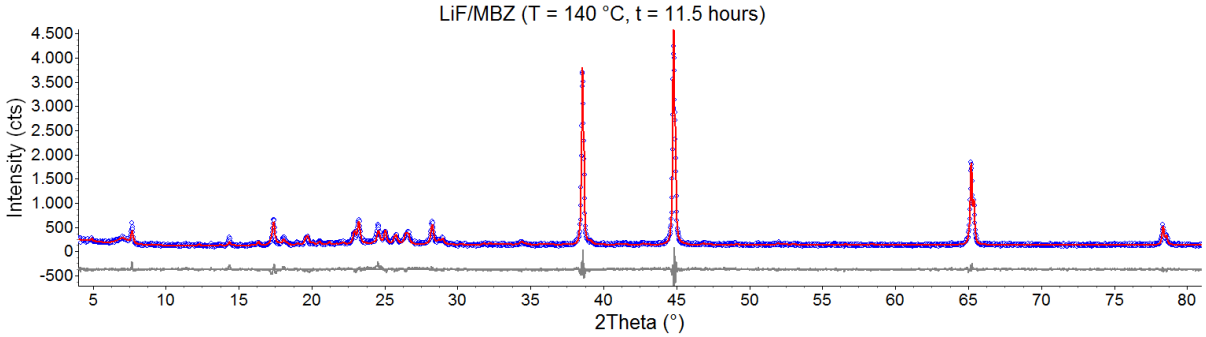

Source: Created by the author.

Figure E.55: Graphical Rietveld refinements obtained for LiF/MBZ at T = 140 °C and t =23 hours. Blue curve – observed data; red curve – calculated data; grey curve – residual curves.

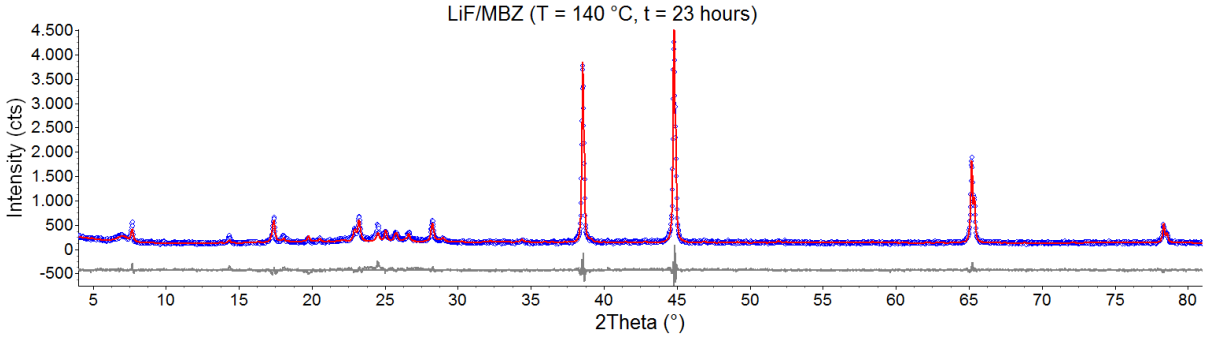

Source: Created by the author.

E.1.1.7. Values calculated at 145°C

Figure E.56: a) Comparison between Rwp (%) behaviour obtained by sequential Rietveld refinement and surface Rietveld refinement in function of time, for sample LiF/MBZ at 145°C; b) Comparison between *gof* behaviour obtained by sequential Rietveld refinement and surface Rietveld refinement in function of time, for sample LiF/MBZ at 145°C.

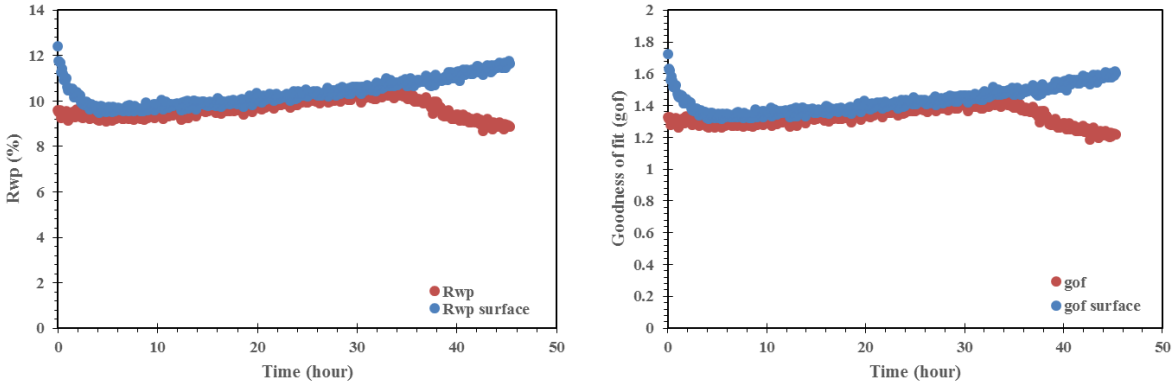

Source: Created by the author.

Figure E.57: a) Comparison between MBZ amorphous quantification calculated by sequential Rietveld refinement and surface Rietveld refinement in function of time, for sample LiF/MBZ at 145°C; b) Comparison between LiF phase quantification calculated by sequential Rietveld refinement and surface Rietveld refinement in function of time, for sample LiF/MBZ at 145°C.

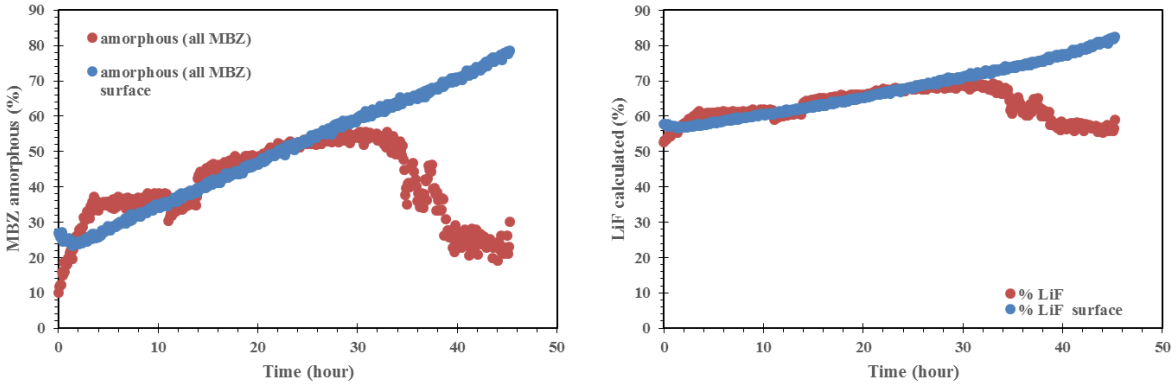

Source: Created by the author.

Figure E.58: a) Comparison between LiF lattice parameter 'a' behaviour determined by sequential Rietveld refinement and surface Rietveld refinement in function of time, for sample LiF/MBZ at 145°C; b) Comparison between LiF volume behaviour determined by sequential Rietveld refinement and surface Rietveld refinement in function of time, for sample LiF/MBZ at 145°C.

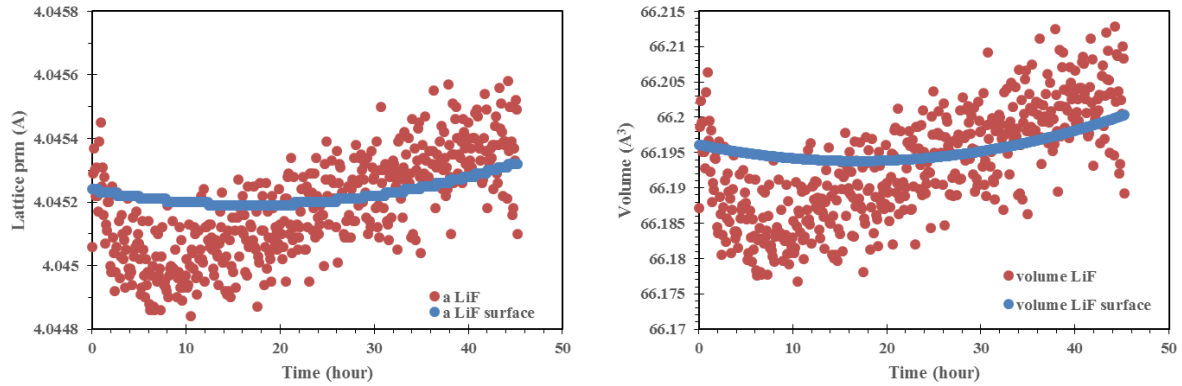

Source: Created by the author.

Figure E.59: a) Comparison between MBZC phase quantification calculated by sequential Rietveld refinement and surface Rietveld refinement in function of time, for sample LiF/MBZ at 145°C; b) Comparison between MBZC phase quantification corrected by internal standard method and calculated by sequential Rietveld refinement and surface Rietveld refinement in function of time, for sample LiF/MBZ at 145°C.

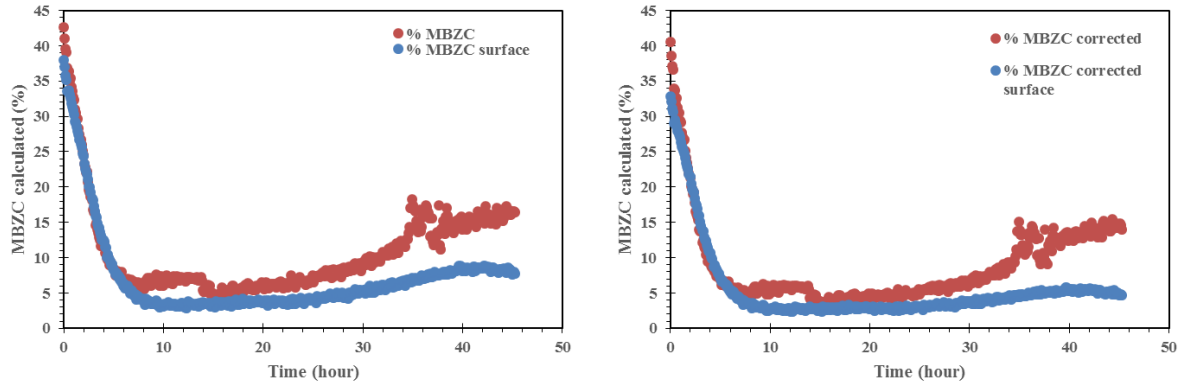

Source: Created by the author.

E.1.1.7. Values calculated at 145°C

Figure E.60: a) Comparison between MBZC lattice parameter 'a' behaviour determined by sequential Rietveld refinement and surface Rietveld refinement in function of time, for sample LiF/MBZ at 145°C; b) Comparison between MBZC lattice parameter 'b' behaviour determined by sequential Rietveld refinement and surface Rietveld refinement in function of time, for sample LiF/MBZ at 145°C.

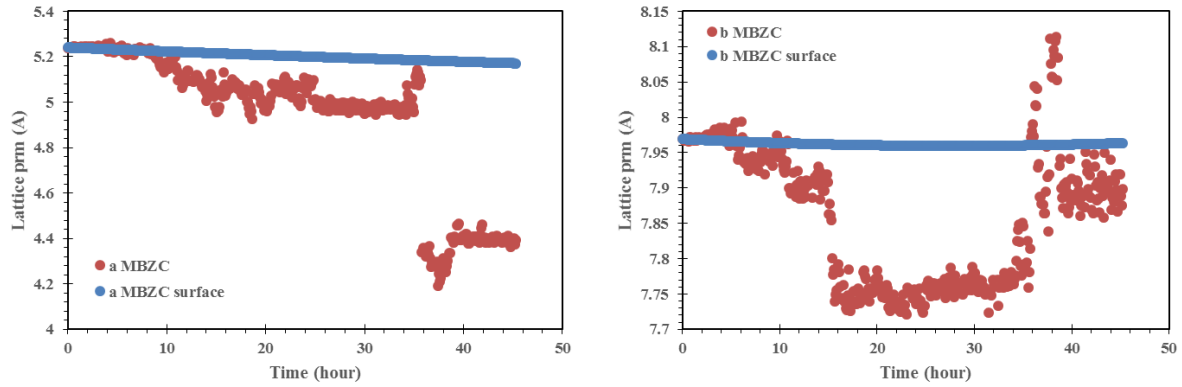

Source: Created by the author.

Figure E.61: a) Comparison between MBZC lattice parameter 'c' behaviour determined by sequential Rietveld refinement and surface Rietveld refinement in function of time, for sample LiF/MBZ at 145°C; b) Comparison between MBZC lattice parameter 'alpha' behaviour determined by sequential Rietveld refinement and surface Rietveld refinement in function of time, for sample LiF/MBZ at 145°C.

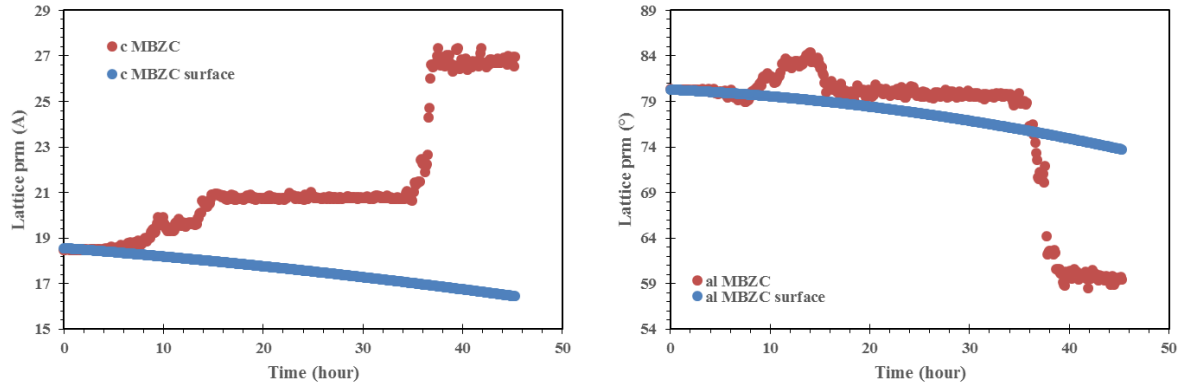

Source: Created by the author.

E.1.1.7. Values calculated at 145°C

Figure E.62: a) Comparison between MBZC lattice parameter 'beta' behaviour determined by sequential Rietveld refinement and surface Rietveld refinement in function of time, for sample LiF/MBZ at 145°C; b) Comparison between MBZC lattice parameter 'gamma' behaviour determined by sequential Rietveld refinement and surface Rietveld refinement in function of time, for sample LiF/MBZ at 145°C.

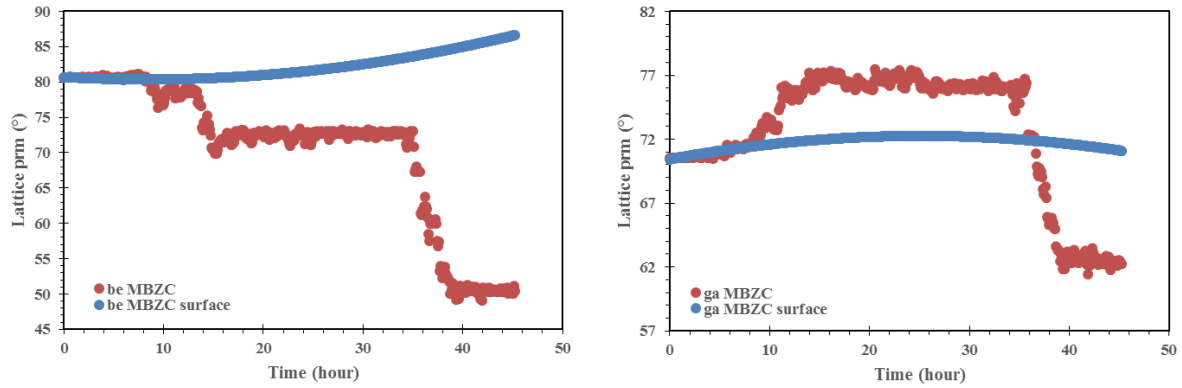

Source: Created by the author.

Figure E.63: a) Comparison between MBZC volume behaviour determined by sequential Rietveld refinement and surface Rietveld refinement in function of time, for sample LiF/MBZ at 145°C; b) Comparison between MBZA phase quantification calculated by sequential Rietveld refinement and surface Rietveld refinement in function of time, for sample LiF/MBZ at 145°C.

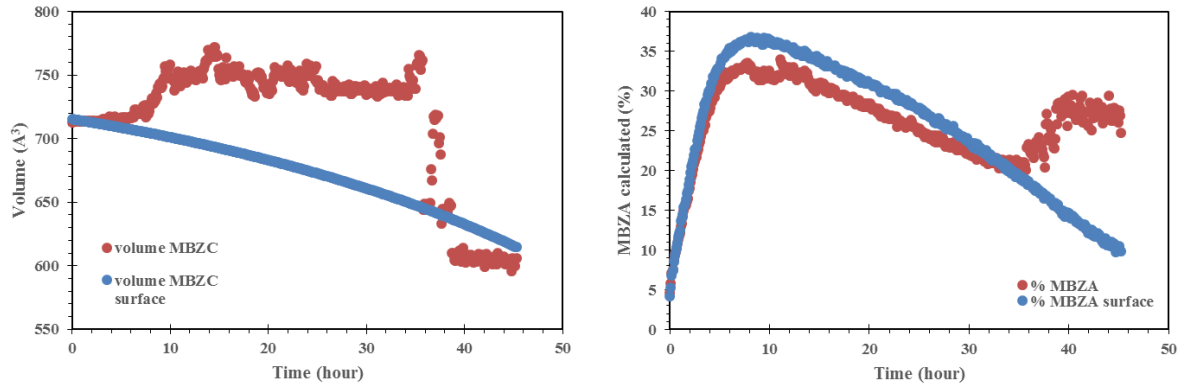

Source: Created by the author.

Figure E.64: a) Comparison between MBZA phase quantification corrected by internal standard method and calculated by sequential Rietveld refinement and surface Rietveld refinement in function of time, for sample LiF/MBZ at 145°C; b) Comparison between MBZA lattice parameter 'a' behaviour determined by sequential Rietveld refinement and surface Rietveld refinement in function of time, for sample LiF/MBZ at 145°C.

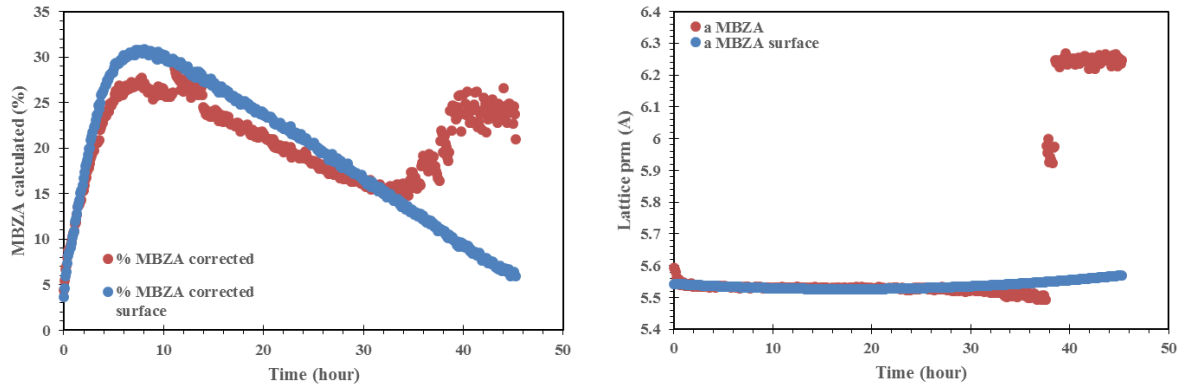

Source: Created by the author.

Figure E.65: a) Comparison between MBZA lattice parameter 'b' behaviour determined by sequential Rietveld refinement and surface Rietveld refinement in function of time, for sample LiF/MBZ at 145°C; b) Comparison between MBZA lattice parameter 'c' behaviour determined by sequential Rietveld refinement and surface Rietveld refinement in function of time, for sample LiF/MBZ at 145°C.

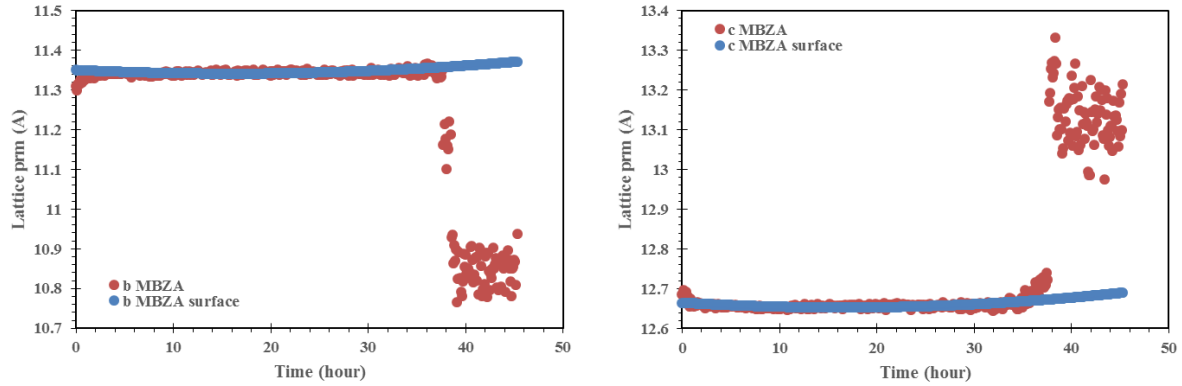

Source: Created by the author.

Figure E.66: a) Comparison between MBZA lattice parameter 'alpha' behaviour determined by sequential Rietveld refinement and surface Rietveld refinement in function of time, for sample LiF/MBZ at 145°C.; b) Comparison between MBZA lattice parameter 'beta' behaviour determined by sequential Rietveld refinement and surface Rietveld refinement in function of time, for sample LiF/MBZ at 145°C.

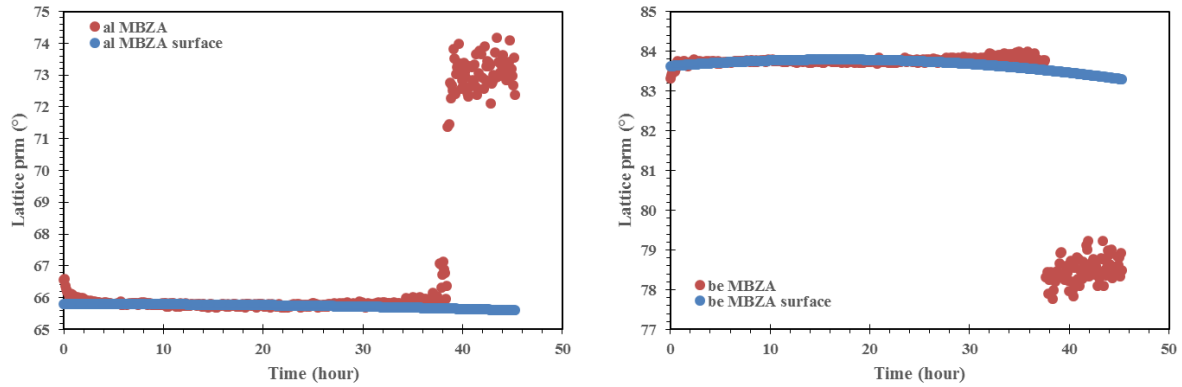

Source: Created by the author.

Figure E.67: a) Comparison between MBZA lattice parameter 'gamma' behaviour determined by sequential Rietveld refinement and surface Rietveld refinement in function of time, for sample LiF/MBZ at 145°C; b) Comparison between MBZA volume behaviour determined by sequential Rietveld refinement and surface Rietveld refinement in function of time, for sample LiF/MBZ at 145°C.

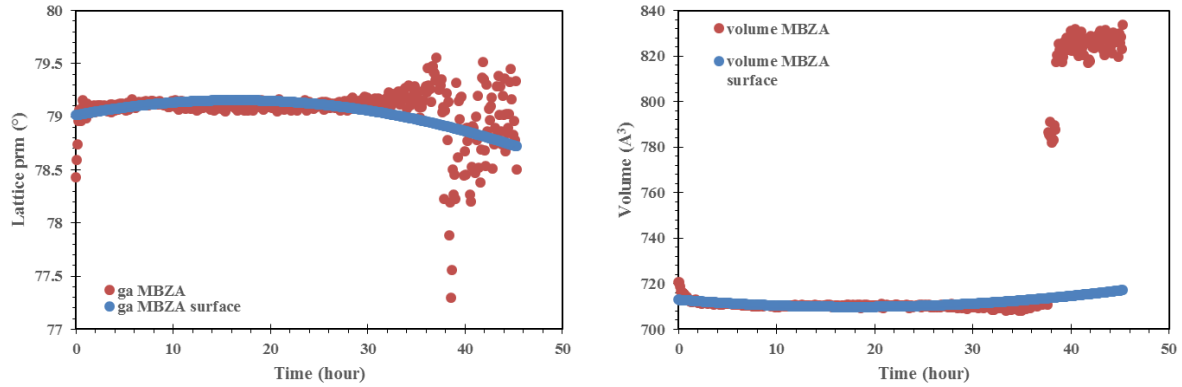

Source: Created by the author.

E.1.1.8. Graphical fits from surface Rietveld refinement at 145°C

Figure E.68: Graphical Rietveld refinements obtained for LiF/MBZ at T = 145 °C and t = 0 hour. Blue curve – observed data; red curve – calculated data; grey curve – residual curves.

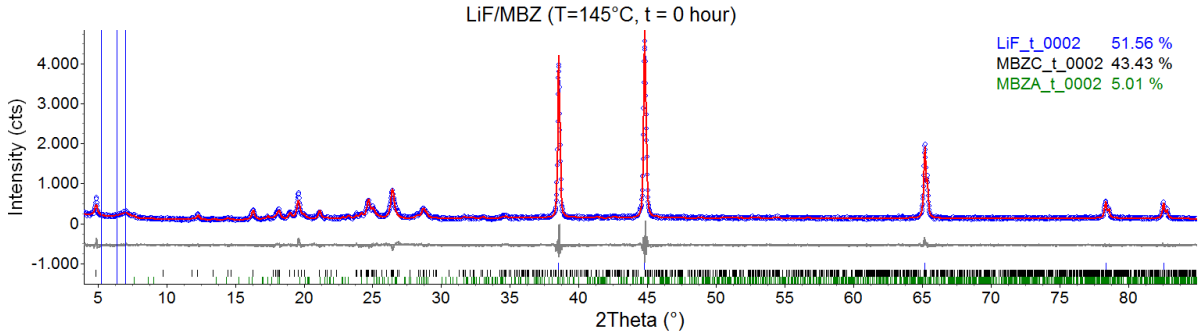

Source: Created by the author.

Figure E.69: Graphical Rietveld refinements obtained for LiF/MBZ at T = 145 °C and t = 22.5 hour. Blue curve – observed data; red curve – calculated data; grey curve – residual curves.

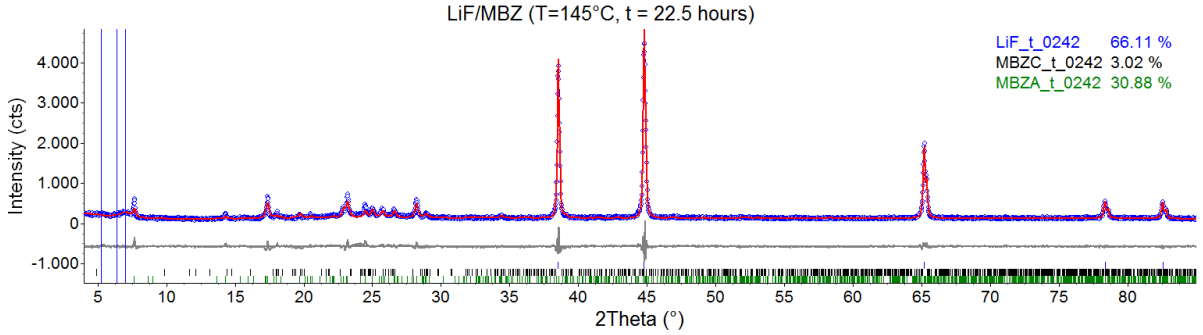

Source: Created by the author.

Figure E.70: Graphical Rietveld refinements obtained for LiF/MBZ at T = 145 °C and t = 45.5 hour. Blue curve – observed data; red curve – calculated data; grey curve – residual curves.

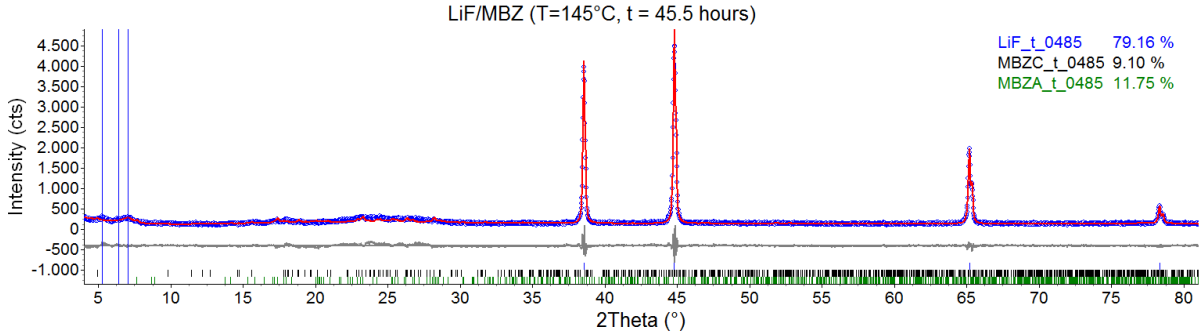

Source: Created by the author.

E.1.1.9. Values calculated at 150°C

Figure E.71: a) Comparison between Rwp (%) behaviour obtained by sequential Rietveld refinement and surface Rietveld refinement in function of time, for sample LiF/MBZ at 150°C; b) Comparison between *gof* behaviour obtained by sequential Rietveld refinement and surface Rietveld refinement in function of time, for sample LiF/MBZ at 150°C.

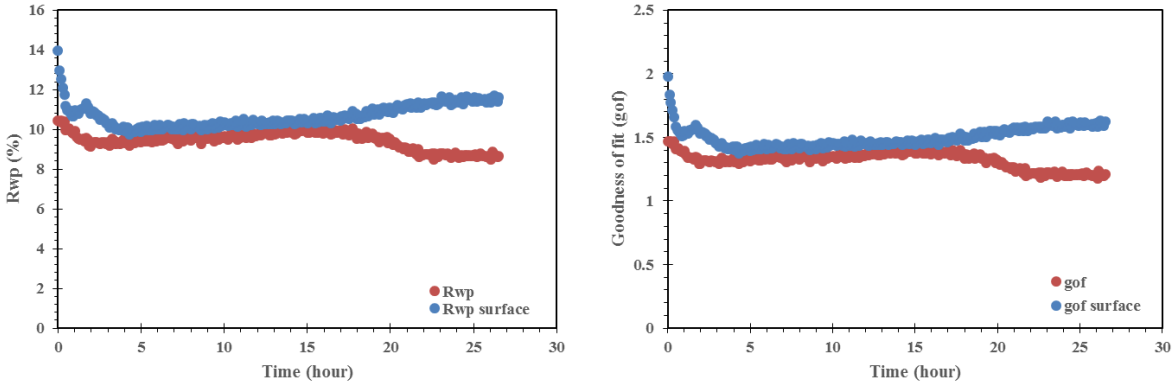

Source: Created by the author.

Figure E.72: a) Comparison between MBZ amorphous quantification calculated by sequential Rietveld refinement and surface Rietveld refinement in function of time, for sample LiF/MBZ at 150°C; b) Comparison between LiF phase quantification calculated by sequential Rietveld refinement and surface Rietveld refinement in function of time, for sample LiF/MBZ at 150°C.

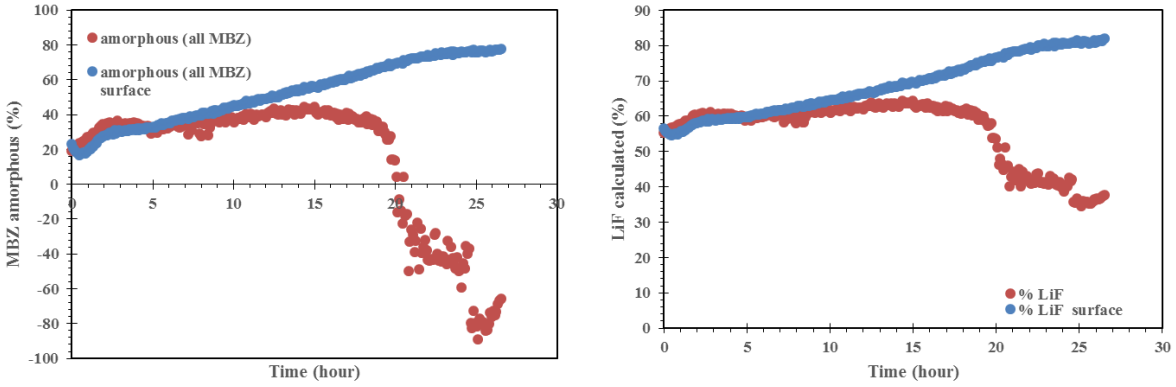

Source: Created by the author.

Figure E.73: a) Comparison between LiF lattice parameter 'a' behaviour determined by sequential Rietveld refinement and surface Rietveld refinement in function of time, for sample LiF/MBZ at 150°C; b) Comparison between LiF volume behaviour determined by sequential Rietveld refinement and surface Rietveld refinement in function of time, for sample LiF/MBZ at 150°C.

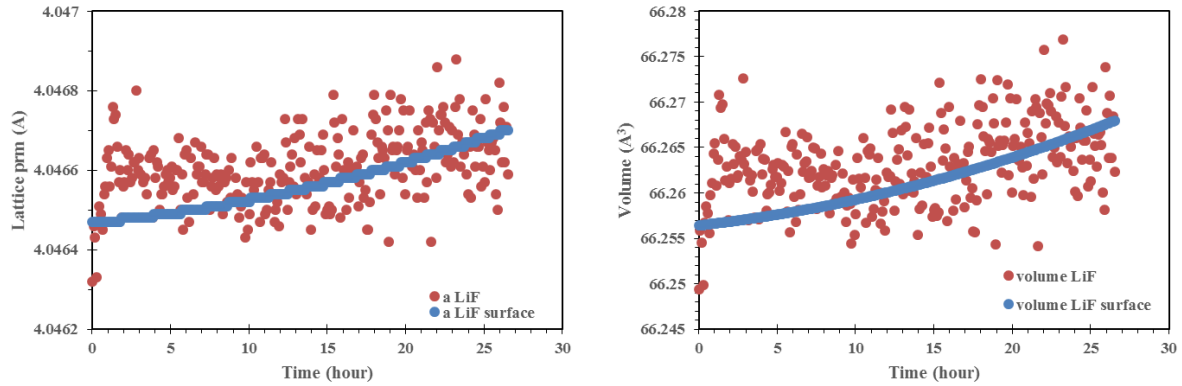

Source: Created by the author.

Figure E.74: a) Comparison between MBZC phase quantification calculated by sequential Rietveld refinement and surface Rietveld refinement in function of time, for sample LiF/MBZ at 150°C; b) Comparison between MBZC phase quantification corrected by internal standard method and calculated by sequential Rietveld refinement and surface Rietveld refinement in function of time, for sample LiF/MBZ at 150°C.

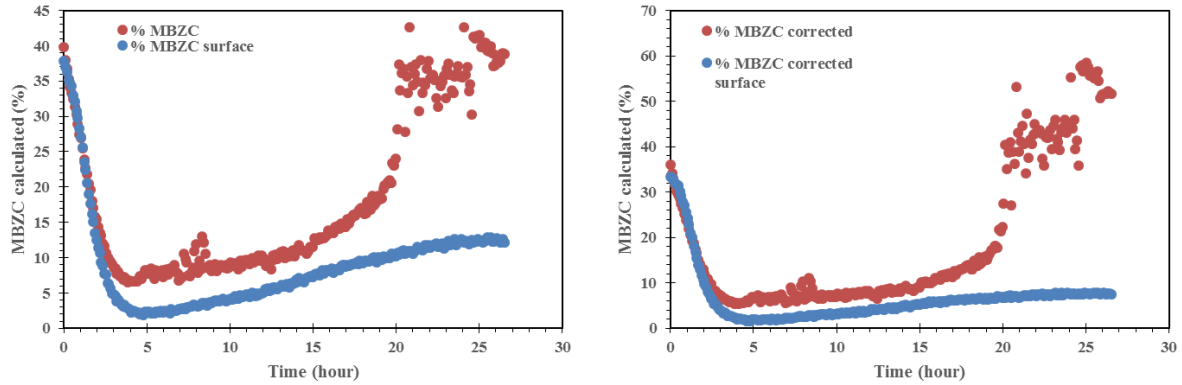

Source: Created by the author.

Figure E.75: a) Comparison between MBZC lattice parameter 'a' behaviour determined by sequential Rietveld refinement and surface Rietveld refinement in function of time, for sample LiF/MBZ at 150°C; b) Comparison between MBZC lattice parameter 'b' behaviour determined by sequential Rietveld refinement and surface Rietveld refinement in function of time, for sample LiF/MBZ at 150°C.

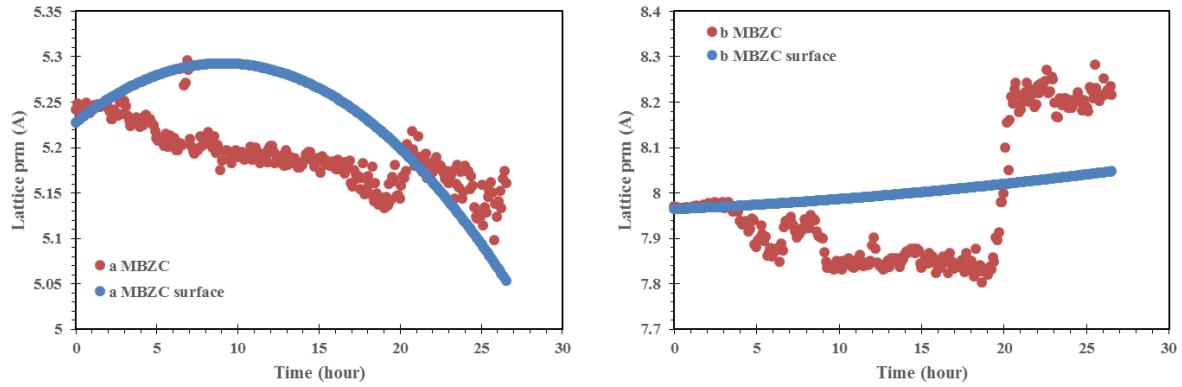

Source: Created by the author.

Figure E.76: a) Comparison between MBZC lattice parameter 'c' behaviour determined by sequential Rietveld refinement and surface Rietveld refinement in function of time, for sample LiF/MBZ at 150°C; b) Comparison between MBZC lattice parameter 'alpha' behaviour determined by sequential Rietveld refinement and surface Rietveld refinement in function of time, for sample LiF/MBZ at 150°C.

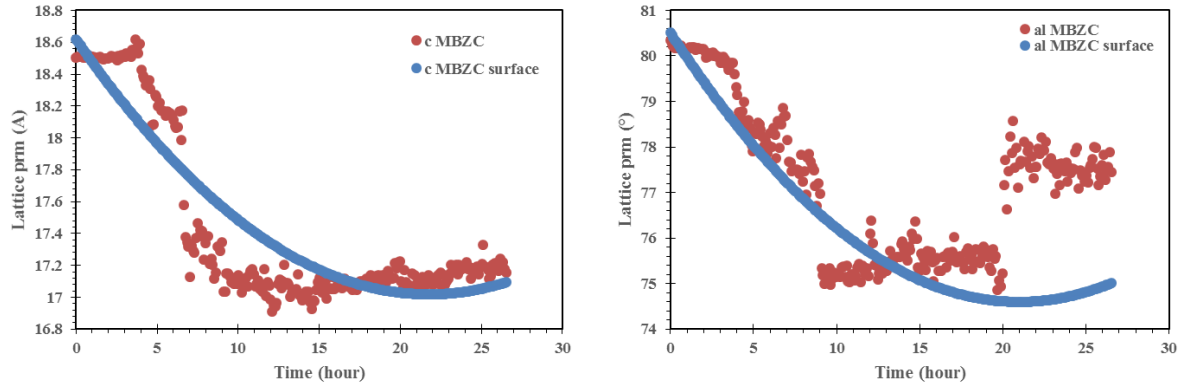

Source: Created by the author.

Figure E.77: a) Comparison between MBZC lattice parameter 'beta' behaviour determined by sequential Rietveld refinement and surface Rietveld refinement in function of time, for sample LiF/MBZ at 150°C; b) Comparison between MBZC lattice parameter 'gamma' behaviour determined by sequential Rietveld refinement and surface Rietveld refinement in function of time, for sample LiF/MBZ at 150°C.

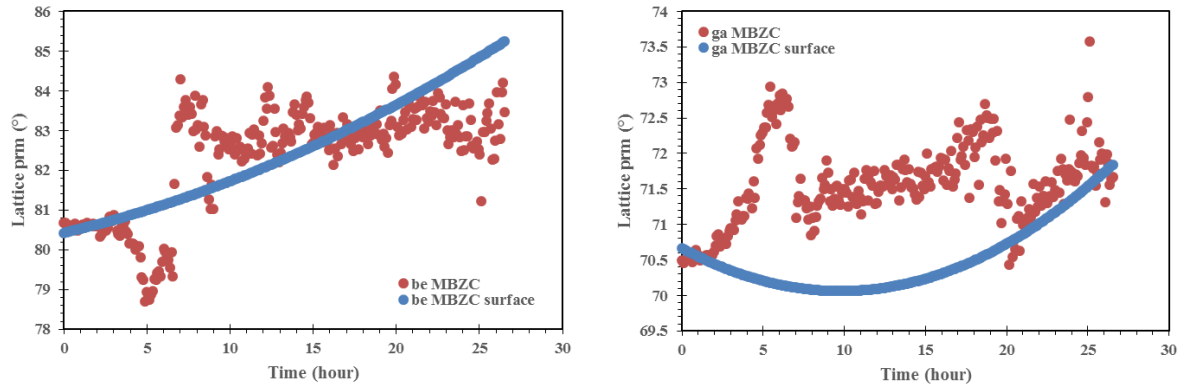

Source: Created by the author.

Figure E.78: a) Comparison between MBZC volume behaviour determined by sequential Rietveld refinement and surface Rietveld refinement in function of time, for sample LiF/MBZ at 150°C; b) Comparison between MBZA phase quantification calculated by sequential Rietveld refinement and surface Rietveld refinement in function of time, for sample LiF/MBZ at 150°C.

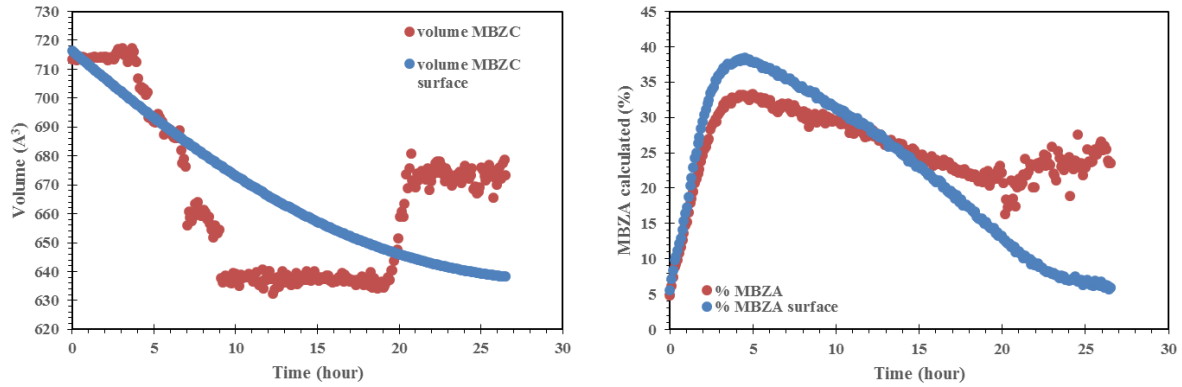

Source: Created by the author.

E.1.1.9. Values calculated at 150°C

Figure E.79: a) Comparison between MBZA phase quantification corrected by internal standard method and calculated by sequential Rietveld refinement and surface Rietveld refinement in function of time, for sample LiF/MBZ at 150°C; b) Comparison between MBZA lattice parameter 'a' behaviour determined by sequential Rietveld refinement and surface Rietveld refinement in function of time, for sample LiF/MBZ at 150°C.

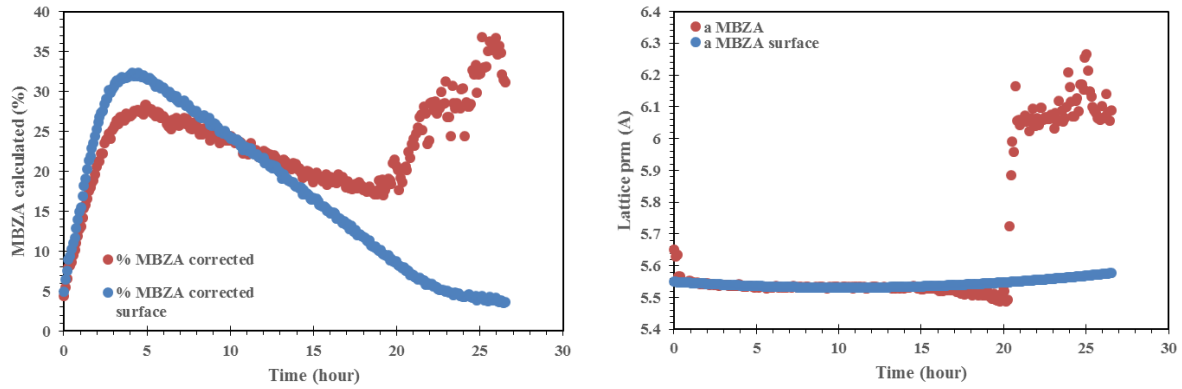

Source: Created by the author.

Figure E.80: a) Comparison between MBZA lattice parameter 'b' behaviour determined by sequential Rietveld refinement and surface Rietveld refinement in function of time, for sample LiF/MBZ at 150°C; b) Comparison between MBZA lattice parameter 'c' behaviour determined by sequential Rietveld refinement and surface Rietveld refinement in function of time, for sample LiF/MBZ at 150°C.

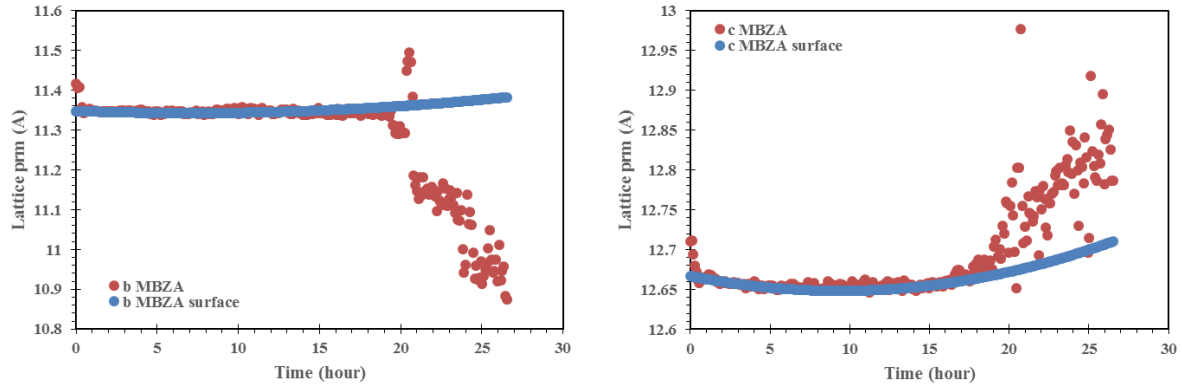

Source: Created by the author.

Figure E.81: a) Comparison between MBZA lattice parameter 'alpha' behaviour determined by sequential Rietveld refinement and surface Rietveld refinement in function of time, for sample LiF/MBZ at 150°C.; b) Comparison between MBZA lattice parameter 'beta' behaviour determined by sequential Rietveld refinement and surface Rietveld refinement in function of time, for sample LiF/MBZ at 150°C.

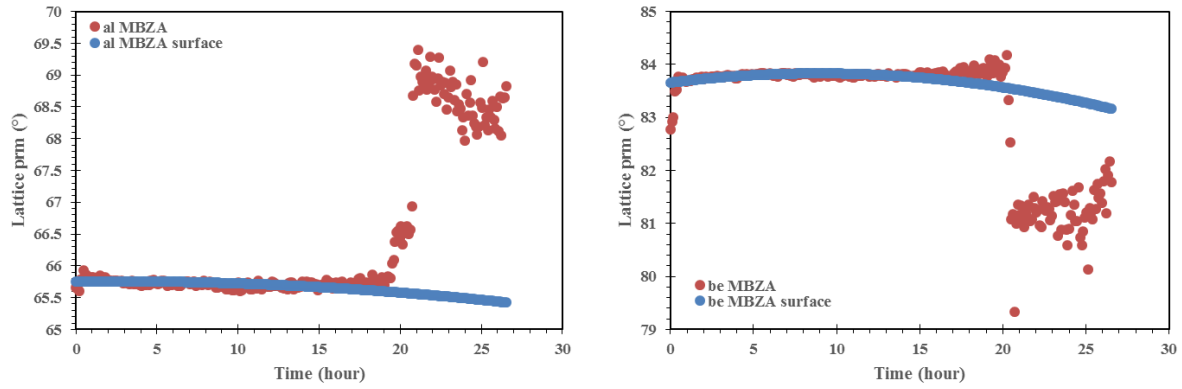

Source: Created by the author.

Figure E.82: a) Comparison between MBZA lattice parameter 'gamma' behaviour determined by sequential Rietveld refinement and surface Rietveld refinement in function of time, for sample LiF/MBZ at 150°C; b) Comparison between MBZA volume behaviour determined by sequential Rietveld refinement and surface Rietveld refinement in function of time, for sample LiF/MBZ at 150°C.

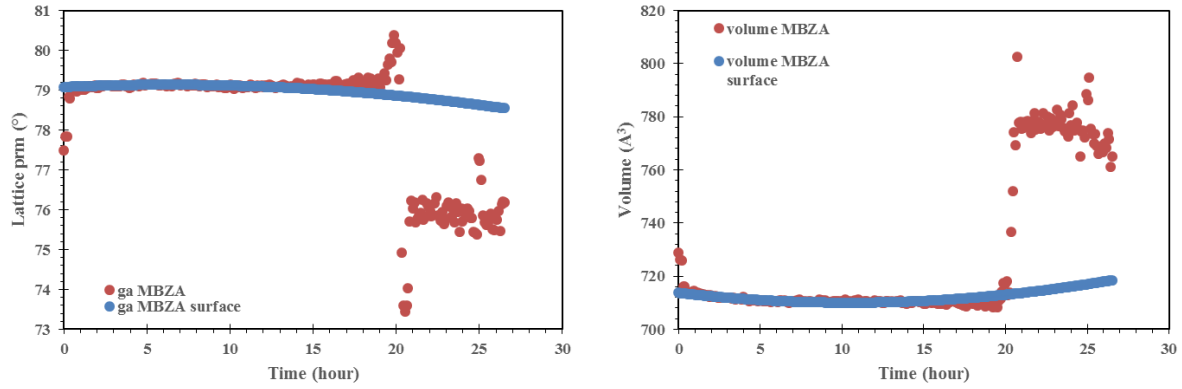

Source: Created by the author.

E.1.1.10. Graphical fits from surface Rietveld refinement at 150°C

Figure E.83: Graphical Rietveld refinements obtained for LiF/MBZ at T = 150 °C and t = 0 hour. Blue curve – observed data; red curve – calculated data; grey curve – residual curves.

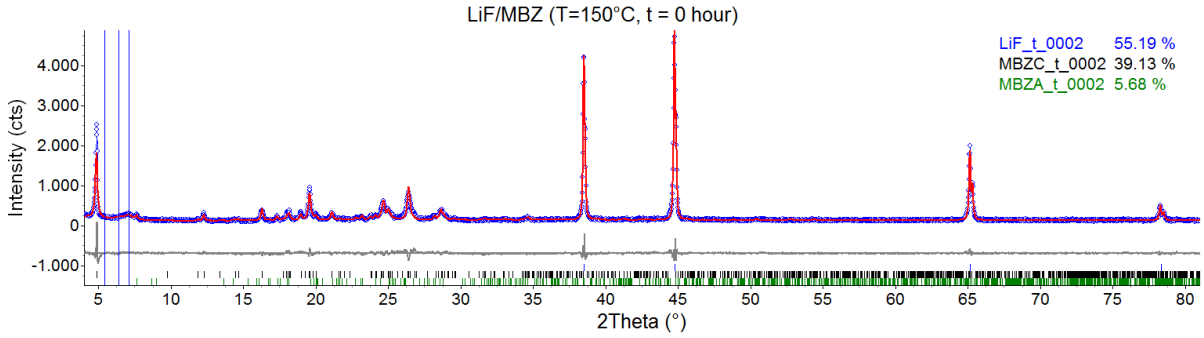

Source: Created by the author.

Figure E.84: Graphical Rietveld refinements obtained for LiF/MBZ at T = 150 °C and t = 13 hours. Blue curve – observed data; red curve – calculated data; grey curve – residual curves.

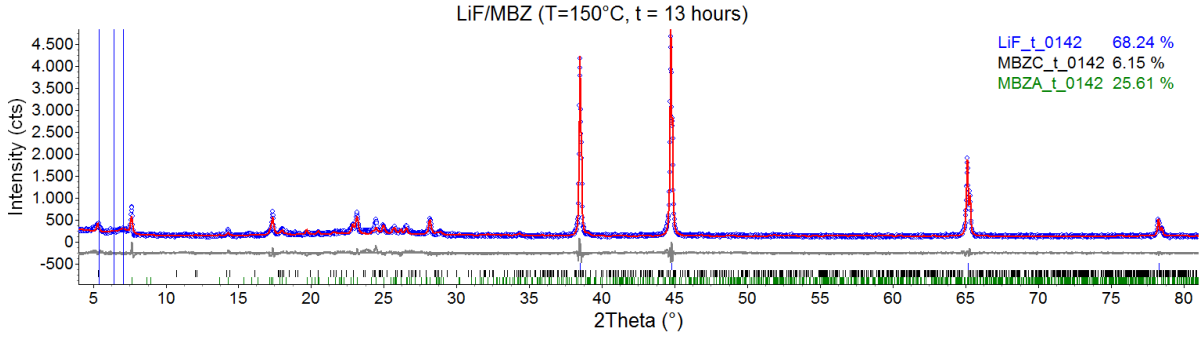

Source: Created by the author.

Figure E.85: Graphical Rietveld refinements obtained for LiF/MBZ at T = 150 °C and t = 26.5 hour. Blue curve – observed data; red curve – calculated data; grey curve – residual curves.

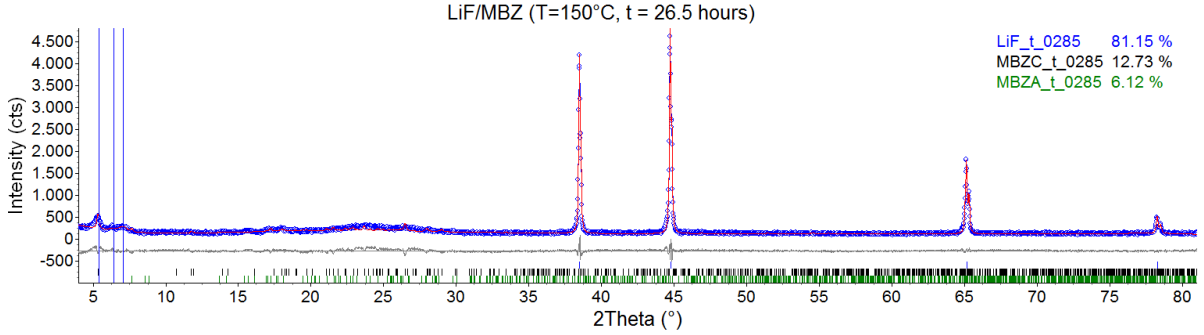

Source: Created by the author.

E.1.1.11. Values calculated at 155°C

Figure E.86: a) Comparison between Rwp (%) behaviour obtained by sequential Rietveld refinement and surface Rietveld refinement in function of time, for sample LiF/MBZ at 155°C; b) Comparison between *gof* behaviour obtained by sequential Rietveld refinement and surface Rietveld refinement in function of time, for sample LiF/MBZ at 155°C.

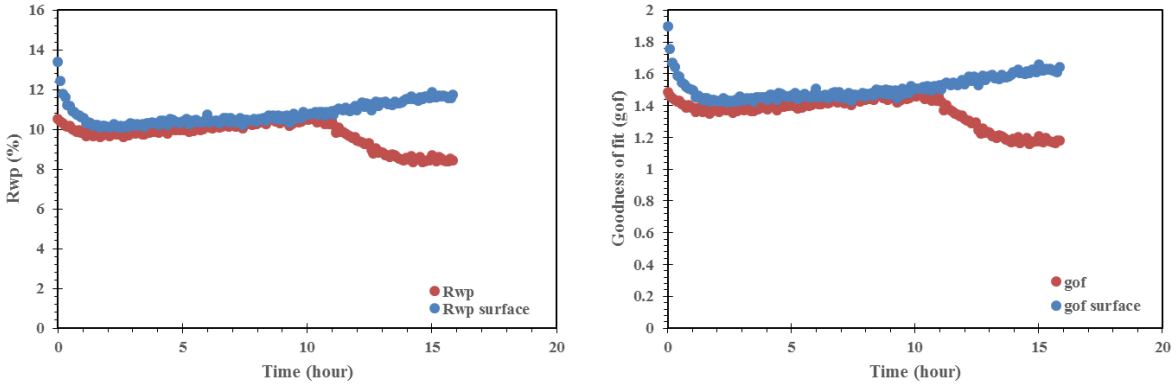

Source: Created by the author.

Figure E.87: a) Comparison between MBZ amorphous quantification calculated by sequential Rietveld refinement and surface Rietveld refinement in function of time, for sample LiF/MBZ at 155°C; b) Comparison between LiF phase quantification calculated by sequential Rietveld refinement and surface Rietveld refinement in function of time, for sample LiF/MBZ at 155°C.

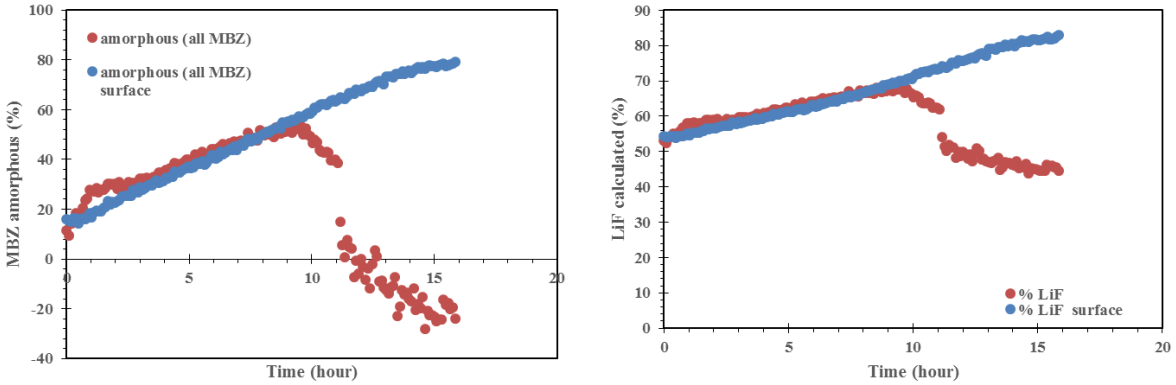

Source: Created by the author.

Figure E.88: a) Comparison between LiF lattice parameter 'a' behaviour determined by sequential Rietveld refinement and surface Rietveld refinement in function of time, for sample LiF/MBZ at 155°C; b) Comparison between LiF volume behaviour determined by sequential Rietveld refinement and surface Rietveld refinement in function of time, for sample LiF/MBZ at 155°C.

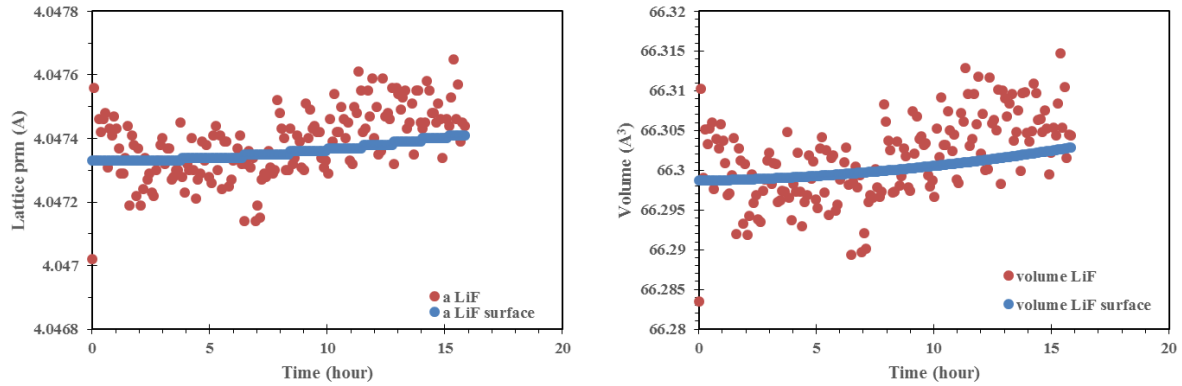

Source: Created by the author.

Figure E.89: a) Comparison between MBZC phase quantification calculated by sequential Rietveld refinement and surface Rietveld refinement in function of time, for sample LiF/MBZ at 155°C; b) Comparison between MBZC phase quantification corrected by internal standard method and calculated by sequential Rietveld refinement and surface Rietveld refinement in function of time, for sample LiF/MBZ at 155°C.

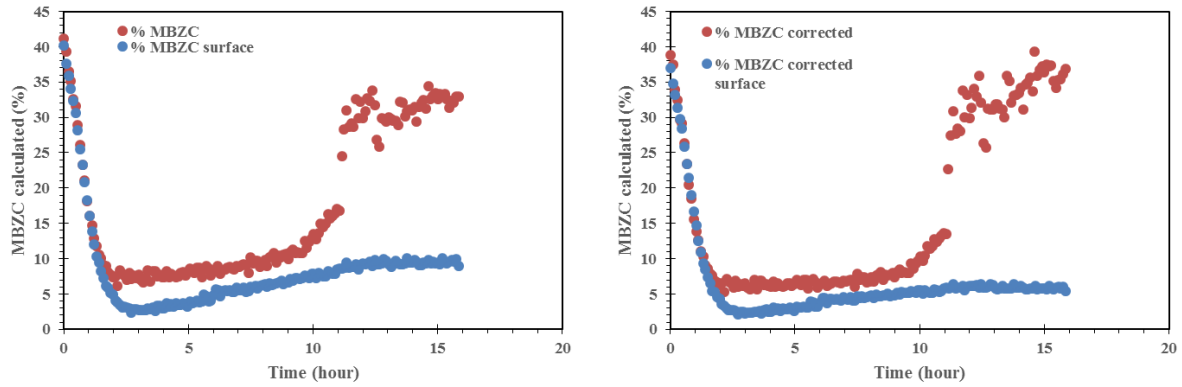

Source: Created by the author.

Figure E.90: a) Comparison between MBZC lattice parameter 'a' behaviour determined by sequential Rietveld refinement and surface Rietveld refinement in function of time, for sample LiF/MBZ at 155°C; b) Comparison between MBZC lattice parameter 'b' behaviour determined by sequential Rietveld refinement and surface Rietveld refinement in function of time, for sample LiF/MBZ at 155°C.

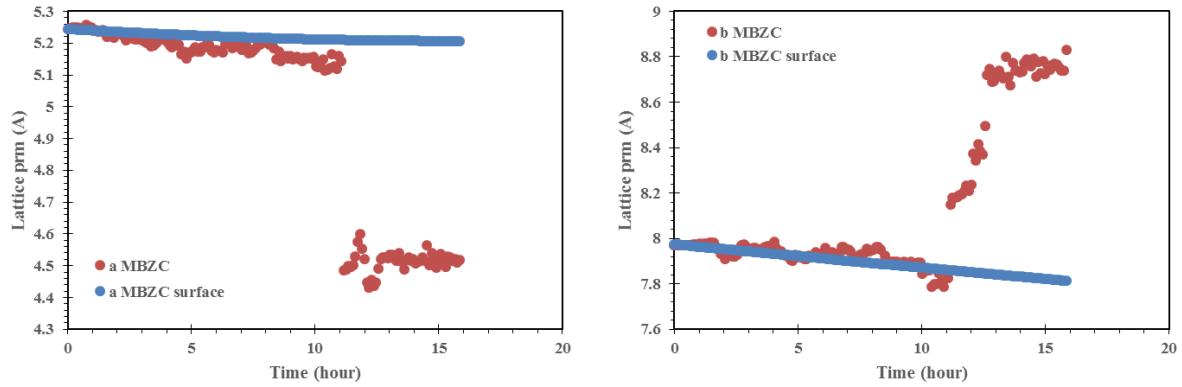

Source: Created by the author.

Figure E.91: a) Comparison between MBZC lattice parameter 'c' behaviour determined by sequential Rietveld refinement and surface Rietveld refinement in function of time, for sample LiF/MBZ at 155°C; b) Comparison between MBZC lattice parameter 'alpha' behaviour determined by sequential Rietveld refinement and surface Rietveld refinement in function of time, for sample LiF/MBZ at 155°C.

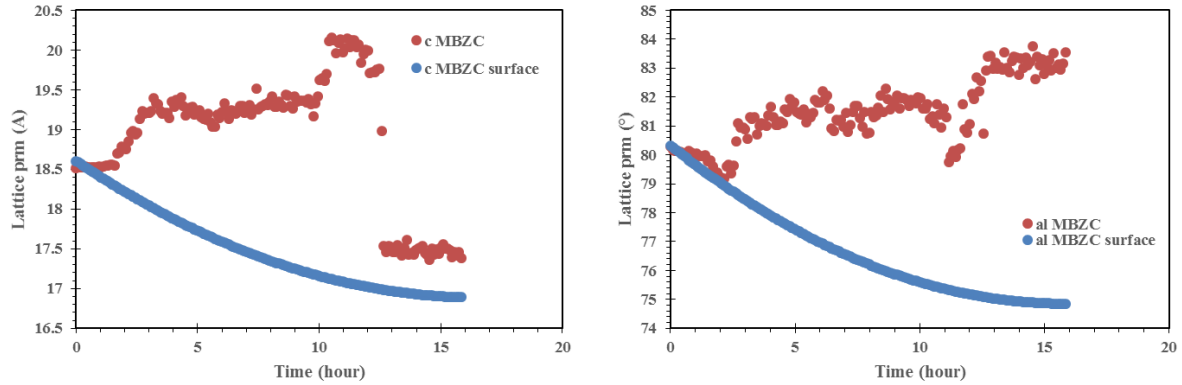

Source: Created by the author.

Figure E.92: a) Comparison between MBZC lattice parameter 'beta' behaviour determined by sequential Rietveld refinement and surface Rietveld refinement in function of time, for sample LiF/MBZ at 155°C; b) Comparison between MBZC lattice parameter 'gamma' behaviour determined by sequential Rietveld refinement and surface Rietveld refinement in function of time, for sample LiF/MBZ at 155°C.

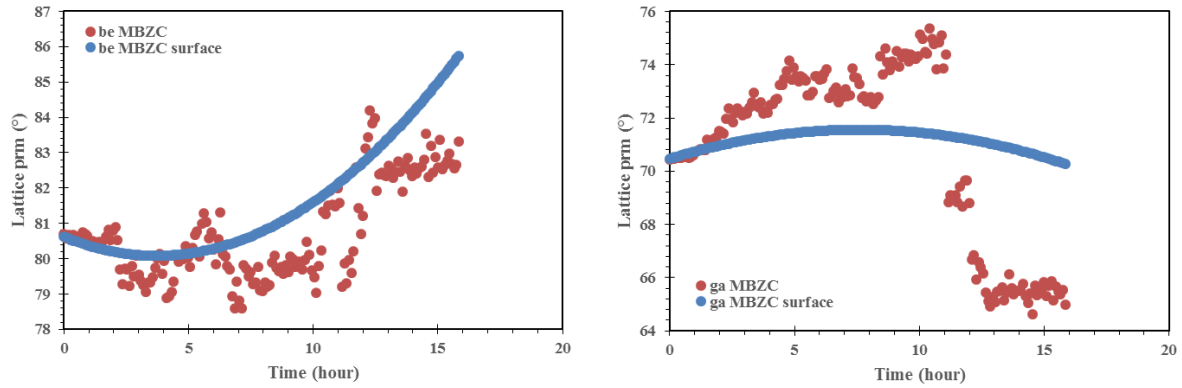

Source: Created by the author.

Figure E.93: a) Comparison between MBZC volume behaviour determined by sequential Rietveld refinement and surface Rietveld refinement in function of time, for sample LiF/MBZ at 155°C; b) Comparison between MBZA phase quantification calculated by sequential Rietveld refinement and surface Rietveld refinement in function of time, for sample LiF/MBZ at 155°C.

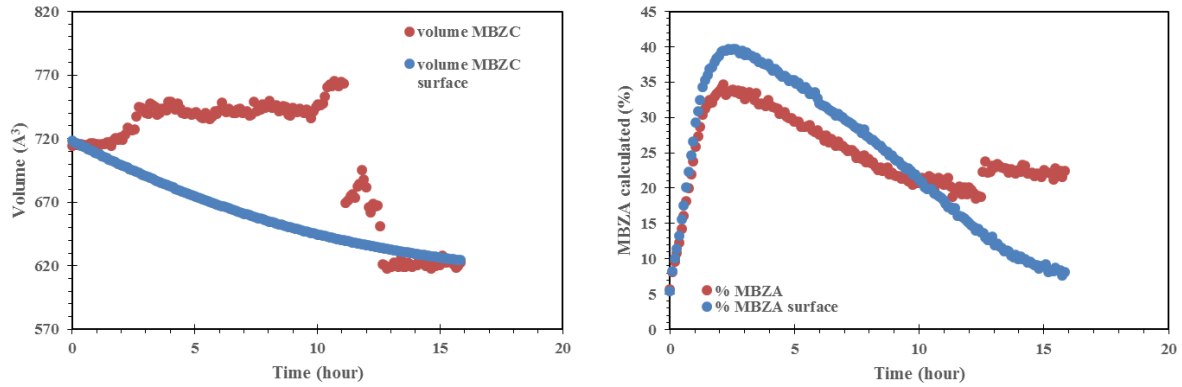

Source: Created by the author.

Figure E.94: a) Comparison between MBZA phase quantification corrected by internal standard method and calculated by sequential Rietveld refinement and surface Rietveld refinement in function of time, for sample LiF/MBZ at 155°C; b) Comparison between MBZA lattice parameter 'a' behaviour determined by sequential Rietveld refinement and surface Rietveld refinement in function of time, for sample LiF/MBZ at 155°C.

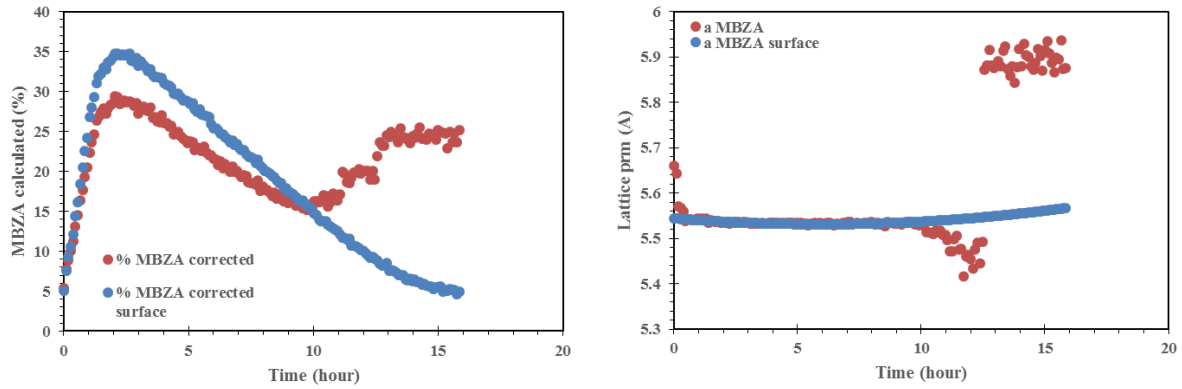

Source: Created by the author.

Figure E.95: a) Comparison between MBZA lattice parameter 'b' behaviour determined by sequential Rietveld refinement and surface Rietveld refinement in function of time, for sample LiF/MBZ at 155°C; b) Comparison between MBZA lattice parameter 'c' behaviour determined by sequential Rietveld refinement and surface Rietveld refinement in function of time, for sample LiF/MBZ at 155°C.

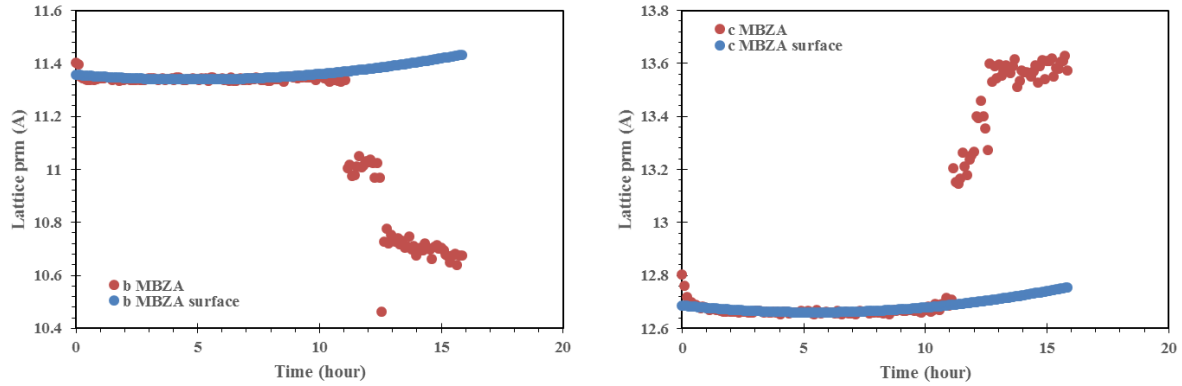

Source: Created by the author.

Figure E.96: a) Comparison between MBZA lattice parameter 'alpha' behaviour determined by sequential Rietveld refinement and surface Rietveld refinement in function of time, for sample LiF/MBZ at 155°C.; b) Comparison between MBZA lattice parameter 'beta' behaviour determined by sequential Rietveld refinement and surface Rietveld refinement in function of time, for sample LiF/MBZ at 155°C.

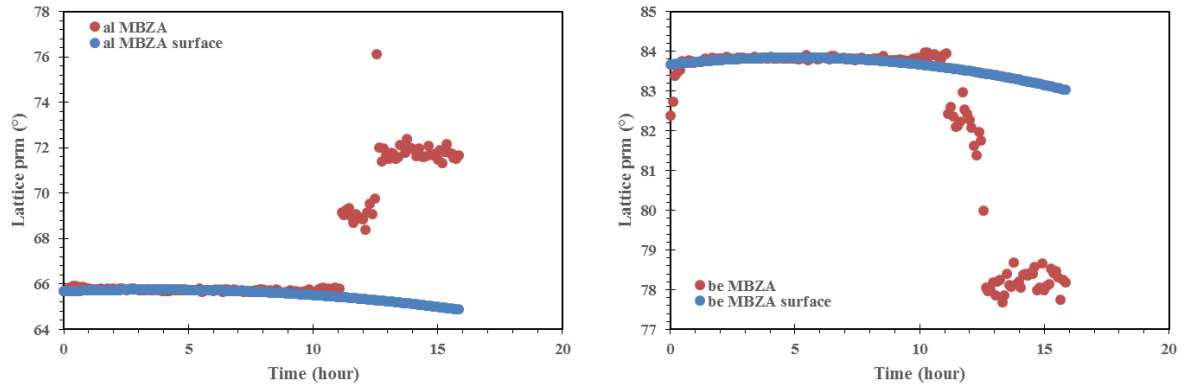

Source: Created by the author.

Figure E.97: a) Comparison between MBZA lattice parameter 'gamma' behaviour determined by sequential Rietveld refinement and surface Rietveld refinement in function of time, for sample LiF/MBZ at 155°C; b) Comparison between MBZA volume behaviour determined by sequential Rietveld refinement and surface Rietveld refinement in function of time, for sample LiF/MBZ at 155°C.

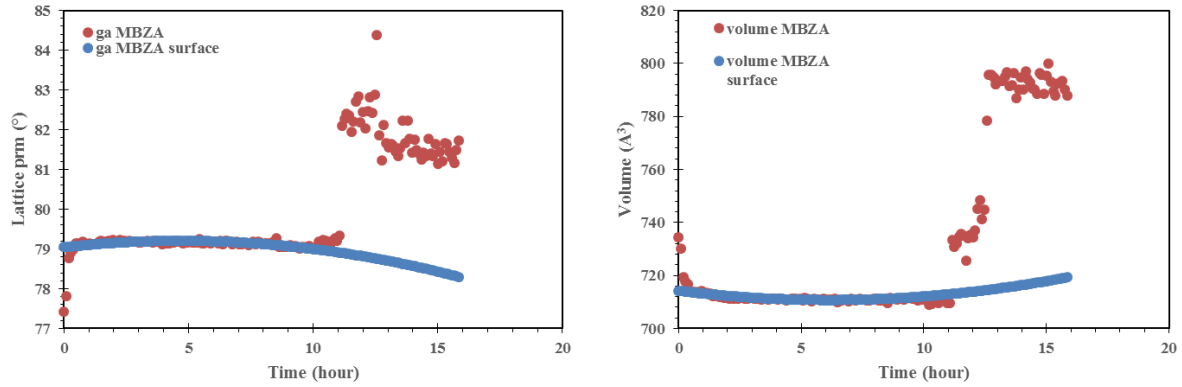

Source: Created by the author.

E.1.1.12. Graphical fits from surface Rietveld refinement at 155°C

Figure E.98: Graphical Rietveld refinements obtained for LiF/MBZ at T = 155 °C and t = 0 hour. Blue curve – observed data; red curve – calculated data; grey curve – residual curves.

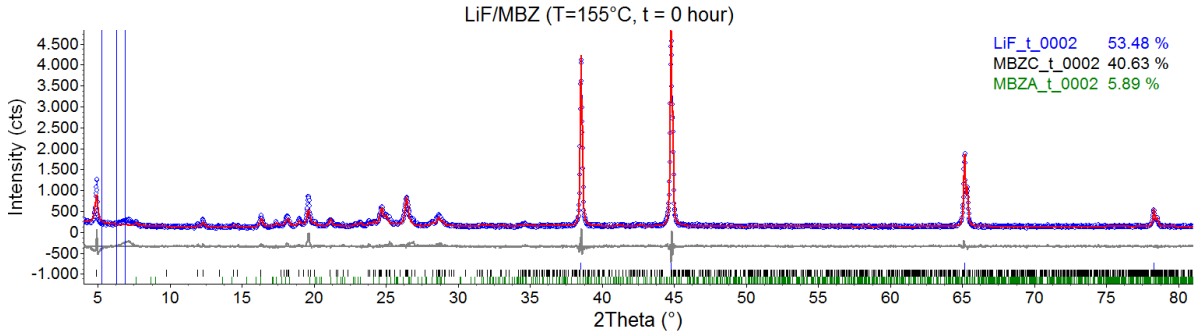

Source: Created by the author.

Figure E.99: Graphical Rietveld refinements obtained for LiF/MBZ at T = 155 °C and t = 8 hours. Blue curve – observed data; red curve – calculated data; grey curve – residual curves.

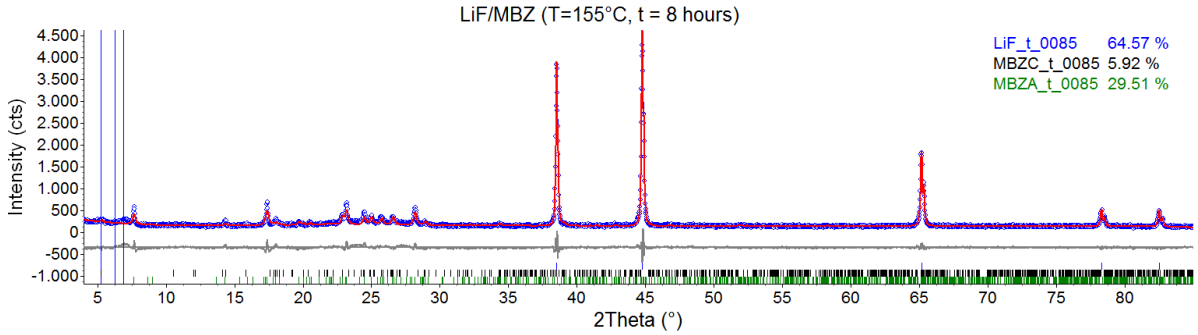

Source: Created by the author.

Figure E.100: Graphical Rietveld refinements obtained for LiF/MBZ at T = 155 °C and t = 16 hours. Blue curve – observed data; red curve – calculated data; grey curve – residual curves.

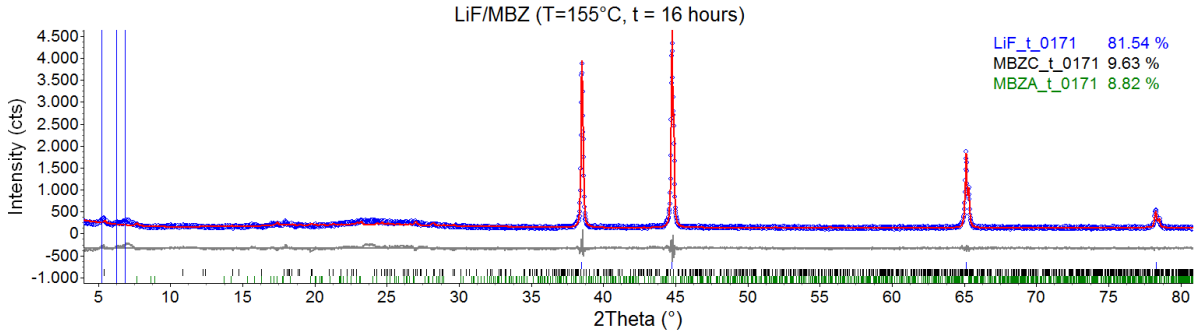

Source: Created by the author.

E.1.1.13. Values calculated at 160°C

Figure E.101: a) Comparison between Rwp (%) behaviour obtained by sequential Rietveld refinement and surface Rietveld refinement in function of time, for sample LiF/MBZ at 160°C; b) Comparison between *gof* behaviour obtained by sequential Rietveld refinement and surface Rietveld refinement in function of time, for sample LiF/MBZ at 160°C.

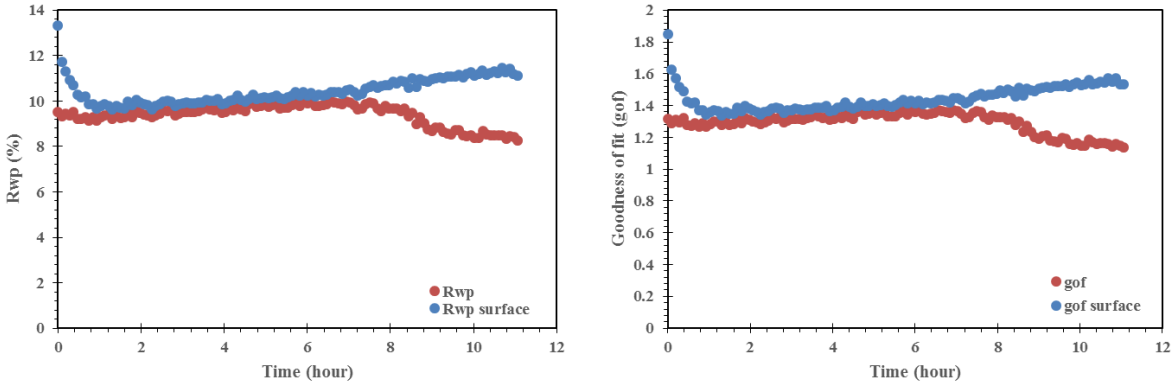

Source: Created by the author.

Figure E.102: a) Comparison between MBZ amorphous quantification calculated by sequential Rietveld refinement and surface Rietveld refinement in function of time, for sample LiF/MBZ at 160°C; b) Comparison between LiF phase quantification calculated by sequential Rietveld refinement and surface Rietveld refinement in function of time, for sample LiF/MBZ at 160°C.

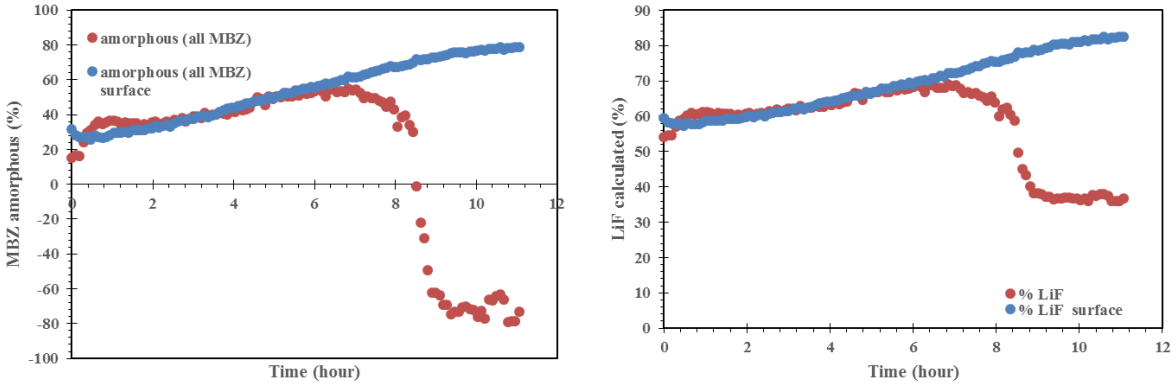

Source: Created by the author.

Figure E.103: a) Comparison between LiF lattice parameter 'a' behaviour determined by sequential Rietveld refinement and surface Rietveld refinement in function of time, for sample LiF/MBZ at 160°C; b) Comparison between LiF volume behaviour determined by sequential Rietveld refinement and surface Rietveld refinement in function of time, for sample LiF/MBZ at 160°C.

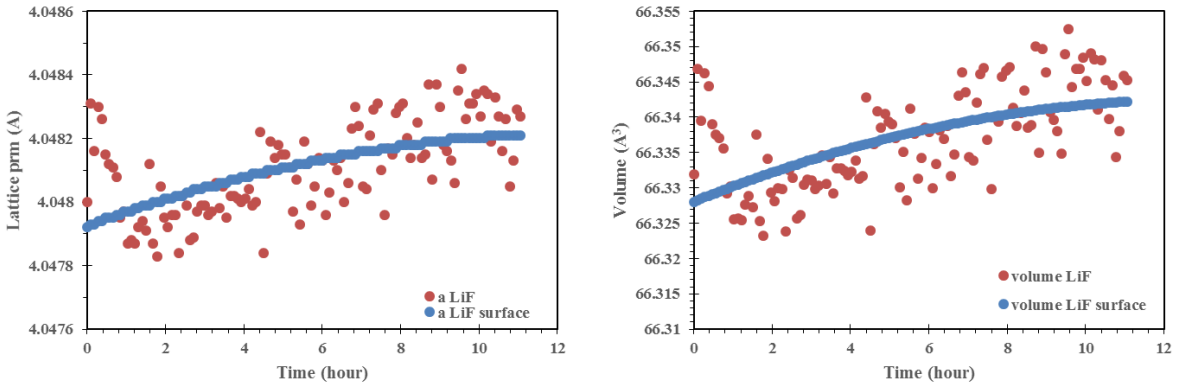

Source: Created by the author.

Figure E.104: a) Comparison between MBZC phase quantification calculated by sequential Rietveld refinement and surface Rietveld refinement in function of time, for sample LiF/MBZ at 160°C; b) Comparison between MBZC phase quantification corrected by internal standard method and calculated by sequential Rietveld refinement and surface Rietveld refinement in function of time, for sample LiF/MBZ at 160°C.

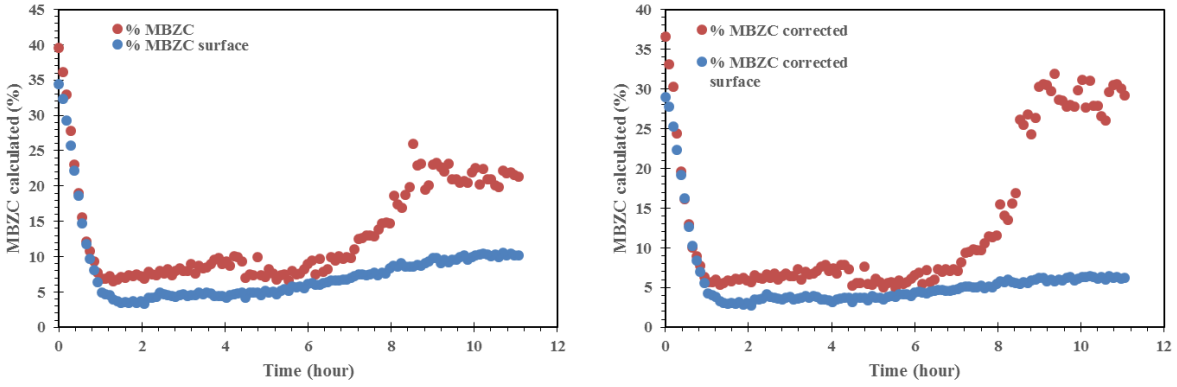

Source: Created by the author.

Figure E.105: a) Comparison between MBZC lattice parameter 'a' behaviour determined by sequential Rietveld refinement and surface Rietveld refinement in function of time, for sample LiF/MBZ at 160°C; b) Comparison between MBZC lattice parameter 'b' behaviour determined by sequential Rietveld refinement and surface Rietveld refinement in function of time, for sample LiF/MBZ at 160°C.

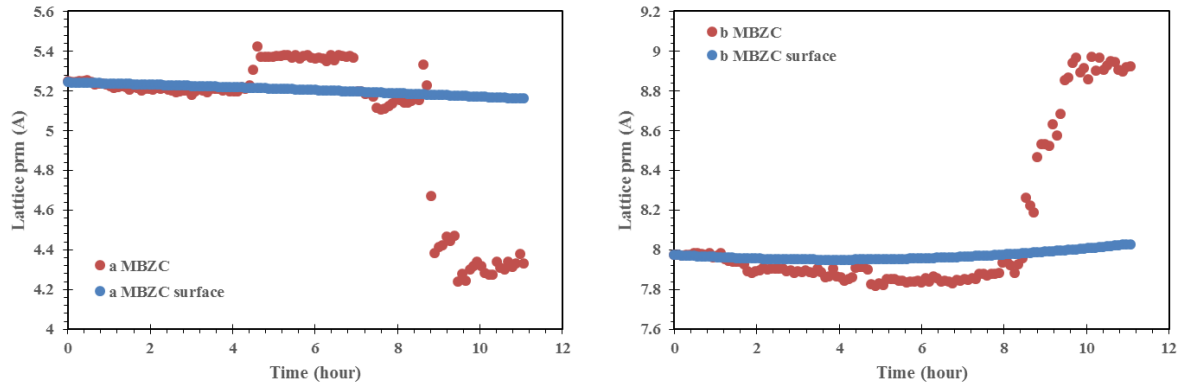

Source: Created by the author.

Figure E.106: a) Comparison between MBZC lattice parameter 'c' behaviour determined by sequential Rietveld refinement and surface Rietveld refinement in function of time, for sample LiF/MBZ at 160°C; b) Comparison between MBZC lattice parameter 'alpha' behaviour determined by sequential Rietveld refinement and surface Rietveld refinement in function of time, for sample LiF/MBZ at 160°C.

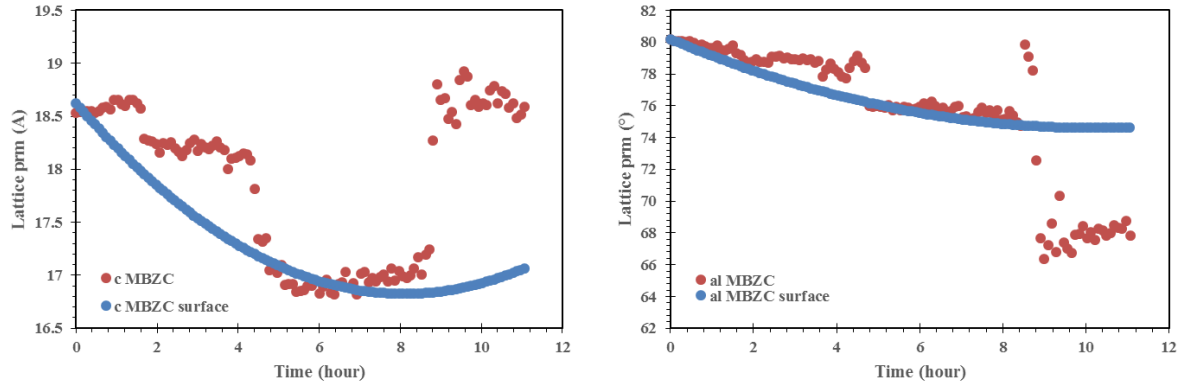

Source: Created by the author.

Figure E.107: a) Comparison between MBZC lattice parameter 'beta' behaviour determined by sequential Rietveld refinement and surface Rietveld refinement in function of time, for sample LiF/MBZ at 160°C; b) Comparison between MBZC lattice parameter 'gamma' behaviour determined by sequential Rietveld refinement and surface Rietveld refinement in function of time, for sample LiF/MBZ at 160°C.

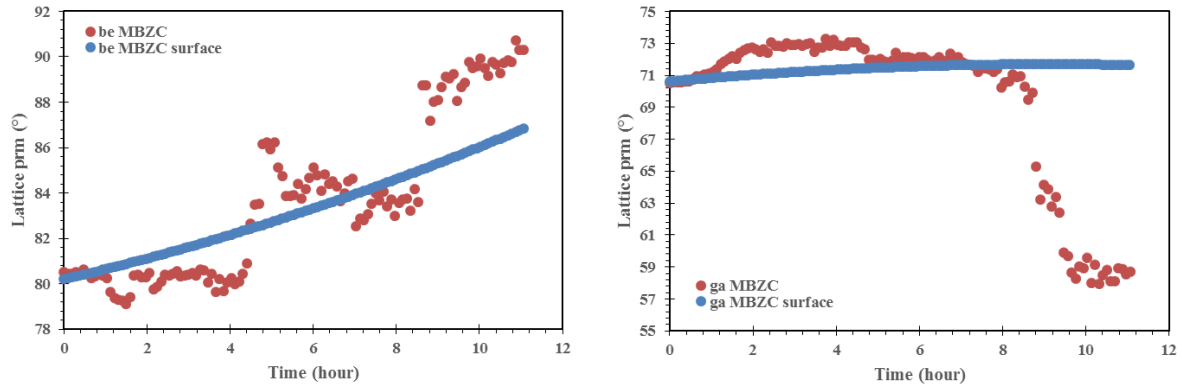

Source: Created by the author.

Figure E.108: a) Comparison between MBZC volume behaviour determined by sequential Rietveld refinement and surface Rietveld refinement in function of time, for sample LiF/MBZ at 160°C; b) Comparison between MBZA phase quantification calculated by sequential Rietveld refinement and surface Rietveld refinement in function of time, for sample LiF/MBZ at 160°C.

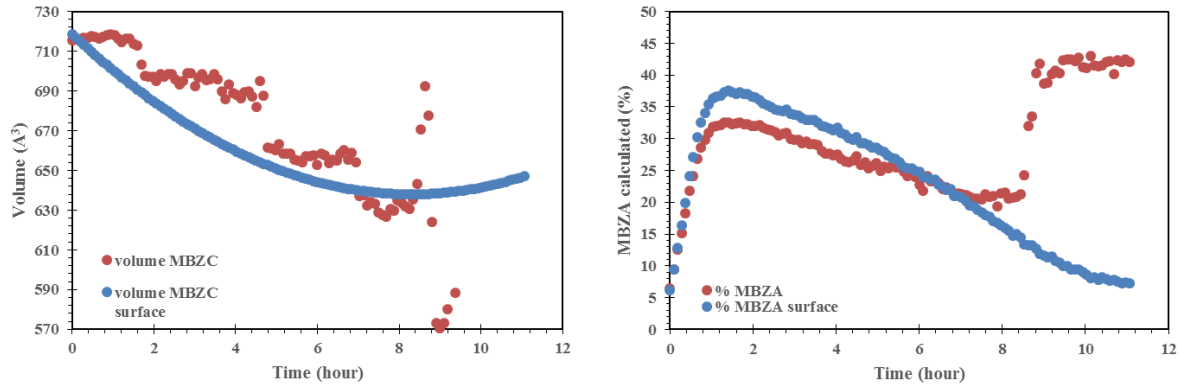

Source: Created by the author.

Figure E.109: a) Comparison between MBZA phase quantification corrected by internal standard method and calculated by sequential Rietveld refinement and surface Rietveld refinement in function of time, for sample LiF/MBZ at 160°C; b) Comparison between MBZA lattice parameter 'a' behaviour determined by sequential Rietveld refinement and surface Rietveld refinement in function of time, for sample LiF/MBZ at 160°C.

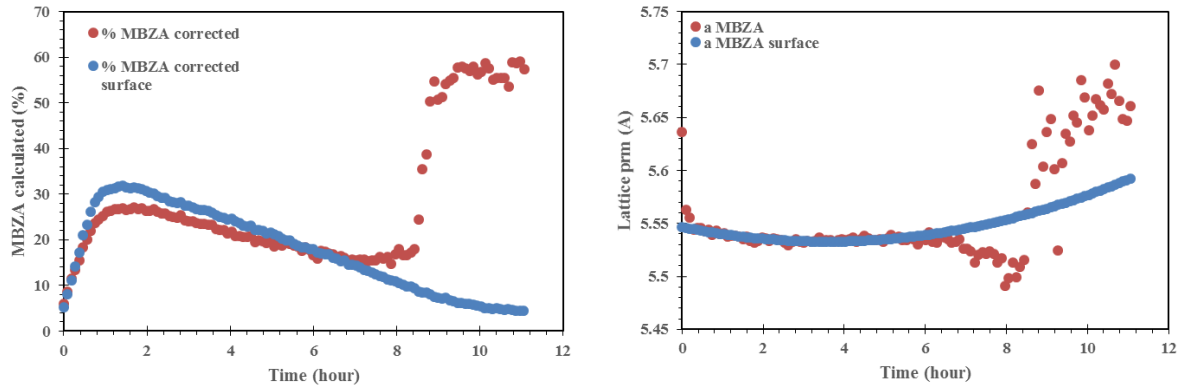

Source: Created by the author.

Figure E.110: a) Comparison between MBZA lattice parameter 'b' behaviour determined by sequential Rietveld refinement and surface Rietveld refinement in function of time, for sample LiF/MBZ at 160°C; b) Comparison between MBZA lattice parameter 'c' behaviour determined by sequential Rietveld refinement and surface Rietveld refinement in function of time, for sample LiF/MBZ at 160°C.

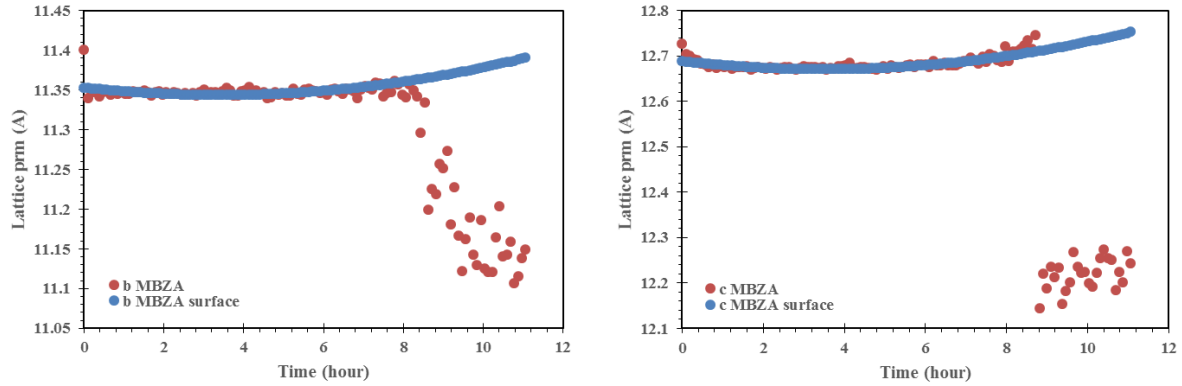

Source: Created by the author.

Figure E.111: a) Comparison between MBZA lattice parameter 'alpha' behaviour determined by sequential Rietveld refinement and surface Rietveld refinement in function of time, for sample LiF/MBZ at 160°C.; b) Comparison between MBZA lattice parameter 'beta' behaviour determined by sequential Rietveld refinement and surface Rietveld refinement in function of time, for sample LiF/MBZ at 160°C.

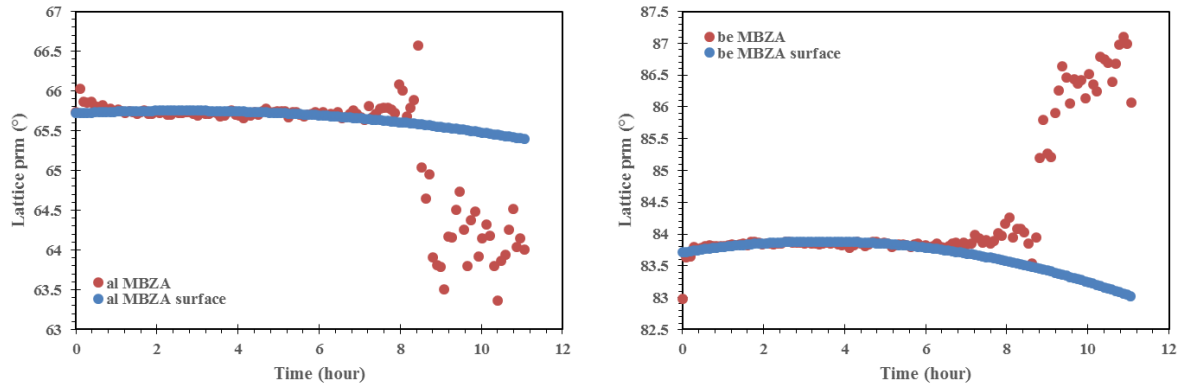

Source: Created by the author.

Figure E.112: a) Comparison between MBZA lattice parameter 'gamma' behaviour determined by sequential Rietveld refinement and surface Rietveld refinement in function of time, for sample LiF/MBZ at 160°C; b) Comparison between MBZA volume behaviour determined by sequential Rietveld refinement and surface Rietveld refinement in function of time, for sample LiF/MBZ at 160°C.

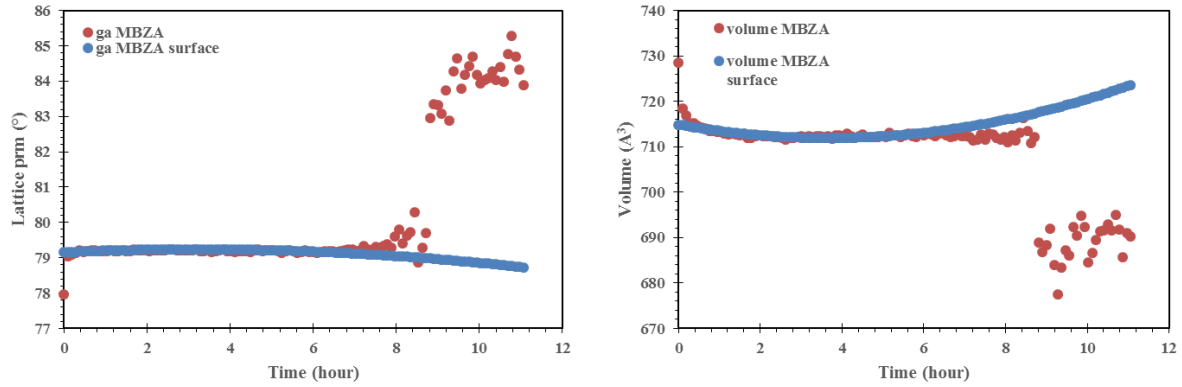

Source: Created by the author.

E.1.1.14. Graphical fits from surface Rietveld refinement at 160°C

Figure E.113: Graphical Rietveld refinements obtained for LiF/MBZ at T = 160 °C and t = 0 hour. Blue curve – observed data; red curve – calculated data; grey curve – residual curves.

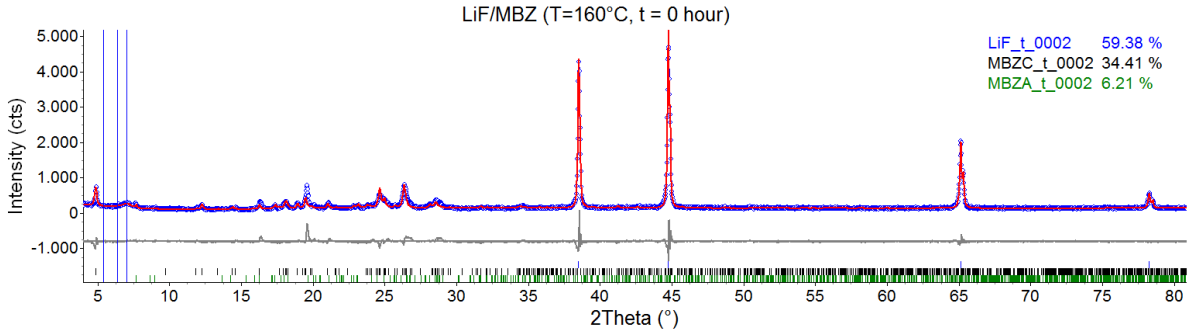

Source: Created by the author.

Figure E.114: Graphical Rietveld refinements obtained for LiF/MBZ at T = 160 °C and t = 5.5 hours. Blue curve – observed data; red curve – calculated data; grey curve – residual curves.

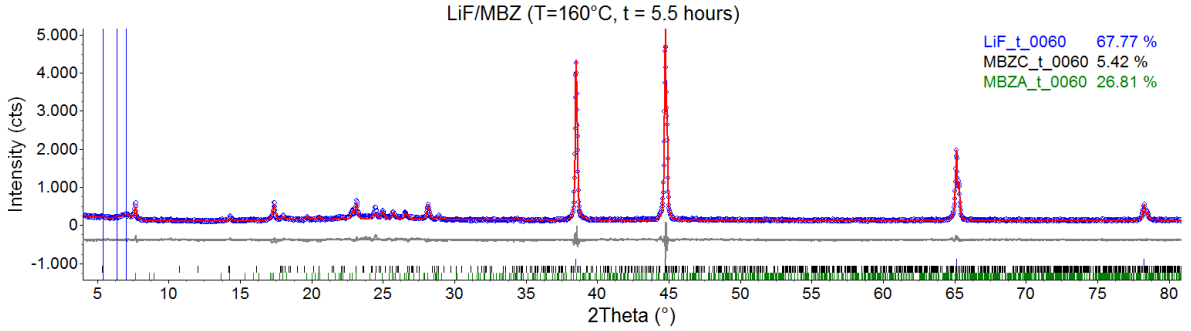

Source: Created by the author.

Figure E.115: Graphical Rietveld refinements obtained for LiF/MBZ at T = 160 °C and t = 11 hours. Blue curve – observed data; red curve – calculated data; grey curve – residual curves.

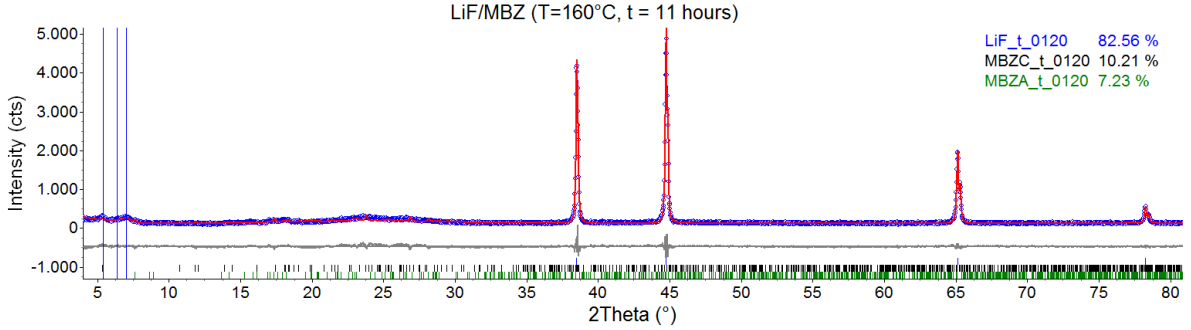

Source: Created by the author.

Appendix F

Mebendazole form B indexation

MBZ form B, recrystallized from MBZ sample in Ethyl acetate solvent, dissolved M/V = 5 mg/ml at 23°C., filtered and then evaporate at room temperature by 15 days.

The indexation attempt of Mebendazole form B made in TOPAS-Academic from space group search considering all crystal systems to adjust with 13 peaks. A list of ten space groups with best fit used in a lattice parameter search and then a Pawley method applied.

Figure F.1: Graphical Pawley fit obtained for MBZB with: Space group P-1, a = 28.738894 Å**,** b = 9.489889 Å**,** c = 11.002775 Å**,** α = 92.65931°, β = 84.45296°, γ = 106.03827°, volume = 2869.864 Å^3, Rwp = 4.87%, *„gof* = 1.426. Blue curve – observed data; red curve – calculated data; grey curve – residual curves.

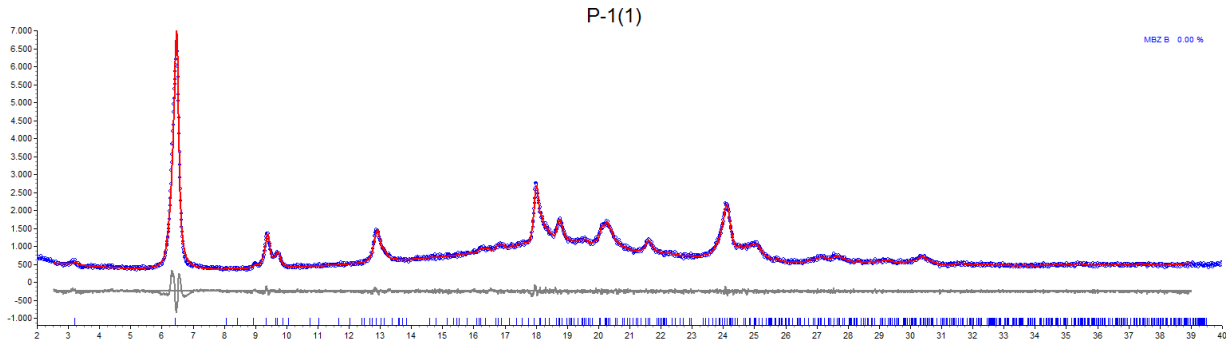

Source: Created by the author.

Figure F.2: Graphical Pawley fit obtained for MBZB with: Space group P-1, a = 29.989282 Å**,** b = 9.933344 Å**,** c = 11.002775 Å**,** α = 90°, β = 98.13515°, γ = 90°, volume = 2585.597Å^3, Rwp = 5.91%, *‚gof* = 1.661. Blue curve – observed data; red curve – calculated data; grey curve – residual curves.

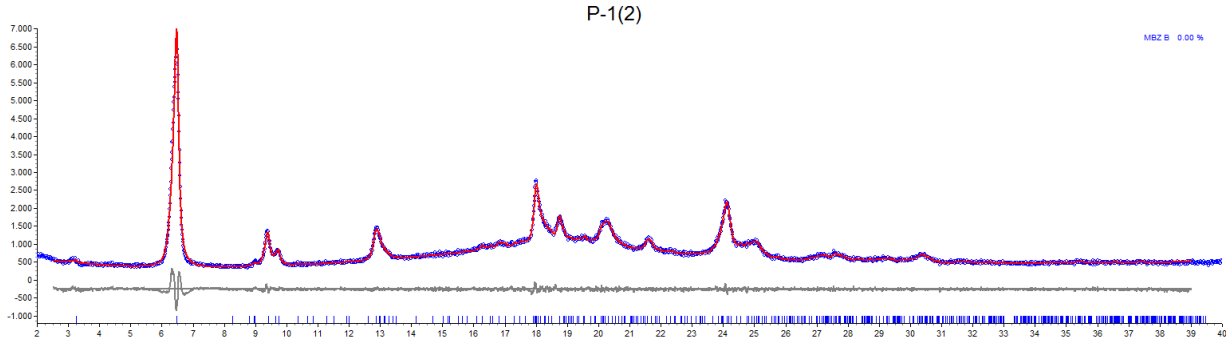

Source: Created by the author.

Figure F.3: Graphical Pawley fit obtained for MBZB with: Space group P2, a = 9.545668 Å**,** b = 27.465567 Å**,** c = 10.746676 Å**,** α = 96.31460°, β = 72.55161°, γ = 75.02921°, volume = 2888.733 Å^3, Rwp = 4.90%, *‚gof* = 1.434. Blue curve – observed data; red curve – calculated data; grey curve – residual curves.

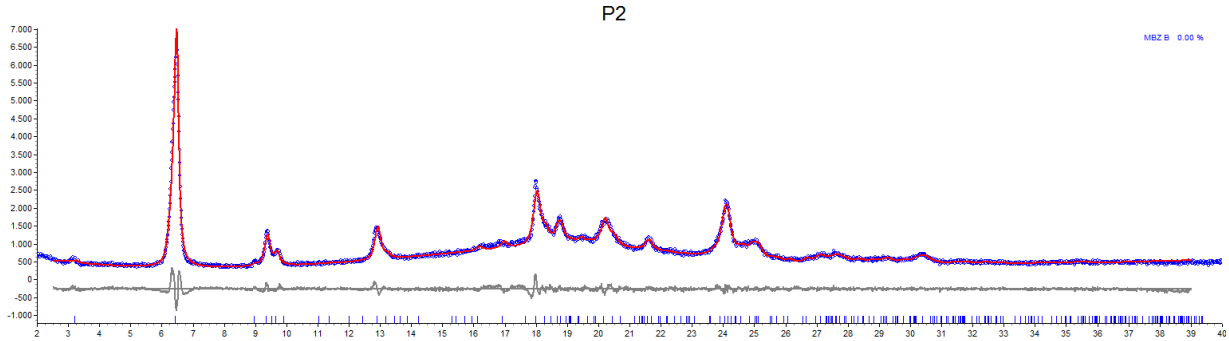

Source: Created by the author.

Annex

Annex I

Sequential Rietveld refinement

Right click on folder -> command window here

- Digit multitopas
- Digit all directory finishing with bar (\)
- Enter ‘raw file’. In this point is necessary put the file that contain all directories of files (datas) to make the refinement. In my case was ‘filename.list’, but is not necessary put the extension
- Enter start, stop, step -> is necessary put the number of the file that we want analise: 1,23,1 -> that means to read scan 1 to 23, 1 by 1
- Enter input file name -> is to put ‘seed.inp’ that we create for refine
- How many times run tc at each temperature: 1
- Read other parms from a file to tell topas: y
- File containing information: temperatures2.val
- Copy output next input: y
- Keep topas output: n

  Now the runmultitopas.bat is done!

Annex II

Parametric Rietveld refinement

In this annex, we will go from fitting a single file to fitting many data sets simultaneously. It is likely that there is only one physically sensible model that will fit all the data simultaneously.

The cell parameters are set up to make possible to refine them as simple polynomial functions. Parameters that must have the same value for all data set are in the "overall" section. From a file 100% equivalent to the file used for simple Rietveld refinement. It is set up in the language needed for surface fitting:

```
prm a_nfx_ses_t0000  = a0_nfx*(1+ax1_nfx*(t0000)+ax2_nfx*(t0000)^2+ax3_nfx*(t0006)^3);:8.88002`
a  = a_nfx_ses_t0006 ;:8.880017`
```

All parameters are named "_0000" this is so they can be automatically expanded into a parametric fit. Everything is contained within "#ifdef use_t_000....#endif" statements, which is a trick for commenting in and out individual datasets.

To create the file parametric.inp, it is necessary to save the portion of previous *.inp file that describes refinement of an individual data set to a separate file. A simple program then automatically replaces parameter names by values specific for each data range. Download substitute.exe[†]. Run substitute.exe and answer the questions. Choose read "temperatures" from a file option and give filename "range.val". Have a look at the files produced "temperatures.prm" has the lines you use to control which datasets are fitted. multi.inp contains instructions for each dataset. These can be combined with the "header" information in previous *.inp file to produce a file equivalent to parametric.inp.

References

ANTONIO, S. G. **Aplicação da difração de raios X por policristais e do método de Rietveld de refinamento de estruturas cristalinas no estudo de polimorfos cristalinos de fármacos**. 2010. 161 f. Tese (Doutorado em Química) - Instituto de Química, Universidade Estadual Paulista, Araraquara, 2010.

ARII, T.; KISHI, A. The effect of humidity on thermal process of zinc acetate. **Thermochimica Acta**, v. 400, p. 175-185, 2003.

BARATTA, F.; GERMANO, A.; BRUSA, P. Diffusion of counterfeit drugs in developing countries and stability of galenics stored for months under different conditions of temperature and relative humidity. **Croatian Medical Journal**, v. 53, p. 173-184, 2012.

BARBAS, R.; PROHENS, R.; PUIGJANER, C. A new polymorph of Norfloxacin. **Journal of Thermal Analysis and Calorimetry**, v. 89, p. 687-692, 2007.

BARBAS, R.; MARTI, F.; PROHENS, R.; PUIGJANER, C. Polymorphism of Norfloxacin: evidence of the enantiotropic relationship between polymorphs A and B. **Crystal Growth & Design**, v. 6, p. 1463-1467, 2006.

BASAVOJU, S.; BOSTRÖM, D.; VELAGA, S. P. Pharmaceutical cocrystal and salts of Norfloxacin. **Crystal Growth & Design**, v. 6, p. 2699-2708, 2006.

BERNSTEIN, J. Introduction and historical background. In:_____. **Polymorphism in molecular crystals**. New York: Oxford University Press, 2002. Chap. 1, p. 1-28.

BEZZON, V. D. N. **Definição de limites para a identificação e quantificação de polimorfos do fármaco finasterida por difração de raios x por policristais**. 2013. 204 f. Dissertação (Mestrado em Química) - Instituto de Química, Universidade Estadual Paulista, Araraquara, 2013.

BRINDLEY, G. W. The effect of grain or particle Size on x-ray reflections from mixed powders and alloys, considered in relation to the quantitative determination of crystalline substances by x-ray methods. **Philosophy Magazine**, v. 36, p. 347-369, 1945.

BRITS, M.; LIEBENBERG, W.; VILLIERS, M. M. Characterization of polymorph transformations that decrease the stability of tables containing the WHO essential drug Mebendazole. **Journal of Pharmaceutical Sciences**, v. 99, p. 1138-1151, 2010.

BYARD, S. J.; JACKSON, A. L.; SMAIL, A.; BAUER, M.; APPERLEY, D. C. Studies on the crystallinity of a pharmaceutical development drug substance. **Journal of Pharmaceutical Sciences**, v. 94, p. 1321-1335, 2005.

CARACCIOLO, G.; PETRUCCETTI, M.; CAMINITI, R. A new experimental setup for the study of lipid hydration by energy dispersive X-ray diffraction. **Chemical Physics Letters**, v. 414, p. 456-460, 2005.

CHONGCHAROEN, W.; BYRN, S. R.; SUTANTHAVIBUL, N. Solid state interconversion between anhydrous norfloxacin and its hydrates. **Journal of Pharmaceutical Sciences**, v. 97, p. 473-489, 2008.

CLINE, J. P.; VON DREELE, R. B.; WINBURN, R.; STEPHENS, P. W.; FILLIBEN, J. J. Addressing the amorphous content issue in quantitative phase analysis: the certification of NIST standard reference material 676a. **Acta Crystallographica Section A**, v. 67, p. 357-367, 2011.

COELHO, A. A. **TOPAS academic**: general profile and structure analysis software for Powder Diffraction Data. Karlsruhe. Version 5. 2012. Disponível em: <http://www.topas-academic.net/>. Acesso em: 20 ago. 2014.

COELHO, A. A. **Technical reference**: TOPAS academic. Version 5. Brisbane, 2013. 180 p.

COSTA, J.; FRESNO, M.; GUZMÁN, L.; IGUAL, A.; OLIVA, J.; VIDAL, P.; PÉREZ, A.; PUJOL, M. Polymorphic forms of Mebenzole: analytical aspects and toxicity. **Circular Farmacêutica**, v. 312, p. 415-424, 1991.

EMERY, E.; OLIVER, J.; PUGSLEY, T.; SHARMA, J.; ZHOU, J. Flowability of moist pharmaceutical powders. **Powder Technology**, v. 189, p. 409-415, 2009.

FERREIRA, F. F.; GRANADO, E.; CARVALHO JUNIOR, W.; KYCIA, S. W.; BRUNO, D.; DROPPA JUNIOR, R. X-ray powder diffraction beamline at D10B of LNLS: application to the Ba_2FeReO_6 double perovskite. **Journal of Synchrotron Radiation**, v. 13, p. 46-53, 2006.

FERREIRA, F. F.; ANTONIO, S. G.; ROSA, P. C. P.; PAIVA-SANTOS, C. O. Crystal structure determination of Mebendazole form A using high-resolution synchrotron x-ray powder diffraction data. **Journal of Pharmaceutical Sciences**, v. 99, p. 1734-1744, 2010.

FLORENCE, A. J.; KENNEDY, A. R.; SHANKLAND, N.; WRIGHT, E.; AL-RUBAYI, A. Norfloxacin dehydrate. **Acta Crystallographica Section C**, v. 56, p. 1372-1373, 2000.

FURUKI, T.; KISHI, A.; SAKURAI, M. De-and rehydration behavior of α, α -trehalose dihydrate under humidity-controlled atmospheres. **Carbohydrate Research**, v. 340, p. 429-438, 2005.

HANCOCK, B. C.; ZOGRAF, G. Characteristics and significance of the amorphous state in pharmaceutical systems. **Journal of Pharmaceutical Sciences**, v. 86, p. 1-12, 1997.

HASHIZUME, H.; SHIMOMURA, S.; YAMADA, H.; FUJITA, T.; NAKAZAWA, H. An X-ray diffraction system with controlled relative humidity and temperature. **Powder Diffraction**, v. 11, p. 288-289, 1996.

HILL, R. J.; HOWARD, C. J. Quantitative phase analysis from neutron powder diffraction data using the Rietveld method. **Journal of Applied Crystallography**, v. 20, p. 467-474, 1987.

HIMMELREICH, M.; RAWSON, B. J.; WATSON, T. R. Polymorphic forms of Mebendazole. **Australian Journal of Pharmaceutical Sciences**, v. 6, p. 123-125, 1977.

HINRICHSEN, B.; DINNEBIER, R. E.; JANSEN, M. Powder3D: an easy to use program for data reduction and graphical presentation of large numbers of powder diffraction patterns. **Zeitschrift für Kristallographie**, v. 23, p. 231-236, 2004.

HU, T.-C.; WANG, S.-L.; CHEN, T.-F.; LIN, S.-Y. Hydration-induced proton transfer in the solid state of Norfloxacin. **Journal of Pharmaceutical Sciences**, v. 91, p. 1351-1357, 2002.

INORGANIC CRYSTAL STRUCTURE DATABASE. Disponível em: <http://www.fiz-karlsruhe.de/news_12.html?&L=0&tx_ttnews[tt_news]=1417&cHash=915834c7eb8b4e0f3135190d1927bd46>. Acesso em: 15 abr. 2013.

INTERNATIONAL CONFERENCE ON HARMONISATION. **Explanatory note on the withdrawal of ICH Q1F for the ICH website**. Disponível em: <http://www.ich.org/fileadmin/Public_Web_Site/ICH_Products/Guidelines/Quality/Q1F/Q1F_Explanatory_Note.pdf >. Acesso em: 02 ago. 2013..

KACHRIMANIS, K.; RONTOGIANNI, M.; MALAMATARIS, S. Simultaneous quantitative analysis of Mebendazole polymorphs A-C in powder mixtures by DRIFTS spectroscopy and ANN modeling. **Journal of Pharmaceutical and Biomedical Analysis**, v. 51, p. 512-520, 2010.

KAKUNO, E. M.; CAMARDA G.; SIDDONS D. P. Cadmium-zinc telluride detector arrays for synchrotron radiation applications. **Proceedings of SPIE**, v. 5198, p. 19-25, 2004.

KATDARE, A. V.; RYAN, J. A.; BAVITZ, J. F.; ERB, D. M.; GUILLORY, J. K. Characterization of hydrates of Norfloxacin. **Mikrochimica Acta**, p. 1-12, 1987.

KATSARAS, J.; WATSON, M. Sample cell capable of 100% relative humidity suitable for x-ray diffraction of aligned lipid multibilayers. **Review of Scientific Instruments**, v. 71, p. 1737-1739, 2000.

KISHI, A.; OTSUKA, M.; MATSUDA, Y. The effect of humidity on dehydration behavior of nitrofurantoin monohydrate studied by humidity controlled simultaneous instrument for x-ray diffractometry and differential scanning calorimetry (XRD-DSC). **Colloids and Surfaces B**: Biointerface, v. 25, p. 281-291, 2002.

KLUG, H. P.; ALEXANDER, L. E. **X-ray diffraction procedures**: for polycrystalline and amorphous materials. 2nd ed. New York: Wiley, 1974. 992 p.

KUMAR, S.; CHAWLA, G.; SOBHIA, M. E.; BANSAL, A. K. Characterization of solid-state forms of Mebendazole. **Pharmazie**, v. 63, p. 136-143, 2008.

LANGFORD, J. I.; LOUËRZ, D. Powder diffraction. **Reports on Progress in Physics**, v. 59, p. 131-234, 1996.

MADSEN, I. C.; SCARLETT, N. V. Y.; KERN, A. Description and survey of methodologies for the determination of amorphous content via X-ray powder diffraction. **Zeitschrift für Kristallographie**, v. 226, p. 944-955, 2011.

MARTINS, F. T.; NEVES, P. P.; ELLENA, J.; CAMÍ, G. E.; BRUSAU, E. V.; NARDA, G. E. Intermolecular contacts influencing the conformational and geometric features of the pharmaceutically preferred mebendazole polymorph C. **Journal of Pharmaceutical Sciences**, v. 98, p. 2336-2344, 2009.

MIURA K.; OSAKA K.; YAMAMURA S.; SUGAWARA Y. Noble humidity control system for in-situ X-ray powder diffraction. **Acta Crystallographica Section A**, v. 67, p. C240, 2011.

MONO, T.; SCHOBER, T. Lattice parameter change in water vapor exposed $Ba_3Ca_{1.18}Nb_{1.82}O_{9-\delta}$. **Solid State Ionics**, v. 91, p. 155-159, 1996.

NATIONAL INSTITUTE OF STANDARDS AND TECHNOLOGY. **Standard reference material 676a**. Gaithersburg, 2008. 7 p.

OETZEL M.; SCHERBERICH F.-D.; HEGER G. Heating device for high temperature X-ray powder diffraction studies under controlled water vapour pressure (0-1000 mbar) and gas temperature (20-200 °C). **Powder Diffraction**, v. 15, p. 30-37, 2000.

PAWLEY, G. S. Unit-cell refinement from powder diffraction scans. **Journal of Applied Crystallography**, v. 14, p. 357-361, 1981.

PUIGJANER, C.; BARBAS, R.; PORTELL, A.; FONT-BARDIA, M.; ALCOBÉ, X.; PROHENS, R. Revisiting the solid state of Norfloxacin. **Crystal Growth & Design**, v. 10, p. 2948-2953, 2010.

RASBAND, W. S. **ImageJ**. Disponível em: <http://imagej.nih.gov/ij/download.html>. Acesso em 01 abr. 2012.

RAVINDRA, N. V.; PANPALIA, G. M.; JAGARLAPUDI, A. R. P. S. Norfloxacin sesquihydrate. **Acta Crystallographica Section E**, v. 65, p. o303, 2009.

RIETVELD, H. M. A profile refinement method for nuclear and magnetic structures. **Journal of Applied Crystallography**, v. 2, p. 65-71, 1969.

ROTRONIC. **The Rotronic humidity handbook**: all you never wanted to know about Humidity and didn't want to ask! Huntington, 2005. 130 p. Disponível em: <http://www.southeastern-automation.com/PDF/Rotronic/Humidity_Handbook.pdf>. Acesso em: 20 ago. 2014.

ROY, S.; GOUD, N. R.; BABU, N. J.; IQBAL, J.; KRUTHIVENTI, A. K.; NANGIA, A. Crystal structures of Norfloxacin hydrates. **Crystal Growth & Design**, v. 8, p. 4343-4346, 2008.

SALVI, S. T. B. **Polimorfismo em medicamentos genéricos e similares**. Dissertação (Mestrado em Química) - Instituto de Química, Universidade Estadual Paulista, Araraquara, 2011.

SCARLETT, N. V. Y.; MADSEN, I. C. Quantification of phases with partial or no known crystal structures. **Powder Diffraction**, v. 21, p. 278-284, 2006.

SHAH, B.; KAKUMANU, V. K.; BANSAL, A. K. Analytical techniques for quantification of amorphous/crystalline phases in pharmaceutical solids. **Journal of Pharmaceutical Sciences**, v. 95, p. 1641-1665, 1996.

STINTON, G. W.; EVANS, J. S. O. Parametric Rietveld refinement. **Journal of Applied Crystallography**, v. 40, p. 87-95, 2007.

ŠUŠTAR, B.; BUKOVEC, N.; BUKOVEC, P. Polymorphism and stability of Norfloxacin, (1-ethyl-6-fluoro-1,4-dihydro-4-oxo-7-(1-piperazinil)-3-quinolinocarboxylic acid. **Journal of Thermal Analysis**, v. 40, p. 475-481, 1993.

SWANEPOEL, E.; LIEBENBERG, W.; DEVARAKONDA, B.; VILLIERS, M. M. Developing a discriminating dissolution test for three Mebendazole polymorphs based on solubility differences. **Pharmazie**, v. 58, p. 117-121, 2003.

TAYLOR, D. Negative thermal expansion materials. **British Ceramic Transactions and Journal**, v. 83, p. 92-98, 1984.

TAYLOR, J. C.; MATULIS, C. E. Absorption contrast effects in the quantitative XRD analysis of powders by full multiphase profile refinement. **Journal of Applied Crystallography**, v. 24, p. 14-17, 1991.

TIAN, F.; QU, H.; ZIMMERMANN, A.; MUNK, T.; JØRGENSEN, A. C.; RANTANEN, J. Factors affection crystallization of hydrates. **Journal of Pharmacy and Pharmacology**, v. 62, p. 1534-1546, 2010.

TICEHURST, M. D.; STOREY, R. A.; WATT, C. Application of slurry bridging experiments at controlled water activities to predict the solid-state conversion between anhydrous and hydrated forms using theophylline as a model drug. **International Journal of Pharmaceutics**, v. 247, p. 1-10, 2002.

TITA, D. L. **Caracterização de polimorfos em comprimidos distribuídos pela Secretaria de Saúde de Araraquara por difração de raios X**. Dissertação (Mestrado em Química) – Instituto de Química, Universidade Estadual Paulista, Araraquara, 2014.

TRASK, A. V.; MOTHERWELL, W. D. S.; JONES, W. Pharmaceutical cocrystallization: engineering a remedy for caffeine hydration. **Crystal Growth & Design**, v. 5, p. 1013-1021, 2005.

VILLIERS, M. M.; TERBLANCHE, R. J.; LIEBENBERG, W.; SWANEPOEL, E.; DEKKER, T. G.; SONG, M. Variable-temperature X-ray powder diffraction analysis of the crystal transformation of the pharmaceutically preferred polymorph C of Mebendazole. **Journal of Pharmaceutical and Biomedical Analysis**, v. 38, p. 435-441, 2005.

WAGNER, W.; PRUß, A. The IAPWS formulation 1995 for the thermodynamic properties of ordinary water substance for general and scientific use. **Journal of Physical and Chemical Reference Data**, v. 31, p. 387-535, 2002.

YOUNG, R. A. **The Rietveld method**, 1st ed. New York: Oxford University Press, 1993. 310 p.

YUASA, R.; IMAI, J.; MORIKAWA, H.; KUSAJIMA, H.; UCHIDA, H.; IRIKURA, T. Pharmaceutical studies on hydrates of AM-715 physical characteristics and intestinal absorption. **Yakugaku Zasshi**, v. 102, p. 469-476, 1982.